Low Speed Wind Tunnel Testing and Data Correction Methods for Aircraft Models in Ground Effect

by

Benjamin Albert Broughton

A thesis submitted in partial fulfilment of the
requirements for the degree of

MASTER OF MECHANICAL ENGINEERING

in the Faculty of Engineering

University of Pretoria

PRETORIA

May 1999

To my parents, Benjamin and Letitia Broughton

ABSTRACT

LOW SPEED WIND TUNNEL TESTING AND DATA CORRECTION METHODS FOR AIRCRAFT MODELS IN GROUND EFFECT

By **Benjamin Albert Broughton**

Supervisors:

Dr. C.P. Crosby,

Department of Mechanical and Aeronautical Engineering

Professor E.H. Matthews,

Department of Mechanical and Aeronautical Engineering

Degree: Master of Mechanical Engineering

Keywords: Low speed wind tunnels, ground effect, boundary corrections, tare and interference, moving belt, Heyson's method, moment transfers, external balance, telescopic fairing, blockage corrections

In this thesis, techniques for testing aircraft models in ground effect in a low speed wind tunnel are investigated. Although these types of tests have been done before, the current study is unique in that forces are measured with an overhead balance instead of an internal balance. This has the advantage that the types of models that are difficult to mount on a sting with an internal balance, can often be mounted with a strut protruding from the top of the model. Positioning a sting-mounted model close to the ground at a high angle-of-attack is also usually difficult if not impossible. Finally, drag measurements are often more accurate when measured with an overhead balance rather than with an internal sting-type balance.

The disadvantages associated with this method of testing are identified and solutions suggested. These include accurate moment transfers and correcting for support tares and interference. The thesis also investigates general procedures associated with ground effect testing such as proper boundary corrections and the necessity of a rolling floor.

A simplified preliminary test series was performed in order to identify shortcomings in the existing equipment and procedures. This series is explained in Chapter 2. Chapter 4 and 5 describe changes made to the existing equipment following this test series. These include a novel telescopic fairing to shroud the mounting strut and an internal pitching mechanism. The correction techniques and general theory are summarised in Chapter 3.

The author concludes in Chapter 6 that with the application of the techniques described in this thesis, the test engineer should be able to obtain accurate and reliable data from most aircraft configurations. Additional suggestions for testing models in ground effect are also given in this chapter. Finally, a few shortcomings that still need to be investigated are mentioned at the end of Chapter 6.

SAMEVATTING

LAESPOED-WINDTONNEL TOETS- EN DATA KORREKSIE METODES VIR VLIEGTUIGMODELLE IN GRONDEFFEK

Deur **Benjamin Albert Broughton**

Studieleiers:

Dr. C.P. Crosby,
Departement van Meganiese en Lugvaartkundige Ingenieurswese

Professor E.H. Matthews,
Departement van Meganiese en Lugvaartkundige Ingenieurswese

Graad: Magister in Meganiese Ingenierswese

Sleutelwoorde: Laespoed-windtonnels, grondeffek, wandkorreksies, sleur- en steuringseffekte, rolvloer, Heyson se metode, momenttransformasies, eksterne balans, teleskopiese windskerm, blokkasie korreksies

Hierdie verhandeling ondersoek tegnieke om vliegtuigmodelle in grondeffek in ’n laespoed-windtonnel te toets. Alhoewel hierdie tipe van toetse al voorheen gedoen is, is die huidige studie uniek deurdat ’n oorhoofse balans eerder as ’n interne balans gebruik word. Die voordeel hiervan is dat modelle wat moeilik op ’n naald- of “sting”-balans monteer kan word, baie keer makliker monteer kan word met ’n stang wat deur die bokant van die model steek. Posisioneering van ’n naald-gemonteerde model naby aan die vloer van die tonnel by hoë invalshoeke is gewoonlik ook baie moeilik indien nie onmoontlik nie. Laastens is sleurkrag-metings wat met ’n oorhoofse balans gemeet is gewoonlik meer akkuraat as sleurkrag-metings wat met ’n interne naald-tipe balans gedoen is.

Die nadele wat met hierdie toetsmetode geassosieer kan word, word geïdentifiseer en moontlike oplossing word voorgestel. Hierdie sluit die berekening in van akkurate moment-transformasies en monteersleureffekte en -steurings. Die verhandeling ondersoek ook algemene prosedures wat met grondeffektoetse geassosieer kan word, byvoorbeeld akkurate wandkorreksies en die nodigheid van die rolvloer.

’n Vereenvoudigde vooraf-toetsreeks was uitgevoer om moontlike tekortkominge in die bestaande toerusting en prosedures te identifiseer. Hierdie toetsreeks word in Hoofstuk 2 bespreek. Hoofstuk 4 en 5 verduidelik die veranderinge wat aan die bestaande toerusting gemaak is na aanleiding van hierdie toetsreeks. Hierdie veranderinge sluit ’n teleskopiese windskerm in om die monteerstang te isoleer van die wind, sowel as ’n interne heimeganisme om die invalshoek van die model te verstel. Die korreksieprosedures en algemene teorie word in Hoofstuk 3 opgesom.

Die outeur se gevolgtekking in Hoofstuk 6 stel dat die toetsingenieur, met behulp van die gebruik van die tegnieke in hierdie verhandeling beskryf, in staat behoort te wees om betroubare metings te kan neem van meeste vliegtuigkonfigurasies. Verdere voorstelle vir die toets van modelle in grondeffek word ook in hierdie hoofstuk gemaak. Uiteindelik word ’n paar tekortkominge genoem wat moontlik in ’n toekomstige studie ondersoek kan word.

TABLE OF CONTENTS

LIST OF FIGURES

Number *Page*

LIST OF TABLES

Number *Page*

ACKNOWLEDGEMENTS

The author wishes to thank the following persons and institutions for their contribution to this research:

Dr. Charles Crosby for his support and assistance. Without his leadership and supervision this thesis would not have been possible.

José Martins for helping both on a technical and an administrative level. Without him this project would never even have been initiated. Also for his willingness to allow (and help) me to test after-hours, over weekends and on public holidays in order to complete the experimental work in time.

The Defence Aeronautics program at Aerotek (now Defencetek), C.S.I.R., for granting the funding for the research and again I would like to thank José Martins, Trevor Kirsten and Dr. Rob Hurlin in particular. Also for the people at the C.S.I.R. who helped with the wind tunnel testing. In particular I would like to thank Peter Skinner for his help with the software and Danie von Willich for assisting me with the actual testing.

The people from Manserv at the C.S.I.R. for manufacturing the pitching mechanism and also for helping with the manufacture and modification of various brackets and electrical devices.

Chris Adrian for allowing me to use the C.S.I.R. composites workshop (now LST) and for giving immeasurable advice on composites manufacturing. I would also like to thank him and the rest of the workshop personnel for always finding time to help and give advice.

I would like to thank my parents for all their support and encouragement until now.

Finally, I would like to praise the Creator for His obvious presence throughout my studies.

NOMENCLATURE

$\bar{c}$	Mean aerodynamic chord (also MAC)
α	½ Thread angle
α	Angle of attack
γ	Strength of trailing vortex
χ	Wake skew angle
ρ	Air density
δ	Correction factor
μ	Friction coefficient
ζ	Ratio of tunnel semi-height to model height (H/h)
γ	Ratio of tunnel width to height
Λ	Wing quarter-chord sweep angle
$\Delta\alpha i$	Induced AOA
τ_1	Solid blockage coefficient due to wind tunnel/model relation
λ_3	Body-shape factor for three-dimensional bodies
ΔC_D	Drag coefficient increment in ground effect
ΔCD_i	Induced drag coefficient increment in ground effect
ΔC_L	Lift coefficient increment in ground effect
ΔC_M	Pitching moment coefficient increment in ground effect
ΔC_{mRPt}	Change in pitching moment coefficient about a reference point due to the tail
ΔD_B	Change in drag due to buoyancy
ε_{sb}	Solid blockage ratio
η_t	Ratio of dynamic pressure at tail to dynamic pressure at wing
η_t	Ratio of dynamic pressure at tail to that at the wing. Also used to account for "blanketing" of tail by fuselage
α_t	Tail incidence angle
σ_w	Ratio of wing-span to full test-section width
ε_{wb}	Wake blockage ratio
ζ_x	$\zeta\frac{x}{H}$
ζ_y	$\zeta\frac{y}{H}$
ζ_z	$\zeta\frac{z}{H}$
a	Radius of cylinder modelled by doublet
AC	Wing Aerodynamic centre (1/4c)
A_m	Momentum area
AOA	Angle of attack
AR_t	Tail aspect ratio
A_T	Windtunnel cross-sectional area
b	Geometric wing span
B	Tunnel semi-width

b	Wing span
b_e	Effective vortex span
BTC	Balance to centre distance
BTF	Balance to floor distance
b_v	Vortex span
c *(subscr.)*	Corrected
C	Tunnel test section area
C.S.I.R.	Council for Scientific and Industrial Research, Pretoria, South Africa
C_D	Wing or model drag coefficient
C_{D0}	Zero-lift drag coefficient
C_{Di}	Induced drag coefficient
C_L	Wing or model lift coefficient
C_{LW}	Wing lift coefficient (typically measured by tail-off testing)
C_M	Pitching moment coefficient
C_{mRP}	Pitching moment coefficient about a reference point
C_{mRPt}	Pitching moment coefficient about the reference point due to the tail
D	Drag
$D_{inverted}$	Drag on model when tested inverted. This should be equal to $D_{upright}$, except for possible misalignment
d_m	Screw diameter
D_{meas}	Measured drag
dp/dl	Slope of static pressure variation in test section
$D_{upright}$	Drag on model when tested upright
F	Axial force
$F_{subscript}$	Force, sometimes also refers to moment
G.E.T.S.	Ground effect test section
h	Height of model above tunnel floor
H	Tunnel semi-height
Hrp	Height of reference point at zero AOA
$I_{fairing}$	Interference on model and exposed part of upper strut due to strut fairing
I_{lower}	Interference due to lower support system
$I_{M/u\text{-}strut}$	Interference on model due to exposed part of upper strut
I_{upper}	Interference due to upper support system
$I_{u\text{-}strut/M}$	Interference on exposed part of upper strut caused by model
K	Number of superimposed wakes from vanishingly small models
K_1	Solid blockage coefficient for wing
K_3	Solid blockage coefficient for fuselage
K_t	Number of superimposed wakes used to model tail
L	Measured lift-force
l	Pitch length
$LSWT$	Low speed wind tunnel
lt	Tail-length, typically AC_{wing} to AC_{tail}
MAC	Mean aerodynamic chord
M_t	Tunnel mass flow
M_u	Longitudinal mass flow due to drag
M_w	Vertical mass flow due to lift
n	Ratio of final induced velocities in the far wake to initial induced velocities at model
PVT	Pivot
Q	Source strength

R	Radius of tunnel jet
s	Semi-span
S	Wing area
S_t	Tail area
t	Body maximum thickness
T_{lower}	Tare on lower strut
T_{upper}	Tare on upper (actual) strut
u *(subscr.)*	Uncorrected
u_0	Mean longitudinal induced velocity
u_D	Longitudinal induced velocity due to drag
u_L	Longitudinal induced velocity due to lift
V	Tunnel velocity
w	Downwash velocity
w_0	Vertical mean induced velocity at model
w_D	Vertical induced velocity due to drag
w_L	Vertical induced velocity due to lift
w_h	Reference velocity
WIG	Wing-in-ground effect (vehicle)

Chapter 1

Introduction

1.1 Summary

Ground effect is sometimes neglected in the preliminary study of a new aircraft design and very often during the wind tunnel testing phase. In this chapter, the motivation behind the current research is summarised. It also includes a short summary of the history and state-of-the-art in wind tunnel ground effect testing. The current study is unique in that it makes use of an external balance for the measurement of the forces on the model. Possible problems to be expected during the development of the testing procedures and data reduction methods are identified. Finally, the strategy followed during the current research is summarised.

1.2 Ground effect

Ground effect can be described as *the effect the close proximity of a surface, such as the ground, has on an object moving through a fluid, such as an aircraft flying close to the ground*. Most aircraft experience ground effect at least twice during their mission profiles: when taking off and when landing. Unfortunately, this is one of the aspects of a new aircraft's flight characteristics that can sometimes be neglected during the initial analysis, and very often during the wind tunnel testing phase of an aircraft's development.

Reasons for neglecting ground effect testing include the following:

1. Most aerodynamacists assume the effects of the ground to be negligible during most phases of the typical mission profile.

2. Ground effect is normally stabilising of nature and can be ignored since it is not a "worst case" scenario.

3. A simple analysis such as a panel method should give reasonable answers.

4. Wind tunnel testing is prohibitively costly and complex.

5. No dedicated ground effect wind tunnel testing facility is available in a country such as South Africa.

Statements 1 and 2 are normally true for most types of aircraft. Still, there are examples of problems that can be overlooked if ground effect analysis is completely ignored. One such an example might for instance be that one needs to verify if the ground effect is not going to change the aircraft stability and pitching moment in the landing configuration so much, that the pilot will run out of elevator control when flaring for a landing. Another may be to find out how ground effect changes an unconventional aircraft configuration such as a canard-configured aircraft's longitudinal stability. When designing a new Wing-In-Ground effect (WIG) vehicle, one needs to verify its optimal operational height. These are all typical questions that should be answered long before a new aircraft's development runs into the prototype phase.

Statement 3 is again valid in many cases, but modelling very complex aircraft configurations can sometimes be difficult and again it is important to verify the answers and more specifically the assumptions at some stage. Also, by the nature of panel methods, the flow is assumed to be inviscid. Effects caused by viscosity will probably have to be predicted by a full CFD analysis, which is extremely costly for a complex body such as a full aircraft.

It was the purpose of this study to tackle problems 4 and 5. Firstly, it was aimed at developing the expertise and equipment needed to perform ground effect testing in South Africa for both local and international clients. Secondly, it was aimed at doing so in an affordable manner by upgrading existing equipment rather than developing a whole range of new and costly specialised equipment.

1.3 Wind tunnel testing procedure

Wind tunnel testing roughly consists of the following stages:

1. Design and preparation of the model to be tested.
2. Experimental set-up of model and equipment in the wind tunnel.
3. Actual testing of the model.
4. Reducing data to a usable form.
5. Analysis and interpretation of data.

Each of these stages could be unique for a specific type of test, or for a specific model. In this thesis an attempt was made to reduce some of these stages to standard methods for the specific type of tests attempted here, i.e. ground effect testing.

The design and preparation of the model will of course always depend on the specific type of aircraft. A large amount of time can, however, be saved if mounting techniques and interfaces can be standardised as far as possible. This is not always possible, due to the large variety of aircraft designs out there. However, an attempt was made to design the mounting equipment in such a way that it should not be too difficult to modify existing models to use the available equipment. These modifications should normally be small and not too costly. All tests in this thesis were done on a generic, straight-wing model of a size typical for models used in the C.S.I.R. low speed and medium speed wind tunnels.

It is also important that wind tunnel equipment are modular and that it can be used without modification to the wind tunnel as far as possible. In the design of support struts and fairings, one should also be careful to ensure that this equipment can easily be installed by the minimum number of people and that this installation can be done in such a way that the exact locations of everything are as repeatable as possible. Any slack in hinges and actuators should be kept to a minimum and stiffness is of utmost importance. In this thesis, it was attempted to keep these general guidelines, which are often conflicting, in mind as far as possible.

To save time during the testing phase, it is also important to carefully prepare a test schedule that will keep the actual testing-time, as well as the tunnel occupation-time, to a minimum as far as possible. Again, standardising to some extent can reduce this time considerably. Part of the present research was an attempt to identify which tests should be done in what sequence to minimise the time spent to complete a test series. It was also attempted to single out tests that are unnecessary, either because they are repetitive or because they attempt to obtain data irrelevant to the type of test being done.

The data-reduction phase of the testing procedure is one phase that can be standardised to a very large extent. A large part of this thesis will concentrate on this component of a typical test-program, since mistakes here can easily nullify the final data. Basically, the data-reduction phase starts out with the raw data as obtained from the various measuring tools and reduce it to a form that is convenient for interpretation, such as graphs or tables. Paragraph 1.5 in this chapter will go into more detail on this topic.

Finally, the analysis of the data is that stage at which the engineer actually starts interpreting the data. In this stage, knowing what to look for and what the accuracies are is very important. Before even starting the tests, the engineer should know what he actually wants to learn from these tests. In the current research, some time was also spent to understand what could be learnt about a design by performing wind tunnel ground effect tests.

1.4 Typical problems associated with ground effect tests

The most obvious problem in performing wind tunnel ground effect tests is the one of mounting the model. Most wind tunnel set-ups simply place the model in the centre of the tunnel and then cancel out the effect of the boundaries at the data-reduction stage. During ground effect testing, the engineer is interested in knowing the effect a ground plane would have on a model flying at different heights above that plane. For this reason, these tests are impossible without a means of changing the distance between the model and the ground plane. In other words, either the model itself or the ground plane needs to be moved. Again an attempt was made to make possible this adjustment in such a way that it can be done easily and quickly, without redesigning the whole test-section.

Another problem is that of boundary layers inside the test-section. This is normally not a problem, since conventional wind tunnel testing is done far outside the effect of the boundary layer. In ground effect however, the model can move so close to the tunnel-floor that the boundary layer on the floor can directly affect the measured data. How large this effect is, at what height it becomes a concern and how to correct for it were all studied in this thesis.

As will be seen later, correcting for the boundaries can be rather unique for ground effect testing. Normally, one is interested in knowing how the real aircraft will behave far from the ground in open air. The effects of the four wind tunnel walls thus have to be cancelled out. Most standard boundary-correction techniques are based on cancelling out all four boundaries. In the case of ground effect testing, in contrast, one is interested in knowing how the real aircraft will behave near the ground. Boundary-corrections need to correct out the effect of only three of the four boundaries. Additionally, the remaining floor has to be “extended” to infinity. A major part of the research was aimed at finding methods to do this and in evaluating and verifying these methods.

Finally, the problem of dynamic testing versus static testing arises. Basically, when an aircraft is landing or taking off, it is moving at a certain rate towards or away from the ground. Simulating this effect is difficult and specialised (but it has been done), so that it was decided to aim the current research only at performing static tests. With certain modifications, however, it should not be too difficult to extend the capability of the current facility into dynamic ground effect testing.

1.5 Data reduction

Since a large part of the typical wind tunnel testing program is spent on tests needed to perform the data reduction, a short summary of what has to be corrected is in order here.

As mentioned earlier, the raw data obtained from wind tunnel tests are not usable until it has been corrected for the various differences between testing inside a tunnel and flying the real aircraft in free-air. The various corrections include:

- Buoyancy-effects due to streamwise static pressure variations: The static pressure in the wind tunnel may vary in the streamwise direction for various reasons, such as build-up of the boundary layer, inaccuracies in the tunnel, or taper of the test-section. Usually, this variation can be described by some polynomial that varies with the dynamic pressure or tunnel-velocity. Since a body in the tunnel will experience a different pressure in front of it than behind it, the body will experience a "drag" –force of which the direction will depend on the specific wind tunnel. This buoyancy-force can be corrected for, if the static pressure variation is known.

- Flow direction: Most wind tunnels have a slight up-flow or down-flow at different locations in the tunnel. This can cause a slight offset between the model incidence and the actual angle-of-attack experienced by the model.

- Weight tares: Since the model itself has a certain weight, the balance has to be set to zero before a test run. This, however, is not sufficient on its own. Most models do not have their mass centres located on their hinge-points. This means that, as the model incidence is changed (as in an angle-of-attack run), the model centre of gravity (CG) will change relative to its hinge point. This causes a change in the pitching moments. Since it is virtually impossible to manufacture everything perfectly, some of the other forces and moments may also be affected slightly by this CG change. "Weight-tare" runs can correct these effects.

- Tare and interference corrections: Since it is impossible to fair the complete mounting strut, a portion of it is normally exposed to the wind, which causes additional forces and moments to be measured. These "tare" values have to be corrected out. Additionally, the presence of the strut/fairing close to the model causes interference in the flow-field, and these "interference" values also have to be corrected out. Usually, the only way to correct for these effects is to do a range of additional tests, which will be discussed in great detail in a Chapter 4.

- Blockage corrections: Any solid body in the wind tunnel, as well as any wakes, will cause blockage effects. These effects cause the dynamic pressure on the model to be slightly different from the dynamic pressure expected due to the wind speed in the tunnel. These effects are usually corrected for by using standard graphs and tables for the specific set-up.

- Moment corrections: The virtual-centre of the balance (that position about which the balance measures all the moments), very seldom agrees with the hinge point and almost never with the model's neutral point or the wing's aerodynamic centre. For this reason, all the measured moments have to be transformed so they are given about some convenient point. For tests where the model constantly changes position relative to the balance's virtual-centre, such as ground effect tests, these corrections can be very time-consuming if not done with a computer.

- Boundary corrections: These were mentioned before and basically correct the data for the proximity of the tunnel boundaries.

- Axis transformation: Not really a correction, but in this step the axis about which all forces and moments were calculated can be transformed to another system. For instance, the data can be transformed from the wind-axis to the stability-axis.

In this thesis, all the above-mentioned corrections were studied and incorporated where necessary. Special attention was given to those corrections requiring special methods for ground effect testing.

1.6 A short history of Ground effect testing

1.6.1 Analytical studies

Ground effect is not particularly complex to model for basic, high-aspect ratio wings. Recently however, very little has been done on this from an analytical viewpoint. There are a number of publications, which study "special" cases, such as unsteady aerodynamics near the ground [1], the effect on small aspect-ratio wings [2] and thickness-effects near ground effect [3]. As can be seen, these are all for very simple and specific problems. Although they are very informative on the nature of ground effect, their actual use in the development of a new aircraft is very limited. One advantage is that some of these research examples look at unsteady effects. This is very difficult to model with most numerical models such as panel methods, and also extremely difficult to measure from an experimental point of view. In these specialised cases, the analytical methods can possibly prove useful for getting a better understanding of a particular problem.

Another specialised case of analytical ground effect modelling, is a paper by Qian-Xi Wang [4]. In this case, Wang looked at a "wavy" ground effect such as a Wing-in-Ground effect (WIG) vehicle might experience when flying close to the sea.

As can be seen from the above, analytical methods are useful for very specialised cases, but for the general case of a full aircraft taking-off or landing, these methods are very limited. This is one justification for the present research where information about a complete aircraft in ground effect is needed. For this type of research, the complex geometry of a full aircraft including a tail and fuselage is beyond the scope of most analytical methods. Even if such methods did exist, their accuracy with all the assumptions they would entail would be very suspect.

1.7 Numerical studies

In this regard, the current state of the technology actually does allow for very accurate modelling of full aircraft geometries in ground effect. Examples of this type of research do sometimes appear in the literature. Studies also vary in the complexity of the geometries modelled. An example of 2-dimensional modelling is the research conducted by Dragos & Dino [5]. They described a method that uses boundary integral equations to predict the characteristics of a lifting airfoil near the ground. Again, though very informative, this method will not really help much in the prediction of the 3-dimensional characteristics of a full aircraft.

Interestingly enough, very few examples appear in the literature of research done with panel methods on complex geometries in ground effect. This is usually very straightforward and can be handled in two different ways:

- Modelling the ground plane by using an image system.
- Modelling the ground plane using source panels, vortex panels or doublet panels.

Both these methods are valid and the selection of a specific method will depend on the specific case to be modelled. Most panel-method software allows for the former, since there are fewer uncertainties involved. Later in this thesis, panel methods will be used to evaluate the accuracy of some of the boundary correction methods.

1.7.1 Empirical and semi-empirical methods

An excellent summary of available empirical methods is that published by Shigenori Ando [6] in regard to the design of Wing-in-Ground (WIG) effect vehicles. This is the method usually used in the design of new aircraft or WIG effect vehicles and specifically for initial performance estimations. Although these methods work well for an initial design-stage, they are based on available data and always have to be verified by extensive wind tunnel and ultimately prototype flight-testing.

1.7.2 Experimental studies

At different stages in the aviation history, scientists and engineers became interested in ground effects, its possible uses and the dangers. As can be seen from the above, mathematical prediction of ground effect can be limited and for this reason, various techniques were developed to test models and full-scale aircraft in ground effect.

The most obvious experimental method is to test a full-size aircraft near the ground. The first dedicated ground effect tests that could be found in the literature were those conducted on a Douglas F5D-1 aircraft with an Ogee wing modification in 1966 [7]. These tests were repeated in various wind tunnels. It seems that no wind tunnel boundary corrections were made for the wind tunnel tests, and consequently the data varied to quite an extent between the flight tests and wind tunnel tests. Interestingly, placing the actual aircraft in the Ames 40x80 feet wind tunnel gave excellent agreement with the flight-test data. In this case, the tunnel was very large in relation to the aircraft. This could be seen as a first indication that proper wind tunnel boundary corrections are essential for obtaining accurate ground effect results.

Another set of ground effect flight-tests were those conducted on the Comet 3B in 1968 [8]. Again there were some discrepancies between the flight-tests and wind tunnel tests, although those were attributed to other factors than boundary-effects at the time. From both the above reports, it was clear that ground effect flight-tests are difficult to perform and impractical for most flight-test programs.

A very complete study was recently done by Deutsche Airbus GmbH on an Airbus A320 model [9]. Although these tests focused primarily on the Turbine Power Simulation (TPS) aspect of the tests, they are very close to the type of tests that were the final objective of this thesis. A major difference between these tests and the tests conducted at the C.S.I.R. is that Airbus used an internal balance. Many of the test procedures used by Airbus were also adopted in the current study. Figure 1-1 shows the basic set-up in the DNW wind tunnel. Note the use of a moving ground-plane and a sting-support with an internal balance.

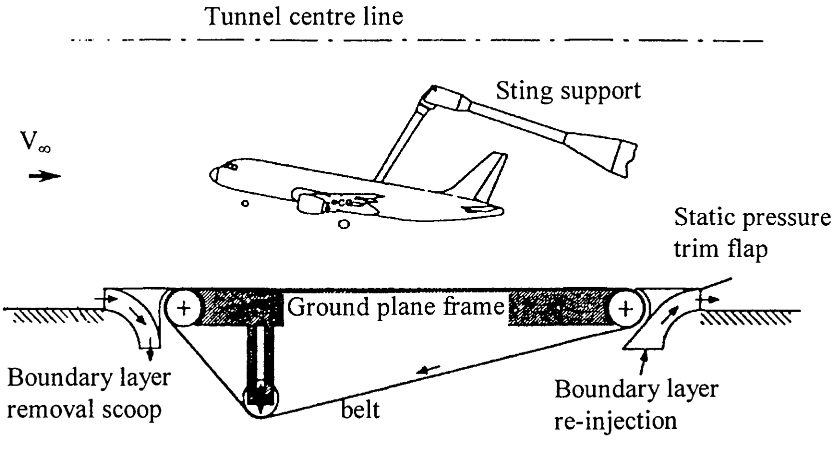

Figure 1-1: Static ground effect testing. Reproduced from reference [9].

Figure 1-2 shows the method used to control the model angle-of-attack and vertical height. Although the principle used in this thesis was similar, the use of an overhead external balance basically precluded using the same set-up. The equipment developed during this thesis did, however, eventually allow simple height-adjustment of the model and automatic angle-of-attack adjustment during a typical test.

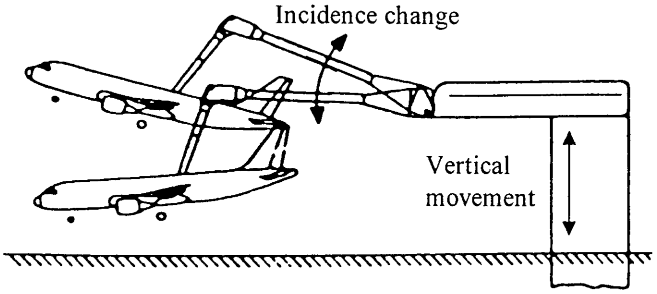

Figure 1-2: Static ground effect testing, model adjustment. Reproduced from reference [9].

Finally, some recent ground effect tests done to compare static tests to dynamic tests should be mentioned. The first is an experimental study where the model was moved towards the ground at a constant sink-rate and angle-of-attack [10]. This simple but effective method is depicted in Figure 1-3.

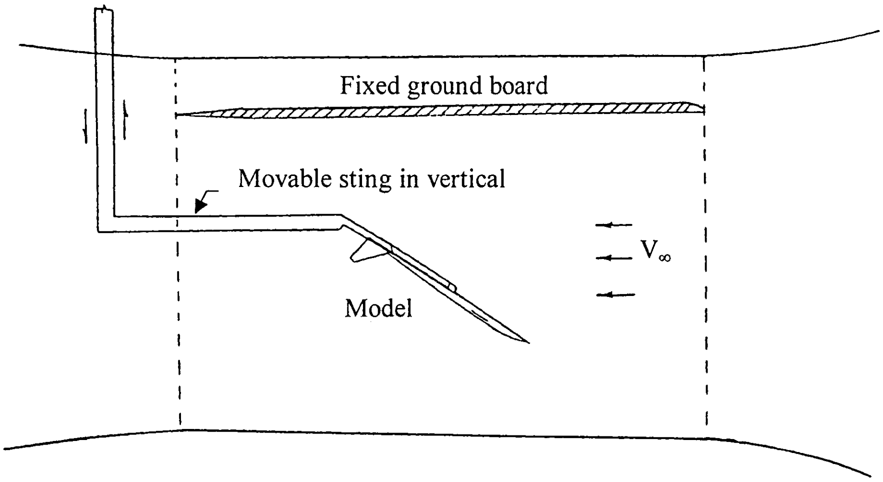

Figure 1-3: Dynamic ground effect testing by the University of Kansas center for Research, Inc. Reproduced from reference [10].

Figure 1-4 shows additional detail on the method used to allow a constant vertical velocity. Note that a dedicated sting/balance had to be made for these tests. The results indicated a small difference between static and dynamic tests. It should be noted that a reason for this uncharacteristically small difference could probably be the fact that the model was a highly swept delta design. As can be seen, this method is slightly limiting in that angle-of-attack is fixed for a specific test-run. To test a whole range of angles of attack would be extremely time-consuming.

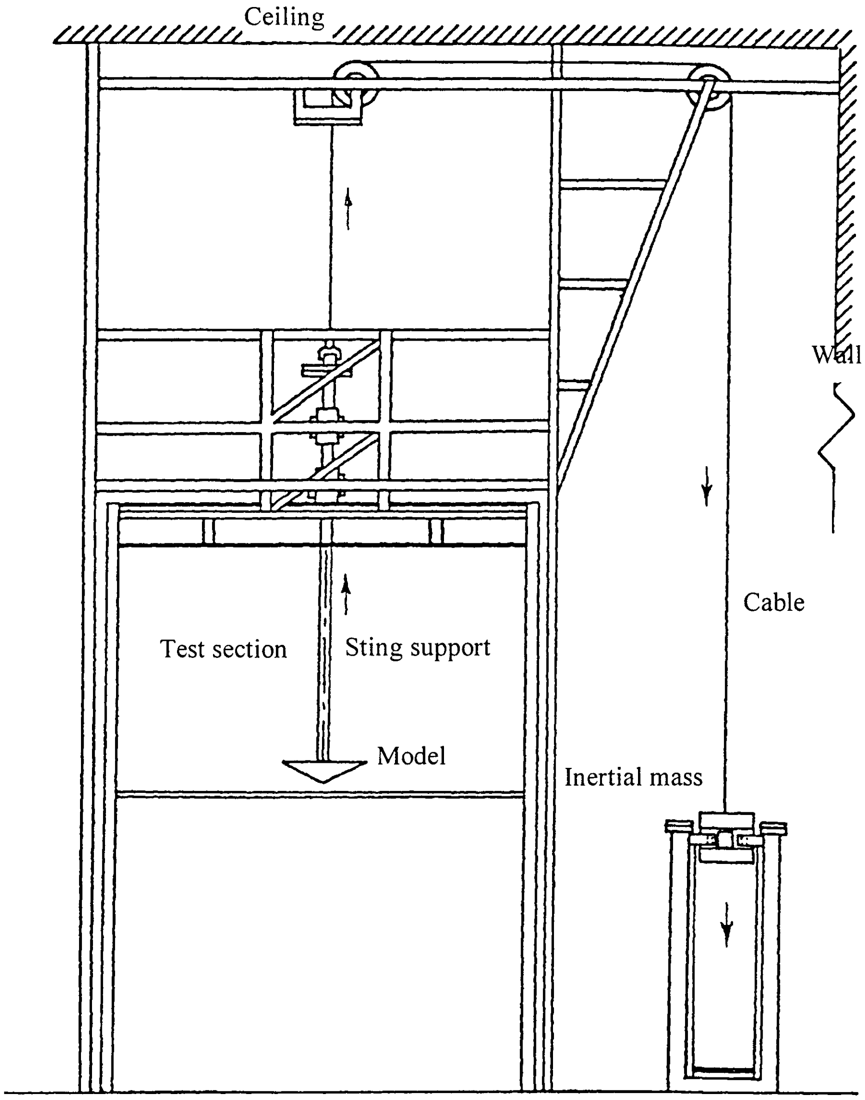

Figure 1-4: Set-up used for dynamic ground effect testing by the University of Kansas center for Research, Inc. Reproduced from reference [10].

During the late 80's, NASA built the Langley Vortex Research Facility (VRF). This facility is uniquely suited for dynamic ground effect testing, in that it uses a moving model over a stationary ground-plane. An internal balance is mounted in the model and the ground-plane is inclined to simulate a set sink-rate. Figures 1-5 and 1-6 illustrate how this facility is used.

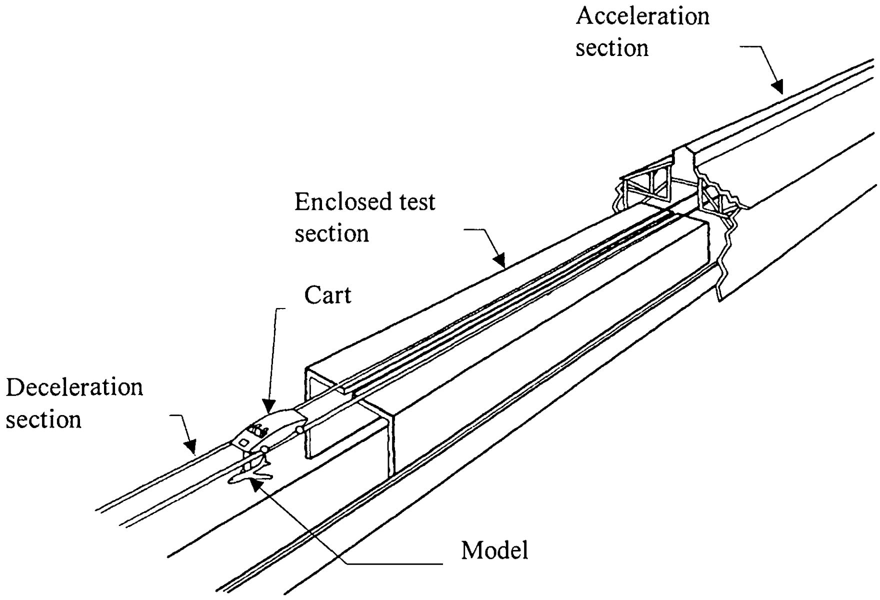

Figure 1-5: Diagram of the Langley Vortex Research Facility. Reproduced from reference [12]

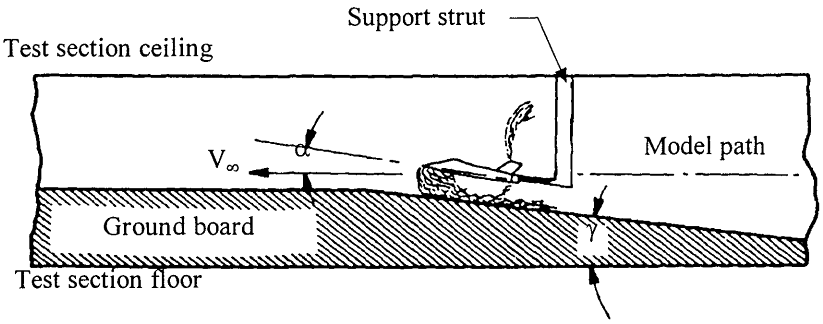

Figure 1-6: Diagram showing inclined ground board used in the VRF. Reproduced from reference [12]

These tests showed a substantial difference between dynamic tests and static tests [11] and [12]. Despite these results, it was decided to limit the present study to static testing.

It should however be noted that it would not be too difficult to extend the capability of the current equipment at the C.S.I.R. to enable dynamic ground effect testing.

1.8 Strategy for this thesis

During the planning phase of the current thesis, it was decided to conduct the research in the following sequence:

1. A thorough literature survey including literature on wind tunnel correction methods.
2. A preliminary testing phase with the minimum amount of changes to existing equipment.
3. Analysis of the preliminary testing method and the results obtained to identify shortcomings.
4. The design of updated equipment as identified in 3.
5. Update of the data-reduction procedures.
6. Verification testing phase.

It was decided to do the preliminary testing directly after the literature survey since this would be the most effective way to determine possible shortcomings. This would also supply a large amount of data that could be used to develop and upgrade the correction software.

After the preliminary testing, the development of the correction software and re-evaluation of all testing techniques were conducted. At this stage, new equipment was designed and manufactured where required.

Finally, the verification-testing phase would be as close as possible to the actual testing procedure that a potential client would require. Due to time and financial limitations, some shortcuts had to be made during this phase, but these were limited as far as possible to techniques that were standard and that did not really require validation. It did however allow the testing of all newly designed and manufactured equipment.

Chapter 2

Preliminary Testing

2.1 Summary

A preliminary test-program was conducted for the following reasons:

1. This would enable the author to get used to the facilities and software.
2. To determine the capabilities of the currently available equipment and facilities.
3. Determine under what conditions the rolling floor becomes a necessity.
4. To obtain data to test the data reduction software on.
5. To identify and understand the shortcomings of the current equipment.
6. To determine whether the overhead balance is accurate and sensitive enough to measure the rather small increments due to ground effect.

The preliminary tests consisted of the testing of a straight-wing configuration in- and out off ground effect and at different heights. The tests were done with the tail on and off, and with- and without the rolling floor. It also included Reynolds number tests to investigate the Reynolds number effects on the specific model.

The initial tests also investigated a simple method of performing tare and interference tests. Although the results were acceptable, this method should only be seen as an interim method since it cannot be used for obtaining aerodynamic data over a complete model. Instead, the data obtained through this method only supplies information on the aerodynamic behaviour of a wing or wing/tail combination.

From these tests the feasibility of the project was confirmed, although a number of required modifications to the existing equipment and techniques were identified. Some of the major issues raised were those of an external- versus internal balance, performing boundary corrections and correcting for support tare and interference.

The results from the initial tests did show all of the expected effects of moving a lifting surface close to a ground plane, namely an increase in lift and a decrease in induced drag. An increase in static stability was also observed, which would be typical for the specific configuration used. It was also shown that the use of the rolling floor is important and does have quite a large effect on the data. It was suggested that future tests should be done with the rolling floor in operation as far as possible.

Some issues raised after these tests were:

- Finding a proper method for performing boundary corrections.
- Developing a better method for support tare and interference corrections.

2.2 Theory

2.2.1 Ground effect

If we consider a simple lifting-line model for a wing, ground effect can be explained using a system of images. Figure 2-1 portrays the two legs of a trailing horseshoe vortex in the transverse plane. The vortex is centred on point *J* along the wing and trails to infinity. The wing is situated at height *h* above the ground.

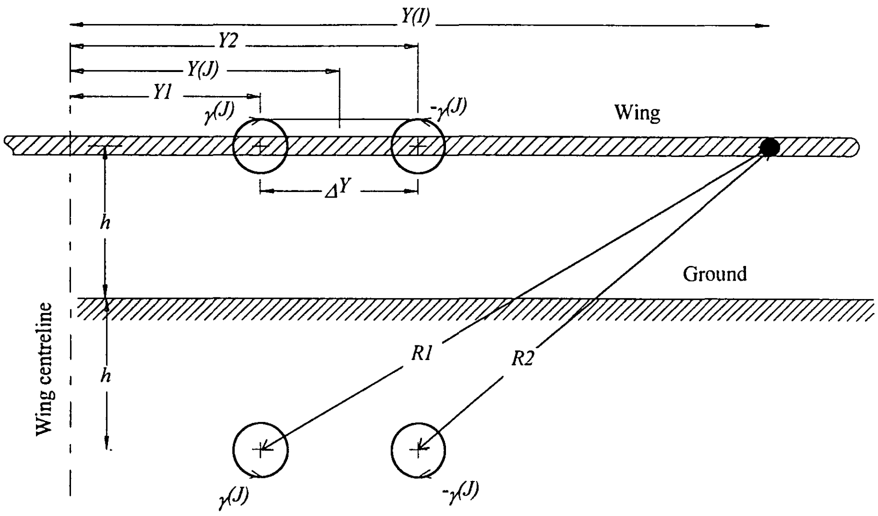

Figure 2-1: Wing in ground effect [13]

Since the ground is a boundary in this case, it can be described by a flow-line in potential flow theory. This means that no flow should cross normal to the ground plane. To obtain this condition, an image system is placed beneath the ground at an equal distance from the ground as the wing. This models the ground by situating a flow line where the ground would be.

The velocity induced by the trailing vortices at point *I* can be calculated as follows [13]:

$$\Delta w(I)=\frac{\gamma(J)}{4\pi}\left[\left(\frac{1}{Y1-Y(I)}\right)-\left(\frac{1}{Y2-Y(I)}\right)\right] \qquad \textbf{(2-1)}$$

And the velocity induced by the image system:

$$\Delta w(I)=-\frac{\gamma(J)}{4\pi}\left[\left(\frac{Y1-Y(I)}{R1^2}\right)-\left(\frac{Y2-Y(I)}{R2^2}\right)\right] \qquad \textbf{(2-2)}$$

Summing these two equations then gives the downwash influence coefficient *w(I,J)*. Since the image system is further away from the control point than the actual model, its effect is opposite but smaller than the model itself. Thus, the effective downwash will be decreased by the image system, which in turn causes an increase in the lift and decrease in the induced drag. These are also the general trends one would expect to obtain during typical aircraft ground effect testing.

2.2.2 Rolling floor

According to the no-slip condition, there can not be any movement on the fluid-body interface when flow occurs around a body. For a viscous fluid, therefore, the total velocity vanishes at the surface. This means that a thin layer of fluid exists around a body where the velocity gradually rises from zero to the free-stream velocity at a small distance from the surface. In a wind tunnel, this boundary layer gets thicker as one move along the surface in the direction of the flow. The problem with ground effect testing is that the model can actually move into this boundary layer situated on the floor of the tunnel. Even if a part of it does not actually move into the boundary layer, the slight deflection of the flow lines can influence the measurements. Since the flow in a real aircraft is relative to the aircraft and not to the ground (disregarding atmospheric winds), the situation in a wind tunnel is not a true representation of the real aircraft in flight. This situation becomes worse as the model moves closer to the ground.

The rolling belt mechanism was developed specifically for testing a vehicle close to the ground. The belt moves relative to the model the same way the ground would move relative to an aircraft in flight. Since there is no relative motion between the belt and the wind, no boundary layer is formed on the tunnel floor. To remove the existing boundary layer in front of the belt, a suction plate with small holes is usually used to suck the boundary layer away. Another method (not used in the current case) is to blow into the boundary layer to restore the energy.

2.2.3 Model

For these initial tests, a generic model was used. The selection of this particular model was due to the fact that it can be configured as a straight-wing, swept-wing or delta-winged model. It can also be mounted in a variety of different ways and can be configured for an internal or external balance. Additionally, the model is simple and can easily be used for computer simulation if such comparison was needed.

Figure 2-2 shows the general dimensions of the straight-wing configuration of the generic model. This model has a low-wing, mid-mounted tail and tubular fuselage. All airfoil sections are NACA0012. The wing has no twist or dihedral. The wingspan is 1200mm and the mean aerodynamic chord 200mm, which gives an aspect ratio of 6.

Although the tail could be removed for tail-on and tail-off tests, the model has no moveable control surfaces. The tail was also set to a fixed incidence angle of 0 degrees, as was the wing. The only instrumentation mounted internally was an inclinometer mounted inside the nose of the model, just behind the nose cone.

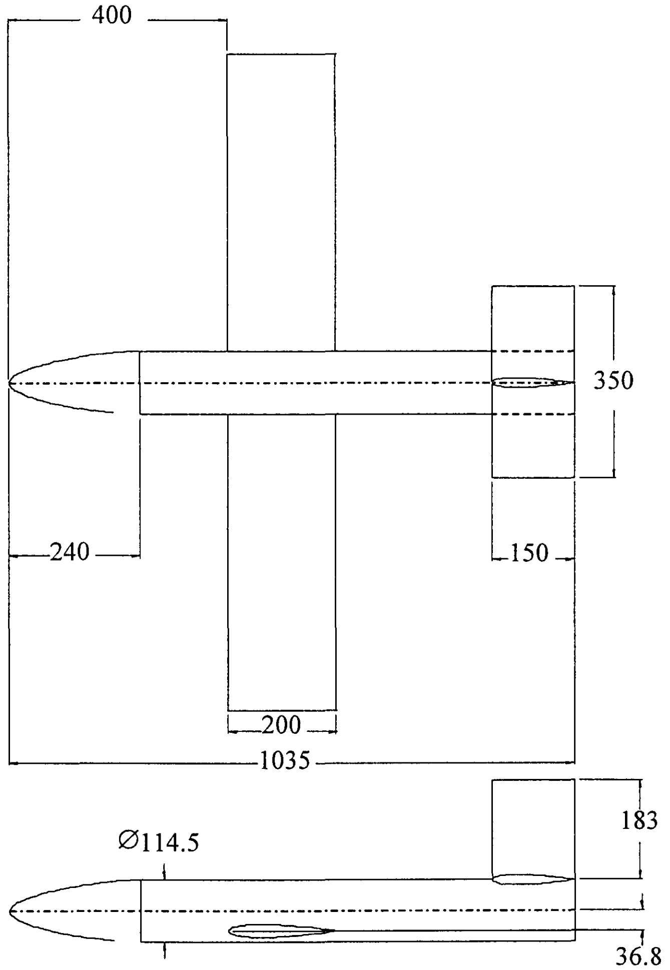

Figure 2-2: Model dimensions

For these initial tests an adapter plate was made for mounting the fuselage inside the wind tunnel without the wing. This plate was necessary since the saddle for mounting the model on the moveable strut is usually mounted directly on the wing. When using the adapter plate and testing without the wing, the openings where the wing used to protrude from the fuselage were simply taped over using aluminium tape.

A tube was also made which protruded from the rear of the fuselage for connecting the back of the fuselage to the pitching strut. (See also Figure 2-4). The rear of the fuselage is closed up using a round plate, which also locates the tube at the rear.

Although this model was designed so it could also be mounted on wing struts, this method was not used during the present study. The openings in the wings for the wing struts were filled using Formula 40 filler that was then sanded flush to the wing surface. The holes were treated with a release wax before filling to enable easy removal of the fillings in future.

2.3 Test facilities and equipment

2.3.1 Wind Tunnel

The aerodynamic test section was used for the initial centre-line tests, while the remaining tests were all performed in the ground effect test section. During testing it is possible to keep the wind tunnel velocity constant within 0.05 m/s, depending on the absolute velocity. After the model stalls, the instability in the wake makes it more difficult to keep the velocity constant. The velocity acquisition software has previously been calibrated for the two different test sections.

The wind tunnel specifications are summarised in Table A-1 in Appendix A.

The arrangement for removing the boundary layer in the C.S.I.R. low speed wind tunnel is shown in Figure 2-3. The system starts with a scoop that is open to the atmosphere. Behind that, the remaining boundary layer is removed using a suction fan. This air is re-routed around the wind tunnel in two large diameter pipes and then blown back into the tunnel behind the test-section.

The rolling floor starts just behind the suction grid. This floor consists of a rubber belt spanning the width of the wind tunnel and is driven by a hydraulic motor. To keep the belt on the drums laterally, a hydraulic steering mechanism connected to the forward drum is used. The control-system uses an optical sensor to measure the belt position. To prevent the belt from lifting up during high-speed operation, a vacuum pump is used to suck the belt down onto the metal backing. During initial tests it was found that the existing vacuum fan was inadequate and two additional portable vacuum fans were added. The floor speed can be controlled quite accurately up to its maximum speed of 35 m/s.

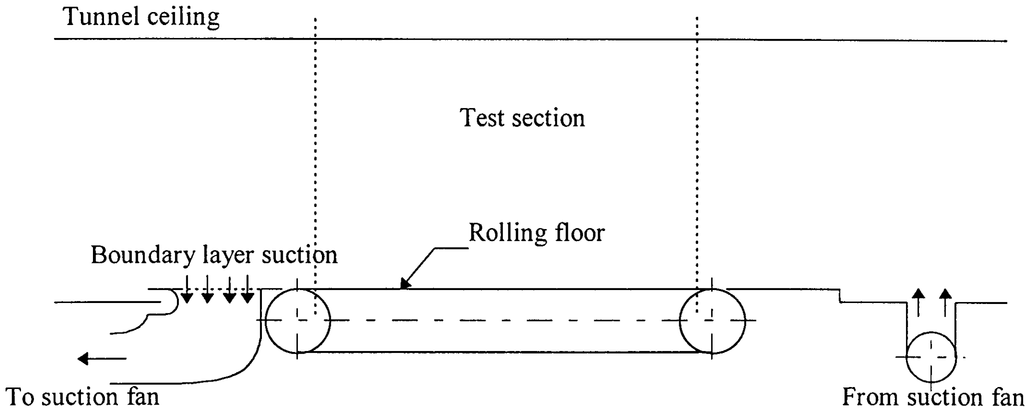

Figure 2-3: Boundary-layer removal system

2.3.2 Data acquisition

All the forces were measured using an external balance. The balance specifications are summarised in Table A-2 and Table A-3 in Appendix A [14].

The data was acquired using the LSWT NEFF 470 data acquisition and control unit. The software used was the existing LSWT control and acquisition software, with slight adjustments for the calibration where required for the specific instrumentation used. For each measurement, 20 samples were taken and their values averaged. At this stage the data was already corrected using a correction matrix for the balance interactions. Temporary coefficient graphs were displayed on the computer after each sample, which made it easy to detect any irregularities in the tests.

2.3.3 Supports

Using the overhead balance for data acquisition necessitates using a strut to mount the model somewhere on its fuselage from the roof. Different struts were used for the centre-line tests and the ground effect tests.

2.3.3.1 Centre-line tests

For these tests, one of the standard saddles was used with a standard strut protruding from the roof. The fairing is connected to the roof of the tunnel in such a way that there are no interaction between the aerodynamic forces on the fairing and those on the balance. The only part of the strut actually protruding into the wind is the short piece just above the model.

The model was pitched by connecting the LSWT pitching mechanism to a 12mm diameter pitching strut. The whole mechanism was also mounted on the balance. The bottom-end of the strut was connected to the tube protruding from the rear of the model using a single pin. The set-up is similar to that shown in Figure 2-4, except for the use of a different strut to locate the model in the centre of the tunnel.

2.3.3.2 Ground effect tests

The ground effect tests were done using the strut previously used for Formula 1 racing cars. This strut consists of a thin inner strut, connected to the saddle, moving inside a larger outer strut. The movement is controlled using a stepper motor that is connected to a screw thread. The internal strut is mounted on a linear bearing. Although the movement can be controlled (within a few fractions of a millimetre) using software, it was decided to control the movement using a joystick. This made it possible to use the existing LSWT software for the ground effect tests as well. A schematic of the model mounted on the strut is shown in Figure 2-4.

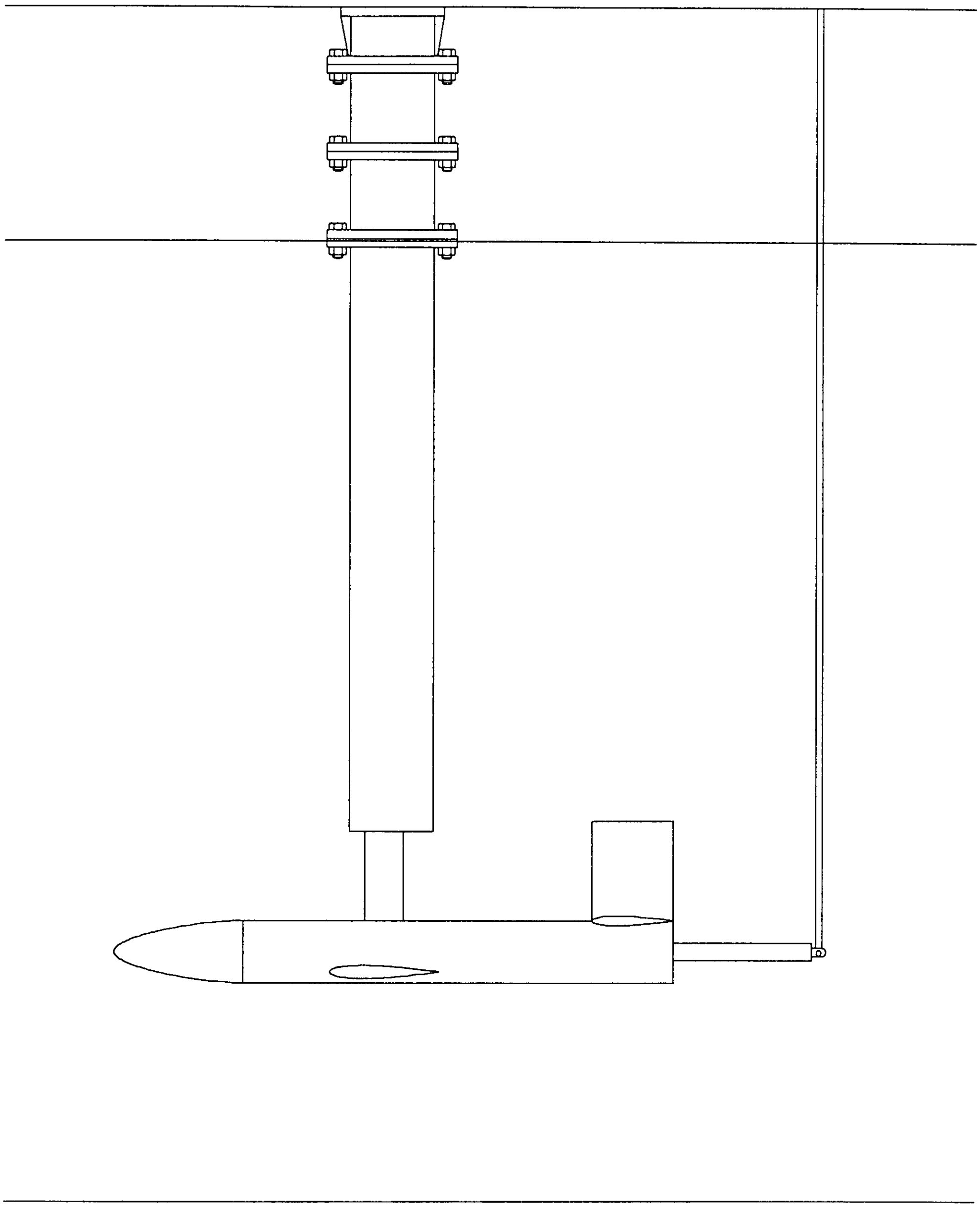

Figure 2-4: Schematic of model mounted in ground effect test section

The linear movement of the internal strut is limited to 160mm, which was sufficient for the Formula 1 tests for which the strut had initially been designed. However, this is not nearly enough for ground effect testing on aircraft. Two flanged inserts were made which makes it possible to change the length of the outside strut as well (See Figure A-1). This effectively allows a travel of 480mm, although the last insert was not removed during the initial tests. This method of lengthening the outside strut is quite time consuming and should be reviewed if commercial testing is ever to be done on a regular basis.

In contrast to the centre-line tests, the fairing for the ground effect tests was mounted directly on the strut. This was largely due to the large size of the strut. Having the fairing mounted on the strut meant that all the aerodynamic forces on the fairing were transmitted to the balance. Since these forces were quite large in relation to the forces acting on the model, the tare and interference corrections had to be done first in order to produce usable data. The fairing also consisted of a number of sections to match the lengths used for the external strut. Again this arrangement is obviously not optimal and was changed after the preliminary testing phase.

The saddle was custom-made for the ground effect tests and is shown in Figure A-2. This saddle is completely enclosed inside the model and connects the strut to either the wing or the mounting-plate if fuselage-only runs are done.

Although it was originally intended to use the pitching mechanism used previously in the Formula 1 tests for pitching the model, it was found that this mechanism did not allow enough travel (160mm plus additional travel for adjusting AOA). However, the mechanism used for the centre-line tests could give as much as 360 mm travel and had the added advantage that the existing control software could be used for conducting the tests. To allow for the different lengths of the main strut, two tail struts were made. They also had different holes along the strut to give extra flexibility in the number of heights for which each could be used. To mount the pitching mechanism on the overhead balance, which had to be turned through 90 degrees for the ground effect tests, it was necessary to make use of an adapter plate between the balance and the pitching mechanism, which was also manufactured specifically for this purpose. Again the unknowns associated with this pitching-strut arrangement would require review of this method after the preliminary tests.

2.4 Data correction

One of the major concerns that had to be addressed for testing in ground effect was the tare and interference correction. Normally the model can be tested inverted and a system of dummy mounts can be used to accurately determine the support tare and interference. With the ground effect testing equipment available at the time, this method would have been virtually impossible. This also meant that a different length of dummy fairing/strut would be required for each height, or that the dummies would have had to be adjustable. These would entail the manufacture of a whole range of new equipment. In addition to these problems, the ground effect test section makes mounting from the floor virtually impossible due to the location of the rolling-floor belt.

To overcome these problems for the initial testing, which was more aimed at obtaining usable data, it was decided to make use of a simplified method that shortens the testing time considerably. However, it must be noted that this method only supplies information on the wing or wing/tail combination and not the whole model. Furthermore, it does not eliminate all the interference effects and therefore only gives a good estimate of the actual forces on the wing and tail.

The method makes use of the fact that the engineer is more interested in the forces acting on the wing in ground effect than on the whole model during this initial testing phase. For each data point, four tests are required: First a weight tare is taken for the model without the wing and the holes where the wing normally protrudes from the fuselage are simply taped up. Then this fuselage-only combination is tested with the wind on and the forces are measured. Thirdly, a weight tare for the complete model is taken and finally the complete model is tested with the wind on.

The actual correction then consists of subtracting the fuselage-only weight tare from the fuselage-only wind-on run. The wing-on weight tare is also subtracted from the wing-on run. Finally the corrected fuselage-only run is subtracted from the corrected wing-on run (in coefficient form). This then gives the forces on the wing, although it disregards interference between the wing and fuselage and the wing and support system. It was found that this method, even with all its assumptions, could supply data that is accurate enough to show all the typical ground effect trends.

The rest of the data correction was done using the standard procedures from Pope and Rae [15]. The sequence was as follows:

1. Weight Tares

2. Tare and interference
3. Blockage
4. Moment Transfers

The tare and interference corrections consisted of the following:

1. Subtract fuselage-only weight tare runs from fuselage-only runs
2. Subtract result from measured data

2.4.1 Buoyancy

As can be seen, no buoyancy corrections were done on the data. This is because the buoyancy effect on a wing alone is very small and usually only taken into account for a body such as a fuselage. Although the tests were done with the fuselage, it must be remembered that the fuselage was taken as part of the mounting system and its effect was subtracted when performing the tare and interference corrections.

2.4.2 Weight tares

The weight tare corrections were done by simply subtracting the weight tare measurements (in force units) from the wind-on runs. Where necessary, the weight tare values were interpolated using linear regression. This feature was already built into the existing correction software.

2.4.3 Support tare and interference

This was done using the new method described above. Some re-programming of the existing software was necessary for this.

2.4.4 Blockage

Both solid and wake blockage were taken into account and calculated using the methods described in chapter 6 of Pope and Rae [15]. The actual values used for the corrections are listed in Table A-4.

2.4.5 Moment transfers

Since the model only moved up and down in the tunnel, the only moment transfers necessary were those affecting the pitching moment. However, since the pivot point was not located exactly on the aerodynamic centre of the model, there was also an interaction with the other moments due to the model changing angle of attack. Moment transfers had to be taken into account due to the following:

1. The aerodynamic centre (taken as ¼ chord for the wing only) was located in front of the hinge point.
2. The aerodynamic centre was located below the hinge point.
3. The hinge point moved due to the adjustable height of the ground effect strut.
4. The hinge point was located slightly in front of the virtual centre

Each of these mismatches caused a pitching moment in one way or another due to the lift or drag not acting through the aerodynamic centre. The actual dimensions are again listed in Table A-4.

2.4.6 Boundary corrections

No boundary corrections were performed on the data, since no proper method had been developed for ground effect tests at this stage. Boundary corrections will be discussed in more detail in Chapter 3. These corrections were expected to be small, which was later confirmed during the boundary correction study.

2.5 Test procedure

For these initial tests, it was decided to test the model with- and without the tail and also in the fuselage-only configuration for the tare and interference purposes as previously described. A complete summary of the initial test program for the straight wing model appears in Appendix A-3.

It must be noted that more than the necessary number of weight tare runs were conducted. This was because the model had to be removed and replaced often for the different configurations. A number of checks were also made after a configuration change (usually deleted again), to check the zero of the inclinometer and change it when necessary. These small changes were necessary since the different components used in a certain configuration could slightly alter the initial angle of the inclinometer after re-assembly. This change was never more than 22', but it was nevertheless reset every time.

As can be seen from the test planning, the centre-line tests were a bit more comprehensive than the ground effect tests and also included some Reynolds number tests.

The sequence for testing in ground effect was as follows:

1. Insert or remove the necessary inserts on the main strut to achieve the required range of heights for the ground effect tests.
2. Choose the required configuration for the model (tail-on, tail-off or fuselage-only).
3. Set the model to the required height using the joystick. A reference point was chosen at the rear of the model for this purpose. The model was first set to the required height. The incidence of the model was then adjusted until zero using the pitching mechanism and a mechanical inclinometer. The height was then verified using a ruler and a square. This method should have given a height accurately to within one to two millimetres, which is quite good since the surface of the belt is not perfectly smooth and flat.

4. The test run was then performed while pitching through the AOA-range. Close to the floor the angle was limited due to the proximity of the moving belt, but higher up the model was always tested past the stall which occurs between 15 and 16 degrees AOA for this model.

5. Steps 3 and 4 were then repeated for the required height range, changing the length of the pitching strut where required.

6. Steps 2 to 5 were repeated for the different configurations.

7. The whole sequence was repeated for the next insert on the external strut.

All the ground effect tests were performed using the boundary layer suction equipment. The fan was set to maximum for all tests since the velocity in the test section was calibrated only for a maximum fan setting. The ground effect testing was initially done without the rolling floor running and then repeated with the rolling floor in operation in order to determine the effect the floor has on the results.

2.6 Results

The complete results are graphically displayed in Appendix A. The graphs are shown as follows in the appendix:

Figure A-3 to Figure A-5: Reynolds number scan

Figure A-6 to Figure A-12: Tail off, Floor off

Figure A-13 to Figure A-18: Tail off, Floor on

Figure A-19 to Figure A-24: Tail on, Floor off

Figure A-25 to Figure A-31: Tail on, Floor on

Some of the results will be summarised or repeated in this chapter for the purpose of their discussion.

2.6.1 Centre line

From the lift curves it can be seen that the model stalls between 15° and 16° angle of attack. The first thing that is immediately obvious in Figure 2-5 is the "kink" in the lift curve around 5° angle of attack. This "kink" causes a slight decrease in the lift curve slope above the corresponding angle of attack. In Figure 2-5 it can be seen that increasing the velocity from 35m/s to 100m/s removes this effect to some degree, indicating a Reynolds number related phenomenon. This was confirmed by a 2-dimensional numerical study with XFOIL and seems to be a characteristic of the NACA0012 airfoil. The results are shown in Figure A-32 in Appendix A-5. Noteworthy is the fact that the stall angle decreases with increasing velocity. C_{Lmax} for this model is close to 1.0 (out of ground effect). The Reynolds number for the wing at 35 m/s was ±410000 and at 100m/s ±1200000 depending on the actual kinematic viscosity.

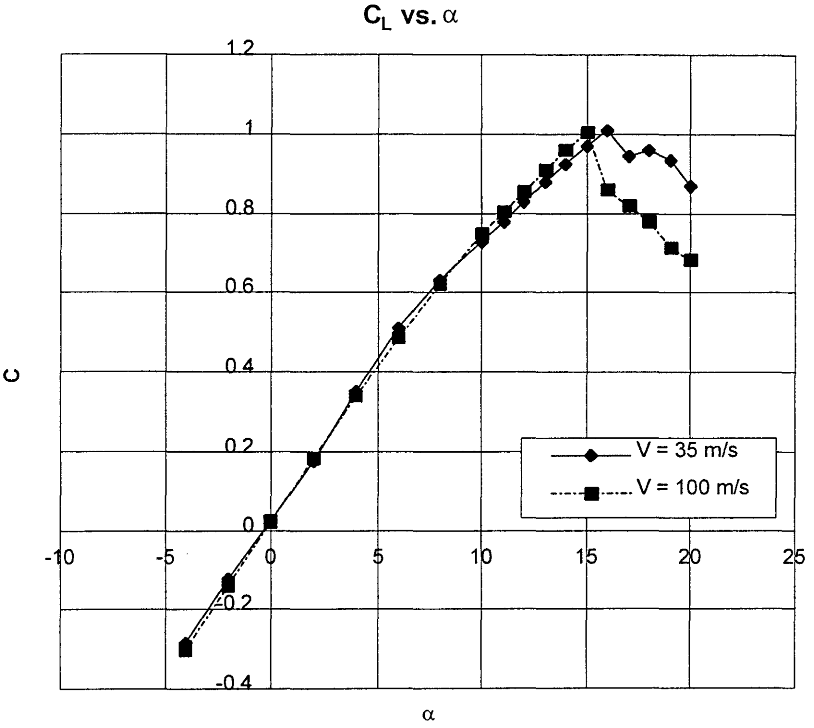

Figure 2-5: Lift-polar at different tunnel velocities

Table 2-1 shows the results obtained after linear curve-fits to the pitching moment data for the tail-off tests, while Table 2-2 shows this data for the tail-on tests. Note that the linear regression was only done on the linear portion of the data, before onset of the stall. These results are also shown graphically in Appendix A-4. Typical pitching moment graphs are shown in Figure 2-8. From these tables and graphs, it can be seen that the pitching moment of the model is neutral for the tail-off configuration and stable for the tail-on configuration. The model is also shown to have stable stalling characteristics both with- and without the tail, as can be seen in the pitching moment graphs in Figure 2-8 and Appendix A-4.

H_{rp}	y-intersect	Slope (1/deg)	Slope(1/rad)
104.5	0.0145	-0.0019	-0.1102
184.5	-0.0072	0.0001	0.0058
262	-0.0069	0.0002	0.0138
302	0.0063	0.0006	0.0324
342	0.0073	0.0003	0.0176
422	0.0156	0.0007	0.0395
Centre	-0.0001	0.0045	-0.0040

Table 2-1: Linear regression on pitching moment slope. Tail-off, Rolling floor on.

H_{rp}	y-intersect	Slope (1/deg)	Slope(1/rad)
104.5	-0.0181	-0.0211	-1.2075
184.5	-0.0339	-0.0169	-0.9664
262	-0.0320	-0.0152	-0.8713
302	-0.0265	-0.0151	-0.8639
342	-0.0255	-0.0147	-0.8417
422	-0.0337	-0.0142	-0.8145
Centre	-0.0172	-0.0120	-0.6849

Table 2-2: Linear regression on pitching moment slope. Tail-on, rolling floor on.

The drag on the model decreases slightly with increasing velocity/Reynolds number. From Figure 2-6 this seems to be true for both the zero-lift drag and the induced drag for this model.

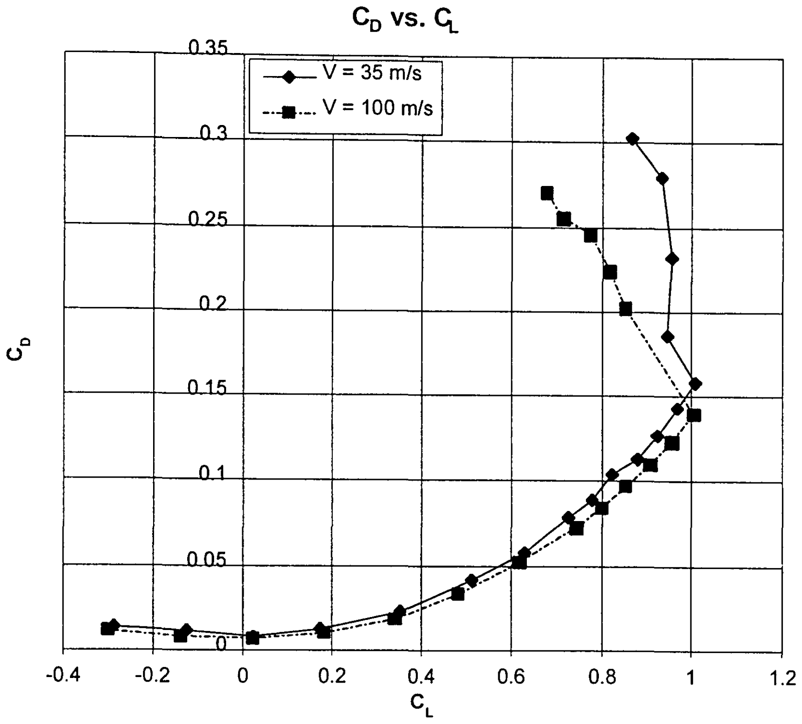

Figure 2-6: Drag polar at different tunnel velocities

2.6.2 Ground effect

From Appendix A-4 and Figures 2-7, 2-8 and 2-9, it can be seen that the ground effect was significant enough to be measured with the existing equipment. The four complete sets of graphs in the appendix show the following results: tail-off with- and without the rolling floor and tail on with- and without the rolling floor. The figures in this section summarise the extreme cases. The graphs consist of the standard lift, pitching moment and drag curves. On each graph the different curves represent the different heights. H_{rp} refers to the height of the reference point (1/4 chord) above the floor in the zero-degree incidence position. In addition to the standard graphs, increment graphs are also shown. These graphs show the increment of coefficients above the centre-line values, which represent the model characteristics at infinite height or free-air. The values on the graphs were calculated by subtracting the centre-line value from the in-ground effect value at each angle of attack. In the case of drag, this was done at different C_L values, interpolating where necessary.

As can be seen from the data, the C_{D0} values were slightly different at the different heights in addition to the induced drag values. Since the ground effect theory principally affects the induced drag, this drag-component was isolated by subtracting the C_{D0} values from the total C_D values. Figure A-11 shows the increment in total drag, while the ΔC_D graphs following that in the appendix only show the isolated induced drag components.

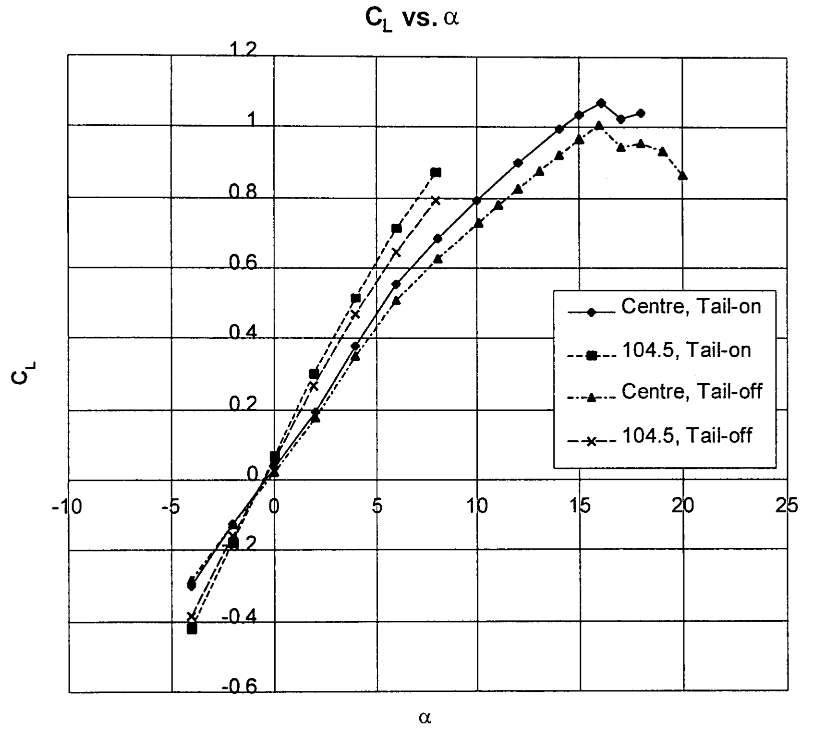

Figure 2-7: Lift coefficient for tail-on and -off, in and out of ground effect

From the lift curves (Figures 2-7, A-7, A-14, A-20 and A-26), it can be seen that there was a noticeable increase in lift as the model moved towards the floor. This increase was noticeable through the complete angle of attack range, even past the stall. Note again the "kink" in the lift curve slope around 5° angle of attack. The ΔC_L curves isolate the increment in C_L. As can be seen, the increment becomes much more pronounced as the model moves towards the floor.

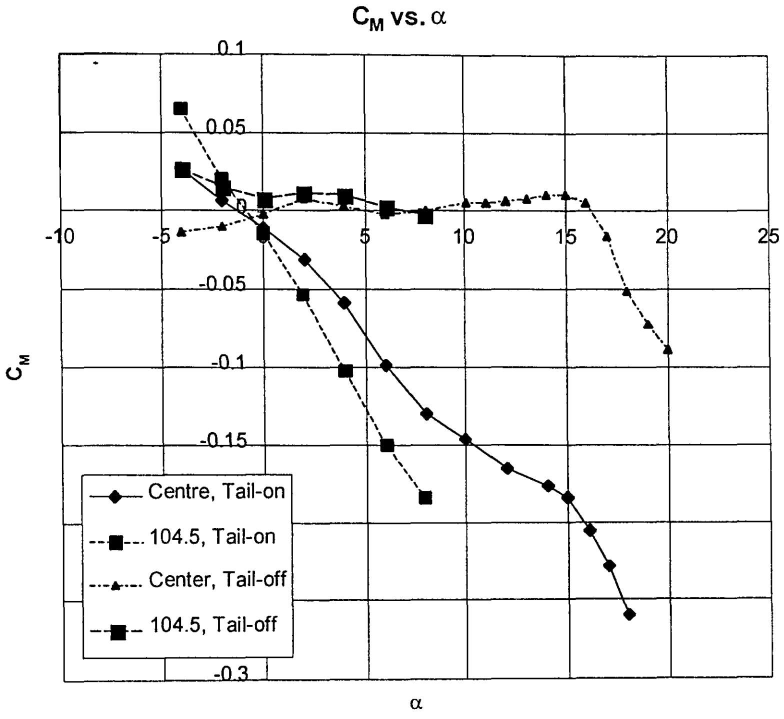

Figure 2-8: Pitching moment for tail-on and -off, in and out of ground effect

The pitching moment curves show two definite trends. Firstly, the ground effect on the tail-off tests had very little effect on the pitching moment. (See also Table 2-1). This can also be seen in Figures 2-8, A-8 and A-15. The trend in the tail-on tests is much more pronounced. From Table 2-2 and Figures 2-8, A-21 and A-27 it can be seen that the model became much more stable as it moved into ground effect.

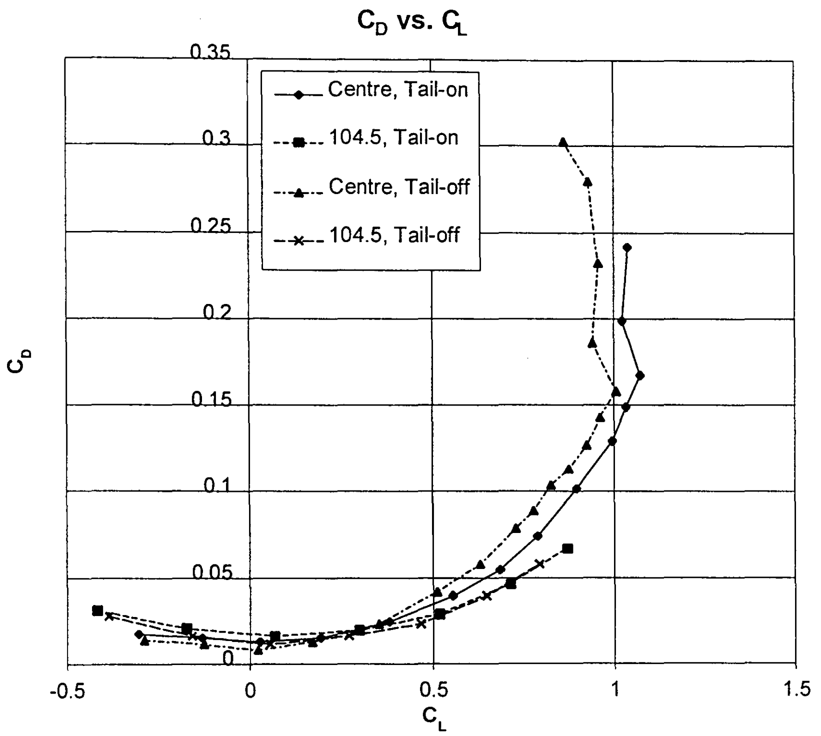

Figure 2-9: Drag polars for tail-on and -off, in and out of ground effect

The induced drag also decreases in ground effect as predicted from the theory. This is visible in all the graphs showing the drag.

2.6.3 Rolling floor

The effect of the rolling floor can be seen by comparing the first two sets of graphs with the last two in Appendix A-4. One such an example (tail-on, pitching moment) is shown in Figure 2-8. An effect of the rolling floor is to smooth out the curves. This is especially visible in the increment graphs in Appendix A-4. Note that no typical effect of the rolling floor in the lift and pitching moment is discernible, other than that it "smoothes" the graphs. In the case of drag however, there seems to be a definite decrease in the induced drag decrement, indicating that the ground effect with the rolling floor running is slightly less than predicted without the rolling floor. Note how the effect becomes much more pronounced as the model moves closer to the ground. In the centre-line tests, there is basically no difference between testing with- and without the rolling floor.

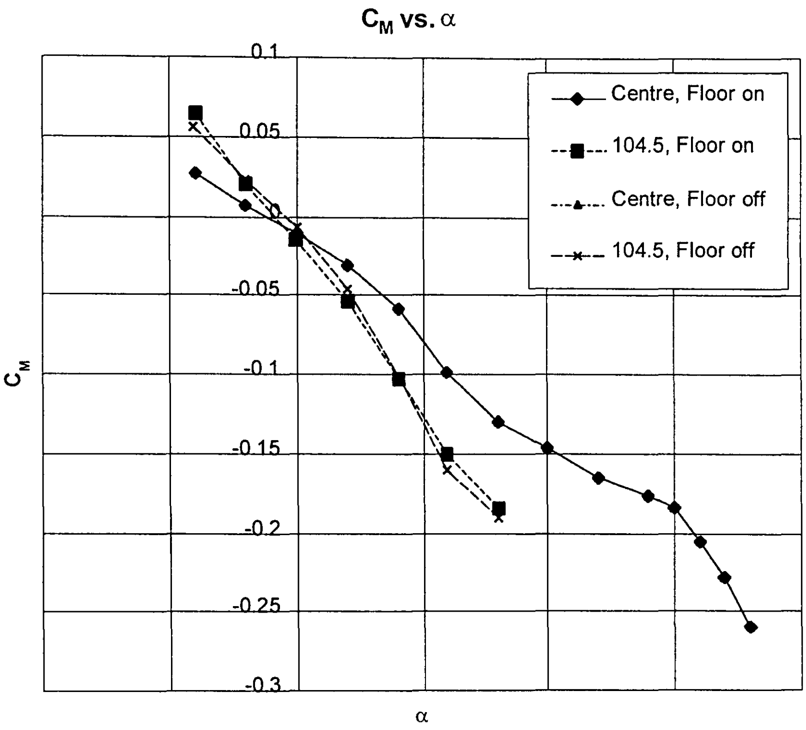

Figure 2-10: Effect of rolling floor on pitching moment

2.7 Discussion of results

2.7.1 Centre-line

The centre-line tests should normally give the standard aerodynamic performance of the model at “infinite” height or in other words, the free-air condition. This is not completely true for the present results, since no boundary corrections were performed at this stage. It must also be remembered that the method used for the tare and interference corrections was far from perfect, although the results were surprisingly good in this initial test series.

It can be seen from the results that testing at 35 m/s does not ensure complete Reynolds number independence. This will of course be very model-specific and will especially be a function of the airfoil used. In the present study this was not really a concern as long as all the tests were conducted at the same Reynolds number.

The almost neutral static stability observed in the tail-off tests compares very well to the data published for the NACA0012 profile. Since the tail is set at a fixed, zero degree incidence, the stability observed in the tail-on tests is also as one would expect.

The decrease in C_{D0} with increasing velocity was again quite predictable since drag is normally quite sensitive to Reynolds number in this range.

2.7.2 Ground effect

The ground effects observed were in most regards exactly as expected from the theory. The general results of ground effect, namely an increase in lift and decrease in induced drag, can be seen quite clearly from the results.

One of the main concerns was the fact that the data seems to display some scatter. Initially this was attributed to the fact that very small increments were measured, which might have influenced the accuracy. Although this was true to some extent, another factor may be the way the wake impinges with the floor as the model moves closer to the belt. One possible explanation is that the wake, instead of simply being swept downstream, actually deflects sideways when impinging on the floor. This was later confirmed when using the rolling floor. The rolling floor effectively removes the boundary layer at the bottom of the test section. This means that the wake can more easily be swept backwards in the faster-moving air, producing much better and repeatable results. A quick inspection of Figures A-23 to A-25 and A-29 to A-31 immediately confirms this. Note that the curves became much smoother when using the moving ground-plane.

Another concern was the fact that changing the inserts on the main strut seemed to have an effect on the data. Figure A-9 shows a good example of this. Note the jump in the increment when the insert was changed. This can be attributed to some of the interference remaining after the tare and interference correction. This effect is explained by Figure 2-11. When the model is at its highest position for a specific insert, the wing and fuselage are quite close to the bottom of the main strut. The next height increment will mean removing the insert and lowering the model on the internal strut travel. This means that, even though the model is further from the floor, it is also now further from the fixed part of the main strut. After this it will travel towards the bottom of the fixed part of the strut until the next insert has to be removed. The interference between the model and the strut changes thus quite considerably with each change of the inserts, which can be detected in the resulting data. This phenomenon was less obvious with the rolling floor running, probably due to a slight change in the flow lines over the model. The only way to eliminate this problem is to find another way of doing the interference corrections, or possibly predicting the interference between the wing and the strut.

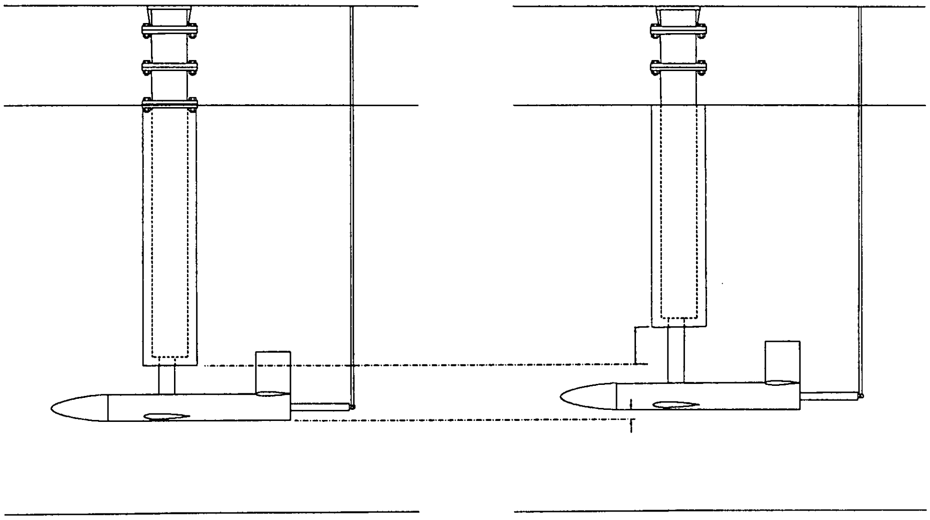

Figure 2-11: Effect of insert-change to interference effect

The very noticeable increase in stability on the tail-on results as the model moved closer to the ground would be typical for a model with a rear tail (as opposed to a canard-configured model). When the model moves down and is set at a certain, positive angle of attack, the tail is in fact closer to the floor than the wing. This means, especially when the model is quite close to the ground, that the tail is experiencing more ground effect than the wing. This increases the lift on the tail (more than on the wing because the tail is closer to the ground), which causes a nose-down pitching moment. The total effect is an increase in static stability or increase in the negative slope of the pitching moment curve when the model moves closer to the floor.

The fact that the decrease in induced drag was less when the rolling floor was running can again be explained by the way in which the wake is swept aft depending on the characteristics of the boundary layer.

2.8 Conclusions

From these initial tests it was demonstrated that the technique of testing a model in ground effect by moving the model with the Formula 1 strut, could give acceptable results. Although a number of small problems occurred, the concept as a whole seems to work quite well.

The two main questions arising from these initial tests are how to perform proper boundary corrections and how to do proper tare and interference corrections. These issues will be addressed in the next two chapters.

It is difficult to compare the actual results with published data, since most of the published reports used different techniques, different equipment and different models. The last is especially a problem since each aerodynamic configuration seems to react differently in ground effect. A delta for instance performs completely differently from a swept wing configuration with a tail. That is one of the reasons why experimental ground effect testing is needed.

Making use of an external balance as opposed to an internal balance seems to have been quite unique for ground effect testing. The initial tests gave surprisingly good results. One of the big advantages of the external balance is obtaining accurate drag data. A large disadvantage of the external balance is the fact that extensive moment transfers have to be made. Although this was done in the initial tests, the accuracy is debatable since the actual position of the model in relation to the balance virtual-centre proved to be quite difficult to determine. An internal balance would have been an advantage in this regard. Making use of an internal balance will also decrease the tare and interference from the support system, which have to be corrected for. This may prove advantageous, although there will always remain some interference that has to be corrected for. Moving the model away from the main strut by using a sting would also decrease the amount of interference. For these reasons, using an internal balance should be considered as a possible alternative at a later stage, although it is not the only solution and not always applicable.

Other, less important items also to be addressed, are getting more complete flow characteristic data for the ground effect test section and also checking the velocity calibration in the ground effect test section with- and without the rolling floor. Flow angularity tests will also be useful, although none of these items were considered very important for the present study. In the case of a commercial test series, these calibration tests should be done in advance of the actual model testing.

In conclusion, the initial tests proved that the facilities, with some attention in certain respects, could be used to obtain data for models in ground effect. It also identified the areas that needed attention and provided a large amount of data to test the reduction software on.

Chapter 3

Data reduction

3.1 Summary

In this chapter, the various corrections associated with wind tunnel data-reduction are described. Those methods that can be used for ground effect testing without any modification are quickly reviewed in the appropriate sections. The corrections associated with tare and interference caused by the support system can be extremely configuration-specific, as was the case here. A separate chapter (Chapter 4) will be devoted to these corrections. The standard boundary corrections are too limited to be used for ground effect testing, so that a different method had to be found. The methods described by Heyson [16-19] were used instead. Since these methods were developed for computers with limited memory and computational power, they were updated for modern PC's. Finally, a novel method for determining the effect of the tail incidence on the model pitching moment coefficient is described and evaluated.

3.2 Introduction

In the previous chapter a basic overview of the data reduction process was given. In this chapter the author will describe the process in more detail. Particular attention will be given to boundary correction methods, since some of the methods used are unique to ground effect testing. The reader may note that support tare and interference corrections will be completely left out. This will be discussed in the next chapter, since it were these corrections that prompted many of the modifications made to the wind tunnel.

The correction procedures described in this chapter are based on those described in reference [15]. These procedures are standard for most of the wind tunnel testing performed in the C.S.I.R. low speed wind tunnel and will not be described in extensive detail except where modified for ground effect testing. Again the exception is those procedures used for the boundary corrections. These are mostly based on the work of Heyson (references [16], [17], [18] and [19]) but various modifications were made and extensive verification as well as sensitivity studies were performed.

The reader is also referred to Appendix B for additional information.

3.3 Buoyancy corrections

The buoyancy effect is primarily produced by the thickening of the boundary layer along the length of the test section. This reduces the effective area of the tunnel towards the rear, which in turn causes a lowering of the static pressure towards the rear. Most wind tunnels thus tend to “draw” the model backwards. This effect is normally slightly reduced by designing in a small taper towards the rear of the test section. Although this will reduce the effect, it is virtually impossible to design a wind tunnel with no static pressure variation under all test conditions.

In addition to the pressure variation, there is also a streamline “squeezing effect” due to the effective change in tunnel area towards the rear.

Pope and Rae [15] use the method derived by Glauert [20]. He has shown that the effect of both the pressure variation and the streamline “squeezing effect” can be calculated using the following equation:

$$\Delta D_B = -\frac{\pi}{4}\lambda_3 t^3 \frac{dp}{dl} \tag{3-1}$$

where:

ΔD_B - Change in drag due to buoyancy

λ_3 - Body-shape factor for three-dimensional bodies

t - Body maximum thickness

dp/dl - Slope of static pressure variation

The slope of the static pressure variation is typically a function of the dynamic pressure. In the case of the C.S.I.R. low speed wind tunnel it was found that the gradient can be calculated using the following quadratic fit:

$$dp/dl = c_0 + c_1 q + c_2 q^2 \tag{3-2}$$

with, for the aerodynamic test section:

c_0 = 10.47

c_1 = $7.576\text{x}10^{-3}$

c_2 = $-4.060\text{x}10^{-7}$

These values give the gradient in Pa/m, which in turn gives the buoyancy "force" in Newton.

The body-shape factor can be estimated from Figure 6.12 in reference [15] for typical bodies. It is also shown in this reference that the effect on thin bodies such as wings are negligible and for this reason was ignored in the preliminary test series. For complete tests this shape-factor should be estimated. The fuselage of the generic model used for the development tests had a fineness ratio of 9.04, which produces a shape-factor of ±4.8. The maximum thickness for this model is simply the fuselage diameter, which is 0.115 m.

3.4 Weight tares

Before every actual wind-on run, a weight tare run is performed with the wind off. As the model pitches through the different angles of attack, the mass centre of the model moves relative to the virtual centre of the balance and accordingly affects the moments. These values are simply subtracted from the wind-on run. The reduction software does this with the forces and moments measured in engineering units.

$$F_{aerodynamic} = F_{wind-on} - F_{wind-off} \tag{3-3}$$

In equation (3-3) the symbol F can denote either force or moment.

This weight tare correction is performed on all six force and moment components.

3.5 Blockage

Before performing the blockage corrections, the support tare and interference corrections are usually done first. As mentioned earlier, these will be described in more detail in chapter 4.

3.5.1 Solid Blockage

The presence of any body in the flow causes a reduction in effective area at that location in the wind tunnel. From Bernoulli's equation, it can be shown that this causes a local increase in velocity that would not be present for an actual aircraft flying in free-air. The increase in velocity at the model is not, however, what one would obtain if one used a direct area-reduction formula, since the flow-lines far from the model are displaced much more than those at the model itself.

To calculate the actual blockage effect experienced by the model, the example of a cylinder in a two-dimensional tunnel can be used. Such a cylinder in an incompressible, inviscid fluid can be simulated using a doublet. To simulate the tunnel walls, an image system stretching into infinity is used. Such a doublet will have a strength of:

$$\mu = 2\pi V a^2 \tag{3-4}$$

where:

a - Radius of cylinder

Now, the axial velocity due to the first image doublet is:

$$\Delta V = \mu / 2\pi h^2 \tag{3-5}$$

where

h - Height of wind tunnel

Now, if we define V_u as the uncorrected velocity, we can write:

$$\Delta V / V_u = a^2 / h^2 \tag{3-6}$$

If we now add all the images, the final solid blockage velocity increment can be written as:

$$\begin{aligned} \varepsilon_{sb} &= \left(\frac{\Delta V}{V_u}\right)_{total} = 2\sum_{1}^{\infty} \frac{1}{n^2}\frac{a^2}{h^2} \\ &= \left(\frac{\pi^2}{3}\right)\left(\frac{a^2}{h^2}\right) \end{aligned} \tag{3-7}$$

Using this method, an "equivalent" cylinder can be used for a more complex shape such as an airfoil. Alternatively, a similar derivation can be done using a set of sources and sinks to represent the shape of the body or in the case of an airfoil, the airfoil thickness distribution. Equation (3-7) does, however, give a very good indication of the variables on which the solid blockage correction depends. Thom (originally reference [21], reproduced in reference [15]) uses a simpler form of Equation (3-7):

$$\varepsilon_{sb} = \frac{K_1(\text{model volume})}{C^{3/2}} \tag{3-8}$$

where

K_1 - Correction factor

C - Tunnel test section area (can be reduced for boundary layer for greater accuracy)

Equation (3-8) is in a more useful form in that K_1 can be pre-calculated or determined experimentally for different configurations.

In the three-dimensional case, a very similar equation is applied, except that an additional factor is used due to the additional dimension of the problem:

$$\varepsilon_{sb\,w} = \frac{\Delta V}{V_u} = \frac{K_1 \tau_1 (\text{wing volume})}{C^{3/2}} \tag{3-9}$$

And, for the fuselage:

$$\varepsilon_{sb\,B} = \frac{\Delta V}{V_u} = \frac{K_3 \tau_1 (\text{b}\mathit{ody}\text{ volume})}{C^{3/2}} \tag{3-10}$$

These two values are simply added for a wing-body combination to calculate the total effect.

In equations (3-9) and (3-10), the coefficients K_1 and K_3 depend on the wing thickness ratio and the fuselage fineness ratio respectively, as well as on the type of airfoil/body. The coefficient τ_1 depends on the model geometric span to wind tunnel width ratio, as well as the tunnel width to height ratio. For all these coefficients pre-determined graphs are published on pages 365 and 366 of reference [15]. The values used for the preliminary testing are shown in Table A-4. Note that the effect of the fuselage was not taken into account since it was cancelled out during the support tare and interference corrections. If a full aircraft model is tested, the fuselage correction should be included.

3.5.2 Wake blockage

The calculation of wake blockage for a three-dimensional model is slightly more complicated than the solid blockage correction, due to a change in behaviour once separated flow occurs (past the stall angle of attack).

Any body in the wind tunnel will have a wake behind it, which starts out as the boundary layer on the body. Since the velocity in the boundary layer (and wake) is lower than the velocity outside it, and the model is inside a closed tunnel, the velocity outside the wake has to be increased slightly to satisfy continuity. Again the slightly higher free-stream velocity has a direct influence on the model and needs to be corrected for.

First, we look at the flow before separation. Since the drag generated by the model is represented by the wake, the wake can be simulated by a source of strength:

$$Q = \frac{D}{\rho V} \tag{3-11}$$

where:

Q - Source strength

D - Drag

Continuity is satisfied by placing a sink far downstream. The tunnel walls are then represented by a doubly infinite (both vertically and horizontally) set of images. The sources in the image system do not induce any axial velocity, but the sinks do. The total induced velocity at the model is:

$$\Delta V = \frac{Q}{2Bh} \tag{3-12}$$

with:

B - Tunnel width

h - Tunnel height

After substituting equation (3-11) into (3-12) and rewriting drag in coefficient form, one obtains:

$$\varepsilon_{wb} = \frac{\Delta V}{V_u} = \frac{S}{4C} C_{Du} \tag{3-13}$$

In this equation, S denotes the wing area of the model. The subscript u refers to the uncorrected values.

Reference [15] also notes that the pressure gradient affects the drag and it also suggests a correction for the drag. However, these values are extremely small and the general convention is to simply ignore them. This was also adopted in the present study.

Figure 3-1 shows the different parts that make up the total drag on a finite wing. As can be deduced from this figure, the correction is incomplete once moving into the separated flow region. Maskell added a term to correct for the separated flow region. The total wake-blockage correction can then be written as:

$$\varepsilon_{wbt} = \frac{S}{4C} C_{D0} + \frac{5S}{4C}(C_{Du} - C_{Di} - C_{D0}) \tag{3-14}$$

The second term on the right of this equation vanishes (see Figure 3-1), for angles of attack lower than the separation or stall value.

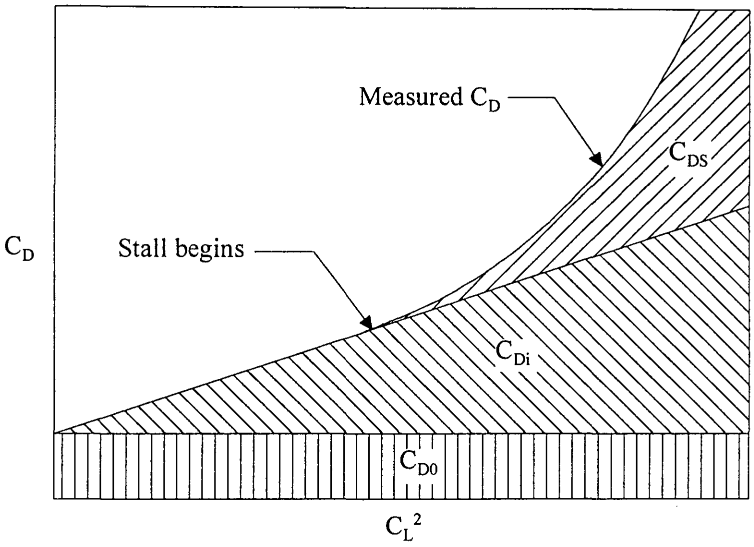

Figure 3-1: Drag analysis for a finite wing. Reproduced from reference [15]

The difficulty in applying equation (3-14) lies in separating the drag into the three different components. The approach followed by the data reduction software is as follows:

1. The user specifies the stall angle of attack.

2. The program uses linear regression to fit a straight line through the data in the unseparated region. The intersection with the y-axis at zero lift coefficient determines C_{D0}

3. The induced-drag coefficient (C_{Di}) is determined by the linear fit once in the separated region so that the separated-drag coefficient can be isolated.

4. Once the three components are isolated, equation (3-14) is applied directly to the data.

3.6 Moment transfers

Since the position of the virtual centre differs from the point about which the moments are needed, some form of moment transfer has to be performed. These corrections depend on the support system used for the tests, as well as the test section used. The most general case is that where the ground effect strut is used. The general layout is shown in Figure 3-2. The abbreviations used are:

BTC - Balance to centre

BTF - Balance to floor

Hrp - Height reference point at zero AOA

PVT - Pivot

AC - Wing Aerodynamic centre (1/4c)

Additional detail in the region of the model is shown in Figure 3-3. Now, considering these two figures, it is possible to calculate the moment arms.

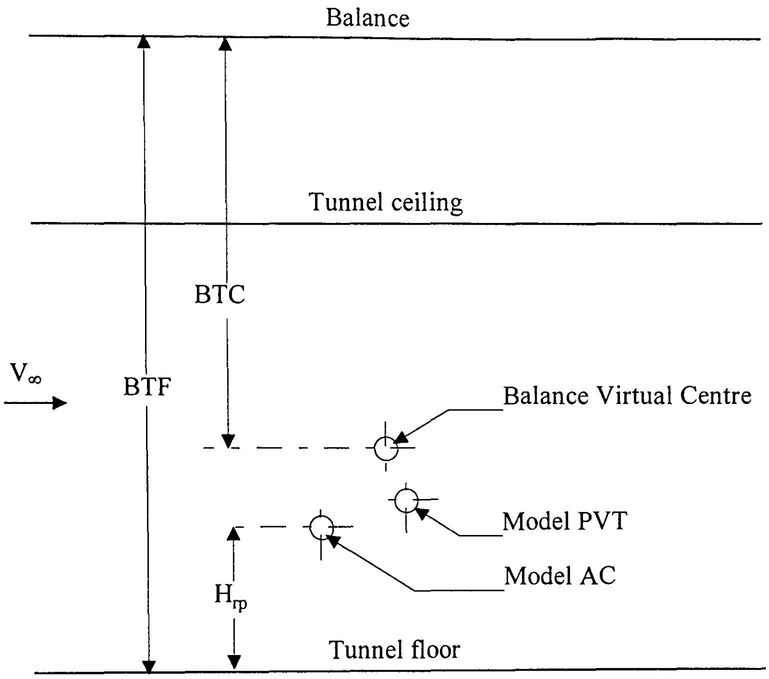

Figure 3-2: General layout with ground effect strut.

From fundamental trigonometry:

$$x = \bar{x}\cos\alpha + \bar{z}\sin\alpha$$

since

$$\bar{r}_x = x - CTP$$

$$\bar{r}_x = \bar{x}\cos\alpha + \bar{z}\sin\alpha - CTP \quad (3\text{-}15)$$

$$\bar{r}_x = x - CTP \quad (3\text{-}16)$$

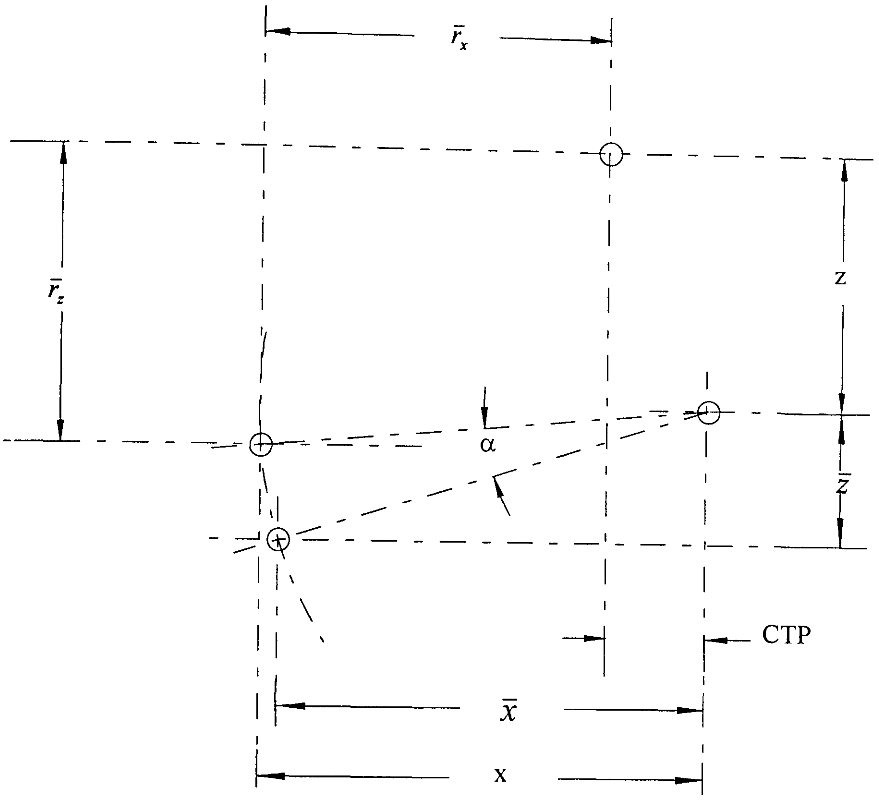

Figure 3-3: Detail of AC, Pivot point and Virtual Centre.

Similarly, for the vertical moment arm:

$$\bar{r}_z - z = \bar{z}\cos\alpha - \bar{x}\sin\alpha$$
$$\therefore \bar{r}_z = \bar{z}\cos\alpha - \bar{x}\sin\alpha + z$$

But, since:

$$z = BTF - BTC - H_{rp} - \bar{z}$$

$$\bar{r}_z = \bar{z}\cos\alpha - \bar{x}\sin\alpha + BTF - BTC - H_{rp} - \bar{z} \qquad \textbf{(3-17)}$$

Once the moment arms have been calculated using equations (3-15) and (3-17), the actual pitching moment through the wing's aerodynamic centre can be calculated as follows:

$$C_M = C_M - \frac{\bar{r}_x}{\bar{c}} C_L + \frac{\bar{r}_z}{\bar{c}} C_D \qquad \textbf{(3-18)}$$

Note that equation (3-18) uses the mean aerodynamic chord ($\bar{c}$) to non-dimensionalise the values for correction to the coefficients rather than actual forces. This is the way it was implemented in the computer program, but note that there is no reason other than convention why the correction cannot be done on the actual forces. In the computer implementation, allowance was also made for side-slip angles, but these are immaterial for the current study, since the present study did not include side-slip variations. The derivation would follow the same procedure as above, but would also influence the yawing and rolling moments.

3.7 Boundary corrections

The boundary corrections are needed due to the deflection of the streamlines caused by the proximity of the wind tunnel walls. Before discussing the more complicated method used for the ground effect testing, it is worthwhile to look at the standard boundary corrections normally used. In addition to the basic insight, these standard correction procedures can be used for verifying the method to be discussed later under certain special conditions. The basic principles for both methods are the same.

3.7.1 Classical Glauert Corrections

The boundaries of a closed wind tunnel can normally be modelled by placing images of the actual model vortex system outside the tunnel as mirror images. How these images are placed depends on the tunnel shape. The configuration is chosen in such a way that the simulated flow field is forced to have flow lines where the tunnel boundaries should be. In the simulation, this has the same effect as a physical boundary in the actual flow in that no flow is allowed to flow normal through the boundary.

As an example, a bound vortex and two semi-infinite trailing vortices trailing from the wingtips can be used to model a wing with a constant span loading. By adding vortices of similar strength outside the tunnel as shown in Figure 3-4, one of the streamlines in the flow field will describe a circle, also shown in the figure. Changing the position of the image vortices can control the size of this circle. The complete flow field is now similar to what an actual wing, with constant span loading, would experience in a closed wind tunnel with a round jet.

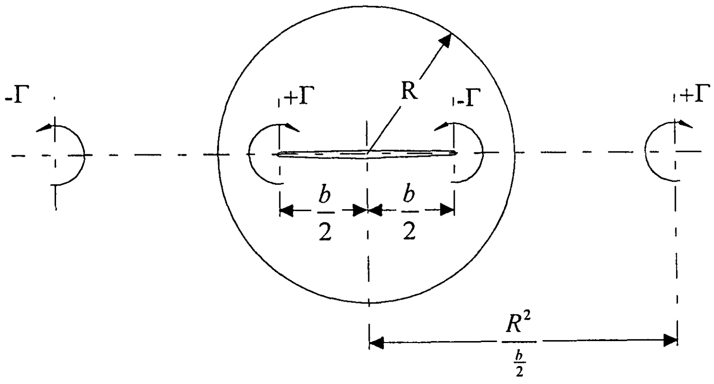

Figure 3-4: Location of vortices to model a closed round jet

The circulation strength can be calculated from the lift of a uniformly loaded wing:

$$\Gamma = \frac{SVC_L}{2b} \qquad \textbf{(3-19)}$$

From the Biot-Savart law, the up-wash at a distance *r* from a semi-infinite vortex can be calculated using:

$$w = \frac{\Gamma}{4\pi R^2} \qquad \textbf{(3-20)}$$

Finally, for the two additional vortices located as shown in Figure 3-4, the total up-wash is:

$$w = \frac{\Gamma b}{8\pi R^2} \qquad \textbf{(3-21)}$$

Now, substituting equation (3-19) into this equation, it becomes:

$$w = \frac{SV / \pi R^2}{8} C_L \tag{3-22}$$

An induced angle due to the boundaries can now be calculated:

$$\Delta\alpha_i = \frac{w}{V} = \frac{S / C}{8} C_L \tag{3-23}$$

And it can be shown that the induced drag increment becomes:

$$\Delta C_{Di} = \Delta\alpha_i C_L = \frac{S / C}{8} C_L^2 \tag{3-24}$$

These values can now be added to the uncorrected values. Of course, this correction only holds for round jet wind tunnels and wings with a constant loading. All combinations can be shown to have a correction of the form:

$$\alpha = \alpha_u + \delta \frac{S}{C} C_{LW} \frac{180}{pi} \tag{3-25}$$

and

$$C_D = C_{Du} + \delta \frac{S}{C} C_{LW}^2 \tag{3-26}$$

Where δ is unique for a specific tunnel/model configuration. In the example above, its value was 0.125. The factor at the end of the AOA correction is simply to convert the value from radians to degrees. Graphs are available for approximating δ for many typical wind tunnel/model configurations.

The uniform loading assumption can be corrected for by using the effective vortex span rather than the geometric span:

$$b_e = \frac{b + b_v}{2}$$

Where:

b - Geometric wing span

b_v - Vortex span

b_e - Effective vortex span

The vortex span can be determined from standard published graphs.

These corrections take care of the wing, but not of the tail. As one move further downwind of the wing, the induced velocities from the semi-infinite vortices increase. This is due to the fact that, beginning at the wing these vortices are modelled simply as semi-infinite vortices. Downwind of the wing, there are still a semi-infinite part trailing further downwind, but there are now also a remaining part trailing upwind to the bound vortex. This additional component of the vortex increases the induced velocity quite rapidly. The up-wash due to the image system becomes, at a distance l_t downwind of the wing:

$$w_k = \delta \frac{S}{C} C_{LW}(1 + \tau_2)V \tag{3-27}$$

Where:

C_{LW} - Wing lift coefficient (normally measured from tail-off tests)

V - Tunnel velocity

τ_2 - Downwash correction factor (read from published graphs)

In Rae and Pope [15], the centre of gravity is used as the reference point (since this is needed for static stability corrections). The present study uses the quarter chord point as the reference point, since it is simple to define and all moments can simply be transferred to the chosen centre of gravity location at a later stage.

The moment about the reference point (RP), due to the lift generated by the tail, can be written as:

$$C_{mRPt} = -\left(\frac{S_t l_t}{S\bar{c}}\right)\left(\frac{q_t}{q}\right)C_{Lt} = -\bar{V}\eta_t a_t \alpha_t \tag{3-28}$$

Where:

C_{mRPt} - Pitching moment coefficient about the reference point due to the tail

S_t - Tail area

l_t - Distance from reference point to tail aerodynamic center

$\bar{c}$ - Wing MAC

$\frac{q_t}{q}$ - Ratio of dynamic pressure at tail to dynamic pressure at wing (also η_t)

Now, the increment to this value due to the presence of the boundaries can be calculated since the value of $\left(\frac{dC_{mRP}}{d\alpha}\right)_t$ can be measured by testing at different tail incidence angles, or by estimating it using an empirical or numerical/empirical method. Then:

$$\Delta C_{mRPt} = \left(\frac{dC_{mRP}}{d\alpha}\right)_t \Delta\alpha_t \tag{3-29}$$

The value of the increment in tail AOA due to the tunnel boundaries ($\Delta\alpha_t$), can be calculated by introducing equation (3-27) into equation (3-29). If $\left(\frac{dC_{mRP}}{d\alpha}\right)_t$ is measured per degree AOA, the equation becomes:

$$\Delta C_{mRPt} = \left(\frac{dC_{mRP}}{d\alpha}\right)_t \delta\tau_2 \left(\frac{S}{C}\right) C_{LW} \frac{180}{\pi} \tag{3-30}$$

The final pitching moment correction becomes:

$$C_{mRP} = C_{mRPu} - \Delta C_{mRPt} \tag{3-31}$$

Again the subscript u refers to the uncorrected value.

3.7.2 Heyson's boundary corrections

Heyson's method was originally developed for V/STOL aircraft and helicopters. These aircraft have highly deflected wakes, which dominate the correction factors. More importantly for the purposes of this study, these aircraft are often tested in ground effect. Heyson's method was derived to cover just these types of wind tunnel corrections. A large part of the present research was spent in determining the applicability of these correction procedures and to apply it in a form that is practical for general wind tunnel corrections, without having to use a large number of graphs to determine the correction factor for each set-up. Additional sensitivity studies and verification checks had to be done to confirm the accuracy of the method.

In the derivation of the wake blockage equations, it was shown how the wake could be modelled by placing a source at the trailing edge and a sink far downstream. Heyson's method use a more complicated, but similar method. For the basic equations, the assumption is made that the model is vanishingly small and that its wake can be modelled using a string of point doublets. At this stage the effect of the various boundaries are added using systems of images and the correction factor can be calculated either for correction to free air (as was done in the classical analysis above) or to ground effect, which is what was required for the present research. For the more general case of a finite-sized model, the wakes of a number of "vanishingly small models" are superimposed. Additionally, the correction factors behind a wing had to be calculated to correct the boundary effects on a tail.

3.7.2.1 The vanishingly small model

As mentioned above, the wake behind a vanishingly small model can be modelled using a string of semi-infinite point doublets. These doublets will be tilted at some angle depending on the wake angle and what the lift and drag on the model are [16]. Figure 3-5 shows the distribution of inclined doublets to model such a wake.

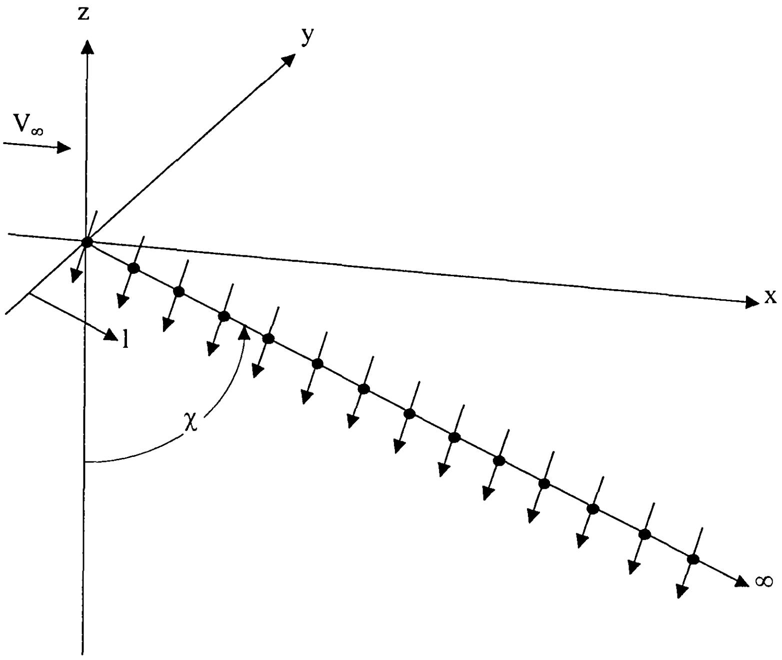

Figure 3-5: Wake in free air (reproduced from reference [16])

The downwash or upwash produced by these doublets can be calculated at any point in the tunnel from a simple potential-flow analysis. To model the floor and boundaries of the tunnel, a similar method to that described in section 3.7.1 is used. By adding different combinations of images, it is possible to correct for any practical combination of boundaries. The floor-image is treated slightly differently to the other images in that a skew wake will eventually intersect the floor. Figure 3-6 shows how this intersection is modelled. If the wake is only slightly deflected, however, the effect is small since the intersection with the floor would be very far downstream. Since the floor boundary is slightly differently modelled than the other boundaries, the model and floor-images are usually used in pairs in the image system.

This method again produces a δ-value unique for any model/tunnel combination. It has the advantage that the effect of the system of wakes and images can be calculated by a computer while performing the data-reduction, so that the user is not limited to the use of pre-determined graphs.

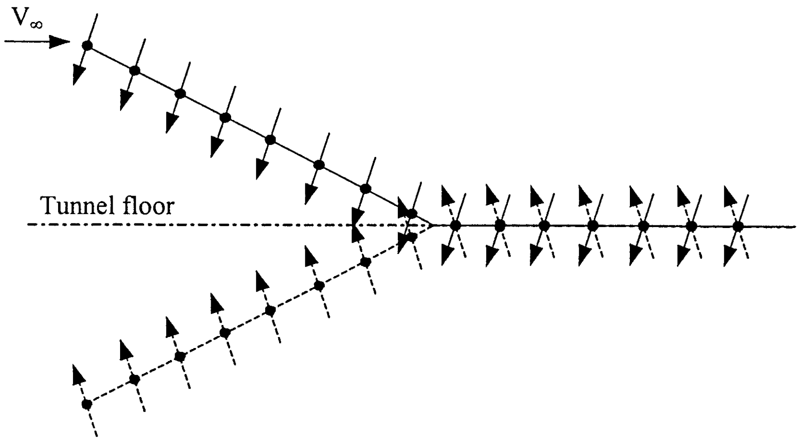

Figure 3-6: Wake intersection with floor

Since the derivations of the applicable formulas are quite involved, a full explanation and derivation of the correction equations for a vanishingly small model is shown in Appendix B-1. The δ-value can be calculated for a certain tunnel/model combination at any point relative to the model in the tunnel. Since the analysis is of a linear nature, it is also possible to combine these wakes from vanishingly small models to model the actual flow-field in the tunnel. This will be explained in more detail in the next section.

3.7.2.2 Use of superposition to correct finite wings

If a number of vanishingly small models with wakes, as described above, are placed along the wing of a finite-sized model, the resulting wake system closely represents the wake of an actual model (Reference [19]). In this formulation, η and ζ will be used to denote the origin of the system of wakes. The origin would typically be the aerodynamic centre of the model, which was the convention used in the present study. Following the convention in reference [19], the subscript N will be used to refer to the

N'th vanishingly small model, while the subscript M will be used to refer to the control points.

The non-dimensional location of the reference point is:

$$\begin{aligned} \eta &= \frac{b}{B} \\ \zeta &= \frac{H}{h} \end{aligned} \tag{3-32}$$

The non-dimensional locations of the wakes of the vanishingly small models are:

$$\begin{aligned} \eta_N &= \eta - \frac{1}{\lambda}\left(\frac{y}{H}\right)_N \\ \zeta_N &= \frac{\zeta}{1+\zeta\left(\frac{z}{H}\right)_N} \end{aligned} \tag{3-33}$$

The location of the M'th control point relative to the N'th wake can be written as:

$$\begin{aligned} \left(\frac{x}{H}\right)_{N,M} &= \left(\frac{x}{H}\right)_M - \left(\frac{x}{H}\right)_N \\ \left(\frac{y}{H}\right)_{N,M} &= \left(\frac{y}{H}\right)_M - \left(\frac{y}{H}\right)_N \\ \left(\frac{z}{H}\right)_{N,M} &= \left(\frac{z}{H}\right)_M - \left(\frac{z}{H}\right)_N \end{aligned} \tag{3-34}$$

After adding the contribution of all the wakes, the total is averaged to determine the average interference factor. Thus, the interference factor at reference point M is first determined. This is then averaged over all the control points. By using the same definition for δ as used for the vanishingly small model, the average interference factor can be written as:

$$\delta = \frac{1}{M_{\max}\sum_{N} L_N}\sum_{M}\sum_{N} L_N \times \delta \,\text{at} \left\{ \begin{array}{l} \zeta_N = \zeta / \left[1+\zeta\left(\frac{z}{H}\right)_N\right] \\ \zeta_N = \eta - \frac{1}{\gamma}\left(\frac{y}{H}\right)_N \\ \left(\frac{x}{H}\right)_{N,M} = \left(\frac{x}{H}\right)_M - \left(\frac{x}{H}\right)_N \\ \left(\frac{y}{H}\right)_{N,M} = \left(\frac{y}{H}\right)_M - \left(\frac{y}{H}\right)_N \\ \left(\frac{z}{H}\right)_{N,M} = \left(\frac{z}{H}\right)_M - \left(\frac{z}{H}\right)_N \end{array} \right\} \qquad \textbf{(3-35)}$$

Note that the contribution of each wake is weighted by its lift contribution. If a wing is modelled in this way, the lift distribution over the wing is needed. This can be approximated very accurately using the lifting-line approximation, a vortex-lattice method or a panel method. To assume an elliptical lift distribution is also adequate in many instances, especially in cases where the magnitudes of the boundary corrections are small.

For the general case of a model with a swept wing, the wing is divided into a number of sections. When this theory was developed, Heyson chose a fixed number of sections of 10 over the wing and 4 over the tail. At that stage, the number of control points was limited by the computing power available. Part of the sensitivity study was to determine the relation between the number of control points and the accuracy of the results.

Defining $K = M_{max} = N_{max}$, the locations of the control points and wakes along the quarter-chord line of the wing can be written as:

$$\begin{aligned} \left(\frac{x}{H}\right)_N &= \left|\frac{K+1-2N}{K}\right|\sigma_w\gamma\tan\Lambda\cos\alpha \\ \left(\frac{y}{H}\right)_N &= \frac{K+1-2N}{K}\sigma_w\gamma \\ \left(\frac{z}{H}\right)_N &= -\left|\frac{K+1-2N}{K}\right|\sigma_w\gamma\tan\Lambda\sin\alpha \end{aligned} \qquad \textbf{(3-36)}$$

where:

σ_w - Ratio of wing-span to full test-section width

Λ - Wing quarter-chord sweep angle

α - Angle-of-attack

And equation (3-35) becomes:

$$\delta = \frac{1}{K\sum_{N=1}^{K} L_N} \sum_{\mathrm{M}=1}^{K}\sum_{\mathrm{N}=1}^{\mathrm{K}} L_N \times$$

$$\delta \text{ at} \left\{ \begin{array}{ll} \zeta_N & = \dfrac{\zeta}{1-\left|\dfrac{2N-(K+1)}{K}\right|\sigma_w \gamma \zeta \tan\Lambda \sin\alpha} \\ \zeta_N & = \eta + \dfrac{2N-(K+1)}{K}\sigma_w \\ \left(\dfrac{x}{H}\right)_{N,M} & = \sigma_w \gamma \tan\Lambda \cos\alpha \left(\left|\dfrac{K+1-2M}{K}\right| - \left|\dfrac{K+1-2N}{K}\right|\right) \\ \left(\dfrac{y}{H}\right)_{N,M} & = \dfrac{2}{K}\sigma_w \gamma (N-M) \\ \left(\dfrac{z}{H}\right)_{N,M} & = \sigma_w \gamma \tan\Lambda \sin\alpha \left(\left|\dfrac{K+1-2N}{K}\right| - \left|\dfrac{K+1-2M}{K}\right|\right) \end{array} \right\} \qquad \textbf{(3-37)}$$

The interference distribution can also be calculated if an accurate, corrected, lift-distribution is needed. This was not required for the present study.

3.7.2.3 Interference at the tail

To accurately correct the tail-on data, especially for the pitching moment, it is necessary to know the interference at the tail. Heyson makes two assumptions that are acceptable for most practical configurations:

- Tail sweep and dihedral angles can be ignored and a mean tail position can be used.

- The velocities induced by the tail on itself and the wing are small enough relative to those induced by the wing that they can be ignored.

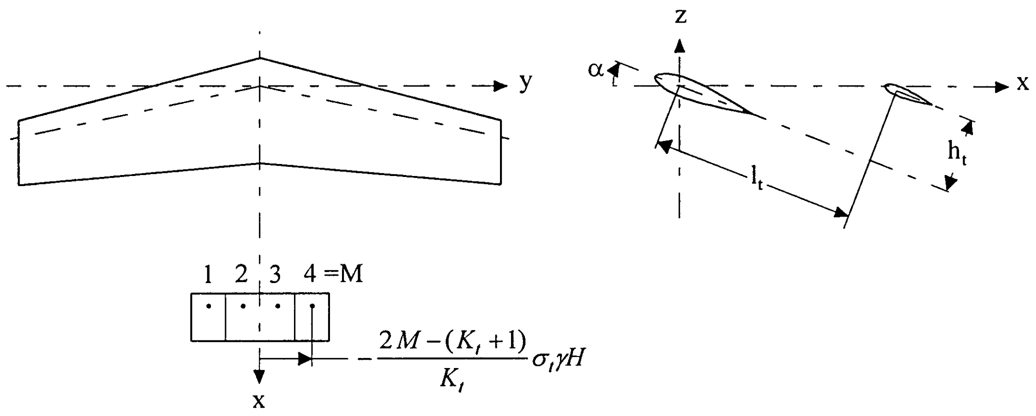

Figure 3-7: Tail geometry for Heyson's method [19]

The configuration used is shown above in Figure 3-7. Again, in Heyson's derivation, he used a fixed number of four locations at the tail for calculating the interference. For the purposes of more generality, the value K_t will be used to define the number of control points at the tail.

The locations of the control points at the tail can be written as:

$$\begin{aligned} \left(\frac{x}{H}\right)_M &= \frac{l_t}{H}\cos\alpha + \frac{h_t}{H}\sin\alpha \\ \left(\frac{y}{H}\right)_M &= \frac{K_t+1-2M}{K_t}\sigma_t\gamma \\ \left(\frac{z}{H}\right)_M &= \frac{h_t}{H}\cos\alpha - \frac{l_t}{H}\sin\alpha \end{aligned} \tag{3-38}$$

The interference factor at the tail can be calculated in a similar way as that over the wing:

$$\delta = \frac{1}{K_\iota \sum_{N=1}^{K} L_N} \sum_{\mathrm{M}=1}^{K_\iota} \sum_{\mathrm{N}=1}^{\mathrm{K}} L_N \times$$

$$\delta \text{ at } \begin{cases} \zeta_N = \dfrac{\zeta}{1 - \left|\dfrac{2N-(K+1)}{K}\right| \sigma_w \gamma \zeta \tan\Lambda \sin\alpha} \\ \zeta_N = \eta + \dfrac{2N-(K+1)}{K}\sigma_w \\ \left(\dfrac{x}{H}\right)_{N,M} = \dfrac{l_\iota}{H}\cos\alpha + \dfrac{h_\iota}{H}\sin\alpha - \sigma_w \gamma \tan\Lambda \cos\alpha \left(\left|\dfrac{K+1-2N}{K}\right|\right) \\ \left(\dfrac{y}{H}\right)_{N,M} = \dfrac{K_\iota + 1 - 2M}{K_\iota}\sigma_\iota \gamma - \dfrac{K+1-2N}{K}\sigma_w \gamma \\ \left(\dfrac{z}{H}\right)_{N,M} = \dfrac{h_\iota}{H}\cos\alpha - \dfrac{l_\iota}{H}\sin\alpha + \sigma_w \gamma \tan\Lambda \sin\alpha \left(\left|\dfrac{K+1-2N}{K}\right|\right) \end{cases} \quad \textbf{(3-39)}$$

3.7.2.4 Calculation of average downwash and wake skew angle

Heyson defines a reference velocity w_h as:

$$w_h = -\sqrt{\frac{L}{n\rho A_m}} \quad \textbf{(3-40)}$$

where:

L - Measured lift-force

n - Ratio of final induced velocities in the far wake to initial induced velocities at model

ρ - Air density

A_m - Momentum area

The value for n was chosen as 2 in this thesis: Assume the total induced velocity at the model, due to the doublet wake, is approximately that of a wake stretching from the model to infinity. This is similar to a semi-infinite vortex wake. Secondly, assume that far downstream, the induced velocity is approximately that induced by an infinite wake. This is a wake that stretches from a point far upstream of the control point, to a point far downstream. The second induced velocity will then, in the limit, be exactly twice the first induced velocity.

The momentum area is more often used for corrections to rotor discs. In the case of a wing, this is the same as an area circumscribing the wingtips, or:

$$A_m = \pi s^2 \tag{3-41}$$

where s is the wing semi-span.

Once w_h is known, the induced velocities at the model, as well as the wake skew angle would normally be read from charts. Since a process as automatic as possible was needed for the current study, another method had to be devised.

Heyson notes in reference [16], that it can be shown that:

$$\left(\frac{w_0}{w_h}\right)^4 = \frac{1}{1+\left(\frac{V}{w_0}+\frac{D_i}{L}\right)^2} \tag{3-42}$$

Where:

V - Wind tunnel velocity

D_i - Induced drag component to total measured drag

L - Measured lift-force

This equation can be rewritten as:

$$\left(\frac{1}{w_h^4}+\frac{D_i^2}{L^2 w_h^4}\right)w_0^4+\left(\frac{2VD_i}{Lw_h^4}\right)w_0^3+\left(\frac{V^2}{w_h^4}\right)w_0^2-1=0 \tag{3-43}$$

This equation is now in a more convenient form and the derivative to w_0 can easily be calculated. Any non-linear solver can now be used to solve the equation. For the present study, the author wrote a simple Newton-Raphson routine in Turbo Pascal to solve equation (3-43) when w_0 is required.

With the vertical mean induced velocity at the model known, it is simple to calculate the longitudinal component, since this is related to the induced drag-to-lift ratio in the following manner:

$$u_0 = \frac{D_i}{L} w_0 \tag{3-44}$$

Note that w_0 will usually be negative, since it was defined as positive upwards.

Finally the skew angle can be calculated:

$$|\chi| = \cos^{-1}\left(\frac{w_0}{w_h}\right)^2 \quad \text{with} \begin{cases} \chi > 0 \ \text{if} \ \dfrac{V}{-w_0} > \dfrac{D_i}{L} \\ \chi < 0 \ \text{if} \ \dfrac{V}{-w_0} < \dfrac{D_i}{L} \end{cases} \tag{3-45}$$

3.7.2.5 Application to data

A computer routine was written to apply the correction methods as described above to the measured data. The procedure is as follows:

- The input to the procedure includes all forces in engineering units (these are converted back to engineering units after the blockage and moment transfer routines).

- Using the same method as was used for the wake blockage, the induced drag is extracted from the total measured drag.

- The reference velocity w_h is calculated using equation (3-40).

- At this stage in the correction process, the blockage corrections had already altered the dynamic pressure and the tunnel velocity. Using V, w_h, D_i and L the value of w_0 is calculated as described in section 3.7.2.4. Finally the skew angle is calculated. Pope and Rae [15] notes that, due to the roll-up of the wake, an "effective" skew angle should rather be used for calculating the interference factors. The wake deflection calculations were developed using momentum-theory assumptions. The actual downward deflection of the wake vorticity is, due to the roll-up, about half the momentum-theory value. Pope and Rae suggest using:

$$\chi_e = \tan^{-1}\left(\frac{\pi^2}{4}\tan\chi\right) \tag{3-46}$$

Note that the induced velocities are still calculated using momentum theory, it is only for calculating the interference factors (δ's) that the effective skew angle is used instead.

- The next step is to calculate the interference factors. Pascal programs were written to do this and to supply both the correction to ground effect and the correction to free-air. The user specifies beforehand which correction is needed.

- For the convenience of using ratios rather than absolute physical values, three new values will be introduced:

M_w - Vertical mass flow due to lift

M_u - Longitudinal mass flow due to drag

M_t - Tunnel mass flow

The computer program then calculates the ratios:

$$\frac{M_w}{M_T} = \frac{A_M / A_T}{V / w_0} \tag{3-47}$$

and

$$\frac{M_u}{M_T} = \frac{M_w}{M_T}\frac{D_i}{L} \tag{3-48}$$

- The induced velocities can now be calculated. Again the ratios are used rather than the absolute values. After introducing equations (3-47) and (3-48), equations B-16 to B-19 in appendix B-1 can be re-written as:

$$\frac{\Delta w_L}{V} = \delta_{w,L} \frac{M_w}{M_T}$$
$$\frac{\Delta u_L}{V} = \delta_{u,L} \frac{M_w}{M_T}$$
$$\frac{\Delta w_D}{V} = \delta_{w,D} \frac{M_u}{M_T} \tag{3-49}$$
$$\frac{\Delta w_L}{V} = \delta_{u,D} \frac{M_u}{M_T}$$

The vertical and longitudinal induced velocities can be added to find the total induced velocities in the vertical and longitudinal directions:

$$\frac{\Delta w}{V} = \frac{\Delta w_L}{V} + \frac{\Delta w_D}{V} \tag{3-50}$$
$$\frac{\Delta u}{V} = \frac{\Delta u_L}{V} + \frac{\Delta u_D}{V} \tag{3-51}$$

- The correction to the angle-of-attack can now be calculated:

$$\Delta\alpha = \tan^{-1}\left(\frac{\Delta w / V}{1 + \dfrac{\Delta u}{V}}\right) \tag{3-52}$$

- The velocity and dynamic pressure are corrected as follows:

$$\frac{q_c}{q} = \left(1 + \frac{\Delta u}{V}\right)^2 + \left(\frac{\Delta w}{V}\right)^2 \tag{3-53}$$

so that:

$$q = \frac{q_c}{q} q$$
$$V_c = \sqrt{\frac{2q_c}{q}} \tag{3-54}$$

- Finally the lift and drag can be corrected for the induced angle-of-attack:

$$L_c = L\cos\Delta\alpha - D\sin\Delta\alpha \tag{3-55}$$
$$D_c = L\sin\Delta\alpha + D\cos\Delta\alpha \tag{3-56}$$

These values can be converted back to coefficients by using the corrected velocity or dynamic pressure.

3.7.2.6 Pitching moment correction

The pitching moment due to a tail can become quite a complex problem due to all the different lifting surfaces and other components interacting with each other. Heyson describes the calculation of the interference factors at the tail in reference [19]. He does not comment on the actual application of these factors, however. It was decided to follow a similar approach as was used for the classical downwash corrections:

- Measure or estimate $\left(\frac{dC_{mRP}}{d\alpha}\right)_t$.
- Use the tail-off runs to calculate the skew-angle of the wake and the interference corrections behind the wake.
- Calculate $\Delta\alpha$ from equation (3-52).
- Calculate the change in pitching moment using equation (3-29).

3.7.2.7 Sensitivity study

As mentioned before, Heyson derived his equations for superposition based on a fixed number of positions along the wing and the tail. He typically used 10 reference points on the wing and 4 on the tail for the superposition calculations and 3 image systems for the vanishingly small case. Part of the current thesis was to determine how fast the results converge for changes in these values. Heyson did a complete range of tests to provide graphs for application of his correction factors to virtually any possible case. At that stage, computer time was very expensive and his corrections were usually applied from the graphs, rather than calculating them as they were needed. With the recent advances in computing power, it is possible to use more control points and image systems to improve the accuracy, while still keeping calculations fast enough to be performed in minimal computing time.

Appendix B-2 shows the results of various sensitivity studies performed to determine the optimal number of control points and image systems. Due to the large number of variables, these graphs are limited to the case of a model of similar size to the generic model used for the present study in a tunnel with the same dimensions as the C.S.I.R. low speed wind tunnel. The model was "placed" in the centre of the tunnel as indicated by ζ and η both being equal to 1.

The first two figures show the effect of the number of image systems on the correction factor. Note the extremely large variation as the correction factors converge. Typically, convergence is obtained only with 10 to 15 image systems. This was one of the most interesting results of this study, since Heyson chose to only use the first three image systems.

Figures B-6, B-7, B-12 and B-13 all indicate that choosing the exact lift distribution is not very critical in determining the average interference. One should, however, be more careful with very large models relative to the tunnel size. Any tests where lift-distribution is important, such as aileron tests or when determining tip-stalling behaviour, should be corrected with care.

From figures B-8, B-9, B-14 and B-15, it can be seen that results are also not very sensitive to the number of control points on the wing. Heyson's choice of 10 points along the wing seems adequate, although some graphs such as the top left graph on B-14 indicate that using 20 control points would be even more accurate.

For the pitching moment correction, figure B-16 seems to indicate that increasing the number of control points from 4 to 6 might be appropriate. Again Heyson's choice was quite accurate.

In summary, it seems that the accuracy of Heyson's method might be increased slightly by using the following combination of variables to calculate interference factors:

Variable	Suggested value
Number of images	15-20 (dependent on computer)
Control points on wing (K)	16
Wing lift distribution	Lifting line/elliptical
Control points on tail (K_t)	6

Table 3-1: Suggested choices for calculating Heyson's correction factors

Note that all the results were very sensitive to accurate wake angle (χ). This angle should always be close to 90° for typical aircraft models without high-lift devices. The method described earlier for calculating wake angle seems to work very well though.

3.8 Estimating pitching moment coefficient derivative

3.8.1 Introduction

The methods described above for correcting the change in pitching moment due to the tunnel boundaries, all need the tail effectiveness derivative. This value $\left(\frac{dC_{mRP}}{d\alpha}\right)_t$ is an indication of how much the pitching moment about some reference point changes when the tail incidence angle is changed. When conducting standard wind tunnel tests, this value is measured by testing at a minimum of three different tail incidence angles. Note that the assumption is that the derivative (or slope of the curve) stays more or less constant with the model at different angles of attack.

As an alternative to actually measuring the value of the tail effectiveness derivative, Rae and Pope [15] suggests using the following equation:

$$\frac{dC_{Lt}}{d\alpha_t} = \frac{0.1AR_t}{AR_t + 2}\eta_t \qquad (3\text{-}57)$$

Where:

α_t - Tail incidence angle

AR_t - Tail aspect ratio

η_t - Ratio of dynamic pressure at tail to that at the wing. Also used to account for "blanketing" of tail by fuselage.

A simple panel method or vortex-lattice study will show this equation to be adequate for most problems. The η_t value is normally taken as 0.80, which seems to be of adequate accuracy for most cases. Equation (3-57) can now be used to calculate the pitching effectiveness:

$$\left(\frac{dC_{mRP}}{d\alpha_t}\right) = -\frac{dC_{Lt}}{d\alpha_t}\left(\frac{S_t l_t}{S\text{MAC}}\right)\eta_t \qquad \textbf{(3-58)}$$

Although this method can be used as a successful alternative to measuring the effectiveness derivative, it is not adequate for ground effect testing. Note that this equation does not take ground effect into account, which can be significant when the model is tested close to the ground. Additionally, the model angle of attack can have a significant effect on the derivative, especially when testing close to the ground. Testing of all the possible combinations can be extremely tedious and costly, so that an alternative method had to be considered. The author developed a simplified vortex-lattice method for this purpose.

3.8.2 Theory

Bertin and Smith [22] described a simple Vortex-Lattice method in Chapter 6 of their book. This method was simplified for the specific purpose of calculating the pitching moment effectiveness of the tail.

The vortex-lattice method uses a system of horseshoe vortices to model a lifting surface or system of lifting surfaces such as a wing/tail combination. The method described by Bertin and Smith uses a large number of these horseshoe vortices placed on the camber surface of the wing and trailing to infinity parallel to the x-axis. This method implies using a large number of these vortices to model the complete wing. To calculate the vortex-strengths, it is necessary to solve a system of linear equations. This system will have the same dimension as the number of vortices on one side of a symmetrical model. In order to interactively calculate the effectiveness for a typical alpha-scan for a ground effect run would require re-establishing the coefficient matrices and solving the system for each test point. This would be extremely time-consuming unless the number of panels could be reduced without seriously affecting accuracy. Note that accurately modelling a model and its image system for ground effect requires one to actually rotate both systems physically. For a model in free-air it is possible to re-use the coefficient matrix for different angles of attack. The ground effect image causes the system to "change geometry" when changing AOA, which precludes this practise.

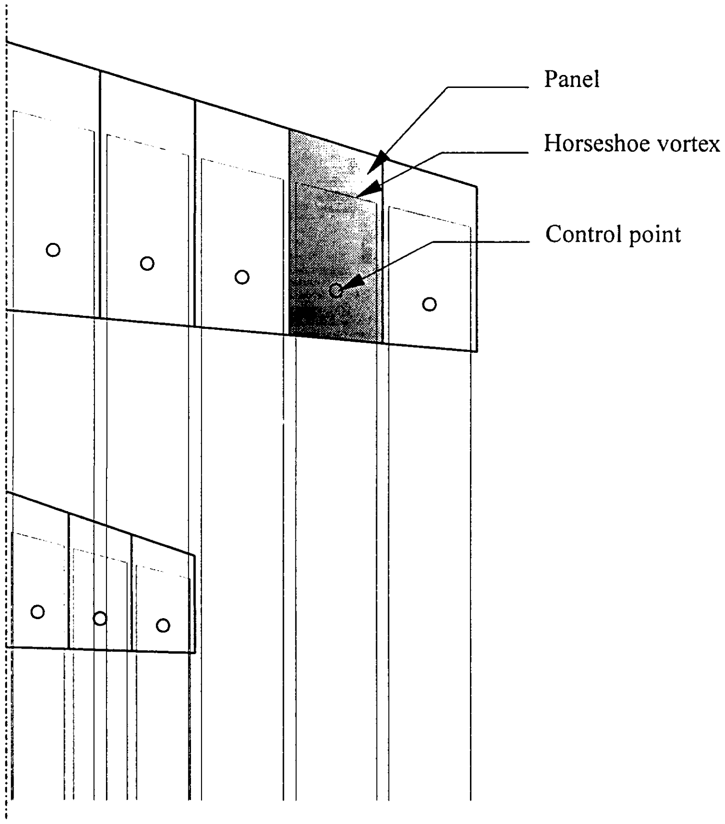

Figure 3-8: Vortex-system used to calculate tail effectiveness derivative

The method developed in this thesis was to use only one chordwise horseshoe vortex for each lifting surface. This is demonstrated by a typical configuration as shown in Figure 3-8.

The number of spanwise vortices needed is usually between 20 and 35. These are shown distributed linearly on the figure. To increase accuracy with the limited number of vortices, a semi-cosine distribution was used for both the wing and tail. The control-points are chosen on the three-quarter line as shown in the figure. It can be shown that this is equivalent to assuming a two-dimensional lift-polar slope of 2π. In cases that other values are needed, this position can be adjusted. It can also be adjusted for the Prandtl-Glauert compressibility corrections when compressibility is determined to be a factor.

The single chord-wise panel will not be able to model camber effect. A similar approach to the "lifting-line method" is used, by applying the concept of a zero-lift AOA. This angle is subtracted and the panel (and control point) rotated about the 25% chord point to account for the camber effect. As an example, a cambered profile with a zero-lift AOA of –3 degrees at 5 degrees AOA would be placed at an effective AOA of 8 degrees. This method cannot calculate the pitching moment caused by the camber of the wing, but since we are only interested in the pitching moment caused by the tail, this is not a problem.

The induced velocities from the vortex system are calculated using the Biot-Savart law for a vortex-filament:

$$\overrightarrow{dV} = \frac{\Gamma_n (\overrightarrow{dl} \times \vec{r})}{4\pi r^3} \tag{3-59}$$

The boundary conditions are applied by forcing the flow to be parallel to the chord-line at the control points. In the program this is done by forcing the total flow parallel to the normal vector to be zero.

Once the vortex-strengths are solved, the total lift and pitching moment caused by the tail behind the wing can be calculated. Repeating at a slightly different tail-incidence angle will give the derivative or slope of the tail pitching moment coefficient polar.

3.8.3 Application of theory

Since the existing correction software was initially developed using Borland Turbo Pascal, it was decided to calculate the tail-corrections in the same language in order for it to run interactively. The procedures needed were grouped into a dynamic object to improve memory allocation.

The input to the procedures includes the model height and model AOA. The configuration and dimensions of the model are saved in a separate file that is read once when initiating the object. The program then sets up the geometry by rotating the model as required for its angle of attack. The ground effect is added by considering an image beneath the model. The panels are then rotated to account for camber as described above. All the normal vectors are calculated and the system of equations is set-up for the solving routines. Note that the system is analysed at a zero-degree angle of attack since the model was already rotated to account for AOA. To prevent division by zero, a very small number is used in practise.

The system of linear equations is solved using Gauss elimination with partial pivoting [23]. This is quite fast for the typical 50x50 system. After calculating actual forces and moments, the process is repeated for a slight change in tail incidence.

Although an output-file can be requested, the results are normally returned to the program as a value for $\left(\frac{dC_{mRP}}{d\alpha}\right)_t$, which is used for the boundary corrections. Note that a value of 0.80 is assumed for η_t.

Figure B-20 in Appendix B-3 shows a flowchart for the computer program.

3.8.4 Verification of method

The simplified method as described above, were compared to an analysis with a full vortex-lattice code for the generic model. It was first necessary to determine the value for which the tail incidence had to be incremented to calculate the derivative numerically. This was done using a simple sensitivity study. The results are shown in Figure 3-9. From these results, a value of Δi=0.00001 were used throughout.

The simplified and vortex-lattice methods are compared in Figure 3-10. Note that there are slight differences, especially in extreme ground effect. Closer inspection will reveal that the differences are small percentages relative to the absolute values. The differences are also extremely small relative to the empirical value of 0.80 assumed for the η_t values.

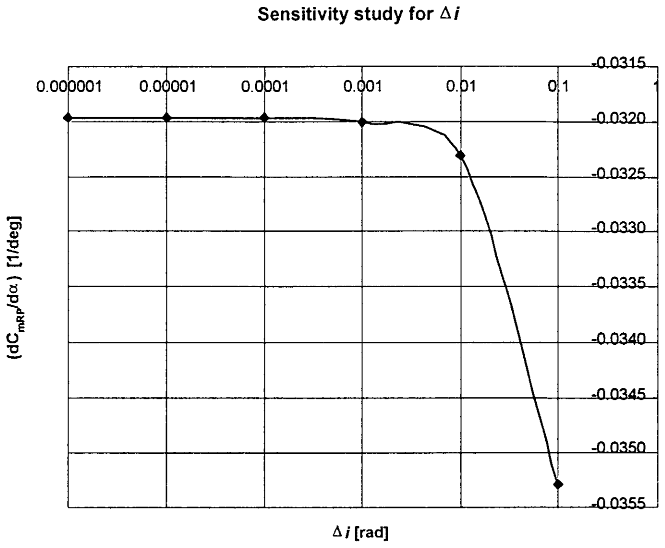

Figure 3-9: Sensitivity study to determine optimal *Δi*

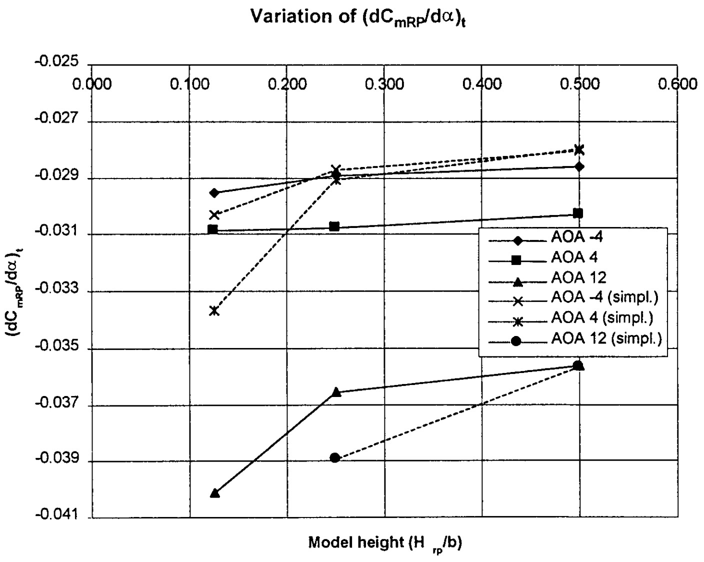

Figure 3-10: Comparison between full vortex-lattice and simplified method

3.9 Conclusions

The basic theory for wind tunnel corrections as applied to ground effect testing were described in this chapter. Most of these methods are based on tried and tested methods and only adapted to the requirements of ground effect testing where necessary. The boundary correction methods of Heyson were incorporated in place of the standard Glauert corrections and slightly improved after a proper sensitivity study. Chapter 4 will deal with the problems associated with support tare and interference corrections. Chapter 5 will compare the different methods and summarise the application of the wind tunnel corrections.

A new method for calculating the tail pitching moment coefficient derivative for application during the boundary corrections was explained. This method seems to be adequate and is much cheaper from a computational point of view than a full vortex-lattice or panel method.

Chapter 4

Tare and Interference Corrections

4.1 Summary

A method is proposed for simplifying tare and interference corrections by the use of a telescopic fairing. This method allows the tare and interference to be measured only once in the centre of the tunnel. The telescopic fairing keeps the tare and interference corrections close to constant when adjusting the ground height of the model, in contrast to the method used in Chapter 2. Tare and interference corrections were further simplified by the elimination of the external pitching mechanism. This mechanism was replaced by a much smaller system that is mounted internally to the model's fuselage.

4.2 Introduction

During the development of the testing procedures, it became clear that correcting for tare and interference due to the support system would be very difficult. The principle problem was that the interference would change as the model changed position in the wind tunnel. Since the fairing was fixed to the strut, the fairing did not move as the model changed height, which meant that each data-point would need a different tare and interference correction.

The above problems were partly eliminated during the initial test series, by using a novel but non-general method. The method was described in paragraph 2.4 in Chapter 2. The disadvantages of this method include the following:

- The results obtained are only for correcting the wing or wing/tail combination data. The forces on the fuselage are corrected out so that the fuselage effectively becomes a part of the support system.

- The flow around the fuselage will be different with the wing in place than without it. This means that the measured tare and interference values would only be approximate.

- The interference of the support system on the wing is unknown, again causing small errors.

- The fact that the model changes position relative to the fairing means that each data-point needs a correction value measured by testing the fuselage alone. This alone causes a substantial increase in the size of the test matrix.

In addition to the problems mentioned above, there is also another one caused by the fact that the fairing is directly connected to the strut. This means that the fairing is "live" and the forces and moments on the fairing itself is large relative to those of the model. Although these are measured by the method mentioned above, the large absolute value of their size means that small percentage errors can still lead to large errors after correction of the raw data. The fairing was also not particularly well manufactured and shaped and its effect on blockage and tunnel turbulence levels would be very difficult to determine.

Although most of the problems mentioned above were acceptable for the initial tests which were aimed specifically at identifying shortcomings, they would certainly not suffice for commercial testing. It was clear that some changes would have to be made to both the techniques and the equipment used. In order to find a better method of performing the tare and interference tests, it is worthwhile to look at the standard tare and interference correction techniques used for external balances.

The standard procedure consists of testing the model both in the normal and inverted attitudes and using dummy struts and fairings to isolate the tare and interference simultaneously. It is also possible to isolate the tare and interference from each other, but this requires additional tests and is almost always unnecessary. The typical procedure is outlined by Rae and Pope [15]:

- The majority of the strut-surface is shielded by a fairing, so that only a small portion of the strut is exposed to the wind just above the model.

  Each test configuration is tested in the normal way with the model upright in the wind tunnel. The drag will be used as an example force, since it is usually the force affected most by the tare and interference. The procedure is also applicable to all other forces. The drag measured by the upright test will consist of:

  $$D_{meas} = D_{upright} + T_{upper} + I_{upper} \tag{4-1}$$

  where:

  $$I_{upper} = I_{M/u-strut} + I_{u-strut/M} + I_{fairing} \tag{4-2}$$

  The symbols used are:

  D_{meas} - Measured drag

  $D_{upright}$ - Drag on model when tested upright

  T_{upper} - Tare on upper (actual) strut

  I_{upper} - Interference due to upper support system

  $I_{M/u\text{-}strut}$ - Interference on model due to exposed part of upper strut

  $I_{u\text{-}strut/M}$ - Interference on exposed part of upper strut caused by model

  $I_{fairing}$ - Interference on model and exposed part of upper strut due to strut fairing

- Next, the model is tested inverted while still supported by the normal supports and fairing. If the model is close to the centre of the tunnel, this configuration is equivalent to supporting the model from the bottom of the tunnel. The forces measured now consist of:

$$D_{meas} = D_{inverted} + T_{lower} + I_{lower} \tag{4-3}$$

where:

$$I_{lower} = I_{M/l-strut} + I_{l-strut/M} + I_{fairing} \tag{4-4}$$

The new symbols are:

$D_{inverted}$	- Drag on model when tested inverted. This should be equal to $D_{upright}$, except for possible misalignment
T_{lower}	- Tare on lower strut
I_{lower}	- Interference due to lower support system

- Finally, a dummy fairing is added beneath the inverted system. This fairing is needed simply to simulate the flow changes caused by the presence of the fairing while the model is still supported as in the previous step. In addition to the fairing, a dummy strut is also added between the model and the dummy fairing. This strut is connected to the model and not the fairing, which means that it is "live" and the wind forces on it will be included in the total forces measured on the model. The dummy strut extends into the dummy fairing without actually touching it. The forces measured in this run consist of:

$$D_{meas} = D_{inverted} + T_{upper} + I_{upper} + T_{lower} + I_{lower} \tag{4-5}$$

- Subtracting equation (4-3) from equation (4-5), leaves $T_{upper} + I_{upper}$ or the total of the interference as well as the tare on the upper (normal) support system. This value can now be subtracted from the initial measured values without the dummy system to leave only the forces that would act on the model in free flight.

The method described above works well for a model tested close to the tunnel centre, but becomes incorrect for models far off-centre such as when testing in ground effect. There are also a number of additional reasons why this method can not be used exactly as explained above for ground effect testing, especially while using the standard equipment:

- Since the size of the exposed part of the strut is changing with changing model height, the two additional runs for each configuration have to be done at every height to be tested.

- When testing in the ground effect test section, which has a rolling floor, it would be very difficult to attach the dummy fairing to the tunnel.

Despite the shortcomings mentioned above, it was thought that this procedure could still be used if certain assumptions were made about the relative sizes of the different interference factors. A large advantage of this method is that it is tried and tested and the resulting tare and interference corrections can normally be used with a high level of confidence. It was also clear, however, that the equipment available at the time would not allow the use of the procedures mentioned above. It seemed possible, however, that if the gap between the model and the fairing could be kept constant, for instance by using a telescopic fairing, many of the problems could be solved or reduced. If this could be achieved, it would be possible to measure the tare and interference once, using the classical method of images and dummies. With such a set-up, the tare would stay constant to a large extent while the model changes height. The largest percentage change in interference when adjusting the model height would be due to a change in the length of the fairing far above the model. Since this is largely a far-field effect, it was thought that this effect would either be small enough to be considered negligible, or that it would be possible to predict it using a potential flow analysis such as a panel method. To determine how large the effect would be and whether it would be necessary to predict or measure it at all, a simple study was done using a panel method.

One aspect of the tare corrections that was not mentioned until now is the problem of the pitching strut used during the initial test series. It is very difficult to correct for this strut accurately. The effect is also quite large, since the entire strut is exposed to the wind and all the aerodynamic forces on the strut are transmitted directly to the balance. To complicate matters further, the pitching mechanism does not move linearly so that the strut change position and angle relative to the model during the pitching process and the height adjustment process. The most obvious solution would be to remove this strut entirely by using an internal pitching mechanism.

4.3 Potential flow study

When using a telescopic fairing, it becomes possible to keep the gap between the model and the fairing constant when making height adjustments. In this localised area, the sharp corners and complex geometry can produce turbulent flow, thick boundary layers and separated flow. Without a proper CFD analysis, this effect will be almost impossible to pre-determine accurately. This is where the tare and interference measurements are most helpful. As the model is lowered or raised, the telescopic fairing helps to keep these effects close to constant. With the local flow conditions where the strut enters the model fuselage being kept close to constant, most of the remaining changes in the interference effect are produced by the part of the fairing far above the model changing length. Since this is a far-field effect, one expects to predict the effects fairly accurately by only using a potential flow method.

In Appendix C, a short description of the panel method model is given. The grids were generated using a CAD package, while the SPARV[1] panel method [24] was used for the analysis. The mesh distribution was chosen in such a way to produce the most accurate results possible for the limited number of panels available.

4.3.1 Results

The results are summarised in Table 4-1.

Config.	C_L	C_M	C_{Di}	Description
wf_2	0.1272	0.00151	0.0044	Wing + fuselage at 2 degrees AOA
wfs_2	0.1424	-0.00358	0.0050	Wing + fuselage + short strut at 2 degrees AOA
wfl_2	0.1431	-0.00414	0.0050	Wing + fuselage + long strut at 2 degrees AOA
wf5_2	0.1337	0.00149	0.0047	Wing + fuselage + floor (500mm) at 2 degrees AOA
wf5s_2	0.1496	-0.00352	0.0052	Wing + fuselage + short strut + floor (500mm) at 2 degrees AOA
wf5l_2	0.1504	-0.00405	0.0053	Wing + fuselage + long strut + floor (500mm) at 2 degrees AOA
wf1_2	0.1733	-0.00091	0.0061	Wing + fuselage + floor (100mm) at 2 degrees AOA
wf1s_2	0.1908	-0.00467	0.0067	Wing + fuselage + short strut + floor (100mm) at 2 degrees AOA
wf1l_2	0.1925	-0.00499	0.0067	Wing + fuselage + long strut + floor (100mm) at 2 degrees AOA
wft_2	0.1417	-0.03009	0.0049	Wing + fuselage + tail at 2 degrees AOA
wfts_2	0.1633	-0.04779	0.0057	Wing + fuselage + tail + short strut at 2 degrees AOA
wftl_2	0.1661	-0.05307	0.0058	Wing + fuselage + tail + long strut at 2 degrees AOA
wft5_2	0.1495	-0.03244	0.0052	Wing + fuselage + tail + floor (500mm) at 2 degrees AOA
wft5s_2	0.1715	-0.04966	0.0060	Wing + fuselage + short strut + tail + floor (500mm) at 2 degrees AOA
wft5l_2	0.1745	-0.05472	0.0061	Wing + fuselage + long strut + tail + floor (500mm) at 2 degrees AOA

---

[1] Short for Source Panel and Ring Vortex

wft1_2	0.1939	-0.04710	0.0068	Wing + fuselage + tail + floor (100mm) at 2 degrees AOA
wft1s_2	0.2157	-0.05926	0.0075	Wing + fuselage + tail + short strut + floor (100mm) at 2 degrees AOA
wft1l_2	0.2189	-0.06293	0.0076	Wing + fuselage + tail + long strut + floor (100mm) at 2 degrees AOA
wf_10	0.6249	0.00723	0.1102	Wing + fuselage at 10 degrees AOA
wfs_10	0.6572	0.00301	0.1159	Wing + fuselage + short strut at 10 degrees AOA
wfl_10	0.6605	0.00255	0.1165	Wing + fuselage + long strut at 10 degrees AOA
wf5_10	0.6445	0.00701	0.1136	Wing + fuselage + floor (500mm) at 10 degrees AOA
wf5s_10	0.6777	0.00289	0.1195	Wing + fuselage + short strut + floor (500mm) at 10 degrees AOA
wf5l_10	0.6816	0.00246	0.1202	Wing + fuselage + long strut + floor (500mm) at 10 degrees AOA
wf1_10	0.7564	-0.00479	0.1334	Wing + fuselage + floor (100mm) at 10 degrees AOA
wf1s_10	0.7979	-0.00791	0.1407	Wing + fuselage + short strut + floor (100mm) at 10 degrees AOA
wf1l_10	0.8045	-0.00822	0.1419	Wing + fuselage + long strut + floor (100mm) at 10 degrees AOA
wft_10	0.6894	-0.13564	0.1216	Wing + fuselage + tail at 10 degrees AOA
wfts_10	0.7239	-0.14385	0.1276	Wing + fuselage + tail + short strut at 10 degrees AOA
wftl_10	0.7288	-0.14777	0.1285	Wing + fuselage + tail + long strut at 10 degrees AOA
wft5_10	0.7147	-0.14781	0.1260	Wing + fuselage + tail + floor (500mm) at 10 degrees AOA
wft5s_10	0.7501	-0.15578	0.1323	Wing + fuselage + short strut + tail + floor (500mm) at 10 degrees AOA
wft5l_10	0.7554	-0.15946	0.1332	Wing + fuselage + long strut + tail + floor (500mm) at 10 degrees AOA
wft1_10	0.9130	-0.38702	0.1610	Wing + fuselage + tail + floor (100mm) at 10 degrees AOA
wft1s_10	0.9560	-0.40172	0.1686	Wing + fuselage + tail + short strut + floor (100mm) at 10 degrees AOA
wft1l_10	0.9642	-0.40631	0.1700	Wing + fuselage + tail + long strut + floor (100mm) at 10 degrees AOA

Table 4-1: Summary of results of potential flow study

The results in the table are sorted so that the coefficients can be compared without the presence of the strut, with a 0.5m strut projecting out above the model and with a 1m strut projecting above the model respectively. Different configurations are compared: no ground-plane, 0.5m above ground-plane and 0.1m above the ground-plane as well as tail-on and tail-off configurations.

4.3.2 Discussion of results of potential flow study

From Table 4-1 it can be seen that the interference effect of the strut is significant, especially when compared with the magnitude of the changes in the coefficients due to ground effect. The effect of the 0.5m strut relative to the 1m strut is very small. This is especially true for the lift and drag coefficients. The effect on the pitching moment coefficient is slightly more pronounced. As an example, compare the tail-on model at 10 degrees angle of attack without the presence of any support fairing:

Config.	C_L	C_M	C_{Di}	Description
wft_10	0.6894	-0.13564	0.1216	Wing + fuselage + tail at 10 degrees AOA
wft5_10	0.7147	-0.14781	0.1260	Wing + fuselage + tail + floor (500mm) at 10 degrees AOA
wft1_10	0.9130	-0.38702	0.1610	Wing + fuselage + tail + floor (100mm) at 10 degrees AOA

Table 4-2: Effect of ground plane on forces acting on model

From this table it can be seen that the incremental percentages due to the ground effect were:

C_L	C_M	C_{Di}
32.43%	185.33%	32.40%

Table 4-3: Total incremental percentages for model in free air moving to half-span from ground

Starting again with the same model in free air:

Config.	C_L	C_M	C_{Di}	Description
wft_10	0.6894	-0.13564	0.1216	Wing + fuselage + tail at 10 degrees AOA
wfts_10	0.7239	-0.14385	0.1276	Wing + fuselage + tail + short strut at 10 degrees AOA
wftl_10	0.7288	-0.14777	0.1285	Wing + fuselage + tail + long strut at 10 degrees AOA

Table 4-4: Effect of addition of support fairing on model

The changes in coefficients due to the addition of the short strut are:

C_L	C_M	C_{di}
5.00%	6.05%	4.93%

Table 4-5: Incremental effect of adding short strut

These changes are significant and contribute to a large part of the interference effect. This confirms in part the need for the initial tare and interference measurements. Note from the table, however, that the offset stays very close to constant for different ground heights. This supports the proposed method, in part, from a potential flow point of view. Note that these values are much smaller than the model in "extreme ground effect"-case.

Finally, the differences between the 0.5m strut and 1.0m strut are as follows:

C_L	C_M	C_{di}
0.68%	2.73%	0.71%

Table 4-6: Percentage change in interference effect between short and long strut

As can be seen, the effect on the lift coefficient and induced drag is insignificant. The effect on the pitching moment is slightly larger, but still smaller than the increment induced by adding a strut and much smaller than the ground effect.

4.3.3 Conclusions

From the potential flow study, the following conclusions can be drawn about the method:

- The viscous effects and initial interference effects of the support system should be "captured" by doing proper support tare and interference corrections.

- The offset due to the above effects should, for most configurations, stay very close to constant when using the proposed telescopic fairing.

- Changes when lowering or raising the model are primarily far-field effects that can be predicted quite accurately by using potential flow methods such as a panel method.

- For tests concerned primarily with lift/drag increments in ground effect, no further correction should be necessary once the tare and interference for the model in the centre of the tunnel have been measured.

- For tests where accurate longitudinal stability measurements are needed, the user can consider preparing an interpolation table from a panel method model similar to that used in the above analysis. See also Appendix C for additional information. The applicable correction can then be read from such a table. In these cases, the procedure can be simplified by using a calibration model to prepare a "standard" correction table. If all the tunnel boundaries are modelled, the solid blockage effect of the "additional" length of the fairing will be included in such a table. Otherwise, the standard solid blockage methods can be used.

- Even where accurate pitching moments are required, the engineer can still consider using only the "tunnel-centre corrections" if the accuracy required is within ± 3-5% of the actual correction value.

4.4 Telescopic Fairing

4.4.1 Specifications

After consideration of the results in section 4.3, it was decided to design and manufacture a telescopic fairing which would be able to comply with the following requirements:

- The fairing should be stiff enough to operate at the design wind-speed of 35 m/s with minimal deflections. In this regard, any play should also be reduced to a minimum.
- The fairing should be adjustable from a minimum of 0.634m from the tunnel roof (model in tunnel-centre for tare and interference tests) to a maximum of 1.116m (model within a half-chord of the tunnel floor).
- The fairing should totally enclose the strut without interfering or "grounding" with the strut. The low-drag profile should be chosen in such a way as to minimise the blockage and interference effects caused by the presence of the fairing.
- Although the fairing in its evaluation form would be hand-adjustable, later automation should be possible without major modifications.

4.4.2 Design

The material used for manufacturing the strut was bi-directional fibreglass cloth in an epoxy matrix. This material provided for a high stiffness-to-weight ratio at relatively low cost. By preparing proper moulds, it was possible to keep the accuracy high enough in order for the different sections to fit inside each other with a close slide-fit, while still keeping the play between the different sections to an absolute minimum.

A layout of the fairing is shown in Figure 4-1. Note that the fairing was made in three parts to enable the large adjustable range required. The assembly drawings shown in Appendix C also include a system for automatically adjusting the height, which could in turn reduce wind tunnel time for future testing programs. The main strut is still adjusted using a stepper motor, with inserts used to increase the range for more complete ground effect tests. The largest section is used on the bottom of the fairing in order to keep the "steps" between the different sections as far away from the model as possible, throughout the operating range.

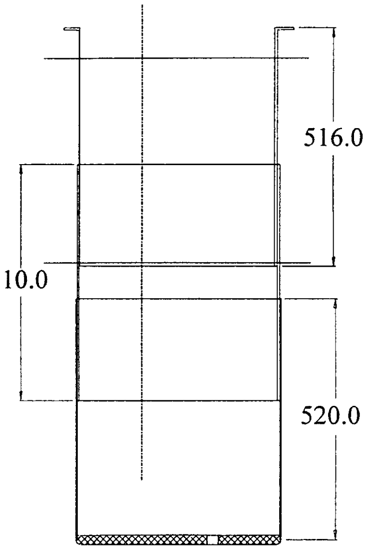

Figure 4-1: Fairing layout

The airfoil section had to enclose the strut, while still only adding a small amount of interference and blockage. Due to the sectional area of the strut (see Figure C-3), the airfoil needed quite a large thickness-to-chord ratio. The finite thickness of the fibreglass shells also caused the actual airfoil shape to change from the outer to the inner section. The three airfoil sections chosen were modifications of the Eppler E864 airfoil section.

The airfoils were analysed using Mark Drela's XFOIL airfoil analysis program [25]. The results are shown in Appendix C-4. Note that the boundary layer, even after the separation bubble, is quite thin. This also has the effect of producing a thin wake behind the model, which has a minimal effect on the streamlines near the model. The fairing was also placed at a small incidence (3°), to determine the effect a small misalignment would have. In this case, the effect is only a slightly thicker wake and a wake deflection due to the circulation. This will have a small effect on the streamlines at the model, but probably still of negligible magnitude. With the previous arrangement, misalignment would cause the generated side-force and rolling moment to be transferred to the balance.

4.4.3 Manufacture

The telescopic fairing was manufactured in the Composite Structures workshop of the C.S.I.R. The procedure is described in Appendix C-2. Using this procedure, it was possible to manufacture a smooth, accurate fairing of which the three sections could slide inside each other with virtually all play eliminated. The “steps” between the sections were sealed using wide adhesive tape during the verification wind tunnel tests (Chapter 5).

4.5 Pitching mechanism

In section 4.2 it was mentioned that the testing and correction process could be simplified significantly if the pitching strut could be eliminated. To do this, a low-cost pitching mechanism was designed that could fit inside the model in order to pitch it with minimal external protrusions.

Figure 4-2 shows the geometry of the pitching mechanism as mounted inside a typical model. The tunnel is limited to a maximum speed of 115m/s. The exact dimensions had to be determined in such a way that:

- The limited torque of a low-cost motor and gear would be able to pitch the model.
- The mechanism would be able to sustain the aerodynamic loads generated at the maximum tunnel speed without being overly bulky.

The geometry of the pitching mechanism was calculated and programmed using a simple MATLAB program. The notes in Appendix C-3 explain the relations between the different angles and summarise the design calculations. In addition to the geometry, the maximum forces and moments in the different components of the pitching mechanism were determined as a function of the mechanism layout. The MATLAB program enables the user to test and plot these design loads as a function of the geometry.

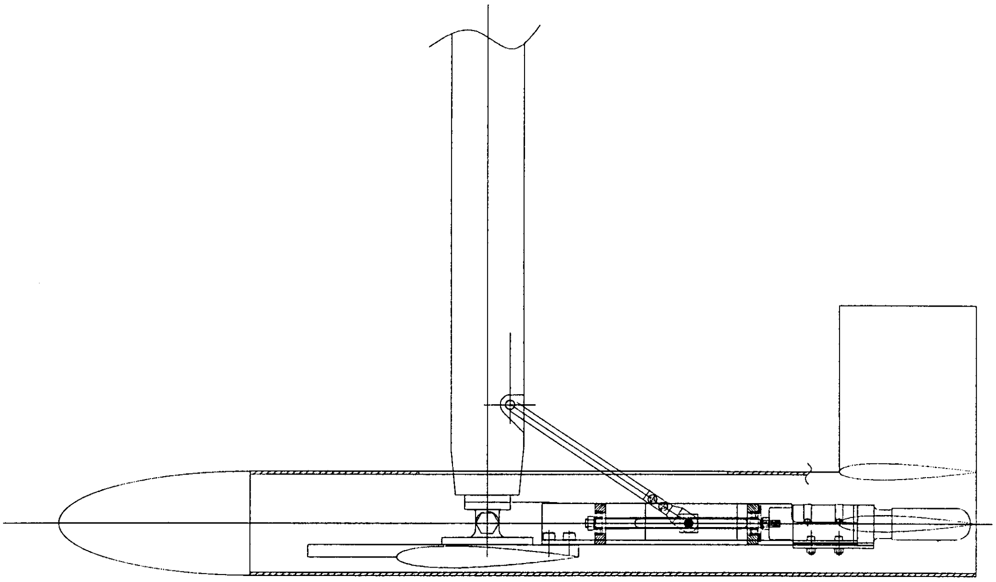

Figure 4-2: Pitching mechanism as mounted in the generic model

Typical aerodynamic forces were calculated for the generic model used in this thesis. This model is of the typical size of models that would be used in the low speed wind tunnel. Different forces such as those that could be obtained for other configurations and/or different sizes of models were taken into account by using a safety factor of at least 2.4 for all calculations on critical parts.

Figure 4-3 shows an assembly of the final pitching mechanism. Additional detail is given in Appendix C-3. The power screw system was chosen so that the thread could be self-locking. This would protect the motor and gearbox from shock-loads such as those experienced when the model is tested past the stall angle of attack. The layout shown also keeps the play in the system to the same order as that experienced in the pivoting mechanism. In practise, the flexibility of the inner strut had more of an effect on the play in the system than either the pitching mechanism or pivot had.

The power screw mechanism was designed using the methods described in Chapter 8 of reference [26]. See also Appendix C-3 for additional design information.

1. Diagonal Strut
2. Angle Section
3. Steel Clamps
4. Bosch Electric Screwdriver
5. Spacer Plate
6. Motor Mounting Plate
7. 4xM5 Cap Screws
8. 4xM3 Cap Screws
9. Face Plate
10. 2xSKF 629-2RS1 Bearings
11. Rear Bearing Block
12. Threaded Block
13. Slide Pin & Brass Wheel
14. Lead Screw
15. Forward Bearing Block
16. M8 Nut and Washer
17. 4xM8 Cap Screws

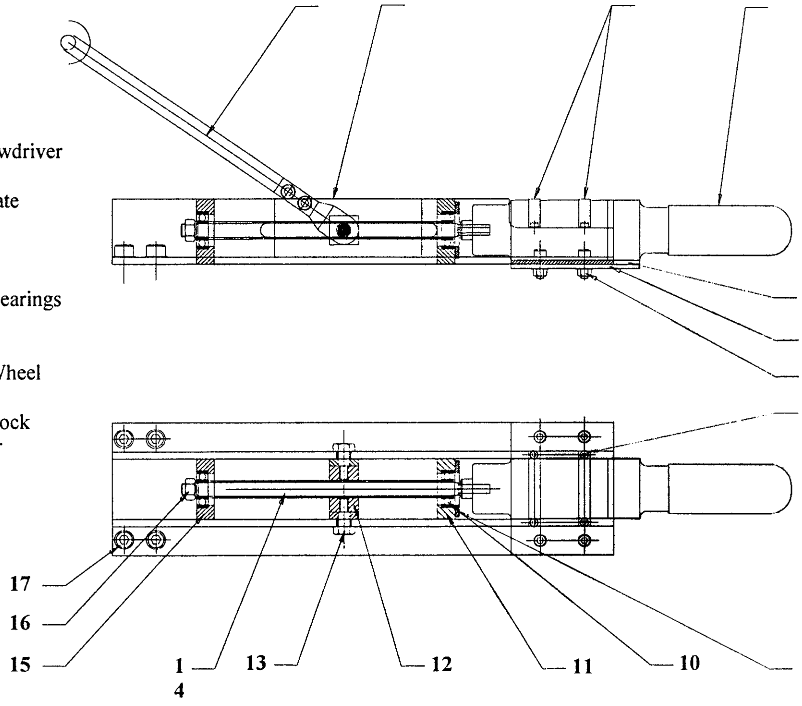

Figure 4-3: Pitching mechanism assembly drawing

The final pitching mechanism specifications were:

Property	Value
Minimum safety factor	2.4
Design axial load in screw (SF incl.)	660 N
Design moment about pivot (SF incl.)	72 Nm
Maximum torque required (SF incl.)	0.51 Nm
Pitching range	-20° to + 20° AOA

Table 4-7: Specifications of pitching mechanism

4.6 Application of method

The method of correcting tare and interference for the ground effect testing with the new equipment is summarised in Figures 4-4 to 4-6.

Figure 4-4 shows the model in the normal, upright position. Note specifically the position of the diagonal of the new pitching mechanism. To correct for this case (and in our procedure for any other case at the same speed and angle of attack), two additional runs have to be made. The first is the inverted run as shown in Figure 4-5. The second is the same inverted run, but with a dummy fairing, dummy strut and dummy pitching mechanism diagonal brace. The dummy strut and pitching mechanism diagonal are attached to the model, with the dummy fairing fixed to the tunnel floor. Note that the mirror image produced by the dummy system should be the same as the initial mounting system. Again note the position of the dummy diagonal in Figure 4-6.

Subtracting the data obtained from the test in Figure 4-5 from the data obtained from the test in Figure 4-6 should leave exactly the tare and interference value for the initial run shown in Figure 4-4.

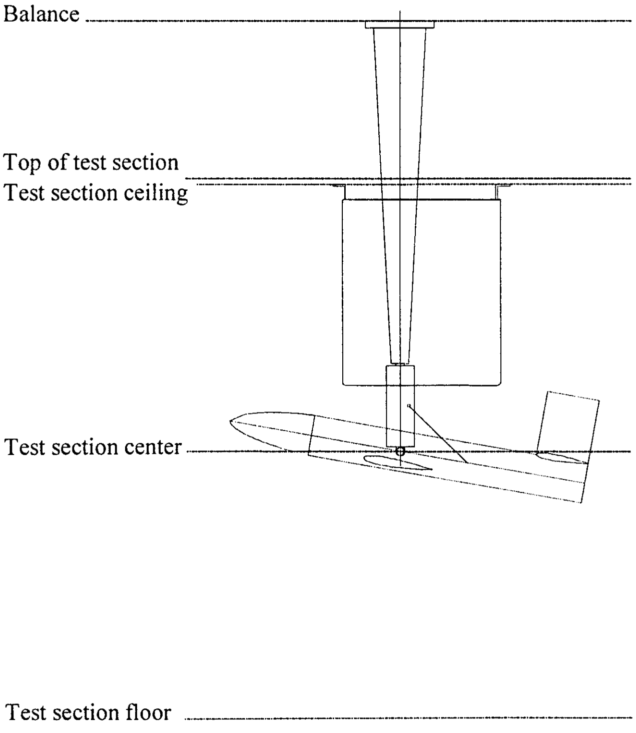

Figure 4-4: Model in normal configuration

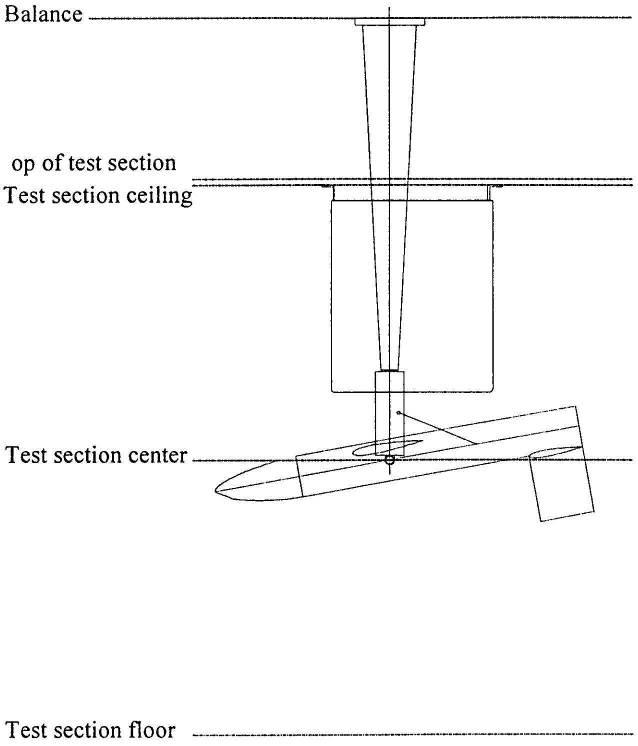

Figure 4-5: Model inverted

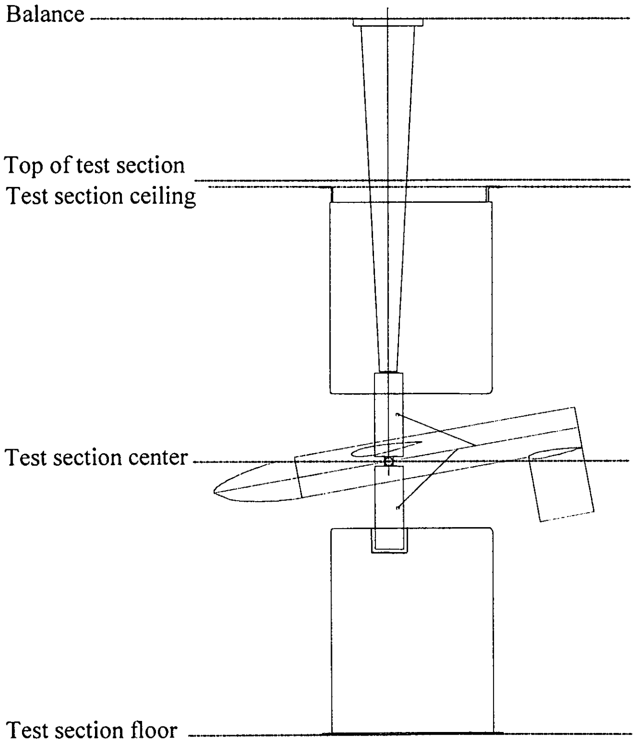

Figure 4-6: Model inverted with dummy strut/fairing

As mentioned earlier, additional corrections may be needed for the far-field effects of the lengthening and shortening of the fairing above the model. This will depend on the accuracy required for tests. In general, a potential flow study similar to the one described in this chapter should give adequate results. The author suggests the use of an interpolation table for such cases.

In the next chapter, a general evaluation and verification of the new methods and equipment will be described.

Chapter 5

Evaluation of Methods and Equipment

5.1 Summary

A short test series was conducted with the objective of verifying that the new pitching mechanism and telescopic fairing were working properly. Additionally, the measured data were to give an indication of any unexpected effects caused by the new system. The boundary correction methods were evaluated by comparing the new method with Glauert's method under certain conditions where both methods are applicable. Heyson's method was also used to correct the ground effect data to the free-air condition. This data was compared with the centre-line tests to give a further indication of accuracy. No new unexpected results were detected, basically verifying the applicability of the new methods and equipment.

5.2 Introduction

In the previous chapter, new methods for supporting the model and screening the strut were described. The telescopic fairing and pitching mechanism was manufactured as explained in Chapter 4 and Appendix C. In order to verify the proper workings of the various new components and more specifically the combination of them, an abbreviated test series was conducted with the new equipment in place. The aims of this series was:

- Verification of the practicality of using the new telescopic fairing. Although the theoretical feasibility had already been investigated in the previous chapter, the practical aspects still needed verification. These included non-grounding of the strut during wind-on tests, ease of adjustment and accuracy of the fairing.

- Testing of the pitching mechanism. This required tests to check that the motor was powerful enough to pitch the model under normal operating conditions, pitching range, and that there were no interference between the different components of the pitching mechanism.

- Although actual tare and interference tests were not conducted, the expected constant offset would allow the test engineer to see from the uncorrected data (which is displayed on the screen during runs), roughly what the final values would be. This was also to be verified during the tests.

- The data recorded were to be checked for scatter, which would be indicative of varying interference between the model and fairing. Any grounding would also be noticeable from “shooters” in the data.

5.3 Equipment evaluation

5.3.1 Model Preparation

Modifications to the model used in the previous test series include the following:

- The old pitching mechanism and all the components in the model used for connecting to the pitching strut were removed. The wing was modified with four more holes drilled and tapped to take the internal pitching mechanism.

- The slot in the wing was enlarged so that the model can be mounted inverted on one of the standard struts. This capability would be needed in future for tare and interference tests as described in Chapter 4.

- The internal part of the ground effect strut was enlarged to the same thickness of the standard strut using a built up balsa fairing and shaped to a 25 mm thick by 80 mm wide elliptical shape.

- The standard fairing used on the ground effect strut was replaced by the new telescopic fairing.

- The hole in the rear plate at the back of the model fuselage was enlarged to allow for the back of the pitching mechanism to fit inside.

5.3.2 Test Procedure

Since this series was only a verification study, it only consisted of a limited number of configurations. The new telescopic fairing also meant that the fuselage-only runs necessary for the preliminary series could be deleted. Since the pitching mechanism was now mounted internally, it was not necessary to do a weight tare check for every testing height. These were included periodically as checks, but proved unnecessary. Of course, the weight tares still had to be done for every model configuration.

Table D-1 in Appendix D-1 summarises the tests performed for this study.

5.3.3 Results

The results are shown in appendix D-2. No tare and interference corrections were made.

5.3.3.1 Telescopic fairing

The telescopic fairing proved to work extremely well. Even without an automatically adjustable system, the amount of time spent to adjust the height was minimal. Basically, the model was set to zero degrees AOA and a spacer used to set the distance from the model to the fairing. The fairing was taped into position, which also sealed the “steps” between the sections. It is the author’s opinion that some time could still be saved by automating the fairing’s height-adjustment through the addition of a power-screw system mounted above the test-section.

The results showed minimal scatter for most of the tests performed with the new fairing. Close to the ground, some scatter appeared, but this was to be expected when testing without the rolling floor. This scatter is not related to instabilities or inaccuracies pertaining to the new fairing but almost certainly due to the presence of the tunnel floor boundary layer.

From the resulting data and rigorous checks before testing, it was found that the clearance between the strut and fairing was adequate and that no grounding occurred. The model also never really came close to touching the fairing at all practical positive and negative incidence angles.

5.3.3.2 Pitching Mechanism

The mounting of the pitching mechanism did not prove particularly difficult, although having a second person to help tended to save some time. As mentioned earlier, changes to the model were minimal.

A simple two-way switching mechanism controlled the pitching mechanism for these tests. The simple nature of the system should make software-controlled pitching easy to implement. In the event, little time was wasted in manually adjusting angle of attack, since the new pitching system moved the model much faster than the previous system.

The play in the pitching mechanism was to the same order of the play in the pivoting mechanism, so that the model would stay very close to the required AOA when taking data. Even past the stall, the mechanism still had no problem in positioning the model. The author did note, however, that the thinner, movable part of the ground effect strut was slightly flexible. This was still within limits, but could prove problematic if tests at full wind tunnel speed (115 m/s) are ever required, especially when testing past the stall AOA.

Practical limits of the pitching mechanism proved to be as follows:

- 10 degrees negative incidence
- 20 degrees positive incidence

At very low heights, the incidence was limited by the proximity of the tunnel floor, rather than by the pitching mechanism.

5.4 Boundary corrections

The modified Heyson's boundary corrections were performed on the results of the preliminary test series for evaluation purposes. For the tunnel-centre tests, the older Glauert method is still applicable. Figure 5-1 compares the tail-off Glauert and Heyson's method when corrected to free-air. Note that both methods are extremely close. Below the stall-angle, there is almost no discernible difference. There is however a small difference for tests past the stall. This is probably due to the fact that the way Heyson's method was applied, induced drag was separated from the other drag components before making the up-wash corrections. In this regard, the Heyson data is probably the more accurate data.

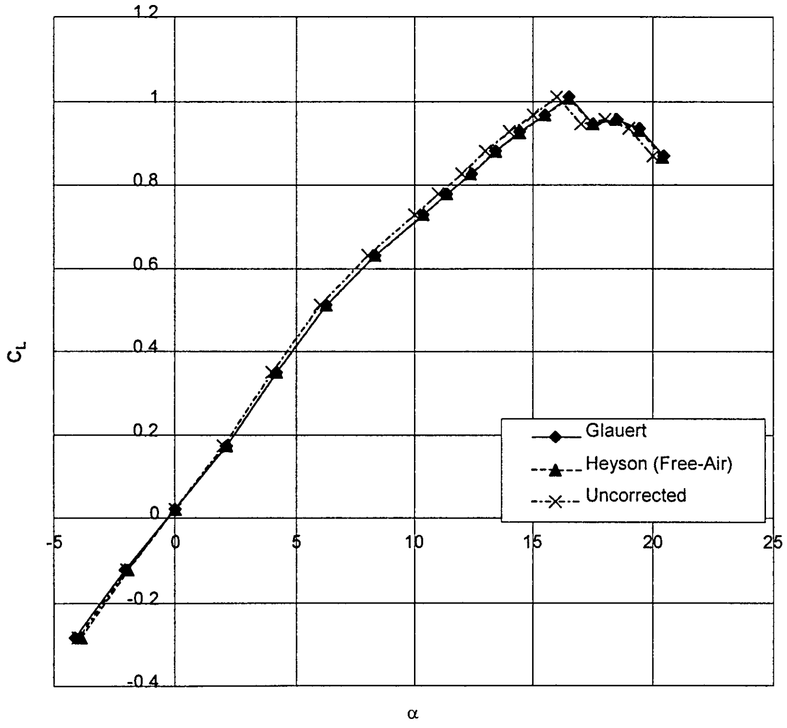

Figure 5-1: Tail-off comparison between updated Heyson's and Glauert's method, tunnel centre to free-air

The tail-on tests are compared in Figures 5-2 and 5-3. Note that the lift-coefficient corrections agree almost exactly again. There are slight differences between the pitching moment corrections, but these are still extremely close.

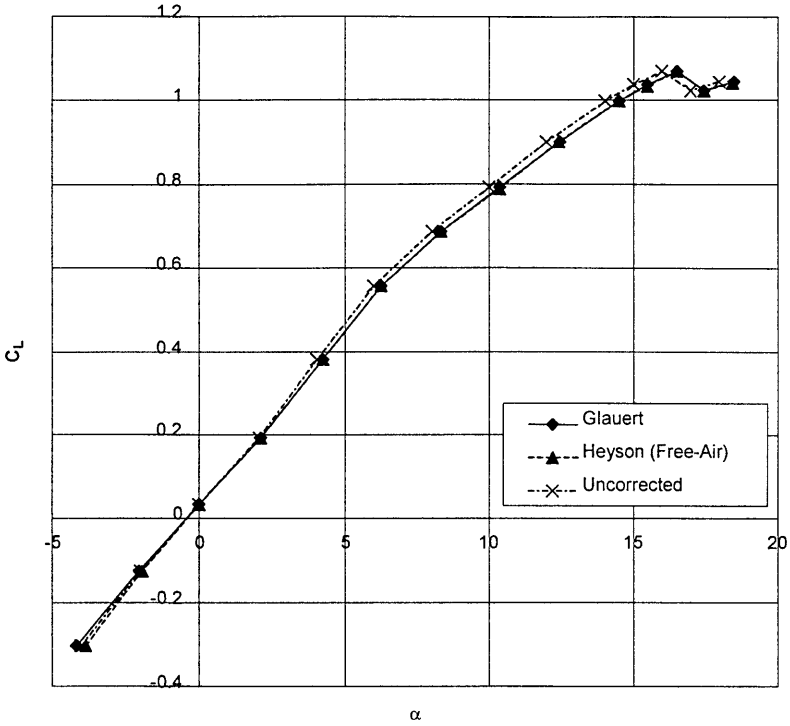

Figure 5-2: Tail-on comparison between updated Heyson's and Glauert's method, tunnel centre to free-air (Lift coefficient)

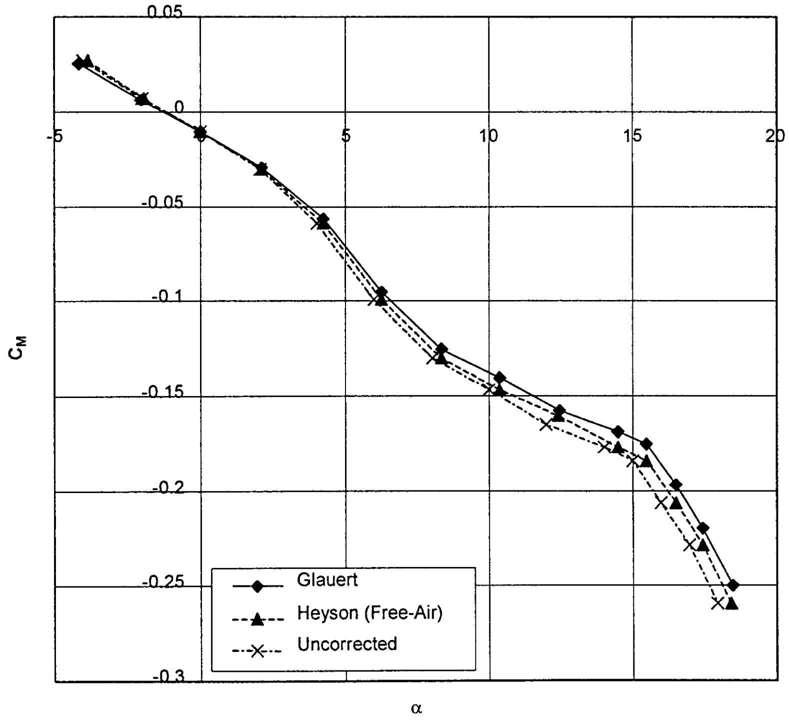

Figure 5-3: Tail-on comparison between updated Heyson's and Glauert's method, tunnel centre to free-air (Pitching-moment coefficient)

Figures 5-4 and 5-5 compare the uncorrected data, Heyson's method to free-air and Heyson's method to ground effect, all for the tail-on case. Although Glauert's method is not capable of correcting to ground effect, these values are expected to lie between the free-air and uncorrected condition. The correction should be smaller than the free-air correction, since the effect of the ground boundary is not taken into account. As can be seen in the figure, this was the case for these corrections.

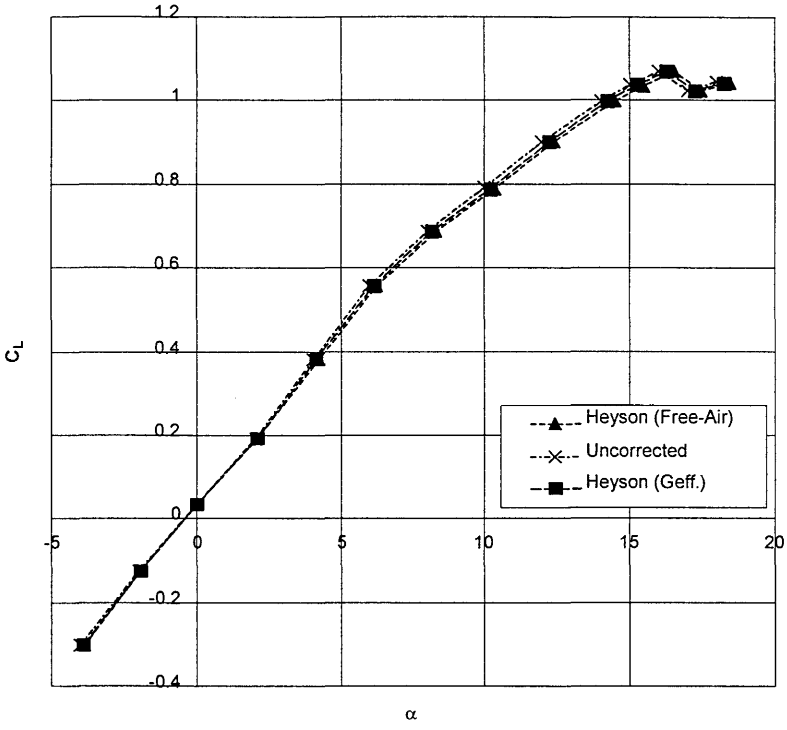

Figure 5-4: Comparison between correction to free-air and ground effect, tunnel centre (Lift coefficient)

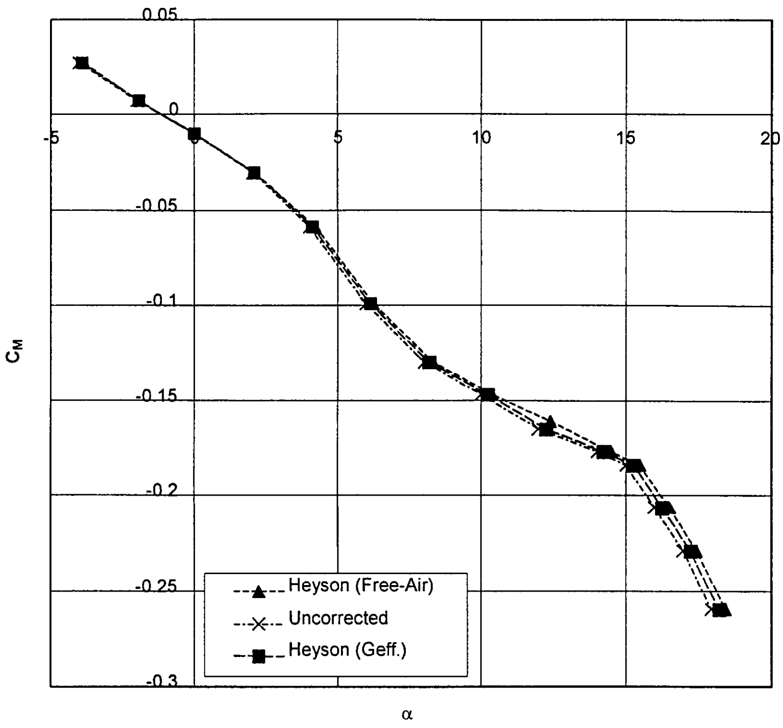

Figure 5-5: Comparison between correction to free-air and ground effect, tunnel centre (Pitching-moment coefficient)

Figure 5-6 shows Heyson's corrections when the model is in ground effect (slightly more than two chord-lengths above the tunnel-floor). Of interest is the correction to free-air which should be the same as the values shown in the previous graphs. The centre-line test corrected to free-air is also displayed for comparison. This is a way of verifying the correction method, since it places very large demands on the accuracy of the correction model. Note that Heyson's method does not perform very well here, which is also mentioned by Heyson [16]. This is not really a concern, since tests performed in ground effect is almost never corrected to the free-air case. Unfortunately it is not possible to check the values for correction to ground effect, but since this correction is very small, it should be much more accurate than the free-air correction.

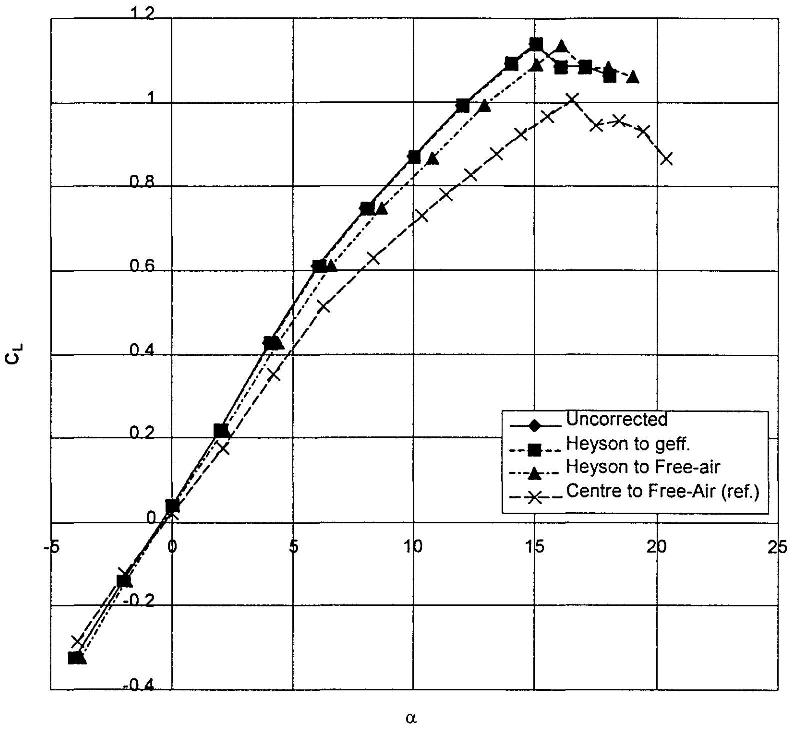

Figure 5-6: Tail-off test in ground effect

Figure 5-7 compares the same values for the tail-on tests, while Figure 5-8 shows the corrections for pitching moments. Note again that the corrections to ground effect are very small. Again Heyson's method does not perform particularly well in correcting to free-air, but as mentioned earlier this is not really a concern as these tests are specifically done to determine ground effect. It was shown previously that the corrections to free-air are accurate enough (compared to Glauert's method) when testing close to the tunnel centre.

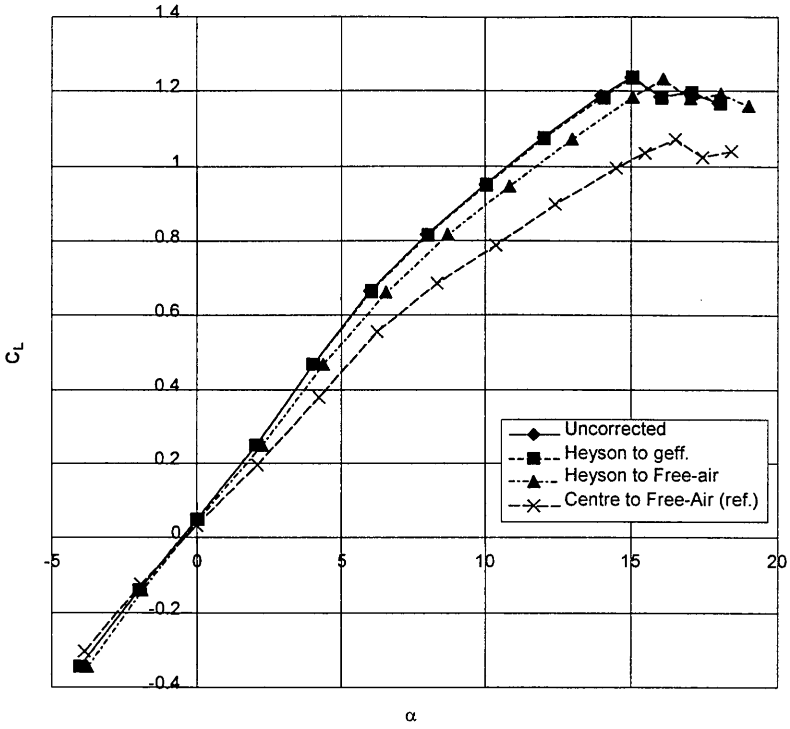

Figure 5-7: Tail-on test in ground effect (Lift coefficient)

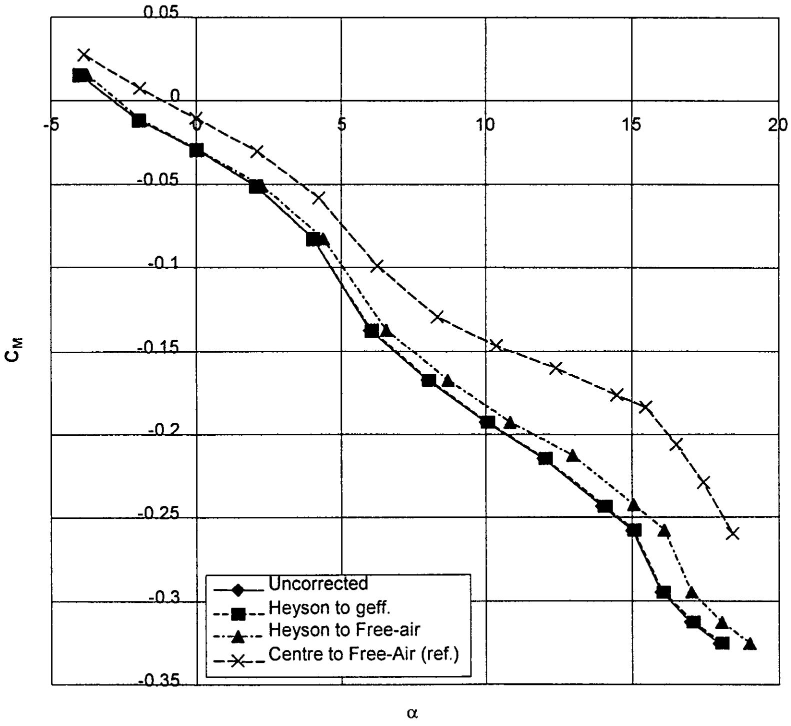

Figure 5-8: Tail-on test in ground effect (Pitching moment coefficient)

5.4.1 Conclusion

From the results above it seems that Heyson's method is more than adequate for correcting the data for the purposes of ground effect testing. It was also shown that tests that are to be corrected to free-air should be performed close to the tunnel centre. Attempts to correct data obtained from testing close to the tunnel floor to free-air will probably result in large inaccuracies when corrected to free-air.

The boundary corrections to ground effect was extremely small for this specific model. The conclusion could be made that it would even be unnecessary for these tests, which is entirely correct. The very small magnitude of these corrections is due to the fact that the model is relatively small in relation to the wind tunnel. There are no high-lift devices on this model, so that the wake-deflection is extremely small. This will not always be the case. In fact, ground effect is of importance during takeoff and landing, which often imply the use of high-lift devices. V/STOL aircraft can even use powered flap or other lift-augmenting devices, which will increase the wake deflection even more. In these cases the boundary corrections can become very large. In these cases the methods described in this thesis could prove very useful.

Chapter 6

Conclusion

6.1 Summary

In this thesis, various problems in the testing of ground effect in wind tunnels were identified and possible solutions suggested or applied. The facilities in the C.S.I.R. low speed wind tunnel were upgraded to such an extent that ground effect testing of most types of aircraft models can now be performed with the minimum of modifications. These additional modifications are in most cases due to the unique nature of each aircraft design.

The data-reduction process was evaluated in detail and changes were made where needed for the special case of ground effect testing. Most of these changes centred on support tare and interference corrections and boundary corrections. The correction software was also upgraded extensively to incorporate the new techniques.

Where new equipment had to be manufactured, these were evaluated in a final testing series and all of them proved to comply with the requirements.

Some suggestions on future development will be made at the end of this chapter. These are mostly limited to techniques and equipment changes that will reduce tunnel-time when conducting a long test-program.

6.2 Data Reduction

The software used by the C.S.I.R. is now capable of applying all the correction procedures described in this thesis. It now allows the user to choose between the old methods (which are still applicable to standard tests) and the newer techniques described in this thesis.

Most of the data reduction techniques are very mature and as shown in this thesis, can be used with a high level of confidence. The basic support tare and interference measurement method, on which the method described in Chapter 4 is based, is used extensively in most wind tunnels and no problems are foreseen in the initial measurement of the tare and interference values. The potential flow tests conducted in Chapter 4 also suggested that interference values would change very little as the model changes height with the new fairing in place. These changes can be predicted, if needed, by a similar potential flow study as that conducted in Chapter 4. It is the author's opinion that tare and interference can now be measured with sufficient accuracy for most test requirements.

The boundary corrections of Heyson, described in Chapter 3, have already been used in some wind tunnels with considerable success. The sensitivity study conducted in Chapter 3, however, did suggest some changes in the number of images and superimposed wakes to use. These were implemented in the new software and the results obtained in Chapter 5 now shows excellent agreement with Glauert's method. The user should be able to use these methods with confidence when correcting ground effect data to the actual ground effect case. It was also shown in Chapter 5 that test results measured with the model far from the tunnel centre should not be corrected to free-air, since the errors introduced could be substantial. Fortunately, these types of corrections are almost never needed.

In Chapter 5 it was also shown that the boundary corrections to ground effect can be very small, as was the case for the model used in this study. The test-engineer can decide whether it is necessary to perform these correction or not, based on the size of the model and the type of configuration used. In general, models that are large relative to the tunnel or models with high-lift devices will need the boundary corrections. Since the software developed in this thesis can perform the boundary corrections almost automatically, it is probably a good idea to perform these corrections when in doubt.

6.3 Telescopic Fairing and Internal Pitching Mechanism

The tests conducted in Chapter 5 showed that both the fairing and pitching mechanism seems to work well. Both had very little play, which meant that the model could be placed accurately at a certain height and AOA and that the measured tare and interference values could be kept very close to constant.

The improvements provided by the telescopic fairing and internal pitching mechanism are well illustrated by the following graphs. These graphs show the case of a model mounted in the centre of the tunnel, at an AOA of 10°. Each correction's magnitude is shown as a percentage of the magnitude of the total correction to that force-component. The corrections to AOA are not included, since the AOA is only affected by boundary corrections (which includes flow angularity offsets) and mechanical calibrations. Since an internal inclinometer was used for the current set-up, mechanical calibrations were not a factor.

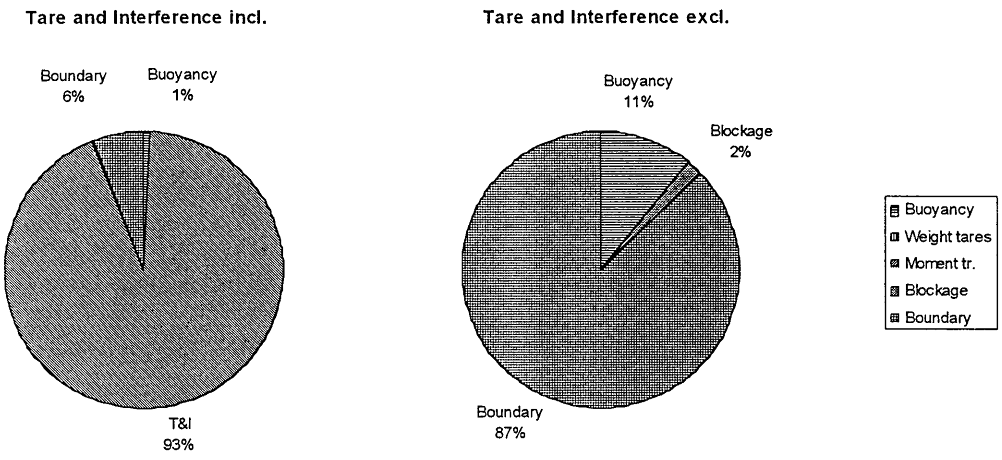

Figure 6-1: Contribution of correction components to drag coefficient correction

Figure 6-1 shows the effect of the corrections on the drag coefficient. Note how the tare and interference corrections used for the preliminary tests completely dominate the changes. The graph on the right shows the relative magnitudes of the corrections when the tare and interference changes are ignored. With the new method, support tare and interference will off course have to be added, but the relative magnitude would still be relatively small. The graph on the right is also very informative in that it shows the importance of calculating the boundary corrections and buoyancy values accurately in order to correct drag coefficient properly.

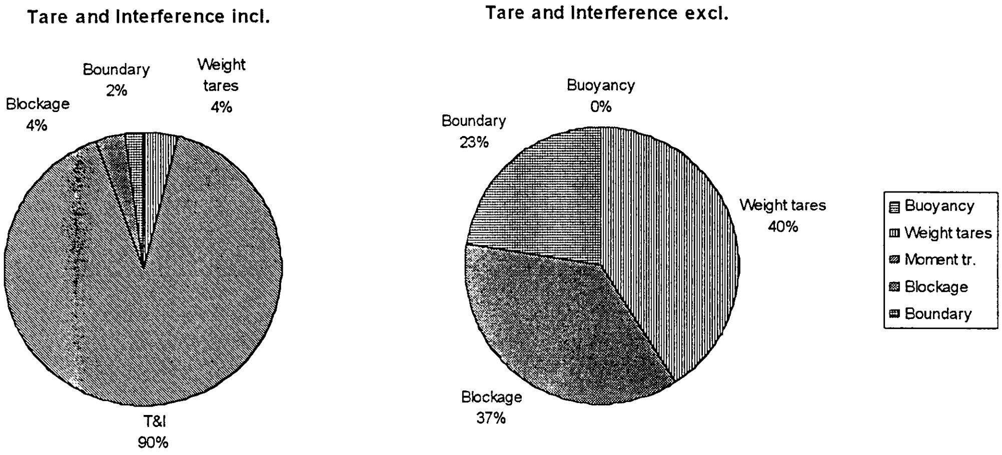

Figure 6-2: Contribution of correction components to lift coefficient correction

Figure 6-2 shows the relative magnitudes of the different corrections on the lift coefficient. The graph on the left again includes the support tare and interference corrections needed for the initial set-up. Again this correction completely dominates the other corrections. The graph on the right shows the relative magnitudes without the support tare corrections. Again, the new method would introduce a small additional correction. It is interesting to note that the largest correction was due to the weight tares. This is because all the corrections were extremely small in magnitude and were almost negligible. Although this would be true for the model used in this specific tunnel and for the model mounted in the centre, the magnitudes of the corrections would change as the model gets nearer to the tunnel floor. The weight tares would not change, so that its relative effect would be much smaller.

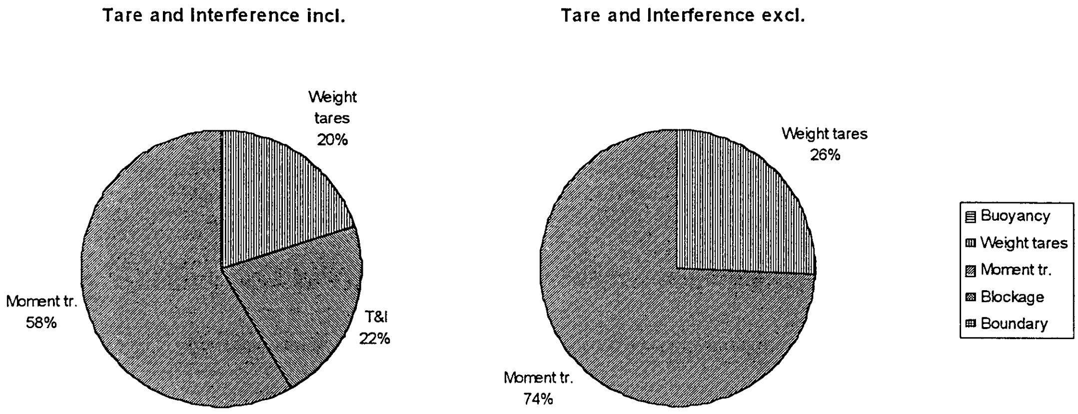

Figure 6-3: Contribution of correction components to pitching moment coefficient correction

Finally, the corrections to pitching moment coefficient are included. Again, the need for the new method of tare and interference corrections is demonstrated. Note, however, that the effect was less pronounced for this case. As could be expected, the moment transfers and weight tares are very important. The moment transfers become even more important when the model is tested in ground effect (far off-centre). This demonstrates the importance of accurately measuring the position of the model. It also shows how important it is to use a support system that has as little play as possible. It is the opinion of the author that most of these issues have been adequately addressed in the current study.

Figures 6-1 to 6-3 all confirm that testing with the fairing live (connected to the balance) is not feasible since the corrections can be extremely large. This would mean that the tare and interference values would have to be determined extremely accurately and that it would have to be ensured that there are no unsteady effects introduced by the large fairing. The new system with the pitching mechanism mounted internally, completely removes the effect of the tare on the pitching strut and the telescopic fairing greatly reduces the magnitude of the tare and interference corrections.

6.4 Rolling Floor

The preliminary test series illustrated the effect the boundary layer on the tunnel floor could have on the test results. This effect becomes more pronounced as the model gets closer to the ground. A large amount of scatter was introduced to the data when testing in extreme ground effect. If such tests are required, the author is of the opinion that the rolling floor should be used to remove the boundary layer.

6.5 Recommendations

This thesis addressed many of the problems associated with ground effect, specifically when using an overhead balance. Making use of an internal balance can alleviate many of these problems. Unfortunately, not all models allow the use of an internal balance due to their geometry. Additionally, using a sting for ground effect tests can prohibit testing the model at certain high angles of attack, which are necessary especially when information on landing or take-off performance are needed. If a requirement for ground effect testing develops for certain large aircraft development programs, the engineer might still consider using a purpose-designed internal balance. Advantages would include smaller pitching moment corrections and smaller or no support tare and interference corrections. An example of such a system was mentioned earlier (see reference [9])

Although all the methods explained in this thesis were tested in principle, certain changes can still be made to improve them. These would probably centre on automation of the new equipment. Components that can be automated include the new pitching mechanism, adjustment of the telescopic fairing's length and automated height adjustment of the model. The current system also makes use of inserts in the mounting strut to extend the height-range. A strut with a range large enough to operate without the inserts could also measurably reduce the wind tunnel occupation time.

When testing highly swept or specifically delta wings, a study on how the geometry affects the boundary corrections might be necessary. The current method does not take into account the effect a highly swept wing might have on pitching moment corrections, which could be significant.

One concern of the author is the problem of accurately measuring the position of the model relative to the balance's virtual centre. This problem was not really resolved by the current study. The reason why it might be so important is that, especially when testing the model far from the virtual centre, the error on pitching moment transfer corrections could become extremely large. A possible solution may be the use of an optical sensor to measure the model's position while testing. It may be possible to calibrate the stepper motor on the strut once for each insert with this system and then simply use these calibrations during the actual testing.

Despite these suggestions and concerns, the author is confident that the current equipment should be adequate for testing a large range of models in ground effect. Some changes may be required for specific configurations, but this is typical for any type of wind tunnel test.

BIBLIOGRAPHY

---

1. Zedan, M.F., Nuhait, A.O., "*Unsteady effects of camber on the aerodynamic characteristics of a thin airofoil moving near the ground*", Aeronautical Journal, November 1992, pp. 343-350.

2. Newman, J.N., "*Analysis of small-aspect-ratio lifting surfaces in ground effect*", Journal of Fluid Mechanics, 1982, Vol. 117, pp. 305-314.

3. Plotkin, A., & Kennell, C.G., "*Thickness-Induced Lift on a Thin Airfoil in Ground Effect*", AIAA Journal, November 1981, Vol. 19, pp. 1484-1486.

4. Wang, Q., "*Flow around an unsteady thin wing closed to curved ground*", Journal of Fluid Mechanics, 1991, Vol. 226, pp. 175-187.

5. Dragos, L. & Dinu, A., "*A direct boundary integral equations method to subsonic flow with circulation past thin airfoils in ground effect*", Computational Methods in Applied Engineering, 1995, Vol. 121, pp. 163-176.

6. Ando, S., "*Note on Prediction of Aerodynamic Lift/Drag Ratio of WIG (Wing-inGround) at Cruise*", Transactions of the Japan Society of Aeronautical and Space Science, February 1995, Vol 37, No. 118, pp. 263-277.

7. Rolls, L.S., Koenig, D.G., "*Flight-Measured Ground Effect on a Low-Aspect-Ratio Ogee Wing, including comparison with Wind tunnel results*", NASA TN D-3431, March 1966.

8. O'Leary, C.O., "*Flight Measurements of Ground Effect on the Lift and Pitching Moment of a Large Transport Aircraft (Comet 3B) and Comparison with Wind Tunnel and Other Data*", RAE Technical Reports and Memoranda No. 3611, June 1968.

9. Flaig, A., "Results of Wind Tunnel Ground Effect Measurements on Airbus A320 Using Turbine Power Simulation and Moving Tunnel Floor Techniques", AIAA Paper 90-1427, AIAA 16th Aerodynamic Ground Testing Conference, Seattle, WA, June 18-20 1990.

10. Lee, P.H., Lan, C.E., & Muirhead, V.U., "*An Experimental Investigation of Dynamic Ground Effect*", NASA Contractor Report 4105, 1987.
11. Paulson, J.W., & Kemmerly, G.T., "*An assessment of Ground Effects determined by Static and Dynamic Testing Techniques*", NASA, Ames Research Centre, The 1987 Ground Vortex Workshop, pp. 121-146, February 1988.
12. Kemmerly, G.T., & Paulson, J.W., Jr., "*Investigation of a Moving-Model Technique for Measuring Ground Effects*", NASA Technical Memorandum 4080, January 1989.
13. McCormick, B.W., "*Aerodynamics, Aeronautics and Flight Mechanics*", 2nd edition, John Wley & Sons, New York, 1995.
14. Skinner, P.J., "*Calibration of The Low Speed Wind tunnel Virtual Centre Balance*", C.S.I.R. Report AERO 96/366, December 1996.
15. Rae, W.H. & Pope, A., "*Low speed Wind tunnel Testing*", 2nd Edition, John Wiley & Sons, New York, 1984.
16. Heyson, H.H., "*Linearized Theory of Wind tunnel Jet-Boundary corrections and Ground Effect for VTOL-STOL Aircraft*", NASA Technical Report R-124, 1962.
17. Heyson, H.H., "*Jet-Boundary Corrections for Lifting Rotors centered in Rectangular Wind Tunnels*" NASA Technical Report R-71, 1960.
18. Heyson, H.H., "*Fortran Programs for Calculating Wind tunnel Boundary Interference*", NASA Technical Memorandum X-1740, 1969.
19. Heyson, H.H., "*Use of Superposition in Digital Computers to Obtain Wind tunnel Interference Factors for Arbitrary Configurations, with Particular Reference to V/STOL Models*", NASA Technical Report R-302, 1969.
20. Glauert, H., "*Wind Tunnel Interference on Wings, Bodies, and Airscrews*", R&M 1566, 1933.
21. Thom, A., "*Blockage Corrections in a High Speed Wind Tunnel*", RM 2033, 1943.
22. Bertin, J.J. & Smith, M.L., "*Aerodynamics for Engineers*", Prentice-Hall, Inc., New Jersey, 1979.

---

23. Burden, R.L., & Faires, J.D., “*Numerical Analysis*”, 5th Edition, PWS Publishing Company, Boston, 1993.

24. Petrie, J.A.H., “*Development of an Efficient and Versatile Panel Method for Aerodynamic Problems*”, Ph.D. Thesis, Department of Applied Mathematical Studies, University of Leeds, March 1979.

25. Drela, M., “*Xfoil: An Analysis and Design System for Low Reynolds Number Airfoils*”, Low Reynolds Number Aerodynamics, 54, Springer-Verlag, 1989.

26. Shigley, J.E., “*Mechanical Engineering Design*”, First Metric Edition, McGraw-Hill, New York, 1986.

APPENDIX A: PRELIMINARY TESTS

APPENDIX A-1: FIGURES - PRELIMINARY TESTS

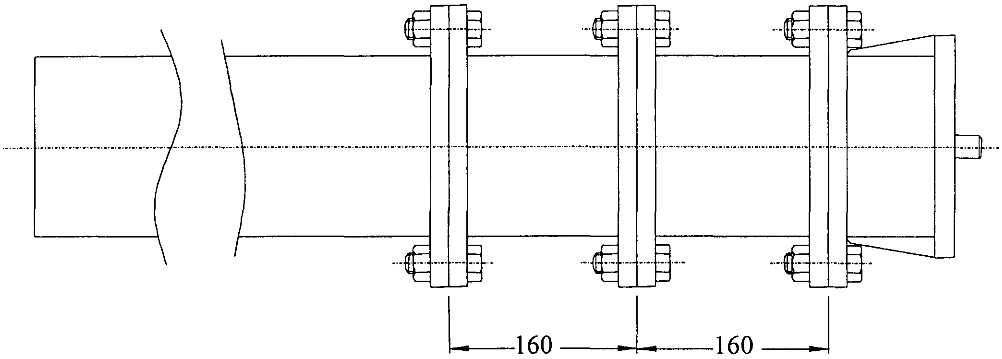

Figure A-1: Strut inserts

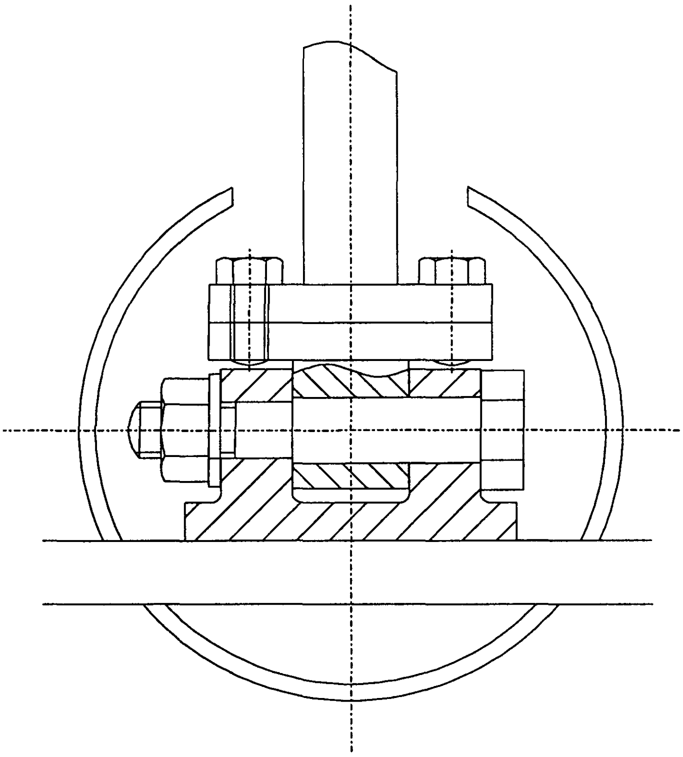

Figure A-2: Detail of saddle for mounting model on ground effect strut

APPENDIX A-2: TABLES - PRELIMINARY TESTS

Property	Value
Dimensions	2.215 m x 1.451 m (Ground effect test section)
	2.202 m x 1.521 m (Aerodynamic test section)
Velocity	Max. 115 m/s
	Max. rolling floor 35 m/s
Rolling floor	Width 1.350 m
	Length 3.700 m

Table A-1: C.S.I.R. Low Speed Wind Tunnel

Component	Units	Load Range
Lift Force	N	-7000 to 7000
Pitch Moment	Nm	-330 to 330
Drag Force	N	-440 to 1750
Side Force	N	-1750 to 1750
Yaw Moment	Nm	-270 to 270
Roll Moment	Nm	-330 to 330

Table A-2: Load Range of the LSWT Overhead Balance

	Lift Force	Pitch Moment	Drag Force	Side Force	Yaw Moment	Roll Moment
Error sample standard deviation (Estds)	0.49	0.24	0.62	1.67	0.18	0.25
2 x Estds	0.98	0.48	1.23	3.34	0.37	0.49
Maximum load applied	2348.7	293.6	1174.3	1370.1	244.7	293.6
2 x Estds/ Max load applied	0.0004	0.0016	0.0010	0.0024	0.0015	0.0017

Table A-3: Overhead balance calibration errors (Forces-N, Moments-Nm)

Aerodynamic	G.E.T.S.
BLOCK.CFG	BLOCK.CFG
$V_{wing} = 4.133756 x 10^{-3}$	$V_{wing} = 4.133756 x 10^{-3}$
$V_{body} = 0$	$V_{body} = 0$
K1 = 1.007	K1 = 1.007
K3 = 0	K3 = 0
$\tau 11 = 0.924$	$\tau 11 = 0.930$
$\tau 13 = 0$	$\tau 13 = 0$
$\alpha_{stall} = 15$	$\alpha_{stall} = 15$
MODEL.CFG	MODEL.CFG
S = 0.240	S = 0.240
B = 1.2	b = 1.2
MAC = 0.2	MAC = 0.2
MOMENT.CFG	MOMENT.CFG
$MRC_x = 0.05$	$MRC_x = 0.05$
$MRC_y = 0$	$MRC_y = 0$
$MRC_z = 0.0227$	$MRC_z = 0.0371$
	BalanceToFloor = 1.916
	BalanceToCentre = 1.2255
	CentreToPivot = 0.0195
TUNNEL.CFG	TUNNEL.CFG
A = 3.0663	A = 2.9736

Table A-4: Constants used in data correction routines. (Note that the moment transfer routine was slightly changed, also changing some of the signs used in indicating a displacement)

APPENDIX A-3: TEST SCHEDULE FOR PRELIMINARY TESTS

Test matrix file	**Hrp**	**α range**	**model**	**test section**	**Velocity**	**Output file**	**Comments**
-	-	-	-	-	-	LS970006	Systems check
-	-	-	-	-	-	LS970007	Clino calibration
-	-	-	-	-	-	LS970008	Check
T0.TMF	Centre	-4° to 20° (+2°)	Gen. mod. str. wing, tail off	Aerodynamic	0 m/s	LS970009	Mass scan
T0.TMF	Centre	-4° to 20° (+2°)	Gen. mod. str. wing, tail off	Aerodynamic	0 m/s	LS970010	Mass scan (repeat)
T0.TMF	Centre	-4° to 10° (+2°), 11° - 20° (+1°)	Gen. mod. str. wing, tail off	Aerodynamic	35 m/s	LS970011	Alpha scan
T0.TMF	Centre	-4° to 10° (+2°), 11° - 20° (+1°)	Gen. mod. str. wing, tail off	Aerodynamic	100 m/s	LS970012	Alpha scan
T0.TMF	Centre	-4° to 20° (+2°)	Gen. mod. str. wing, tail on	Aerodynamic	0 m/s	LS970013	Mass scan
T2.TMF	Centre	-	Gen. mod. str. wing, tail on	Aerodynamic	-	LS970014	Check
T1.TMF	Centre	-4° to 14° (+2°), 15° - 18° (+1°)	Gen. mod. str. wing, tail on	Aerodynamic	35 m/s	LS970015	Alpha scan
T2.TMF	Centre	-4°,3°,15° (8x)	Gen. mod. str. wing, tail on	Aerodynamic	30-100 m/s (+10), 100-30 m/s (-10), 30-100 m/s (+10)	LS970016	Reynolds number scan
T0.TMF	Centre	-4° to 18° (+2°)	Gen. mod. str. wing, Fus.-only	Aerodynamic	0 m/s	LS970017	Mass scan
T0.TMF	Centre	-4° to 18° (+2°)	Gen. mod. str. wing, Fus.-only	Aerodynamic	35 m/s	LS970018	Alpha scan
T0.TMF	Centre	-4° to 18° (+2°)	Gen. mod. str. wing, Fus.-only	Aerodynamic	100 m/s	LS970019	Alpha scan
-	-	-	-	-	-	LS970020	Check
-	-	-	-	-	-	LS970021	Check
-	-	-	-	-	-	LS970022	Check

Test matrix file	Hrp	α range	model	test section	Velocity	Output file	Comments
-	-	-	-	-	-	LS970023	Check
-	-	-	-	-	-	LS970024	Check
T3.TMF	104.5 mm	-4° to 8° (+2°)	Gen. mod. str. wing, Fus.-only	G.E.T.S., floor off, suction off	0 m/s	LS970025	Mass scan
T3.TMF	104.5 mm	-4° to 8° (+2°)	Gen. mod. str. wing, Fus.-only	G.E.T.S., floor off, suction off	0 m/s	LS970026	Ms. (repeat)
T3.TMF	104.5 mm	-4° to 8° (+2°)	Gen. mod. str. wing, Fus.-only	G.E.T.S., floor off, suction on	35 m/s	LS970027	Alpha scan
T4.TMF	144.5 mm	-4° to 10° (+2°)	Gen. mod. str. wing, Fus.-only	G.E.T.S., floor off, suction off	0 m/s	LS970028	Mass scan
T4.TMF	144.5 mm	-4° to 10° (+2°)	Gen. mod. str. wing, Fus.-only	G.E.T.S., floor off, suction on	35 m/s	LS970029	Alpha scan
T5.TMF	184.5 mm	-4° to 14° (+2°)	Gen. mod. str. wing, Fus.-only	G.E.T.S., floor off, suction off	0 m/s	LS970030	Mass scan
T5.TMF	184.5 mm	-4° to 14° (+2°)	Gen. mod. str. wing, Fus.-only	G.E.T.S., floor off, suction on	35 m/s	LS970031	Alpha scan
T6.TMF	224.5 mm	-4° to 14° (+2°), 15° to 17° (+1°)	Gen. mod. str. wing, Fus.-only	G.E.T.S., floor off, suction off	0 m/s	LS970032	Mass scan
T6.TMF	224.5 mm	-4° to 14° (+2°), 15° to 17° (+1°)	Gen. mod. str. wing, Fus.-only	G.E.T.S., floor off, suction on	35 m/s	LS970033	Alpha scan
T7.TMF	262 mm	-4° to 14° (+2°), 15° to 18° (+1°)	Gen. mod. str. wing, Fus.-only	G.E.T.S., floor off, suction off	0 m/s	LS970034	Mass scan
T7.TMF	262 mm	-4° to 14° (+2°), 15° to 18° (+1°)	Gen. mod. str. wing, Fus.-only	G.E.T.S., floor off, suction on	35 m/s	LS970035	Alpha scan
T7.TMF	262 mm	-4° to 14° (+2°), 15° to 18° (+1°)	Gen. mod. str. wing, tail off	G.E.T.S., floor off, suction off	0 m/s	LS970036	Mass scan
T7.TMF	262 mm	-4° to 14° (+2°), 15° to 18° (+1°)	Gen. mod. str. wing, tail off	G.E.T.S., floor off, suction on	35 m/s	LS970037	Alpha scan
T6.TMF	224.5 mm	-4° to 14° (+2°), 15° to 17° (+1°)	Gen. mod. str. wing, tail off	G.E.T.S., floor off, suction off	0 m/s	LS970038	Mass scan
T6.TMF	224.5 mm	-4° to 14° (+2°), 15° to 17° (+1°)	Gen. mod. str. wing, tail off	G.E.T.S., floor off, suction on	35 m/s	LS970039	Alpha scan
T5.TMF	184.5 mm	-4° to 14° (+2°)	Gen. mod. str. wing, tail off	G.E.T.S., floor off, suction off	0 m/s	LS970040	Mass scan
T5.TMF	184.5 mm	-4° to 14° (+2°)	Gen. mod. str. wing, tail off	G.E.T.S., floor off, suction on	35 m/s	LS970041	Alpha scan
T4.TMF	144.5 mm	-4° to 10° (+2°)	Gen. mod. str. wing, tail off	G.E.T.S., floor off, suction off	0 m/s	LS970042	Mass scan
T4.TMF	144.5 mm	-4° to 10° (+2°)	Gen. mod. str. wing, tail off	G.E.T.S., floor off, suction on	35 m/s	LS970043	Alpha scan
T3.TMF	104.5 mm	-4° to 8° (+2°)	Gen. mod. str. wing, tail off	G.E.T.S., floor off, suction off	0 m/s	LS970044	Mass scan
T3.TMF	104.5 mm	-4° to 8° (+2°)	Gen. mod. str. wing, tail off	G.E.T.S., floor off, suction on	35 m/s	LS970045	Alpha scan
T3.TMF	104.5 mm	-4° to 8° (+2°)	Gen. mod. str. wing, tail on	G.E.T.S., floor off, suction off	0 m/s	LS970046	Mass scan
T3.TMF	104.5 mm	-4° to 8° (+2°)	Gen. mod. str. wing, tail on	G.E.T.S., floor off, suction on	35 m/s	LS970047	Alpha scan
T4.TMF	144.5 mm	-4° to 10° (+2°)	Gen. mod. str. wing, tail on	G.E.T.S., floor off, suction off	0 m/s	LS970048	Mass scan
T4.TMF	144.5 mm	-4° to 10° (+2°)	Gen. mod. str. wing, tail on	G.E.T.S., floor off, suction on	35 m/s	LS970049	Alpha scan
T5.TMF	184.5 mm	-4° to 14° (+2°)	Gen. mod. str. wing, tail on	G.E.T.S., floor off, suction off	0 m/s	LS970050	Mass scan
T5.TMF	184.5 mm	-4° to 14° (+2°)	Gen. mod. str. wing, tail on	G.E.T.S., floor off, suction on	35 m/s	LS970051	Alpha scan

Test matrix file	Hrp	α range	model	test section	Velocity	Output file	Comments
T6.TMF	224.5 mm	-4° to 14° (+2°), 15° to 17° (+1°)	Gen. mod. str. wing, tail on	G.E.T.S., floor off, suction off	0 m/s	LS970052	Mass scan
T6.TMF	224.5 mm	-4° to 14° (+2°), 15° to 17° (+1°)	Gen. mod. str. wing, tail on	G.E.T.S., floor off, suction on	35 m/s	LS970053	Alpha scan
T7.TMF	262 mm	-4° to 14° (+2°), 15° to 18° (+1°)	Gen. mod. str. wing, tail on	G.E.T.S., floor off, suction off	0 m/s	LS970054	Mass scan
T7.TMF	262 mm	-4° to 14° (+2°), 15° to 18° (+1°)	Gen. mod. str. wing, tail on	G.E.T.S., floor off, suction on	35 m/s	LS970055	Alpha scan
T8.TMF	302 mm	-4° to 18° (+2°)	Gen. mod. str. wing, tail on	G.E.T.S., floor off, suction off	0 m/s	LS970056	Mass scan
T7.TMF	302 mm	-4° to 14° (+2°), 15° to 18° (+1°)	Gen. mod. str. wing, tail on	G.E.T.S., floor off, suction on	35 m/s	LS970057	Alpha scan
T8.TMF	342 mm	-4° to 18° (+2°)	Gen. mod. str. wing, tail on	G.E.T.S., floor off, suction off	0 m/s	LS970058	Mass scan
T7.TMF	342 mm	-4° to 14° (+2°), 15° to 18° (+1°)	Gen. mod. str. wing, tail on	G.E.T.S., floor off, suction on	35 m/s	LS970059	Alpha scan
T8.TMF	382 mm	-4° to 18° (+2°)	Gen. mod. str. wing, tail on	G.E.T.S., floor off, suction off	0 m/s	LS970060	Mass scan
T7.TMF	382 mm	-4° to 14° (+2°), 15° to 18° (+1°)	Gen. mod. str. wing, tail on	G.E.T.S., floor off, suction on	35 m/s	LS970061	Alpha scan
T8.TMF	422 mm	-4° to 18° (+2°)	Gen. mod. str. wing, tail on	G.E.T.S., floor off, suction off	0 m/s	LS970062	Mass scan
T7.TMF	422 mm	-4° to 14° (+2°), 15° to 18° (+1°)	Gen. mod. str. wing, tail on	G.E.T.S., floor off, suction on	35 m/s	LS970063	Alpha scan
T8.TMF	422 mm	-4° to 18° (+2°)	Gen. mod. str. wing, tail off	G.E.T.S., floor off, suction off	0 m/s	LS970064	Mass scan
T7.TMF	422 mm	-4° to 14° (+2°), 15° to 18° (+1°)	Gen. mod. str. wing, tail off	G.E.T.S., floor off, suction on	35 m/s	LS970065	Alpha scan
T8.TMF	382 mm	-4° to 18° (+2°)	Gen. mod. str. wing, tail off	G.E.T.S., floor off, suction off	0 m/s	LS970066	Mass scan
T7.TMF	382 mm	-4° to 14° (+2°), 15° to 18° (+1°)	Gen. mod. str. wing, tail off	G.E.T.S., floor off, suction on	35 m/s	LS970067	Alpha scan
T8.TMF	342 mm	-4° to 18° (+2°)	Gen. mod. str. wing, tail off	G.E.T.S., floor off, suction off	0 m/s	LS970068	Mass scan
T7.TMF	342 mm	-4° to 14° (+2°), 15° to 18° (+1°)	Gen. mod. str. wing, tail off	G.E.T.S., floor off, suction on	35 m/s	LS970069	Alpha scan
T8.TMF	302 mm	-4° to 18° (+2°)	Gen. mod. str. wing, tail off	G.E.T.S., floor off, suction off	0 m/s	LS970070	Mass scan
T7.TMF	302 mm	-4° to 14° (+2°), 15° to 18° (+1°)	Gen. mod. str. wing, tail off	G.E.T.S., floor off, suction on	35 m/s	LS970071	Alpha scan
T8.TMF	302 mm	-4° to 18° (+2°)	Gen. mod. str. wing, Fus.-only	G.E.T.S., floor off, suction off	0 m/s	LS970072	Mass scan
T7.TMF	302 mm	-4° to 14° (+2°), 15° to 18° (+1°)	Gen. mod. str. wing, Fus.-only	G.E.T.S., floor off, suction on	35 m/s	LS970073	Alpha scan
T8.TMF	342 mm	-4° to 18° (+2°)	Gen. mod. str. wing, Fus.-only	G.E.T.S., floor off, suction off	0 m/s	LS970074	Mass scan
T7.TMF	342 mm	-4° to 14° (+2°), 15° to 18° (+1°)	Gen. mod. str. wing, Fus.-only	G.E.T.S., floor off, suction on	35 m/s	LS970075	Alpha scan
T8.TMF	302 mm	-4° to 18° (+2°)	Gen. mod. str. wing, Fus.-only	G.E.T.S., floor off, suction off	0 m/s	LS970076	Mass scan
T7.TMF	302 mm	-4° to 14° (+2°), 15° to 18° (+1°)	Gen. mod. str. wing, Fus.-only	G.E.T.S., floor off, suction on	35 m/s	LS970077	Alpha scan
T8.TMF	302 mm	-4° to 18° (+2°)	Gen. mod. str. wing, Fus.-only	G.E.T.S., floor off, suction off	0 m/s	LS970078	Mass scan
T7.TMF	302 mm	-4° to 14° (+2°), 15° to 18° (+1°)	Gen. mod. str. wing, Fus.-only	G.E.T.S., floor off, suction on	35 m/s	LS970079	Alpha scan
-	-	-	-	-	-	LS970080	Sign check

Test matrix file	**Hrp**	**α range**	**model**	**test section**	**Velocity**	**Output file**	**Comments**
T8.TMF	422 mm	-4° to 18° (+2°)	Gen. mod. str. wing, tail off	G.E.T.S., floor off, suction off	0 m/s	LS970081	Mass scan
T7.TMF	422 mm	-4° to 14° (+2°), 15° to 18° (+1°)	Gen. mod. str. wing, tail off	G.E.T.S., floor on, suction on	35 m/s	LS970082	Alpha scan
T7.TMF	422 mm	-4° to 14° (+2°), 15° to 18° (+1°)	Gen. mod. str. wing, tail off	G.E.T.S., floor on, suction on	35 m/s	LS970083	As. (repeat)
T7.TMF	342 mm	-4° to 14° (+2°), 15° to 18° (+1°)	Gen. mod. str. wing, tail off	G.E.T.S., floor on, suction on	35 m/s	LS970084	Alpha scan
T7.TMF	302 mm	-4° to 14° (+2°), 15° to 18° (+1°)	Gen. mod. str. wing, tail off	G.E.T.S., floor on, suction on	35 m/s	LS970085	Alpha scan
T8.TMF	302 mm	-4° to 18° (+2°)	Gen. mod. str. wing, tail on	G.E.T.S., floor off, suction off	0 m/s	LS970086	Mass scan
T7.TMF	302 mm	-4° to 14° (+2°), 15° to 18° (+1°)	Gen. mod. str. wing, tail on	G.E.T.S., floor on, suction on	35 m/s	LS970087	Alpha scan
T7.TMF	342 mm	-4° to 14° (+2°), 15° to 18° (+1°)	Gen. mod. str. wing, tail on	G.E.T.S., floor on, suction on	35 m/s	LS970088	Alpha scan
T7.TMF	422 mm	-4° to 14° (+2°), 15° to 18° (+1°)	Gen. mod. str. wing, tail on	G.E.T.S., floor on, suction on	35 m/s	LS970089	Alpha scan
T8.TMF	422 mm	-4° to 18° (+2°)	Gen. mod. str. wing, Fus.-only	G.E.T.S., floor off, suction off	0 m/s	LS970090	Mass scan
T7.TMF	422 mm	-4° to 14° (+2°), 15° to 18° (+1°)	Gen. mod. str. wing, Fus.-only	G.E.T.S., floor on, suction on	35 m/s	LS970091	Alpha scan
T7.TMF	342 mm	-4° to 14° (+2°), 15° to 18° (+1°)	Gen. mod. str. wing, Fus.-only	G.E.T.S., floor on, suction on	35 m/s	LS970092	Alpha scan
T7.TMF	302 mm	-4° to 14° (+2°), 15° to 18° (+1°)	Gen. mod. str. wing, Fus.-only	G.E.T.S., floor on, suction on	35 m/s	LS970093	Alpha scan
T8.TMF	262 mm	-4° to 18° (+2°)	Gen. mod. str. wing, Fus.-only	G.E.T.S., floor off, suction off	0 m/s	LS970094	Mass scan
T7.TMF	262 mm	-4° to 14° (+2°), 15° to 18° (+1°)	Gen. mod. str. wing, Fus.-only	G.E.T.S., floor on, suction on	35 m/s	LS970095	Alpha scan
T5.TMF	184.5 mm	-4° to 14° (+2°)	Gen. mod. str. wing, Fus.-only	G.E.T.S., floor on, suction on	35 m/s	LS970096	Alpha scan
T3.TMF	104.5 mm	-4° to 8° (+2°)	Gen. mod. str. wing, Fus.-only	G.E.T.S., floor on, suction on	35 m/s	LS970097	Alpha scan
T7.TMF	262 mm	-4° to 14° (+2°), 15° to 18° (+1°)	Gen. mod. str. wing, tail off	G.E.T.S., floor off, suction off	0 m/s	LS970098	Mass scan
T7.TMF	262 mm	-4° to 14° (+2°), 15° to 18° (+1°)	Gen. mod. str. wing, tail off	G.E.T.S., floor on, suction on	35 m/s	LS970099	Alpha scan
T5.TMF	184.5 mm	-4° to 14° (+2°)	Gen. mod. str. wing, tail off	G.E.T.S., floor on, suction on	35 m/s	LS970100	Alpha scan
T3.TMF	104.5 mm	-4° to 8° (+2°)	Gen. mod. str. wing, tail off	G.E.T.S., floor on, suction on	35 m/s	LS970101	Alpha scan
T7.TMF	262 mm	-4° to 14° (+2°), 15° to 18° (+1°)	Gen. mod. str. wing, tail on	G.E.T.S., floor off, suction off	0 m/s	LS970102	Mass scan
T7.TMF	262 mm	-4° to 14° (+2°), 15° to 18° (+1°)	Gen. mod. str. wing, tail on	G.E.T.S., floor on, suction on	35 m/s	LS970103	Alpha scan
T5.TMF	184.5 mm	-4° to 14° (+2°)	Gen. mod. str. wing, tail on	G.E.T.S., floor on, suction on	35 m/s	LS970104	Alpha scan
T3.TMF	104.5 mm	-4° to 8° (+2°)	Gen. mod. str. wing, tail on	G.E.T.S., floor on, suction on	35 m/s	LS970105	Alpha scan

APPENDIX A-4: RESULTS OF PRELIMINARY TESTS

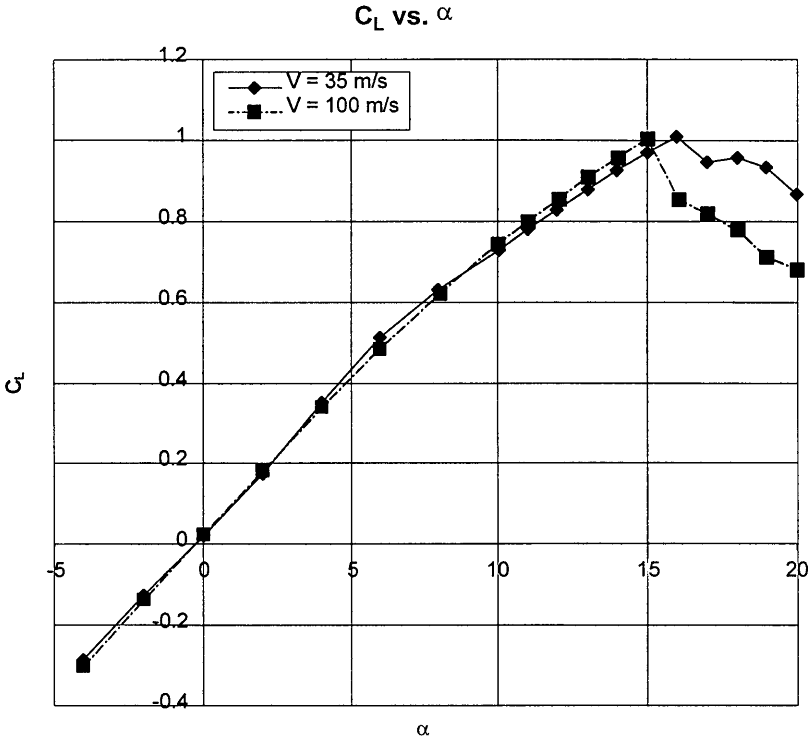

Figure A-3: Effect of velocity on Lift

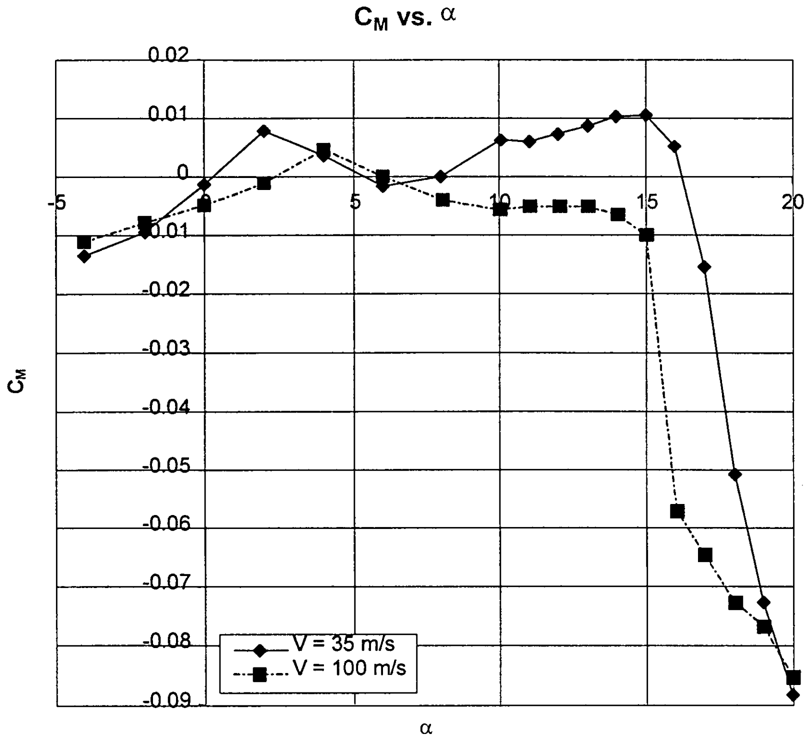

Figure A-4: Effect of Velocity on pitching moment

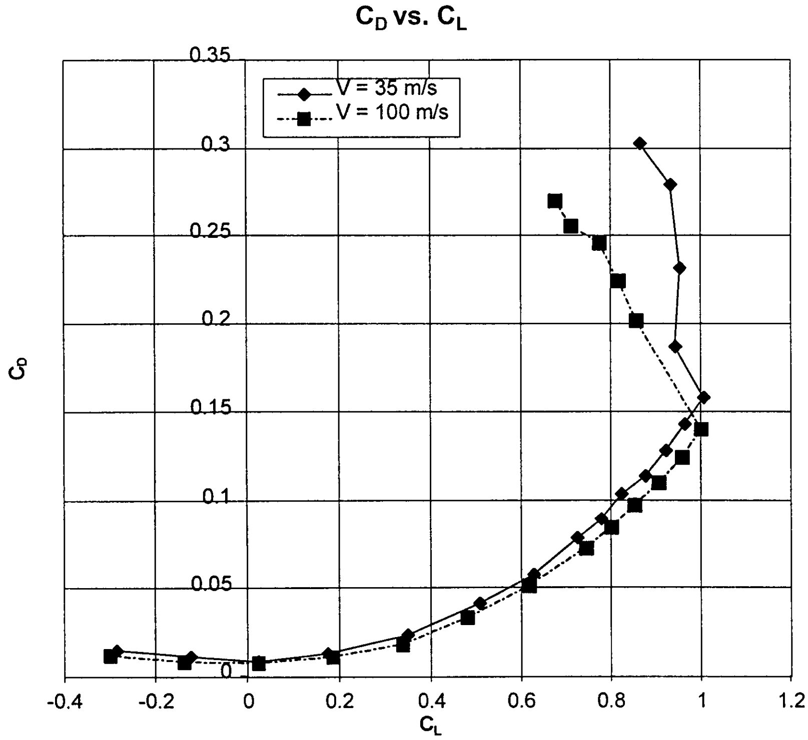

Figure A-5: Effect of Velocity on drag - centre line

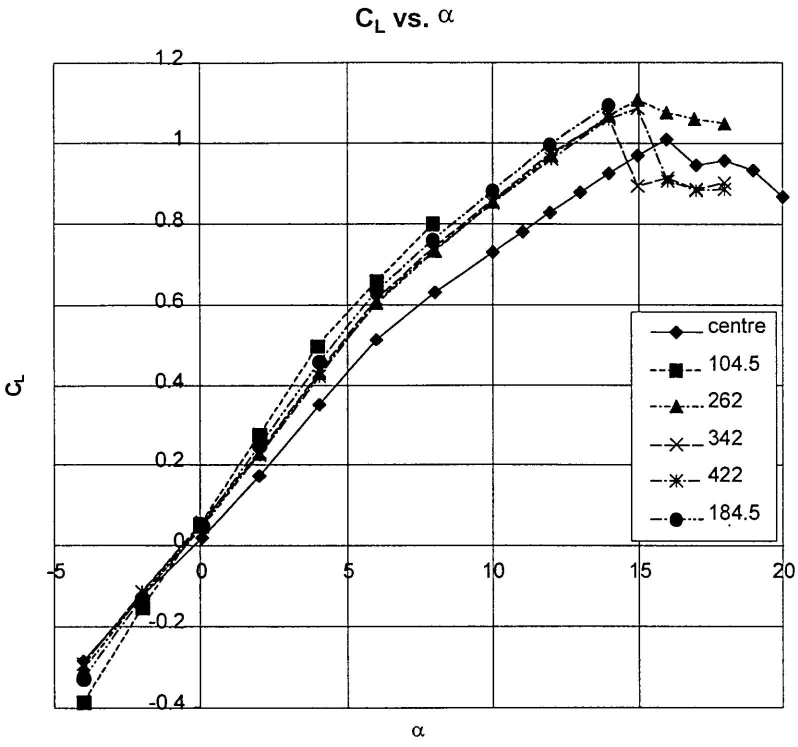

Figure A-6: Lift - Tail off, Rolling Floor off

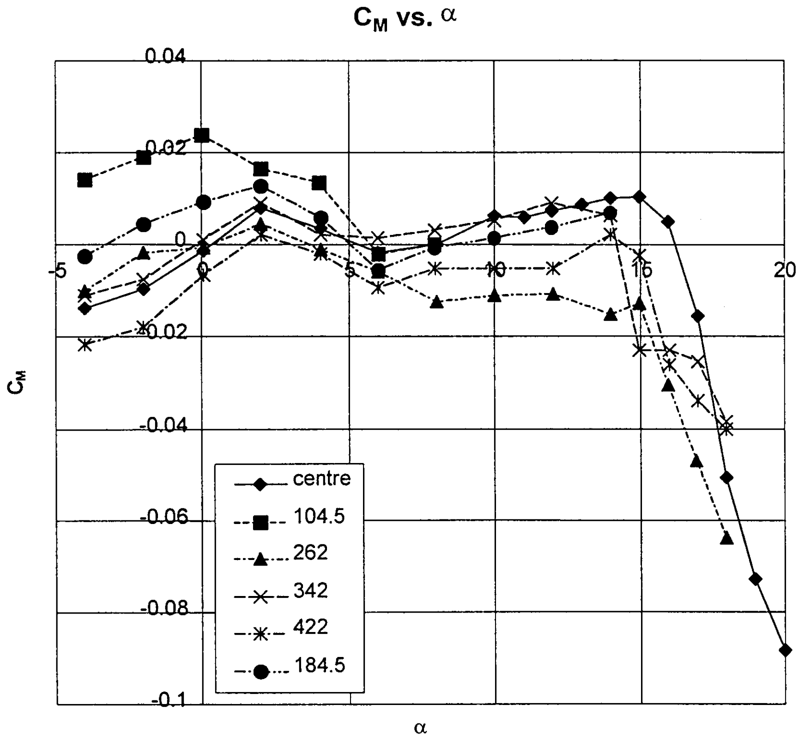

Figure A-7: Pitching moment - Tail off, Rolling Floor off

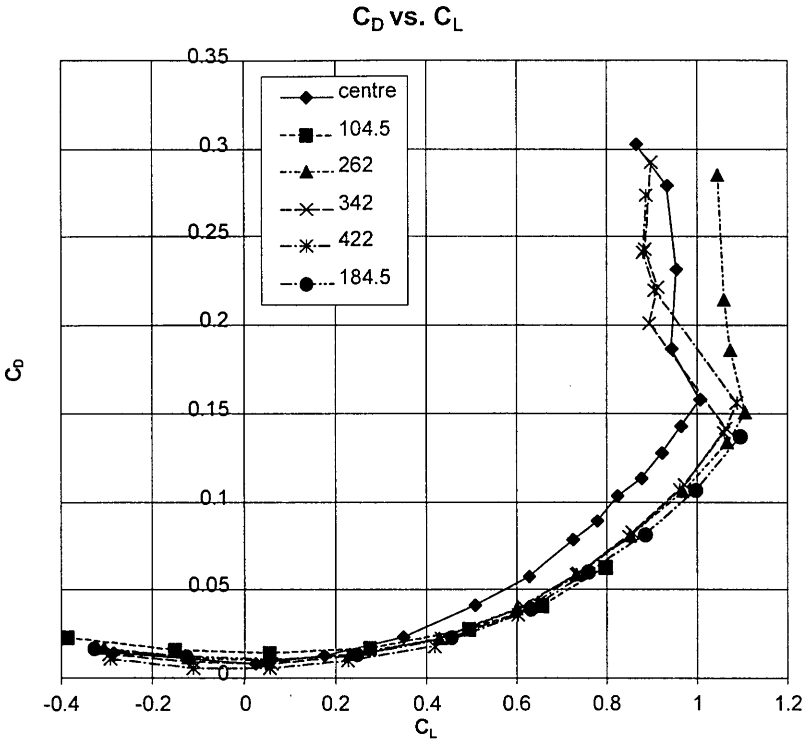

Figure A-8: Drag - Tail off, Rolling Floor off

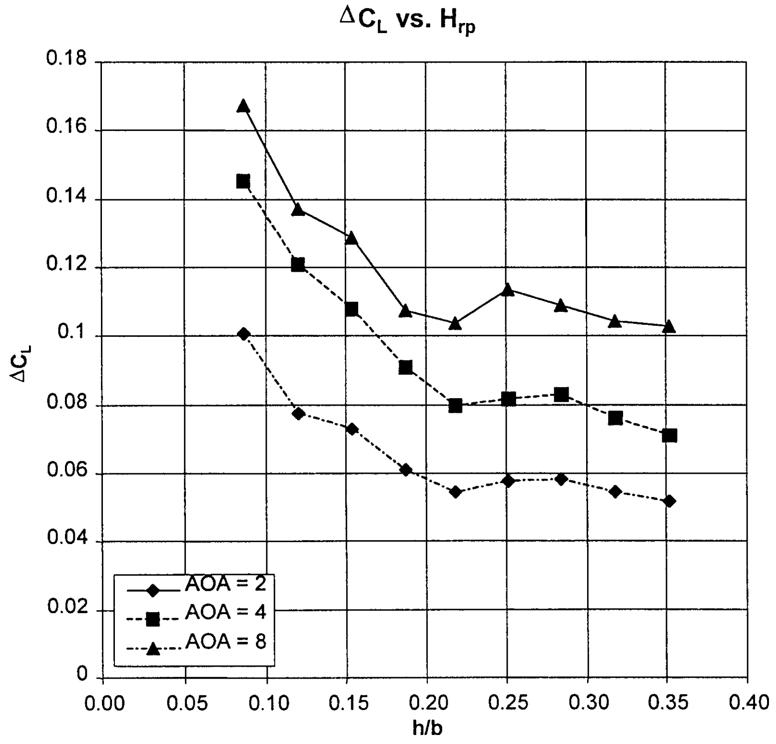

Figure A-9: Increase in Lift - Tail off, Rolling Floor off

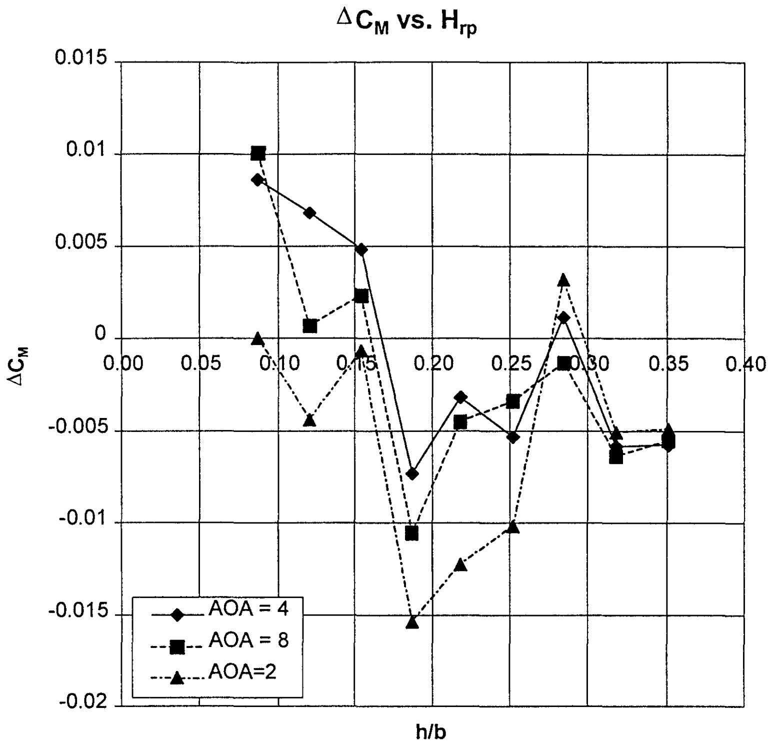

Figure A-10: Increase in Pitching moment - Tail off, Rolling Floor off

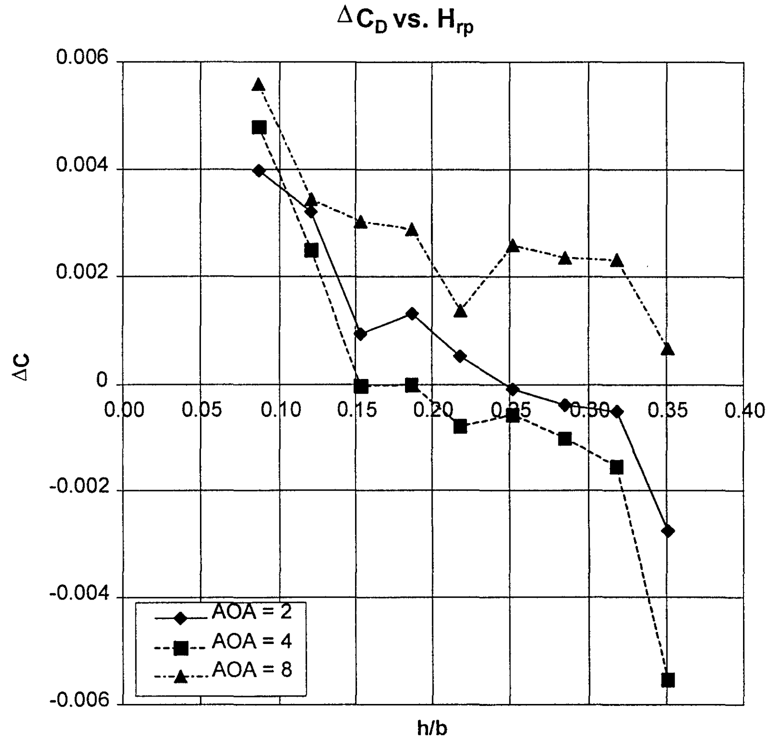

Figure A-11: Increase in Drag - Tail off, Rolling Floor off

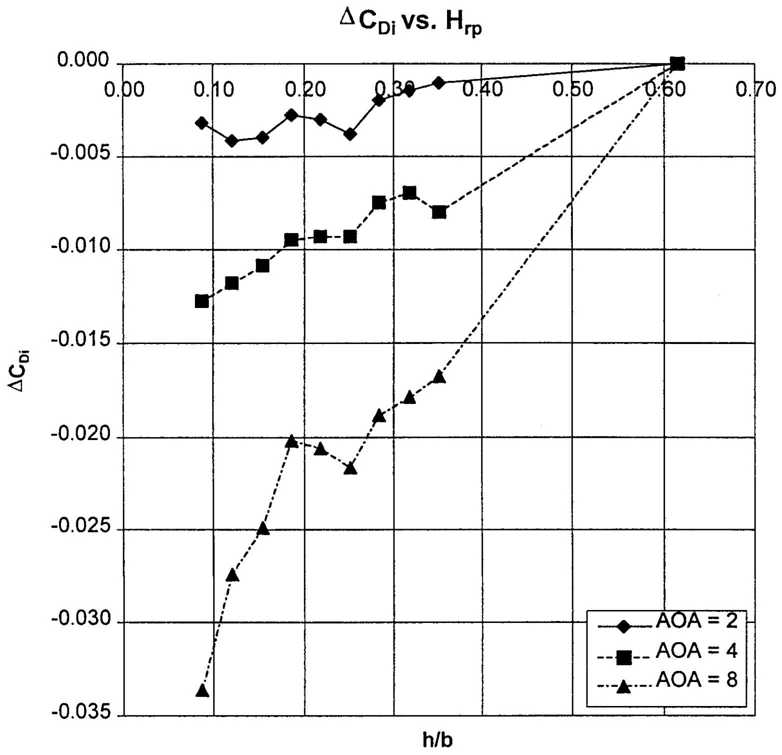

Figure A-12: Increase in Induced Drag - Tail off, Rolling Floor off

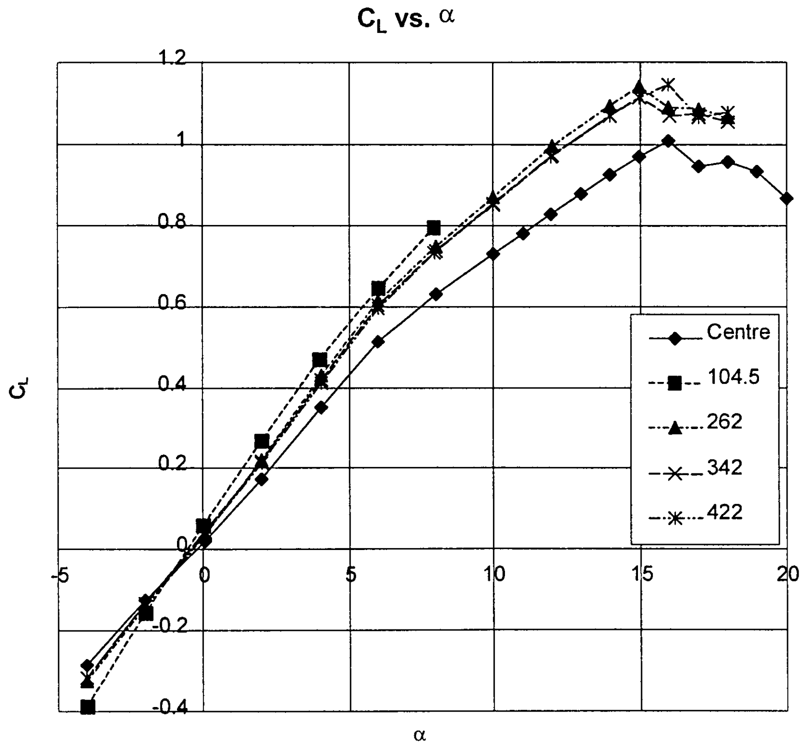

Figure A-13: Lift - Tail off, Rolling Floor on

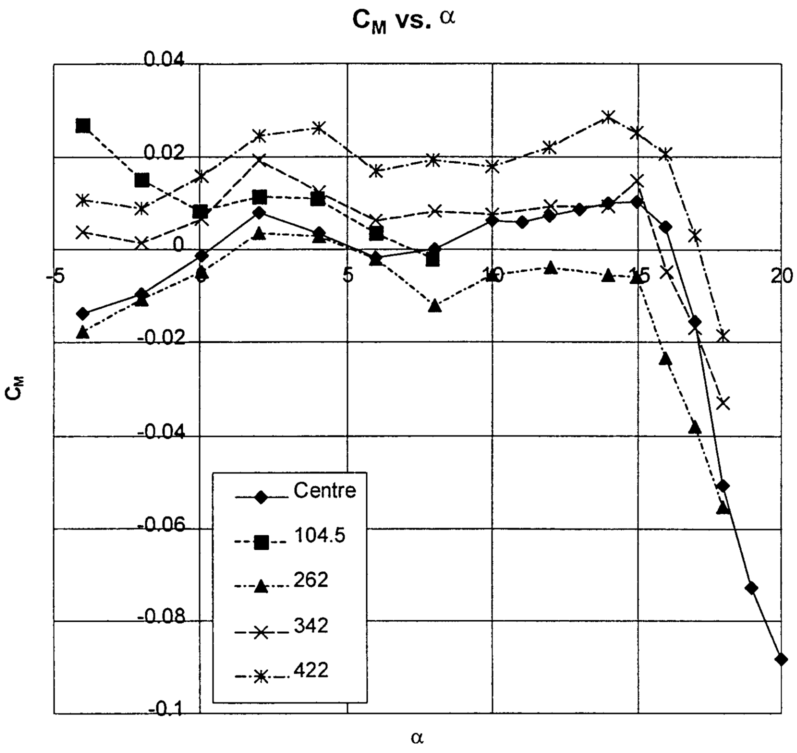

Figure A-14: Pitching moment - Tail off, Rolling Floor on

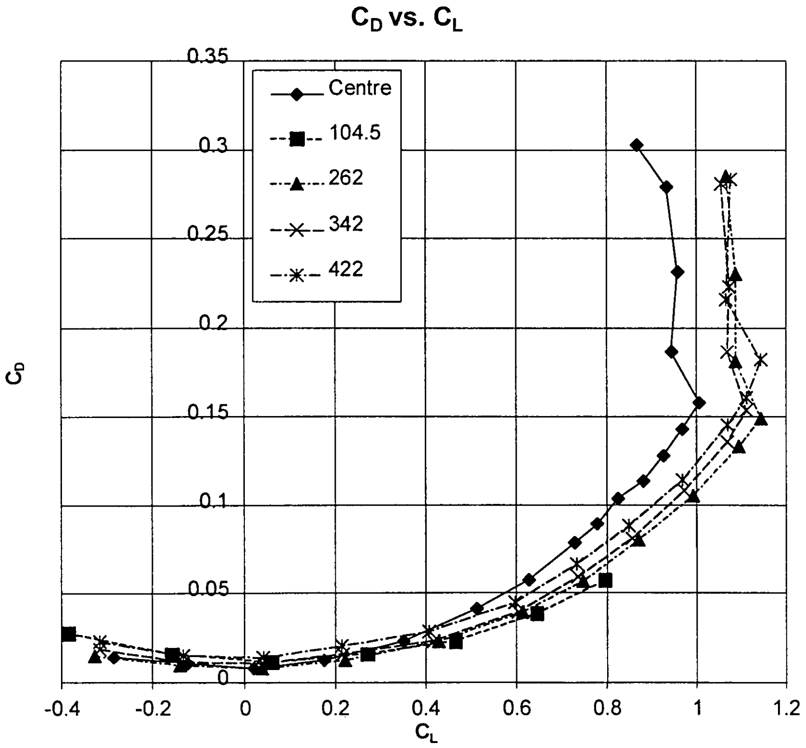

Figure A-15: Drag - Tail off, Rolling Floor on

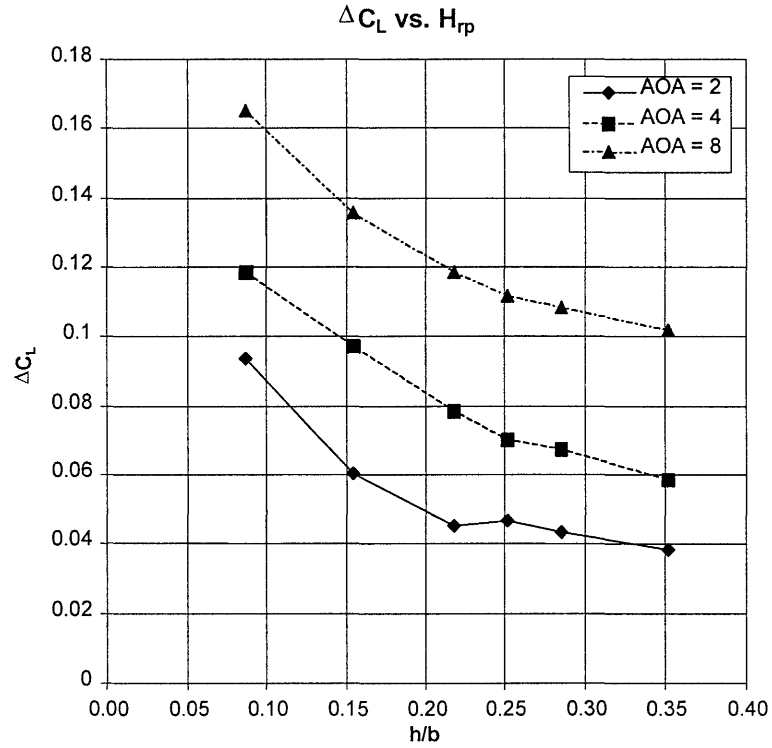

Figure A-16: Increase in Lift - Tail off, Rolling Floor on

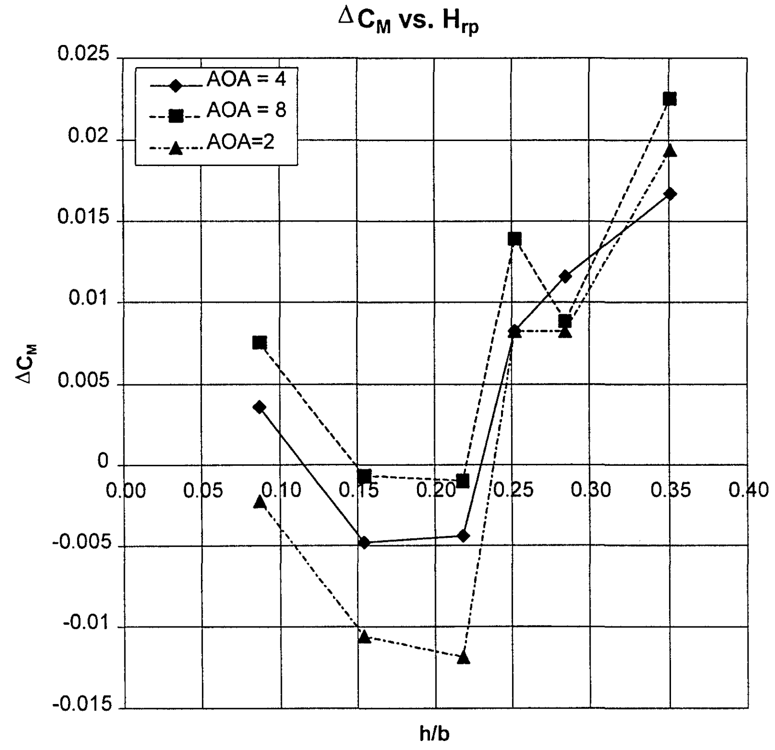

Figure A-17: Increase in Pitching moment - Tail off, Rolling Floor on

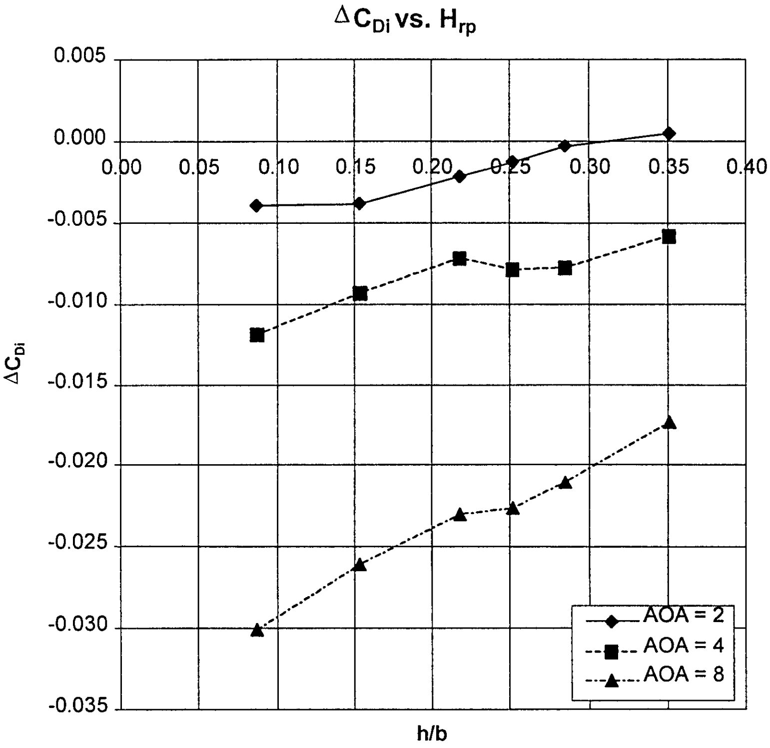

Figure A-18: Increase in Induced Drag - Tail off, Rolling Floor on

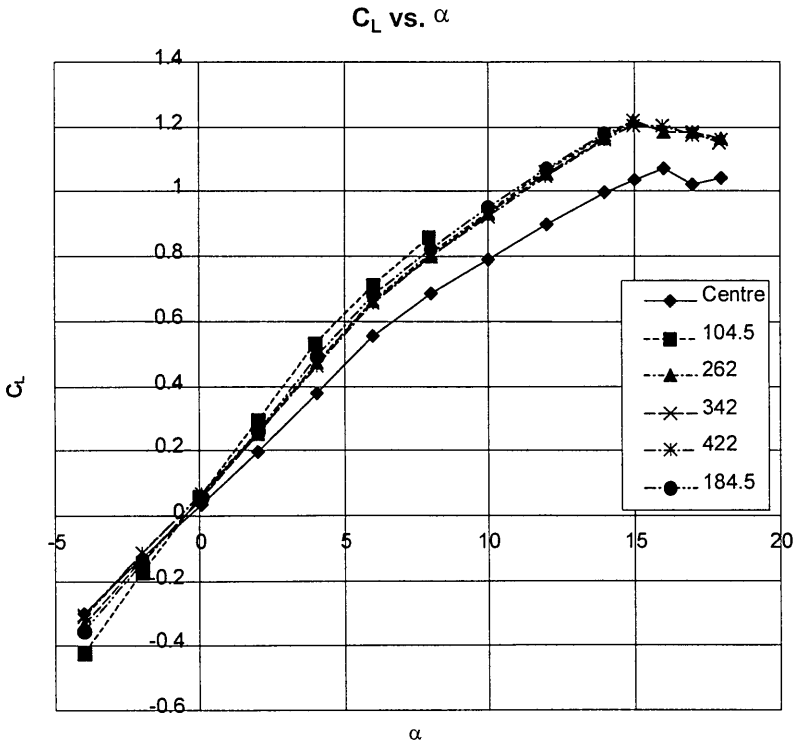

Figure A-19: Lift - Tail on, Rolling Floor off

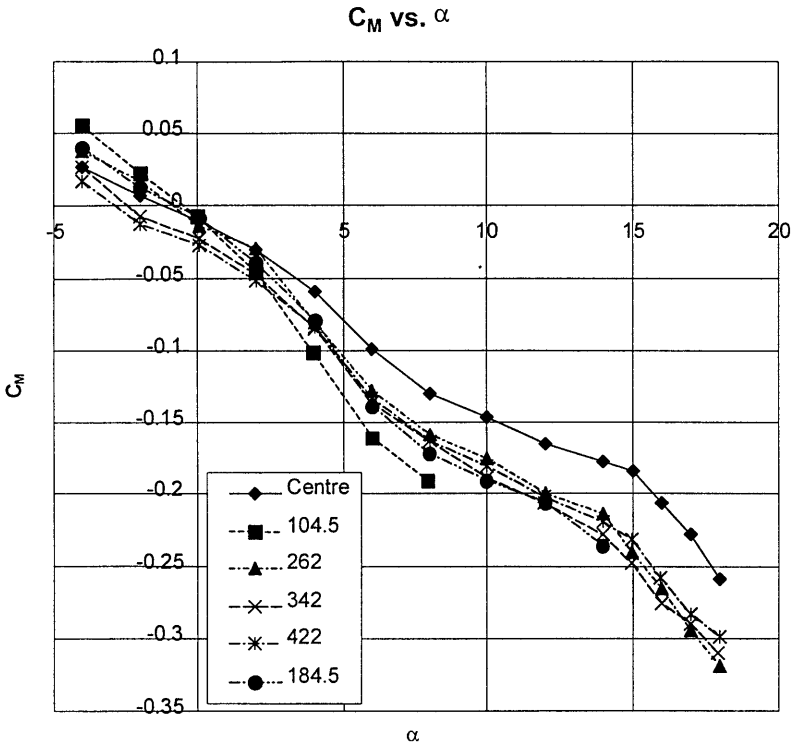

Figure A-20: Pitching moment - Tail on, Rolling Floor off

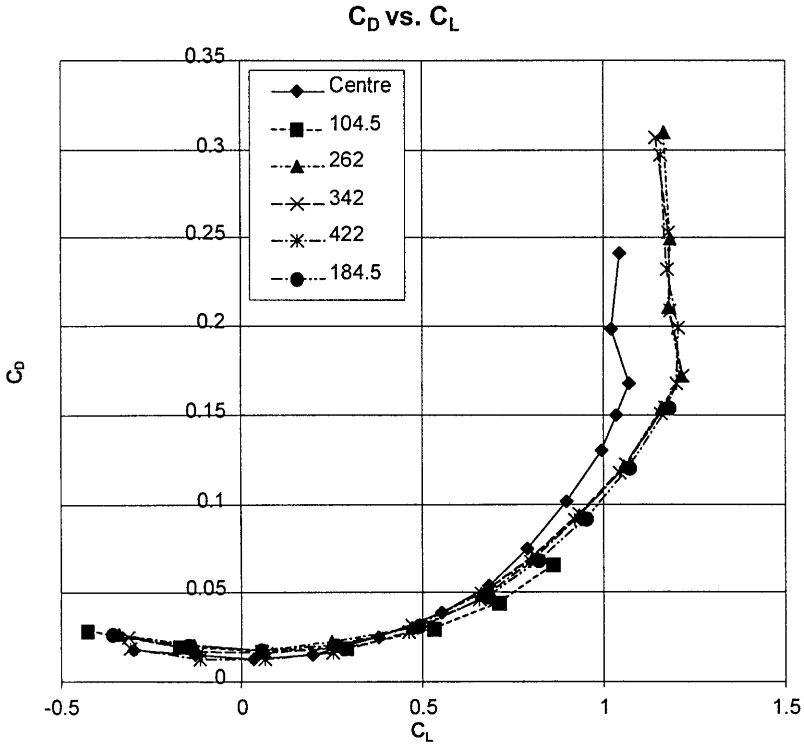

Figure A-21: Drag - Tail on, Rolling Floor off

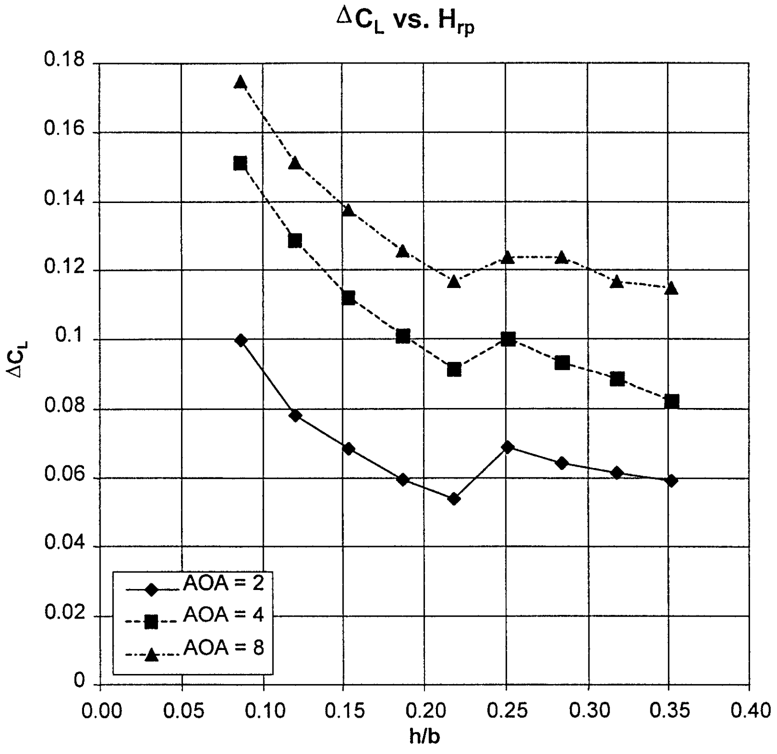

Figure A-22: Increase in Lift - Tail on, Rolling Floor off

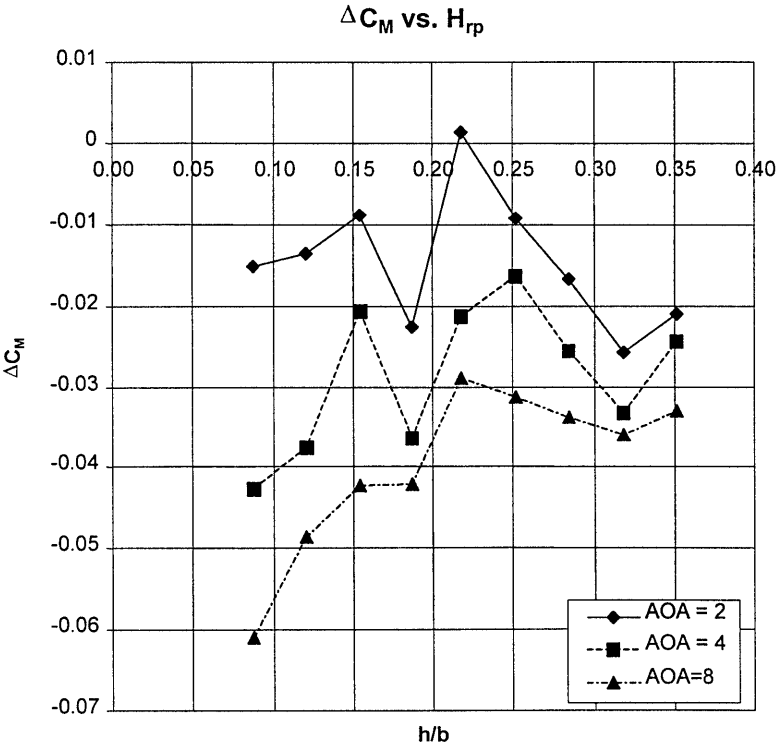

Figure A-23: Increase in Pitching moment - Tail on, Rolling Floor off

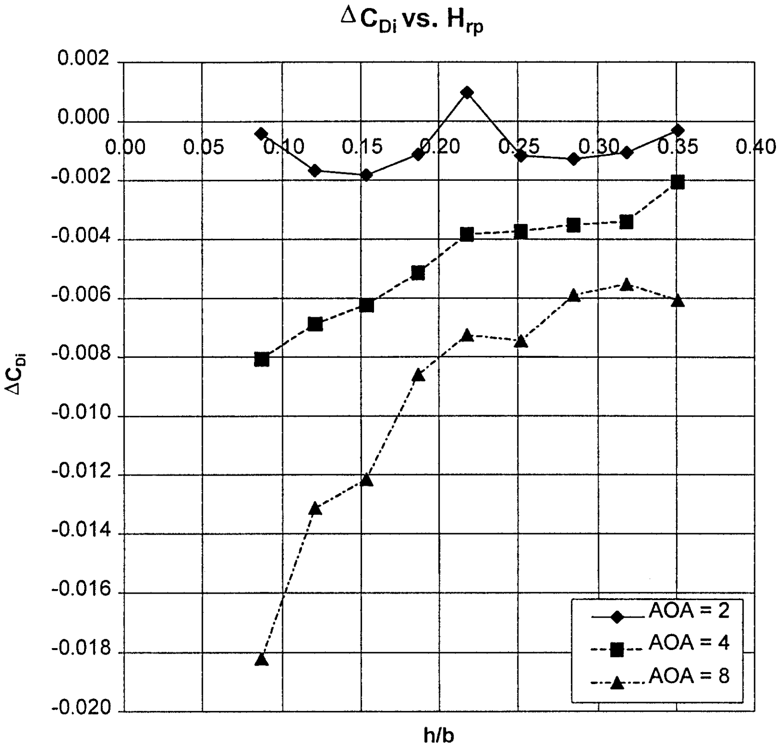

Figure A-24: Increase in Induced Drag - Tail on, Rolling Floor off

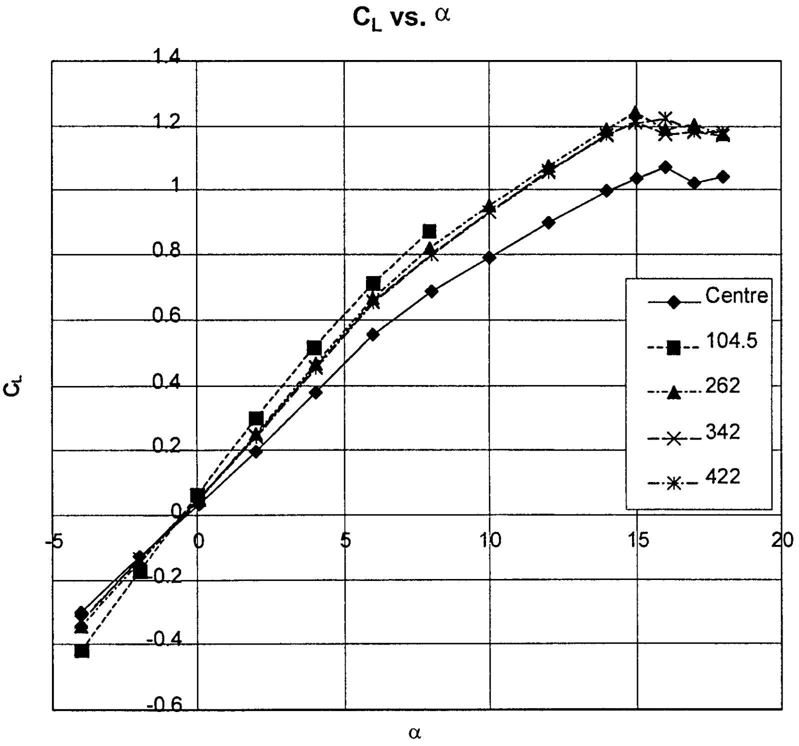

Figure A-25: Lift - Tail on, Rolling Floor on

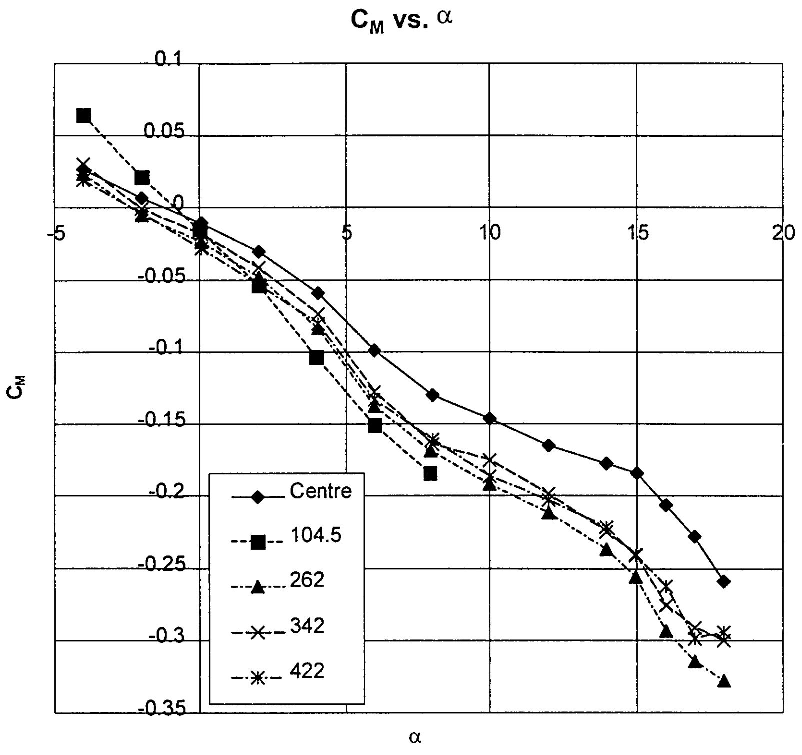

Figure A-26: Pitching moment - Tail on, Rolling Floor on

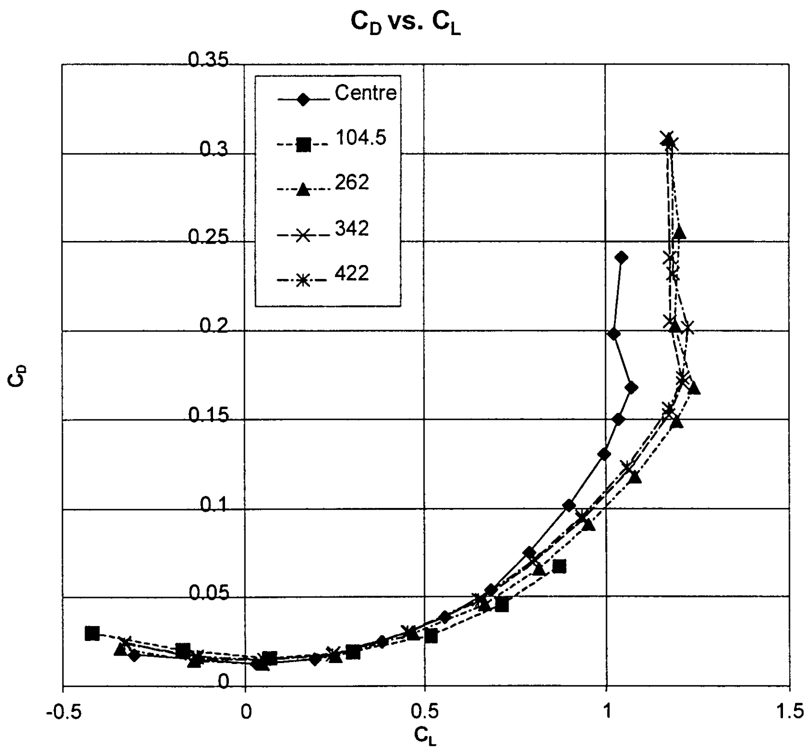

Figure A-27: Drag - Tail on, Rolling Floor on

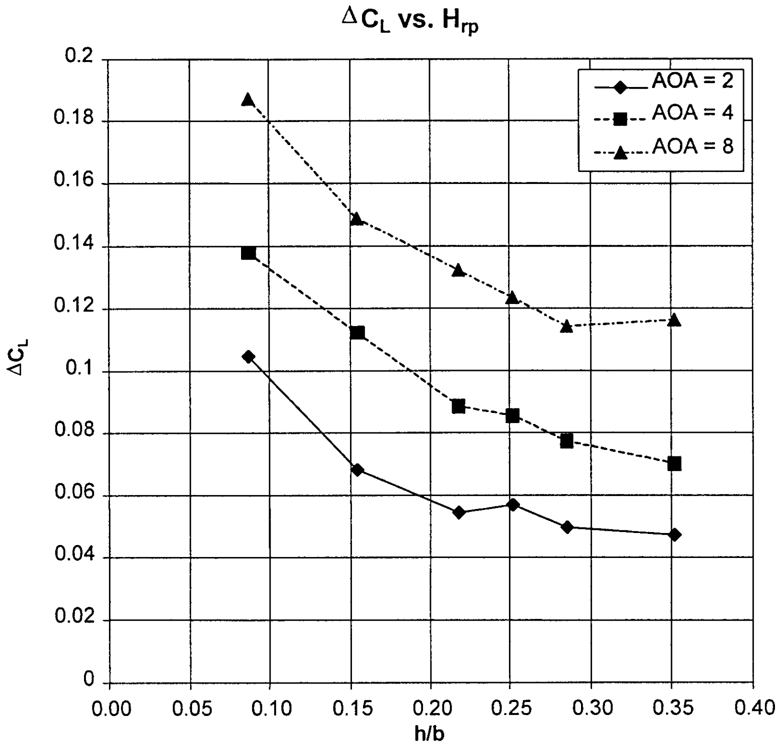

Figure A-28: Increase in Lift - Tail on, Rolling Floor on

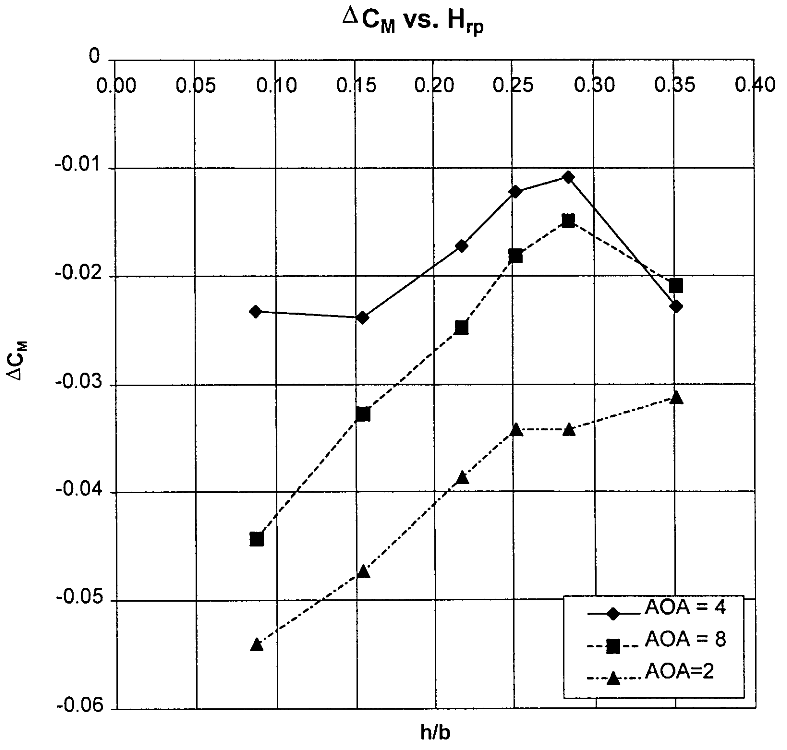

Figure A-29: Increase in Pitching moment - Tail on, Rolling Floor on

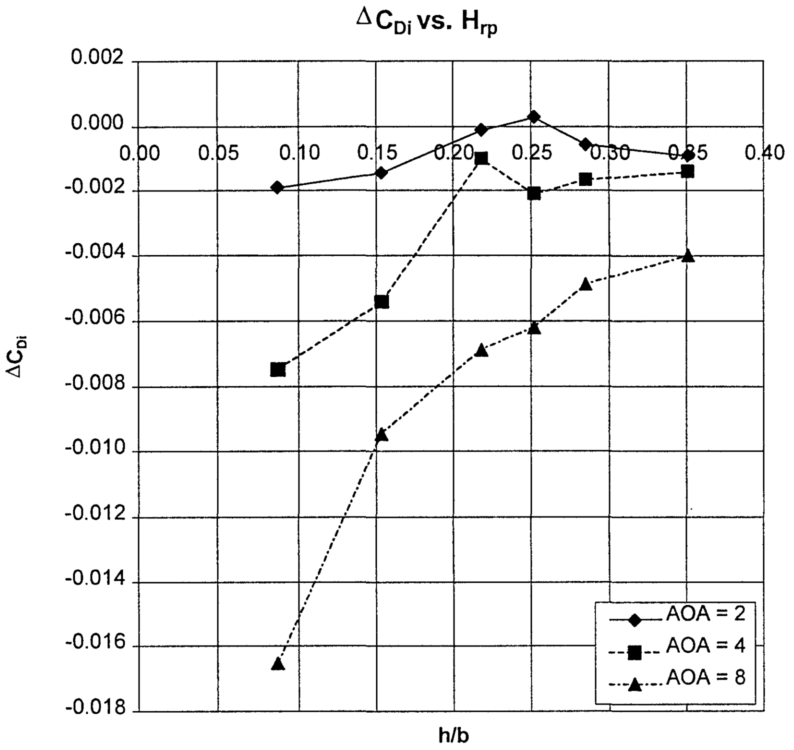

Figure A-30: Increase in Induced Drag - Tail on, Rolling Floor on

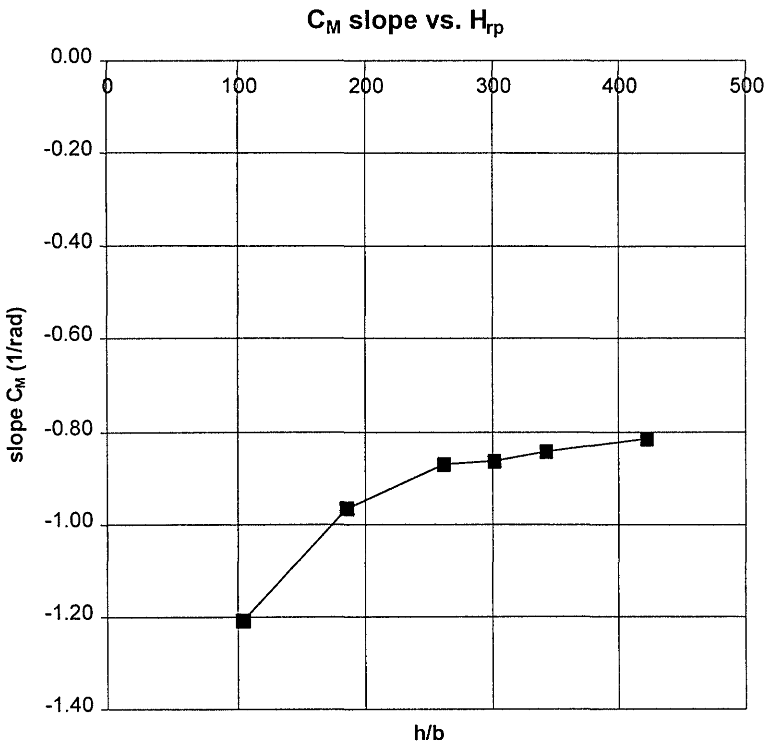

Figure A-31: Slope of Pitching Moment Coefficient - Tail on, Rolling Floor on

APPENDIX A-5: SECTION PROPERTIES OF NACA0012 PROFILE, PREDICTED USING XFOIL

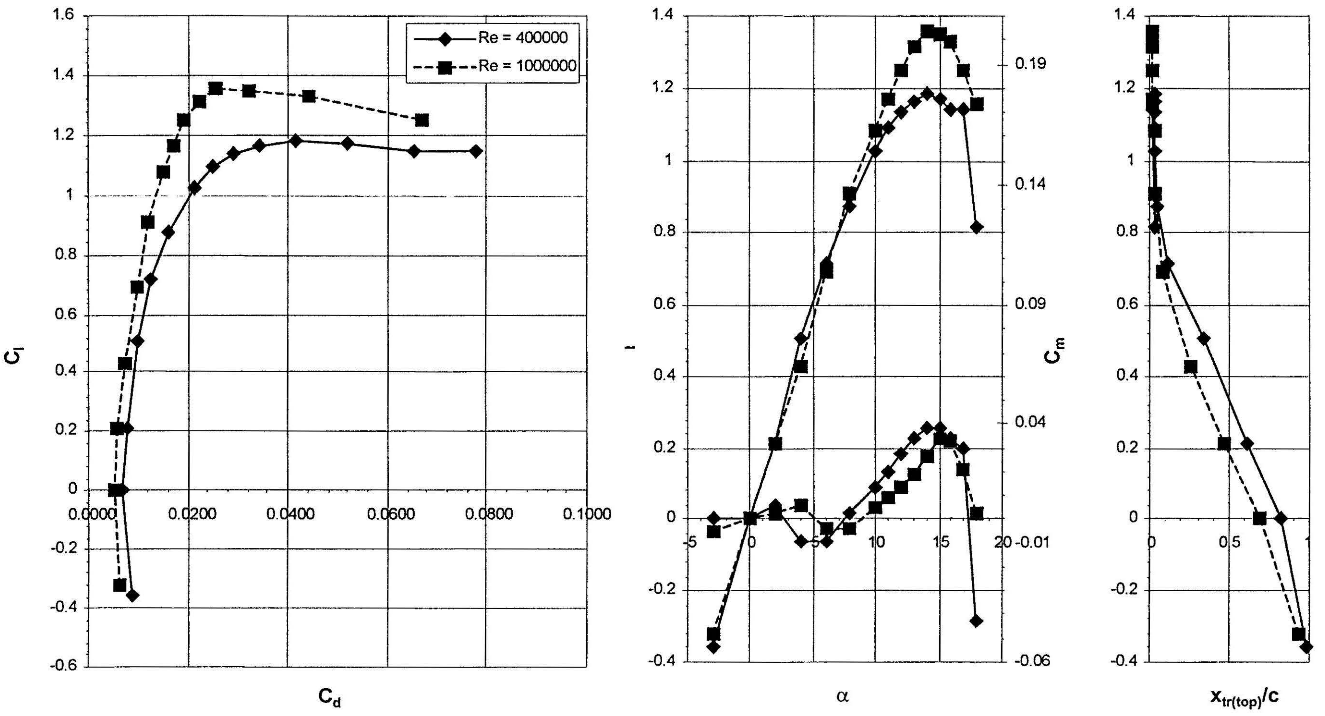

Figure A-32: Sectional properties of NACA0012 profile, Re=400000 and Re = 1000000

APPENDIX A-6: WIND TUNNEL SET-UP USED FOR PRELIMINARY TESTS

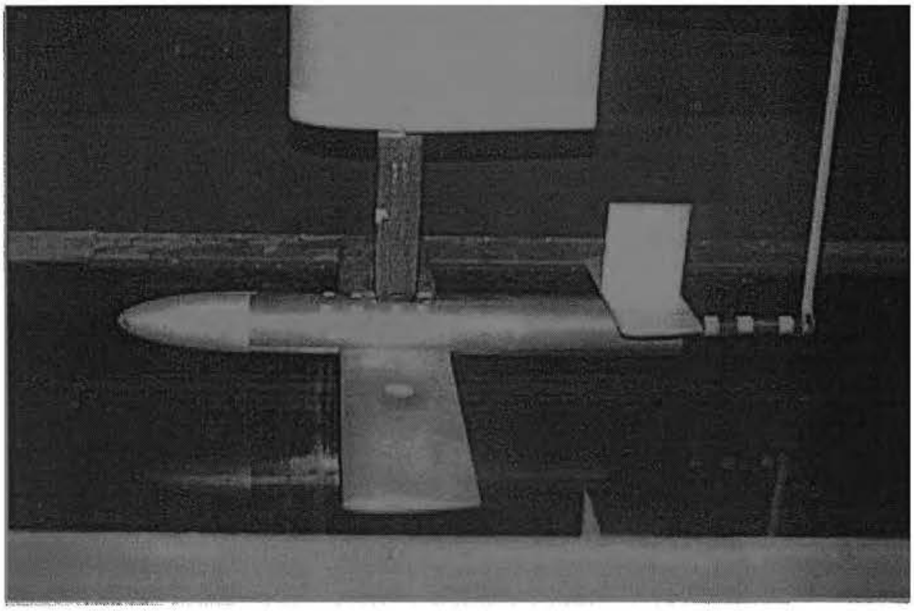

Figure A-33: Side view of model in ground effect test section

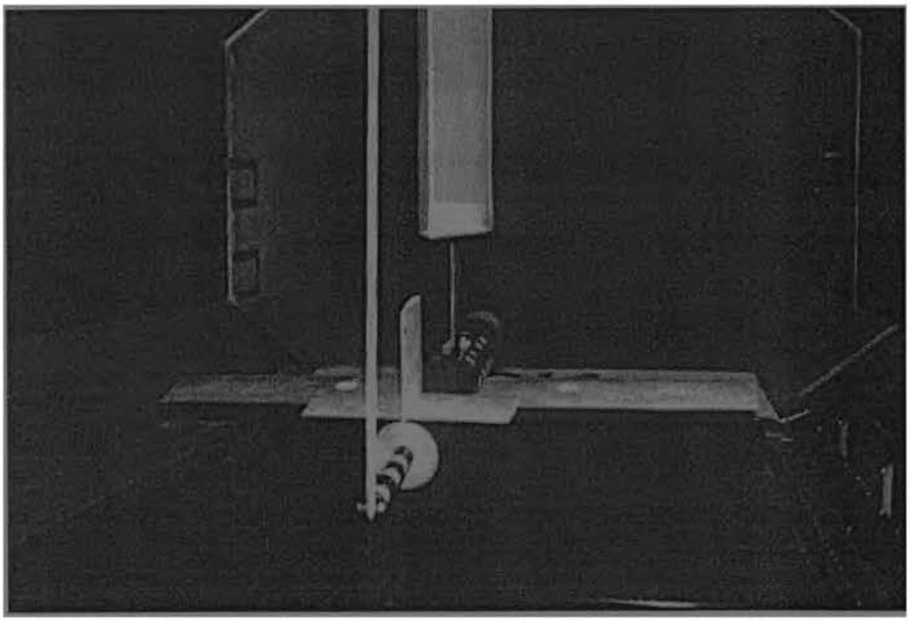

Figure A-34: Rear view of model in ground effect test section

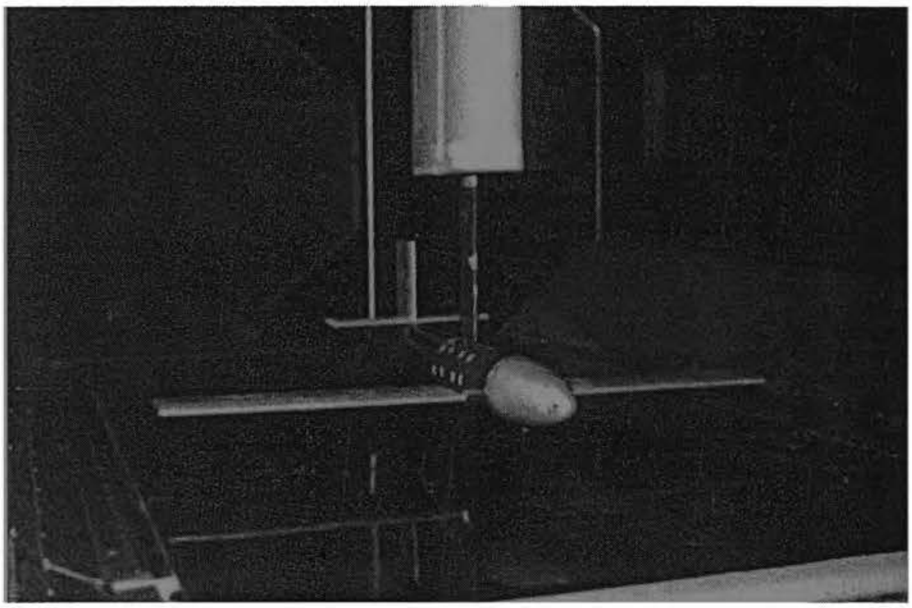

Figure A-35: Front view of model in ground effect test section

APPENDIX B: DATA REDUCTION THEORY

APPENDIX B-1: HEYSON'S THEORY, BOUNDARY CORRECTIONS FOR A VANISHINGLY SMALL MODEL

For this derivation, it is simpler to model the inclined doublets mentioned in Chapter 3 as a linear combination of vertical and longitudinal doublets.

If the line of vertical doublets have a strength of:

$$\frac{dm^*}{dl} = w_0 \frac{A_m}{2\pi} \tag{B-1}$$

Where:

m - Doublet strength

w_0 - Mean value of induced velocity (from momentum theory)

A_m - Momentum area of lifting system. In the case of a rotor, this is the rotor-disc area. For a wing this is the area of a circle circumscribing the wingtips.

Then the vertical induced velocity at a location (x, y, z) can be written as:

$$w_\infty = -\frac{dm^*}{dl}\left\{\frac{x^2+y^2}{\left(\sqrt{x^2+y^2+z^2}+z\cos\chi - x\sin\chi\right)\left(x^2+y^2+z^2\right)^{3/2}} - \left[\frac{z+\cos\chi\sqrt{x^2+y^2+z^2}}{\left(\sqrt{x^2+y^2+z^2}+z\cos\chi - x\sin\chi\right)\left(x^2+y^2+z^2\right)^{3/2}}\right]^2\right\} \tag{B-2}$$

This equation can be non-dimensionalised using the following values:

h - Height of model above tunnel floor

H - Tunnel semi-height

B - Tunnel semi-width

ζ - Ratio of tunnel semi-height to model height (H/h)

γ - Ratio of tunnel width to height

A_T - Windtunnel cross-sectional area

Also, for compactness, the following symbols will be used:

ζ_x - $\zeta \dfrac{x}{H}$

ζ_y - $\zeta \dfrac{y}{H}$

ζ_z - $\zeta \dfrac{z}{H}$

Equation (B-1) then becomes, together with (B-2):

$$w_\infty = w_0 \frac{A_m}{A_T}\left[-\zeta^2 \frac{2\gamma}{\pi} K(\zeta_x, \zeta_y, \zeta_z)\right] \tag{B-3}$$

With:

$$K(\zeta_x, \zeta_y, \zeta_z) = \frac{-\zeta_x^2 + \zeta_y^2}{\left[\sqrt{\zeta_x^2+\zeta_y^2+\zeta_z^2} + \zeta_z \cos\chi - \zeta_x \sin\chi\right]\left[\zeta_x^2+\zeta_y^2+\zeta_z^2\right]^{3/2}} - \left\{\frac{\left[\zeta_z + \cos\chi\sqrt{\zeta_x^2+\zeta_y^2+\zeta_z^2}\right]}{\left[\sqrt{\zeta_x^2+\zeta_y^2+\zeta_z^2} + \zeta_z \cos\chi - \zeta_x \sin\chi\right]\sqrt{\zeta_x^2+\zeta_y^2+\zeta_z^2}}\right\}^2 \tag{B-4}$$

For this same set of vertical doublets, the induced velocity in the longitudinal direction can be shown to be:

$$u_\infty = w_0 \frac{A_m}{A_T}\left[-\zeta^2 \frac{2\gamma}{\pi} K(\zeta_x, \zeta_y, \zeta_z)\right] \tag{B-5}$$

With:

$$K(\zeta_x,\zeta_y,\zeta_z)=\frac{-\zeta_x\zeta_z}{\left[\sqrt{\zeta_x^2+\zeta_y^2+\zeta_z^2}+\zeta_z\cos\chi-\zeta_x\sin\chi\right]\left[\zeta_x^2+\zeta_y^2+\zeta_z^2\right]^{3/2}}-\frac{\left[\zeta_z+\cos\chi\sqrt{\zeta_x^2+\zeta_y^2+\zeta_z^2}\right]\left[\zeta_x-\sin\chi\sqrt{\zeta_x^2+\zeta_y^2+\zeta_z^2}\right]}{\left[\sqrt{\zeta_x^2+\zeta_y^2+\zeta_z^2}+\zeta_z\cos\chi-\zeta_x\sin\chi\right]^2\left[\zeta_x^2+\zeta_y^2+\zeta_z^2\right]} \tag{B-6}$$

These equations give the induced velocities due to the wake of vertical doublets. The longitudinal doublets are handled much in the same way. However, the strength of this row of doublets is written as:

$$\frac{dm^*}{dl}=u_0\frac{A_m}{2\pi} \tag{B-7}$$

Where u_0 is the mean longitudinal induced velocity.

Again, after calculating the induced velocity components and non-dimensionalising, the vertical induced velocity can be written as:

$$w_\infty=u_0\frac{A_m}{A_T}\left[-\zeta^2\frac{2\gamma}{\pi}K(\zeta_x,\zeta_y,\zeta_z)\right] \tag{B-8}$$

With:

$$K(\zeta_x,\zeta_y,\zeta_z)=\frac{-\zeta_x\zeta_z}{\left[\sqrt{\zeta_x^2+\zeta_y^2+\zeta_z^2}+\zeta_z\cos\chi-\zeta_x\sin\chi\right]\left[\zeta_x^2+\zeta_y^2+\zeta_z^2\right]^{3/2}}-\frac{\left[\zeta_z+\cos\chi\sqrt{\zeta_x^2+\zeta_y^2+\zeta_z^2}\right]\left[\zeta_x-\sin\chi\sqrt{\zeta_x^2+\zeta_y^2+\zeta_z^2}\right]}{\left[\sqrt{\zeta_x^2+\zeta_y^2+\zeta_z^2}+\zeta_z\cos\chi-\zeta_x\sin\chi\right]^2\left[\zeta_x^2+\zeta_y^2+\zeta_z^2\right]} \tag{B-9}$$

And the longitudinal induced velocity due to the longitudinal doublets can be shown to be:

$$u_\infty=u_0\frac{A_m}{A_T}\left[-\zeta^2\frac{2\gamma}{\pi}K(\zeta_x,\zeta_y,\zeta_z)\right] \tag{B-10}$$

With:

$$K(\zeta_x,\zeta_y,\zeta_z)=\frac{-\zeta_y^2+\zeta_z^2}{\left[\sqrt{\zeta_x^2+\zeta_y^2+\zeta_z^2}+\zeta_z\cos\chi-\zeta_x\sin\chi\right]\left[\zeta_x^2+\zeta_y^2+\zeta_z^2\right]^{3/2}}-\left\{\frac{\left[\zeta_x-\cos\chi\sqrt{\zeta_x^2+\zeta_y^2+\zeta_z^2}\right]}{\left[\sqrt{\zeta_x^2+\zeta_y^2+\zeta_z^2}+\zeta_z\cos\chi-\zeta_x\sin\chi\right]\sqrt{\zeta_x^2+\zeta_y^2+\zeta_z^2}}\right\}^2 \qquad \textbf{(B-11)}$$

For the wake to be modelled properly, it is paired with its first image beneath the floor. The reason for this can be seen in Figures B-1 and B-2. As can be seen, the wake is modelled as a straight line of doublets until it intersects the floor, after which it trails downstream along the floor of the tunnel. In the case of wings without high-lift devices, the wake deflection is quite small and the intersection with the floor occur so far downstream that the effect is negligible since it is already far behind the actual test section.

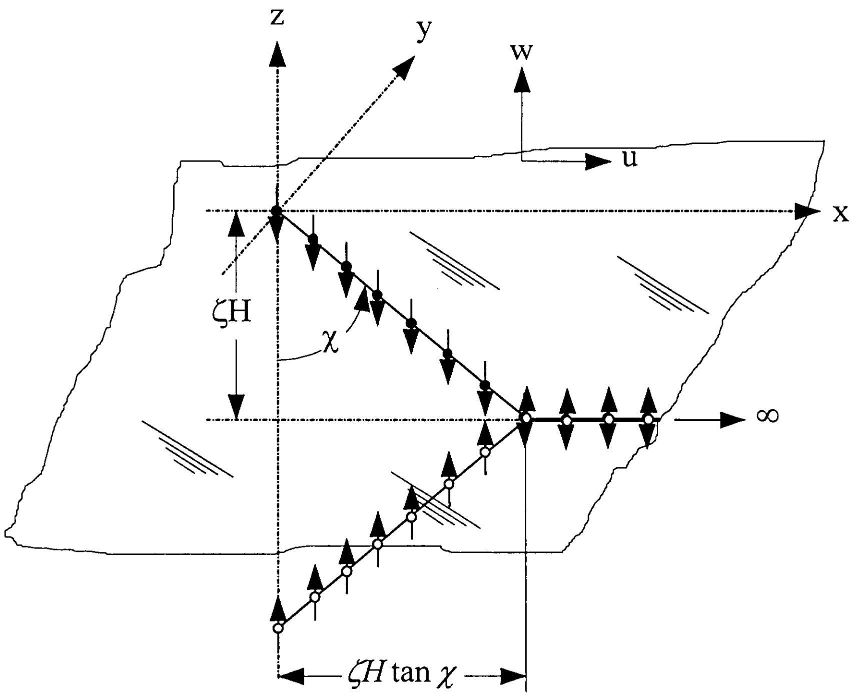

Figure B-1: Wake and image of vertical doublets [16]

For the wake of vertical doublets, the equations derived earlier are added using the images shown in Figure B-1. Since the system of vertical doublets (or more accurately the vertical component of the doublets) is caused by the lift, we will denote the upwash due to vertical doublets as w_L, where L refers to the lift. The longitudinal induced velocity will be called u_L.

From equation (B-3):

$$w_L = w_0 \frac{A_m}{A_T}\left\{-\zeta^2 \frac{2\gamma}{\pi}\left[K(\zeta_x,\zeta_y,\zeta_z) - K(\zeta_x - \tan\chi,\zeta_y,\zeta_z+1) \right.\right.$$
$$\left.\left. -K(\zeta_x,\zeta_y,-\zeta_z-2) + K(\zeta_x - \tan\chi,\zeta_y,-\zeta_z-1)\right]\right\} \qquad \textbf{(B-12)}$$

With K from equation (B-4).

And for the longitudinal induced velocity, from equation (B-5):

$$u_L = w_0 \frac{A_m}{A_T}\left\{-\zeta^2 \frac{2\gamma}{\pi}\left[K(\zeta_x,\zeta_y,\zeta_z) - K(\zeta_x - \tan\chi,\zeta_y,\zeta_z+1) \right.\right.$$
$$\left.\left. +K(\zeta_x,\zeta_y,-\zeta_z-2) - K(\zeta_x - \tan\chi,\zeta_y,-\zeta_z-1)\right]\right\} \qquad \textbf{(B-13)}$$

With K from equation (B-6).

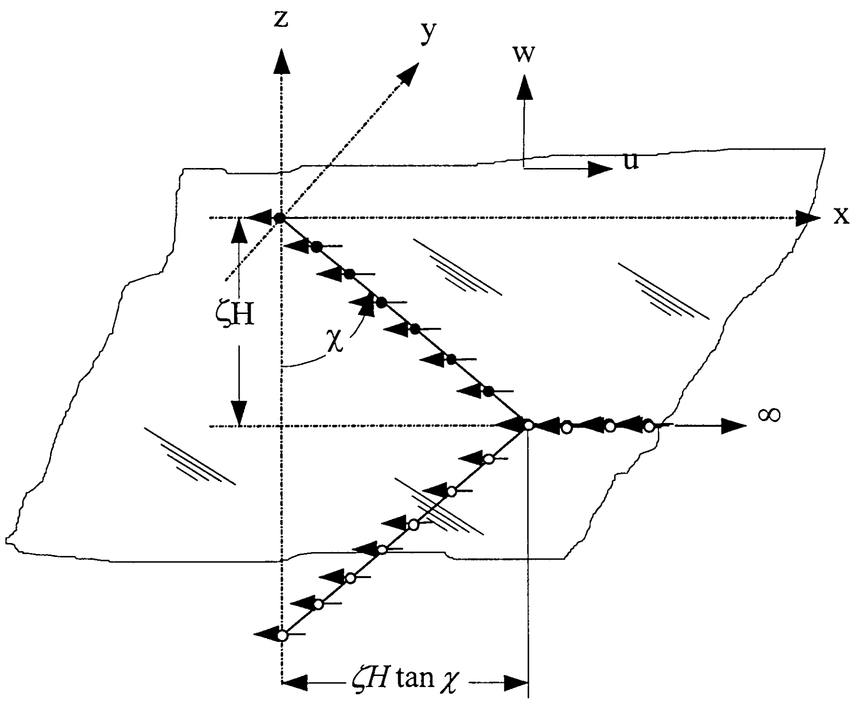

Figure B-2: Wake and image of longitudinal doublets [16]

The image system for the horizontal doublets is shown in Figure B-2. This component is due to the drag generated by the model and the induced velocities will be written as w_D and u_D. From equation (B-8):

$$\begin{aligned} w_D = u_0 \frac{A_m}{A_T} \Bigg\{ -\zeta^2 \frac{2\gamma}{\pi} \Big[& K(\zeta_x, \zeta_y, \zeta_z) - K(\zeta_x - \tan\chi, \zeta_y, \zeta_z + 1) \\ & - K(\zeta_x, \zeta_y, -\zeta_z - 2) + K(\zeta_x - \tan\chi, \zeta_y, -\zeta_z - 1) \\ & + 2K\big|_{\chi = 90^\circ}(\zeta_x - \tan\chi, \zeta_y, \zeta_z + 1) \Big] \Bigg\} \end{aligned} \qquad \textbf{(B-14)}$$

With K from equation (B-9).

And, finally, the longitudinal induced velocity from equation (B-10).

$$\begin{aligned} u_D = u_0 \frac{A_m}{A_T} \Bigg\{ -\zeta^2 \frac{2\gamma}{\pi} \Big[& K(\zeta_x, \zeta_y, \zeta_z) - K(\zeta_x - \tan\chi, \zeta_y, \zeta_z + 1) \\ & + K(\zeta_x, \zeta_y, -\zeta_z - 2) - K(\zeta_x - \tan\chi, \zeta_y, -\zeta_z - 1) \\ & + 2K\big|_{\chi = 90^\circ}(\zeta_x - \tan\chi, \zeta_y, \zeta_z + 1) \Big] \Bigg\} \end{aligned} \qquad \textbf{(B-15)}$$

With K from equation (B-11).

Similar equations can be derived for an open lower boundary, as were done in reference [16], but these are not applicable to the current work. The next step is to derive the equations for a closed wind tunnel.

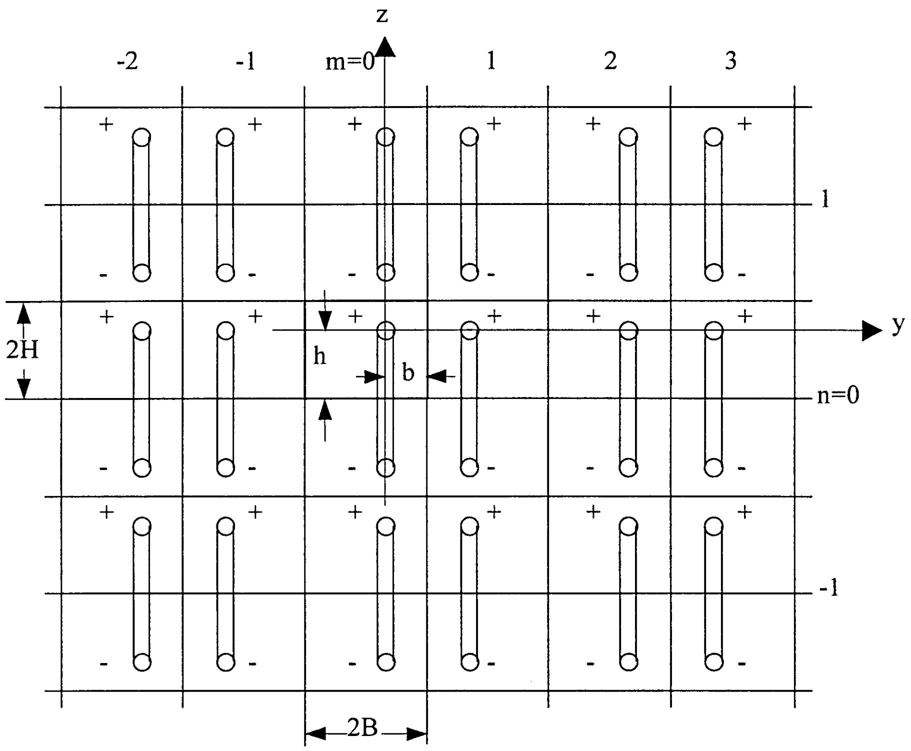

Figure B-3: Closed wind tunnel image system

Figure B-3 shows the image system used for a closed tunnel. The induced velocities as calculated through equations (B-12) to (B-15) are added for the images as shown in the figure. Note that the figure only shows the images for the first three systems, but that these images actually reach into infinity. As with any numerical approximation, as many images as practically possible should be added. The sensitivity analysis will give better insight as to the choice of the size of the image system used. The final set of induced velocities is:

$$\Delta w_L = \delta_{w,L} \frac{A_m}{A_T} w_0 \qquad \textbf{(B-16)}$$

$$\Delta u_L = \delta_{u,L} \frac{A_m}{A_T} w_0 \qquad \textbf{(B-17)}$$

$$\Delta w_D = \delta_{w,D} \frac{A_m}{A_T} u_0 \qquad \textbf{(B-18)}$$

$$\Delta u_D = \delta_{u,D} \frac{A_m}{A_T} u_0 \qquad \textbf{(B-19)}$$

And the δ value, for the case of correcting the closed tunnel to free air, becomes:

$$
\begin{aligned}
\delta = -\frac{2\gamma}{\pi}\zeta^{2}\Biggl\{ & \underset{n=m\neq 0}{\sum_{n=-\infty}^{\infty}\sum_{m=-\infty}^{\infty}} \biggl\{ K\biggl[\zeta\frac{x}{H},\zeta\Bigl(\frac{y}{H}-2m\gamma+\gamma(1-\eta)\bigl[1-(-1)^{m}\bigr]\Bigr),\zeta\Bigl(\frac{z}{H}-4n\Bigr)\biggr] \\
& -K\biggl[\Bigl(\zeta\frac{x}{H}-\tan\chi\Bigr),\zeta\Bigl(\frac{y}{H}-2m\gamma+\gamma(1-\eta)\bigl[1-(-1)^{m}\bigr]\Bigr),\zeta\Bigl(\frac{z}{H}-4n\Bigr)+1\biggr] \\
& -(-1)^{q}K\biggl[\zeta\frac{x}{H},\zeta\Bigl(\frac{y}{H}-2m\gamma+\gamma(1-\eta)\bigl[1-(-1)^{m}\bigr]\Bigr),-\zeta\Bigl(\frac{z}{H}-4n\Bigr)-2\biggr] \\
& +(-1)^{q}K\biggl[\Bigl(\zeta\frac{x}{H}-\tan\chi\Bigr),\zeta\Bigl(\frac{y}{H}-2m\gamma+\gamma(1-\eta)\bigl[1-(-1)^{m}\bigr]\Bigr),-\zeta\Bigl(\frac{z}{H}-4n\Bigr)-1\biggr] \\
& +2sK\big|_{\chi=90^{\circ}}\biggl[\Bigl(\zeta\frac{x}{H}-\tan\chi\Bigr),\zeta\Bigl(\frac{y}{H}-2m\gamma+\gamma(1-\eta)\bigl[1-(-1)^{m}\bigr]\Bigr),\zeta\Bigl(\frac{z}{H}-4n\Bigr)+1\biggr]\biggr\} \\
& +\biggl\{-K\biggl[\Bigl(\zeta\frac{x}{H}-\tan\chi\Bigr),\zeta\frac{y}{H},\zeta\frac{z}{H}+1\biggr]-(-1)^{q}K\biggl[\zeta\frac{x}{H},\zeta\frac{y}{H},-\zeta\frac{z}{H}-2\biggr] \\
& +(-1)^{q}K\biggl[\Bigl(\zeta\frac{x}{H}-\tan\chi\Bigr),\zeta\frac{y}{H},-\zeta\frac{z}{H}-1\biggr]+2sK\big|_{\chi=90^{\circ}}\biggl[\Bigl(\zeta\frac{x}{H}-\tan\chi\Bigr),\zeta\frac{y}{H},\zeta\frac{z}{H}+1\biggr]\biggr\}\Biggr\}
\end{aligned}
$$

(B-20)

The following table shows how *K*, *q* and s are selected:

Correction factor	K from equations	q	s
$\delta_{w,L}$	(B-4)	0	0
$\delta_{u,L}$	(B-6)	1	0
$\delta_{w,D}$	(B-9)	0	1
$\delta_{u,D}$	(B-11)	1	1

Table B-1: Selection of variables for calculating various δ-values

It can be shown that the terms after the summation term in equation (B-20) describe the ground effect exactly. If these terms are deleted, the correction will be made to ground effect rather than to free air. This is exactly the case of interest in this thesis. Equation (B-21) thus describes the correction to ground effect (Table B-1 still holds for this equation):

$$
\begin{aligned}
\delta = -\frac{2\gamma}{\pi}\zeta^2 \Bigg\{ & \sum_{\substack{n=-\infty \\ n=m\neq 0}}^{\infty} \sum_{m=-\infty}^{\infty} \Bigg\{ K\left[\zeta\frac{x}{H},\zeta\left(\frac{y}{H}-2m\gamma+\gamma(1-\eta)\left[1-(-1)^m\right]\right),\zeta\left(\frac{z}{H}-4n\right)\right] \\
& -K\left[\left(\zeta\frac{x}{H}-\tan\chi\right),\zeta\left(\frac{y}{H}-2m\gamma+\gamma(1-\eta)\left[1-(-1)^m\right]\right),\zeta\left(\frac{z}{H}-4n\right)+1\right] \\
& -(-1)^q K\left[\zeta\frac{x}{H},\zeta\left(\frac{y}{H}-2m\gamma+\gamma(1-\eta)\left[1-(-1)^m\right]\right),-\zeta\left(\frac{z}{H}-4n\right)-2\right] \\
& +(-1)^q K\left[\left(\zeta\frac{x}{H}-\tan\chi\right),\zeta\left(\frac{y}{H}-2m\gamma+\gamma(1-\eta)\left[1-(-1)^m\right]\right),-\zeta\left(\frac{z}{H}-4n\right)-1\right] \\
& +2sK\Big|_{\chi=90^\circ}\left[\left(\zeta\frac{x}{H}-\tan\chi\right),\zeta\left(\frac{y}{H}-2m\gamma+\gamma(1-\eta)\left[1-(-1)^m\right]\right),\zeta\left(\frac{z}{H}-4n\right)+1\right]\Bigg\}
\end{aligned}
$$

(B-21)

The implementation of these equations is described in Chapter 3.

APPENDIX B-2: HEYSON'S THEORY, SENSITIVITY STUDY

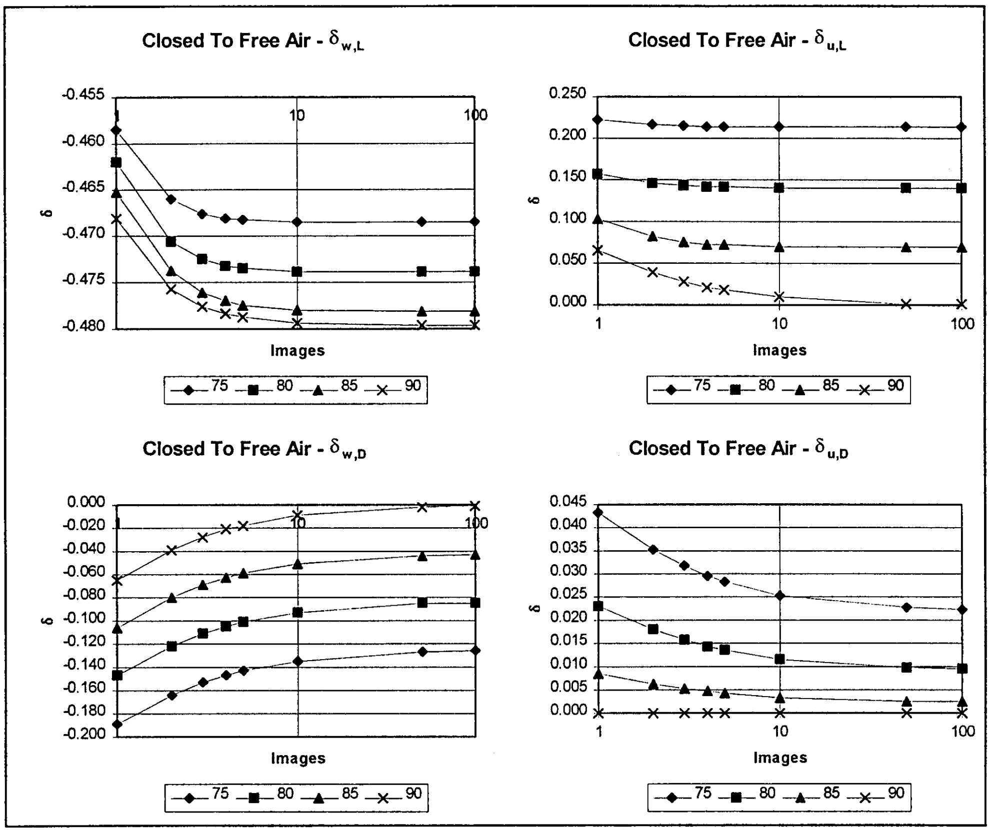

Figure B-4: Effect of number of image systems on correction factor. Vanishingly small model, $\zeta=1$, $\eta=1$, $\gamma=1.527$, $H=1.451$

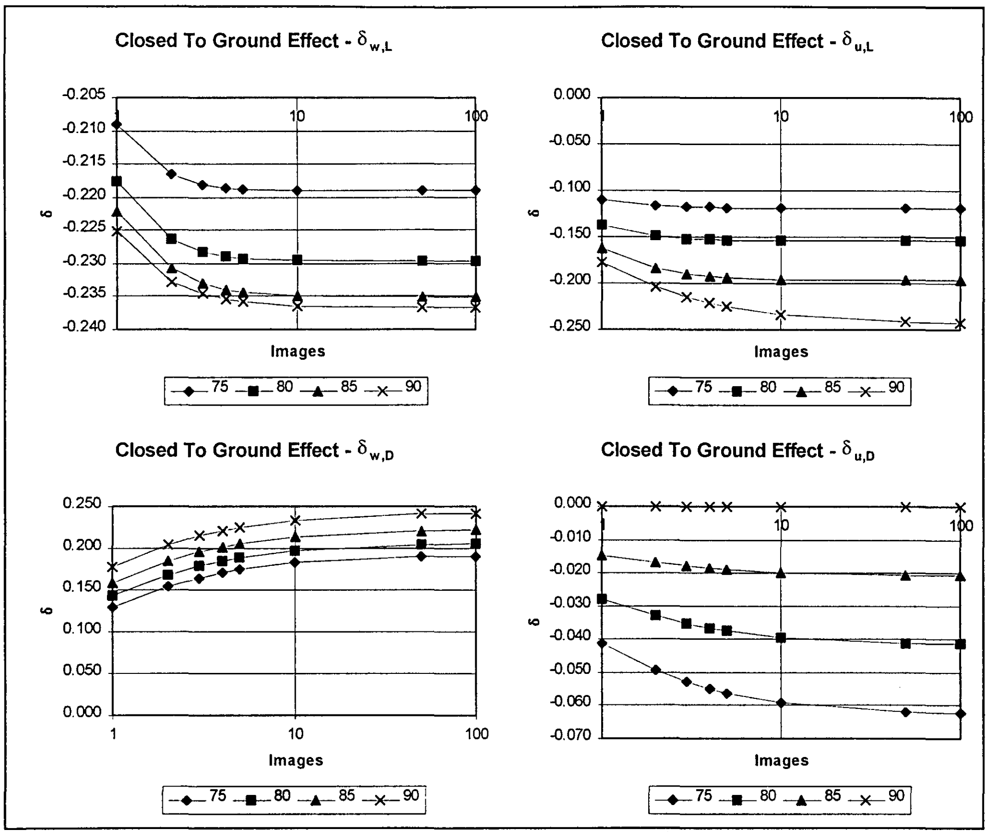

Figure B-5: Effect of number of image systems on correction factor. Vanishingly small model, $\zeta=1$, $\eta=1$, $\gamma=1.527$, $H=1.451$

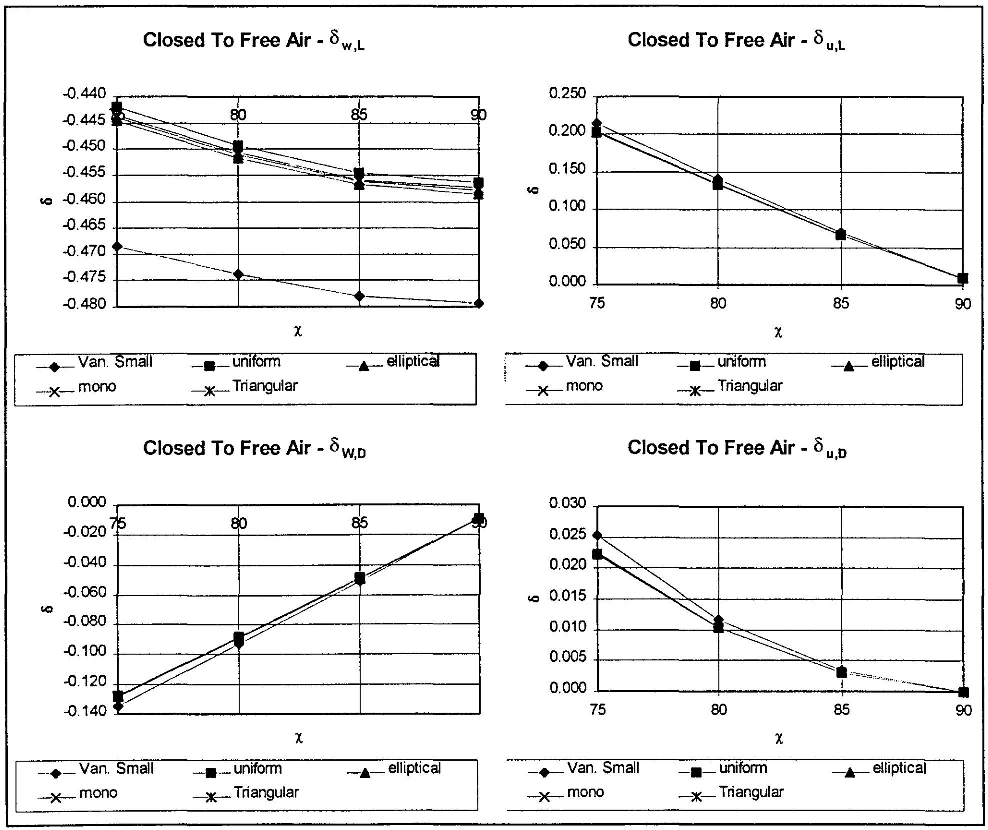

Figure B-6: Effect of lift distribution on correction factors. $\zeta=1$, $\eta=1$, $\gamma=1.527$, $H=1.451$

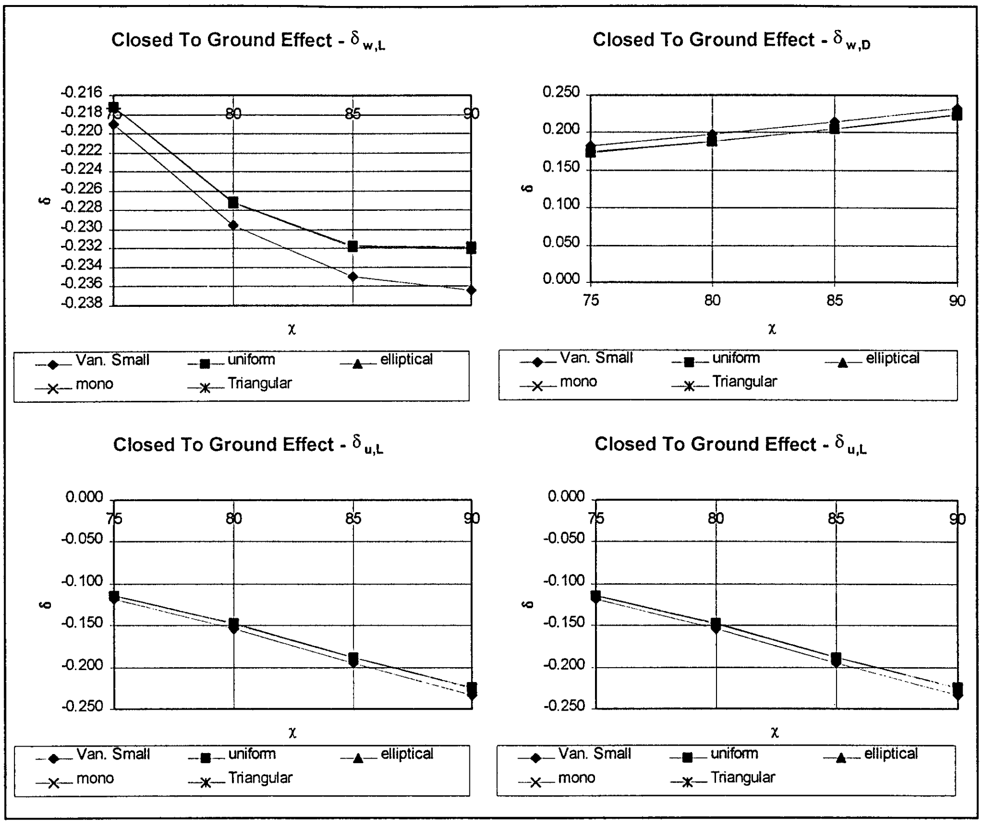

Closed To Ground Effect - $\delta_{w,L}$

Closed To Ground Effect - $\delta_{w,D}$

Closed To Ground Effect - $\delta_{u,L}$

Closed To Ground Effect - $\delta_{u,L}$

Figure B-7: Effect of lift distribution on correction factors. ζ=1, η=1, γ=1.527, H=1.451

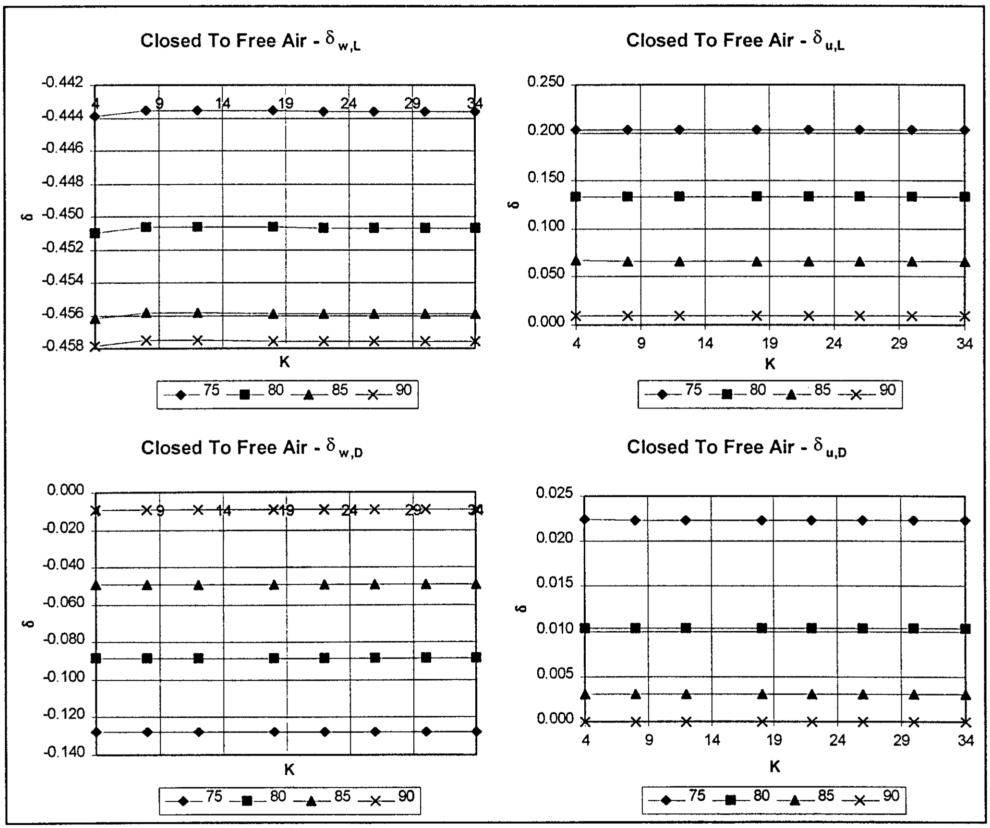

Closed To Free Air - $\delta_{w,L}$

Closed To Free Air - $\delta_{u,L}$

Closed To Free Air - $\delta_{w,D}$

Closed To Free Air - $\delta_{u,D}$

Figure B-8: Effect of number of control points along wing. ζ=1, η=1, γ=1.527, H=1.451, Images = 10

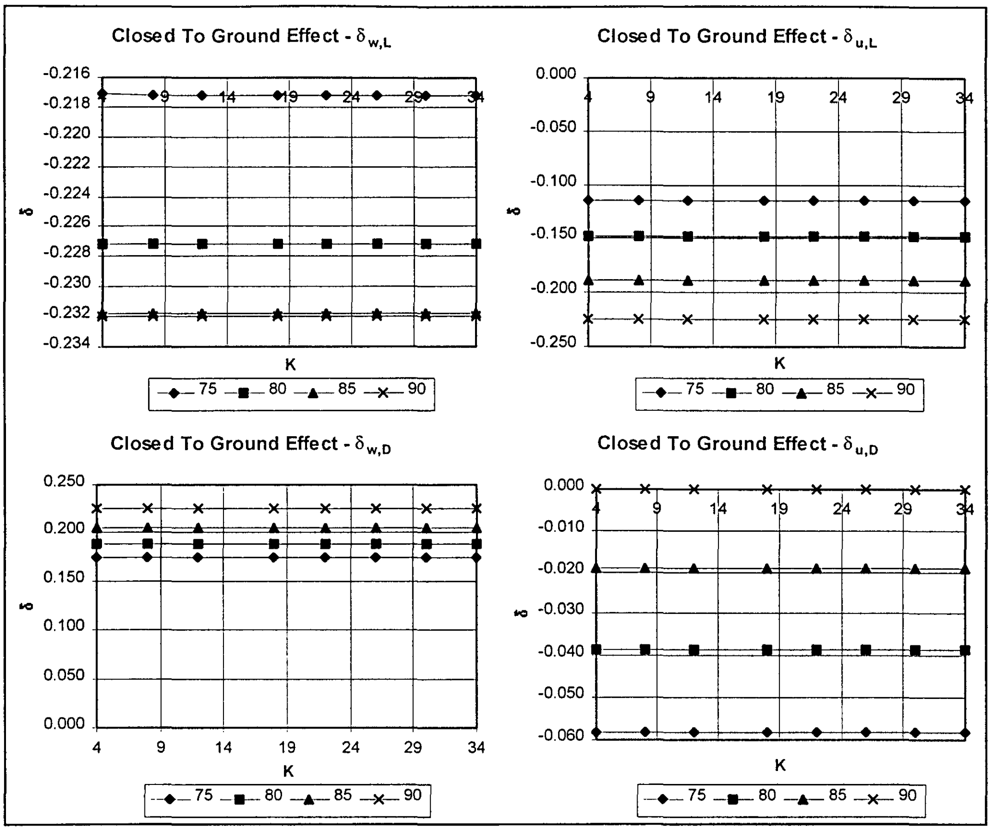

Figure B-9: Effect of number of control points along wing. ζ=1, η=1, γ=1.527, H=1.451, Images = 10

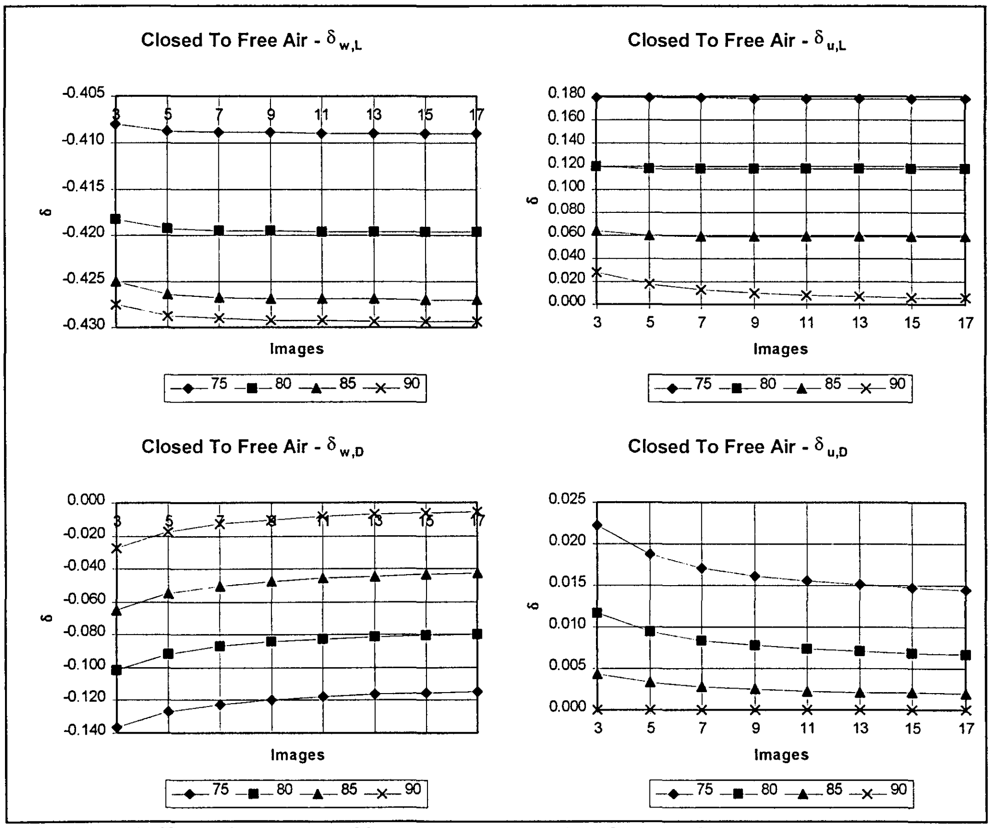

Figure B-10: Effect of number of images on correction factor after superposition. ζ=1, η=1, γ=1.527, H=1.451, K = 20

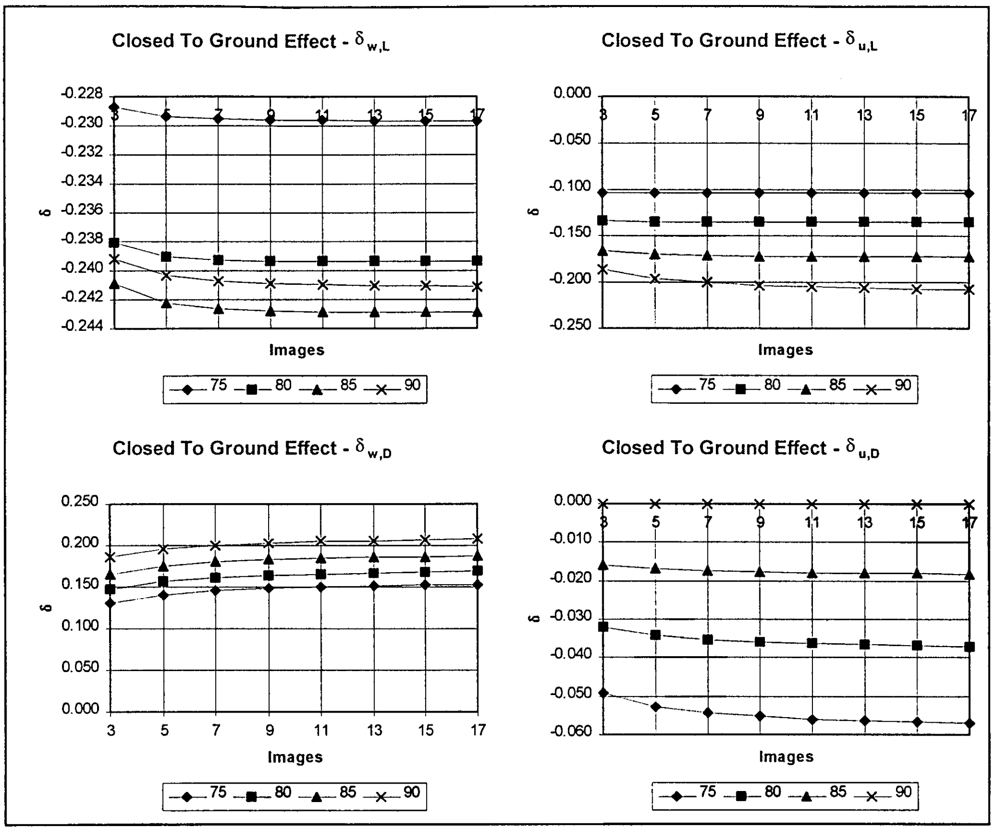

Figure B-11: Effect of number of images on correction factor after superposition. ζ=1, η=1, γ=1.527, H=1.451, K = 20

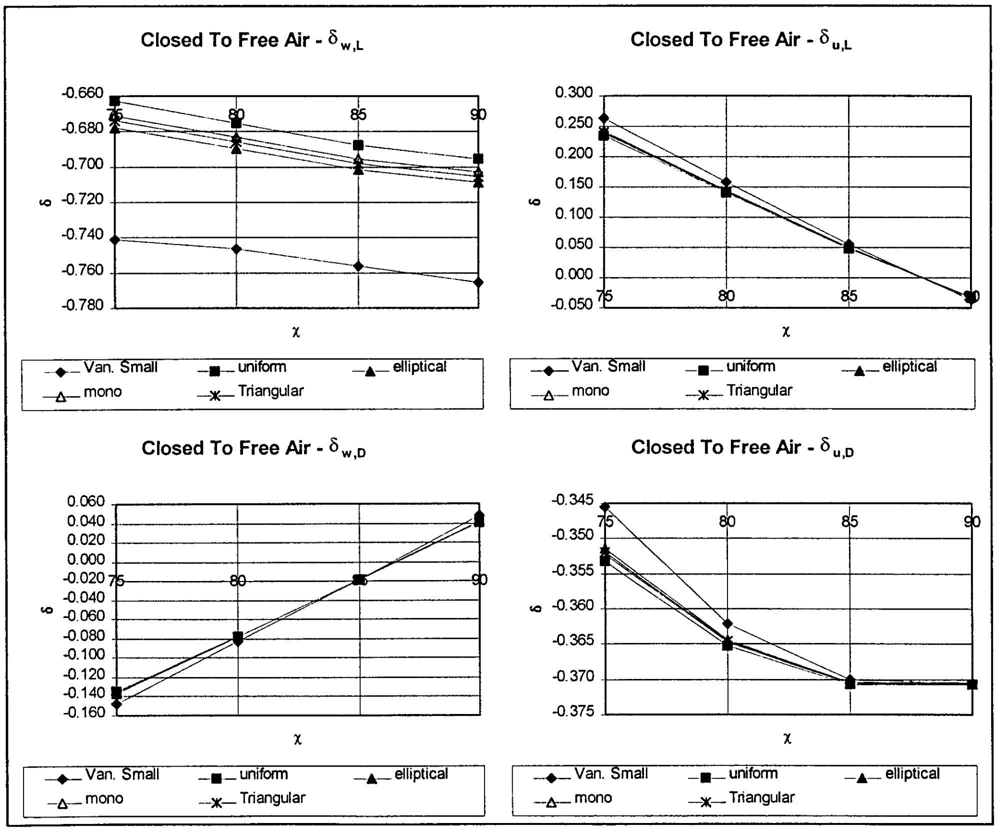

Figure B-12: Effect of lift distribution on wing on correction factor at tail. ζ=1, η=1, γ=1.527, H=1.451, Images = 10, K = 10, K_t = 4

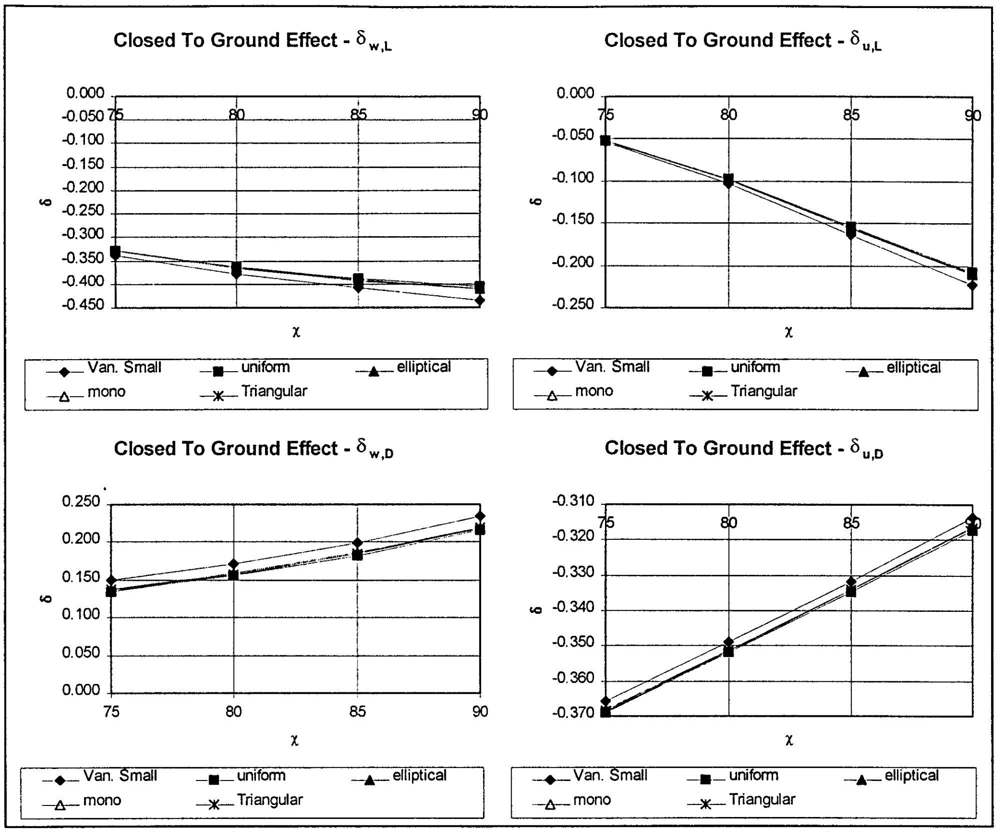

Figure B-13: Effect of lift distribution on wing on correction factor at tail. $\zeta=1$, $\eta=1$, $\gamma=1.527$, $H=1.451$, Images = 10, K = 10, $K_t = 4$

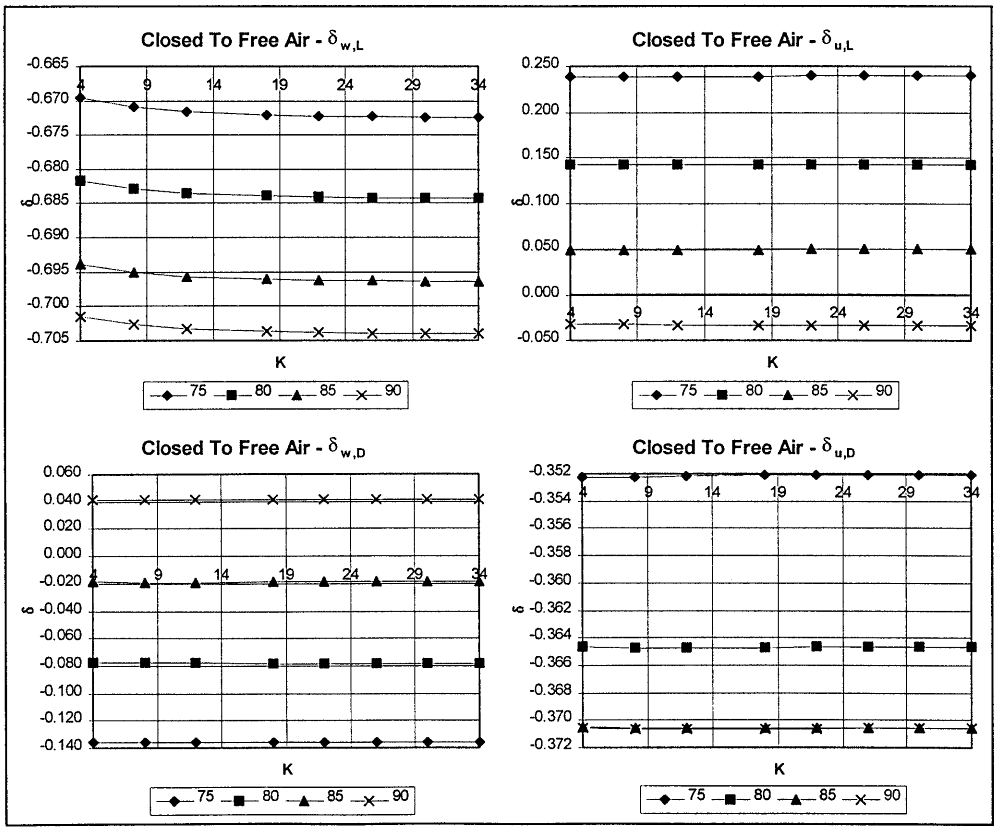

Figure B-14: Effect of number of control points on wing on correction factor at tail. $\zeta=1$, $\eta=1$, $\gamma=1.527$, $H=1.451$, Images = 10, $K_t = 4$

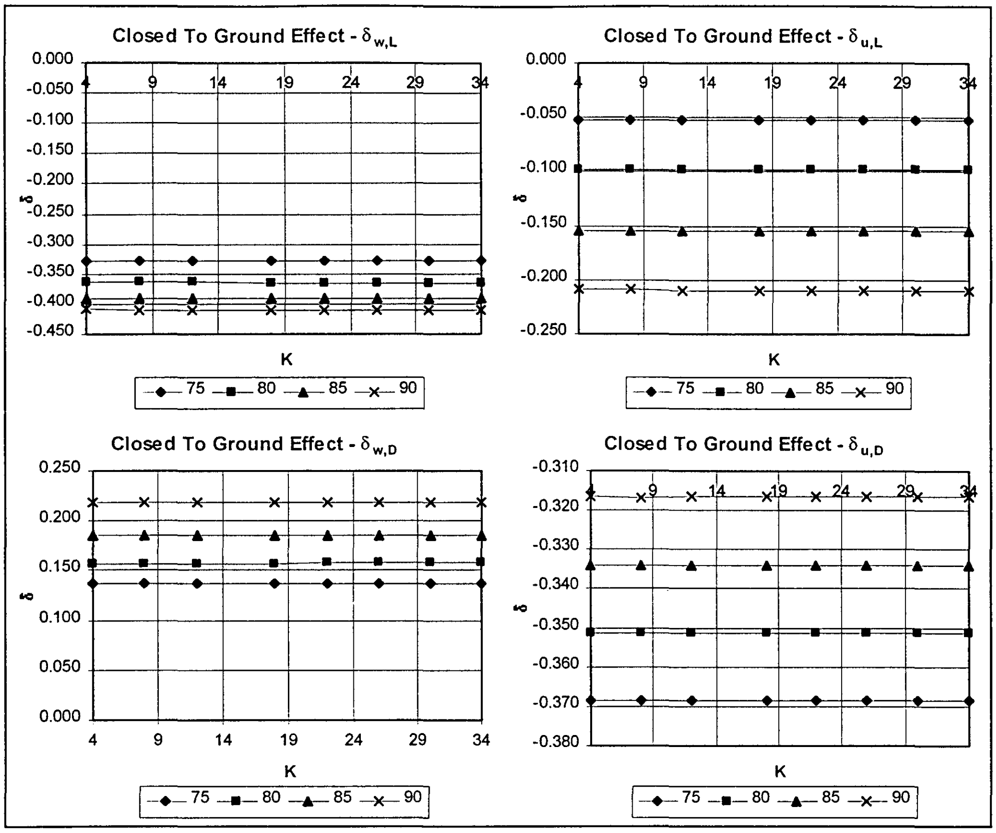

Figure B-15: Effect of number of control points on wing on correction factor at tail. $\zeta=1$, $\eta=1$, $\gamma=1.527$, H=1.451, Images = 10, $K_t = 4$

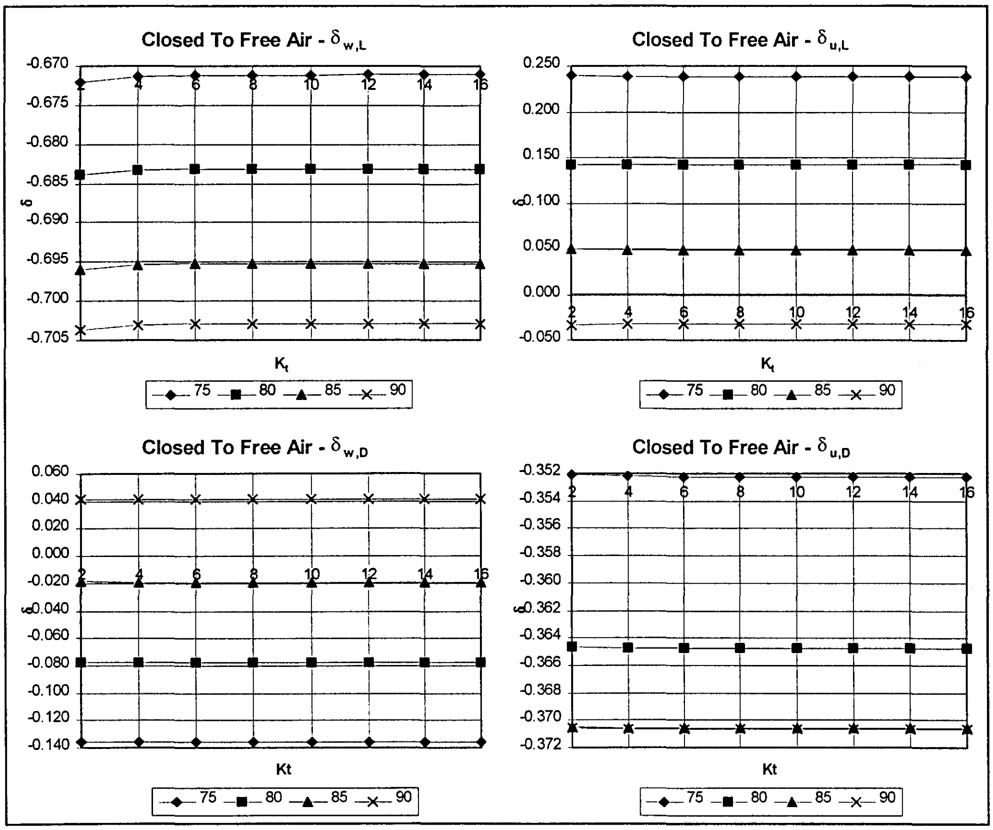

Figure B-16: Effect of number of control points on tail on correction factor at tail. $\zeta=1$, $\eta=1$, $\gamma=1.527$, H=1.451, Images = 10, K = 10

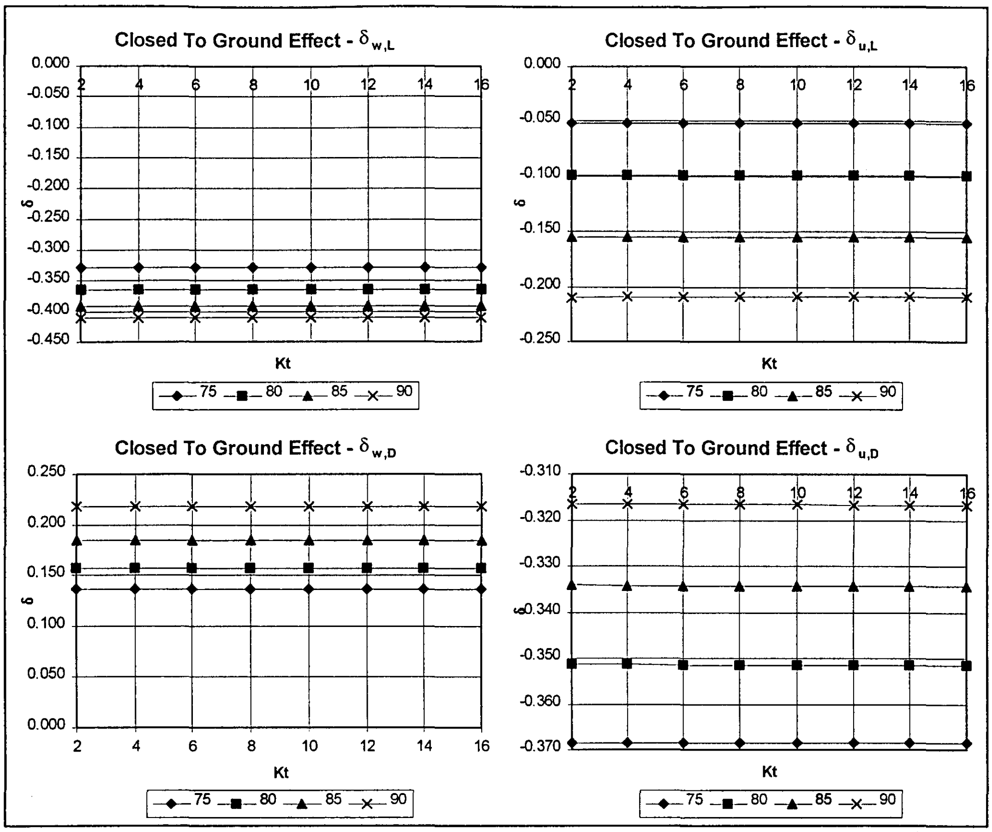

Figure B-17: Effect of number of control points on tail on correction factor at tail. $\zeta=1$, $\eta=1$, $\gamma=1.527$, $H=1.451$, Images = 10, $K = 10$

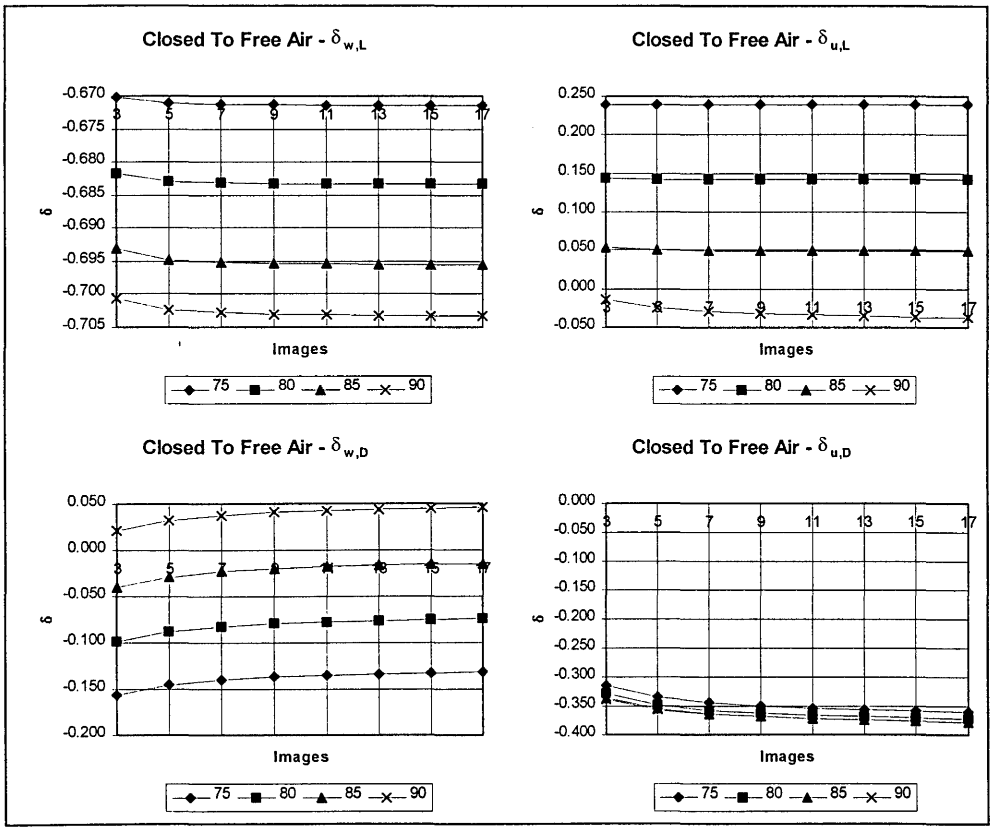

Figure B-18: Effect of number of image systems on interference at tail. $\zeta=1$, $\eta=1$, $\gamma=1.527$, $H=1.451$, $K = 10$, $K_t = 4$

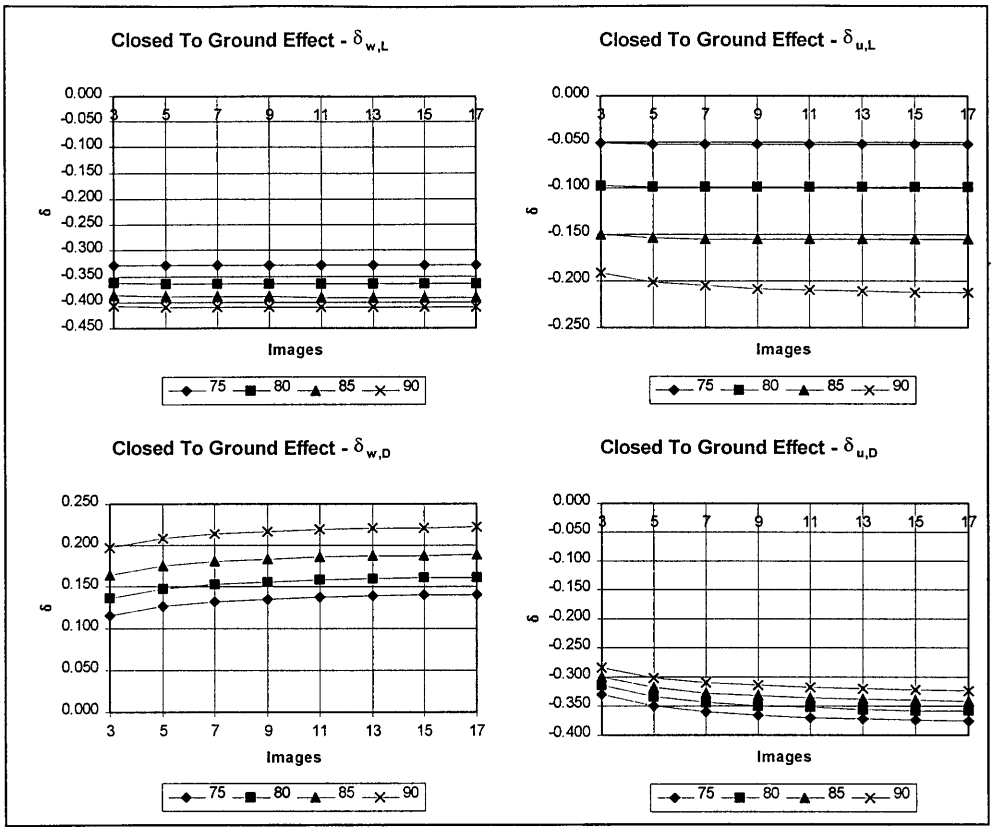

Figure B-19: Effect of number of image systems on interference at tail. $\zeta=1$, $\eta=1$, $\gamma=1.527$, $H=1.451$, $K = 10$, $K_t = 4$

APPENDIX B-3: FLOWCHART

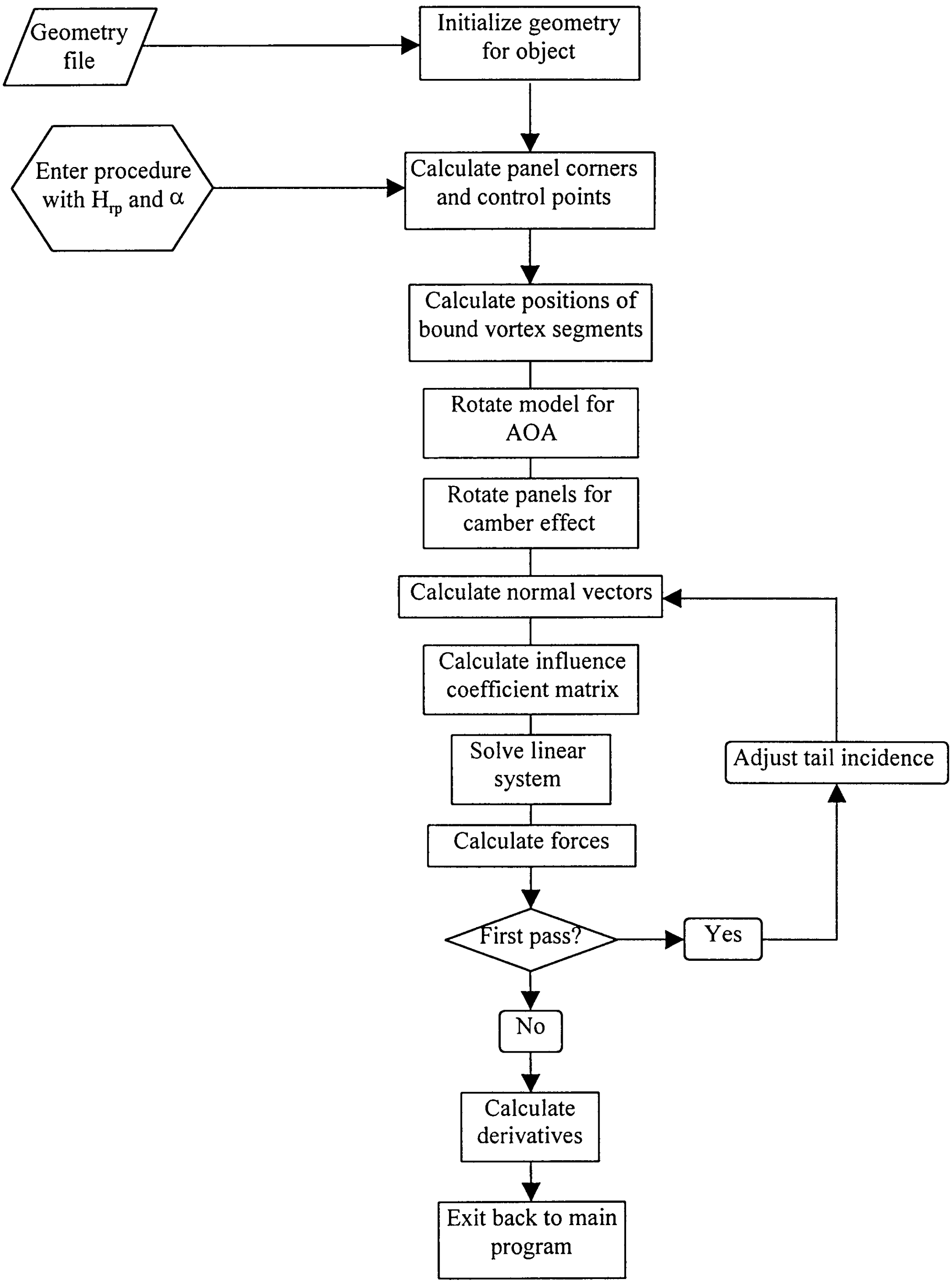

Figure B-20: Flowchart for calculation of tail effectiveness derivative

APPENDIX C: TELESCOPIC FAIRING AND PITCHING MECHANISM DESIGN

APPENDIX C-1: ADDITIONAL DETAIL ON POTENTIAL FLOW STUDY

The potential flow study was done using the SPARV panel method. This method is quite old and needs proper understanding of the code and input and output to use effectively. The input files were created using a CAD package to generate the co-ordinates. Basically, the complete model consists of the following components:

- Wing
- Tail
- Fuselage
- A 0.5 m long fairing
- A 1 m fairing
- A ground plane at 0.5 m below the model
- A ground plane at 0.1 m below the model

In order to position the components correctly, the model co-ordinates (wing, tail and fuselage) were rotated physically to the 2° and 10° incidence angles that were evaluated. All the other components were fixed in the Cartesian co-ordinate system. The free-stream direction was taken as parallel to the x-axis (0° AOA). This has the added advantage that the lift will be equivalent to the z-component of the force while the drag would be parallel to the x-axis. Normally the vector has to be rotated normal to the free-stream direction.

The panels used to generate the lifting components were vortex panels or “thin wing” panels. This reduced the number of panels needed for a lifting surface to one-half that needed for “thick-wing” doublet panels. All the other components were modelled using source panels.

The limitation of SPARV to keep the total number of panels below 1400, meant that the mesh were coarser than one would normally prefer to use. Figures C-1 and C-2 show the grid that was finally used. The number of panels per component were as shown in Table C-1:

Component	No. of Stations	No. of segments per station	Total number of panels	Type
Wing	25	15	375	Vortex
Tail	12	10	120	Vortex
Fuselage	20	10	200	Source
Ground plane	18	18	324	Source
Short strut + base	25	15	375	Source
Long strut + base	17	15	255	Source

Table C-1: Distribution of panels on model

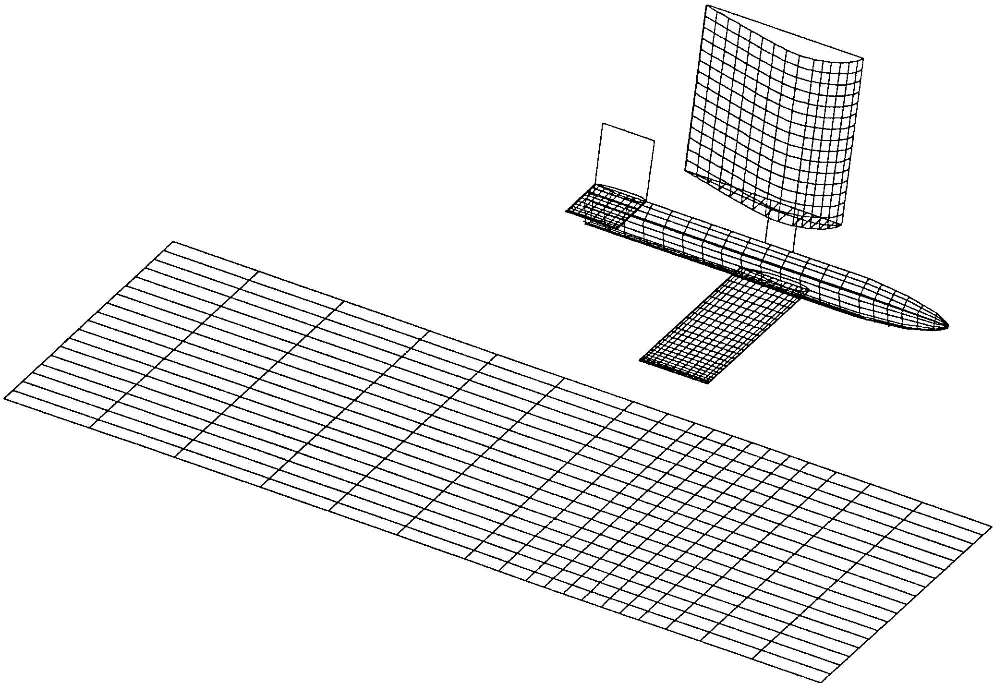

Figure C-1: Grid for complete panel method model

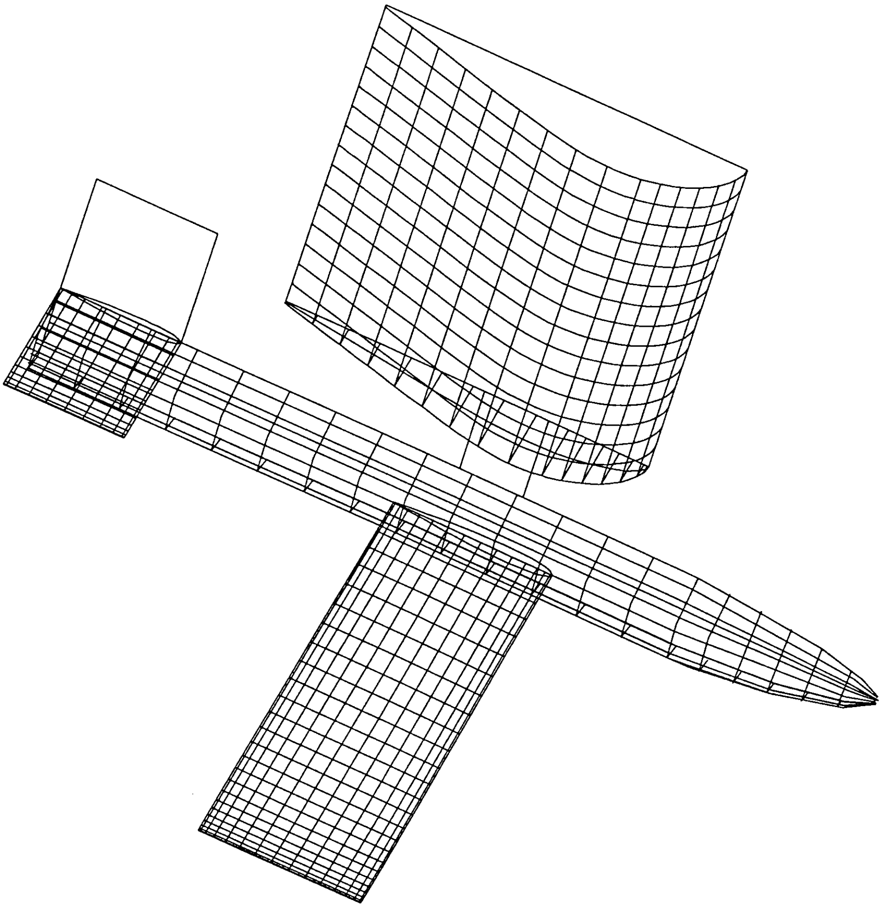

Figure C-2: Mesh for SPARV panel method with floor omitted

In order to correctly model the lift produced by the wing, those panels inside the fuselage had their wakes suppressed. Since the tail was positioned above the fuselage, none of its panels had their wakes suppressed. No wake-relaxation was performed for this analysis.

APPENDIX C-2: DESIGN AND MANUFACTURE OF FAIRING

Figures C-3 to C-5 show sections through the strut and fairing and the general arrangement of the fairing as mounted in the tunnel. The fairing was manufactured by first manufacturing a plug from hot-wired high-density polystyrene. This was then covered with a thin layer of fibreglass and finished using spray-filler. Waviness and taper were eliminated as far as possible to minimise the probability of sections wedging inside each other. A female mould was made of this plug.

The two halves of the inner fairing were produced using the female mould. One centre section was laid up on the plug and its outside surface finished. This part was then treated with a release wax and used, while still on the plug, as a male mould for one side's outer section. The centre and outer sections were removed and a second pair made over the male plug.

This method was extremely time-consuming but the results were excellent and the telescopic fairing was extremely rigid with the absolute minimum of play between sections.

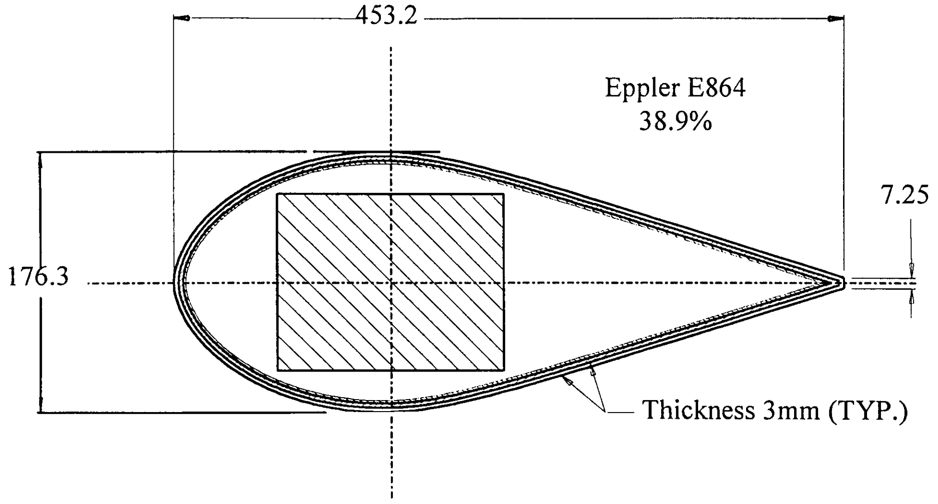

Figure C-3: Section through fairing and outer strut

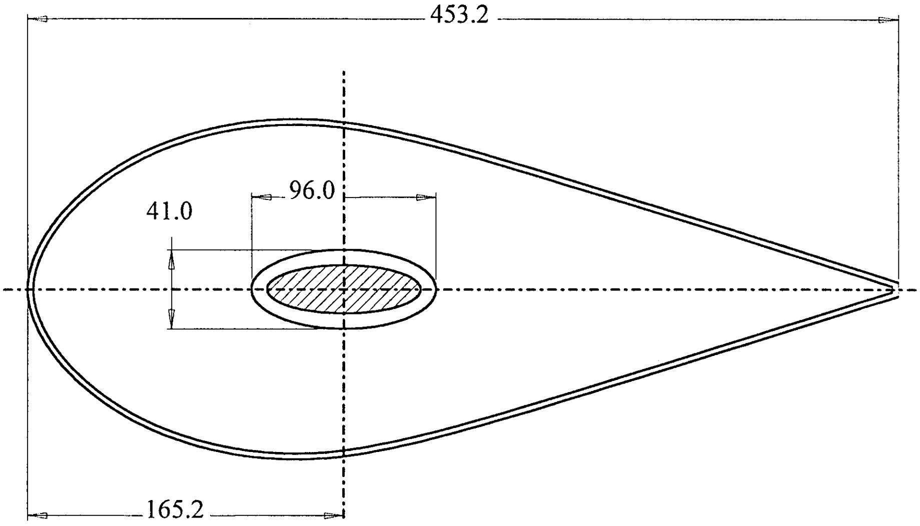

Figure C-4: Section through lower fairing and inner strut

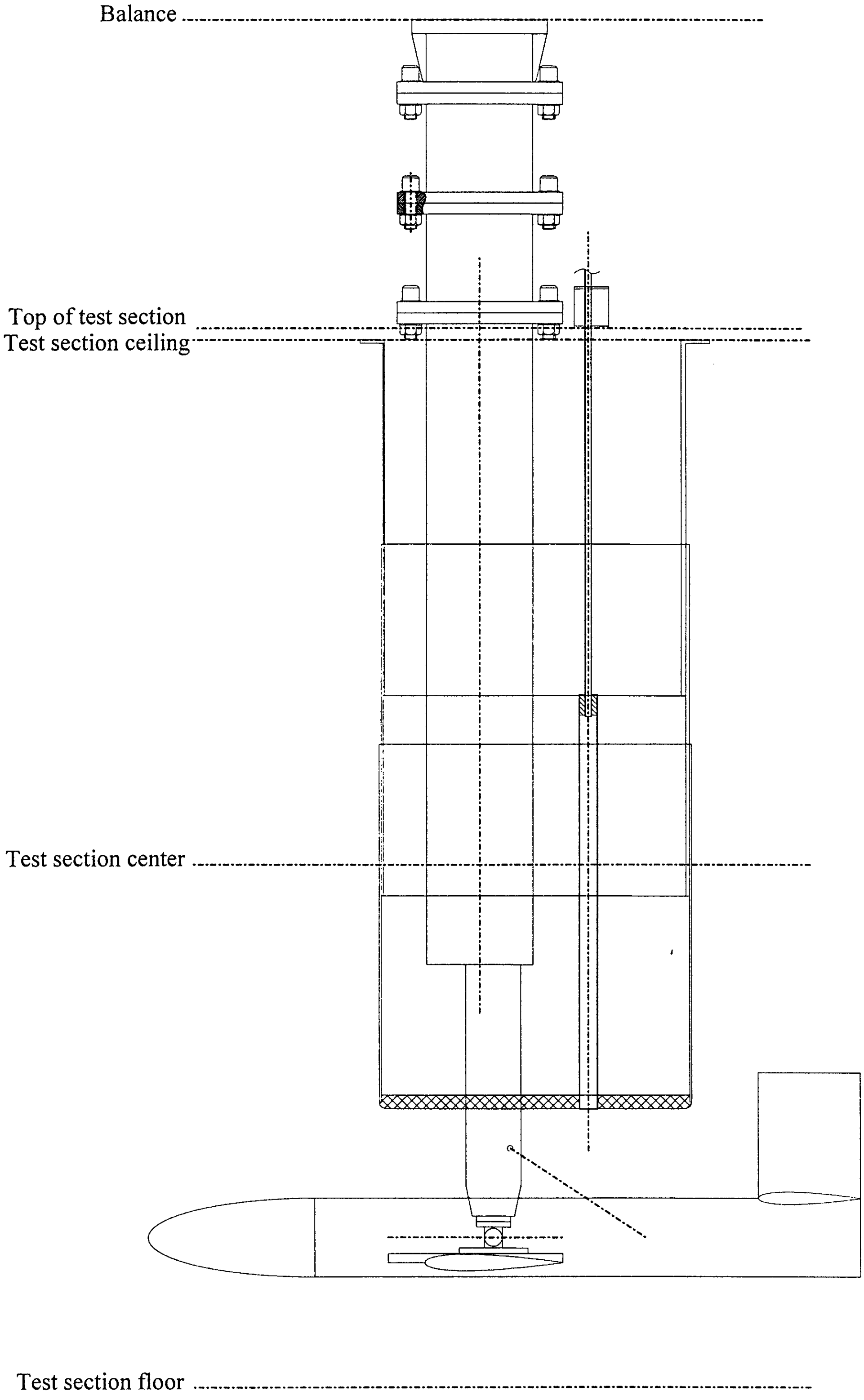

Figure C-5: Layout of Fairing/Strut/Model combination

APPENDIX C-3: DESIGN AND ANALYSIS OF PITCHING MECHANISM

In order to design the pitching mechanism, it was first necessary to calculate all the forces and moments on the mechanism. Unfortunately, it is impossible to determine what a "worst-case" scenario would be for all possible future configurations. Instead, the generic model, which is of a typical size for models tested in the low speed wind tunnel, was used as an example for the forces and moments needed. By making use of a conservative safety factor and designing the system to be self-locking, most possible cases would be covered. The mechanism was also designed for a test-section speed of 115 m/s, which is far above the normal testing speed. Using this value, however, allows the wind tunnel engineer to do tests such as Reynolds number scans without having to resort to alternative equipment.

The forces acting on the model had to be transferred to a pitching moment about the pivot point. This point was used as a reference point throughout. The measured lift, drag and pitching moments were used as input. A simple MATLAB program was written to transfer the loads as the model pitches form –20° to +20° AOA.

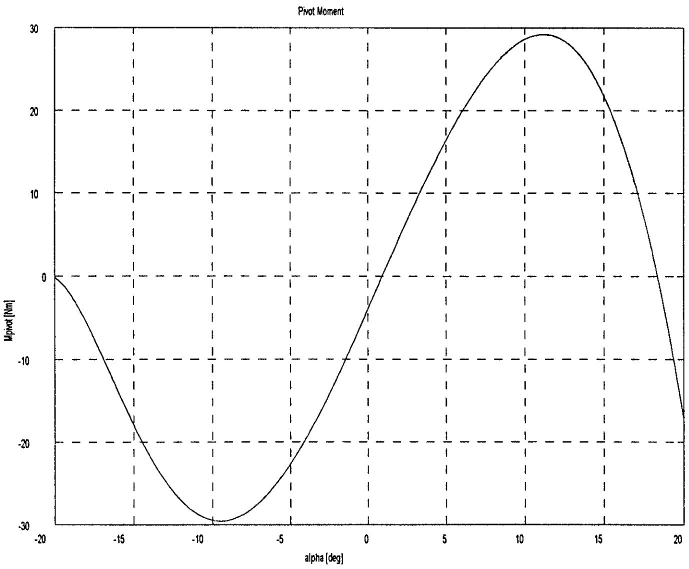

Figure C-6: Pivot moment versus model AOA

The geometry is shown in Figure C-7:

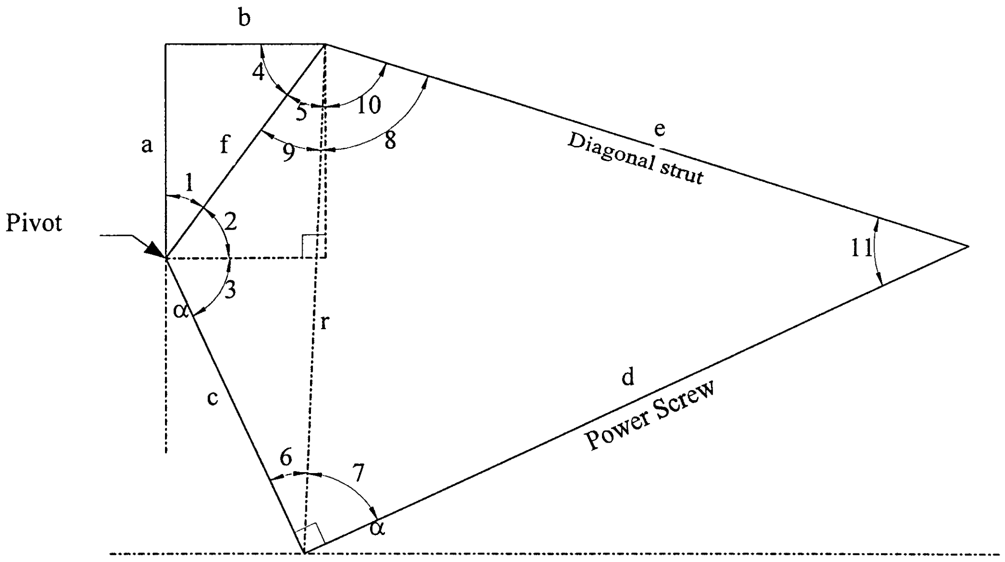

Figure C-7: Pitching mechanism geometry

The angles and sides are related by the following trigonometric equations:

$$f = \sqrt{a^2 + b^2}$$

$$\theta_1 = \sin^{-1}\frac{b}{f}$$

$$\theta_2 = \frac{\pi}{2} - \theta_1 \qquad \theta_3 = \frac{\pi}{2} - \alpha$$

$$\theta_4 = \theta_2 \qquad \theta_5 = \theta_1$$

$$r = \sqrt{c^2 + f^2 - 2cf\cos(\theta_2 + \theta_3)}$$

$$\theta_6 = \sin^{-1}\left(\frac{f\sin(\theta_2 + \theta_3)}{r}\right)$$

$$\theta_7 = \frac{\pi}{2} - \theta_6 \qquad \theta_{11} = \sin^{-1}\left(\frac{r\sin\theta_7}{e}\right)$$

$$\theta_8 = \pi - \theta_7 - \theta_{11}$$

$$d = \sqrt{r^2 + e^2 - 2re\cos\theta_8}$$

$$\theta_9 = \pi - \theta_6 - \theta_3 - \theta_2$$

$$\theta_{10} = \theta_8 + \theta_9 - \theta_5$$

These equations were programmed into a MATLAB routine to determine where the diagonal should be placed and to keep the forces in the diagonal as small as possible. With the geometry and moment known, it is possible to calculate the forces in the mechanism. The results are shown in Figure C-8.

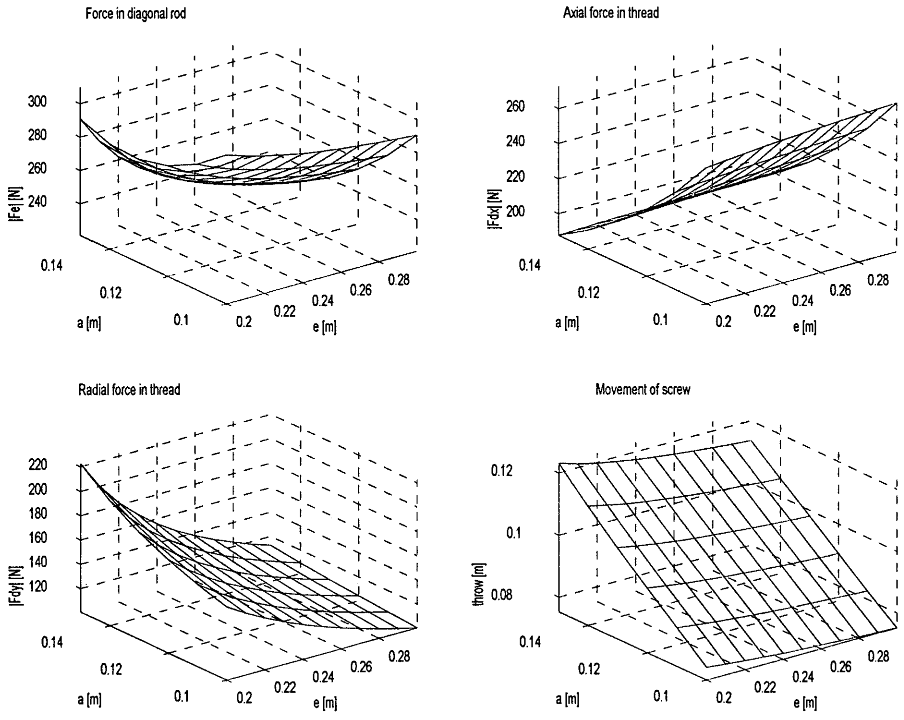

Figure C-8: Results of force/geometry analysis

From these surface plots, it was possible to choose an "optimal" geometry. Note that the geometry was also limited by the space available inside the wind tunnel model. After the final geometry was chosen, similar x-y plots were made to determine the maximum forces to be used in the design calculations. These plots are shown in Figure C-9.

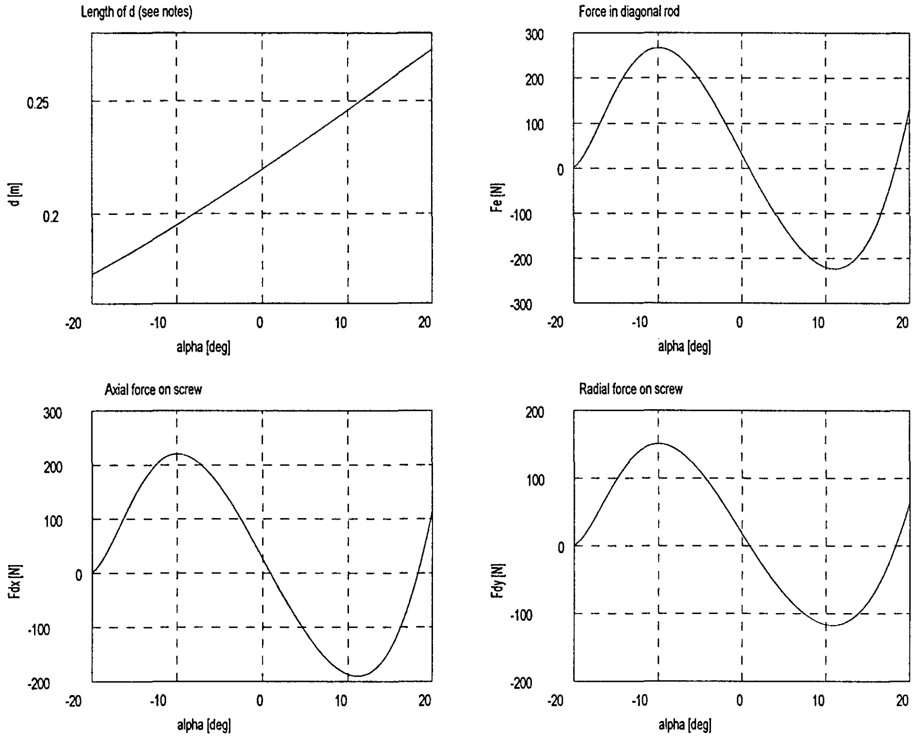

Figure C-9: Forces on pitching mechanism for final geometry

The torque needed to operate the power screw could now be determined using the equations in Chapter 8 of reference [26]:

$$T = \frac{Fd_m}{2}\left(\frac{l + \pi\mu d_m \sec\alpha}{\pi d_m - \mu l \sec\alpha}\right)$$

With:

F - Axial force

d_m - Diameter

μ - Friction coefficient

l - Pitch length

α - ½ Thread angle

After careful consideration, it was decided to use a coarse pitch M12 screw:

$p = 1.75$

$H = 0.5\sqrt{3}p = 1.52$

$d_m = 10.48$ mm

$l = 1.75$ mm

$\alpha = 30°$

$\mu = 0.08$

$T = 0.506$ Nm

This torque is not particularly high and it was found that the electric screwdriver could easily produce this torque. Note that this is a "worst-case" scenario and therefore the screwdriver was expected to be able to easily handle the normal 35m/s testing-speed.

APPENDIX C-4: FAIRING AIRFOIL ANALYSIS

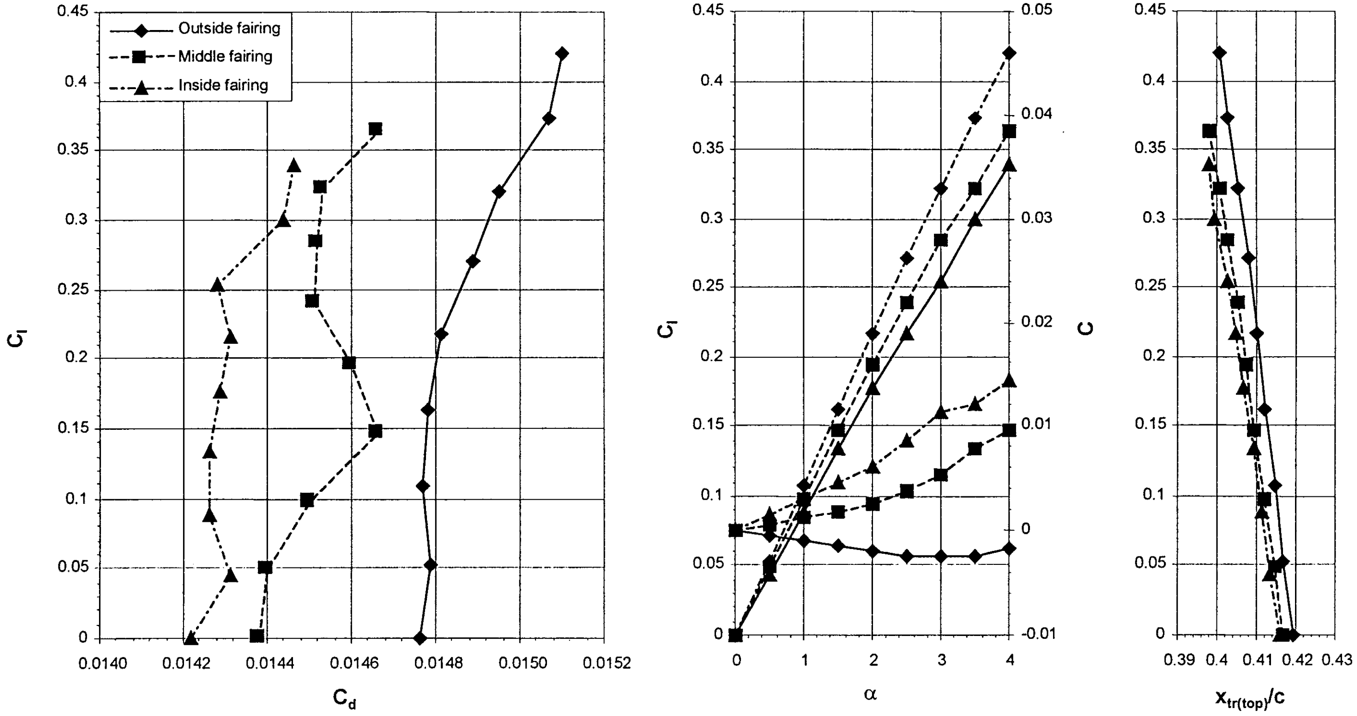

Figure C-10: XFoil (ver 6.8) analysis of fairing airfoils. Re = 850000, N_{crit} = 9, M=0.

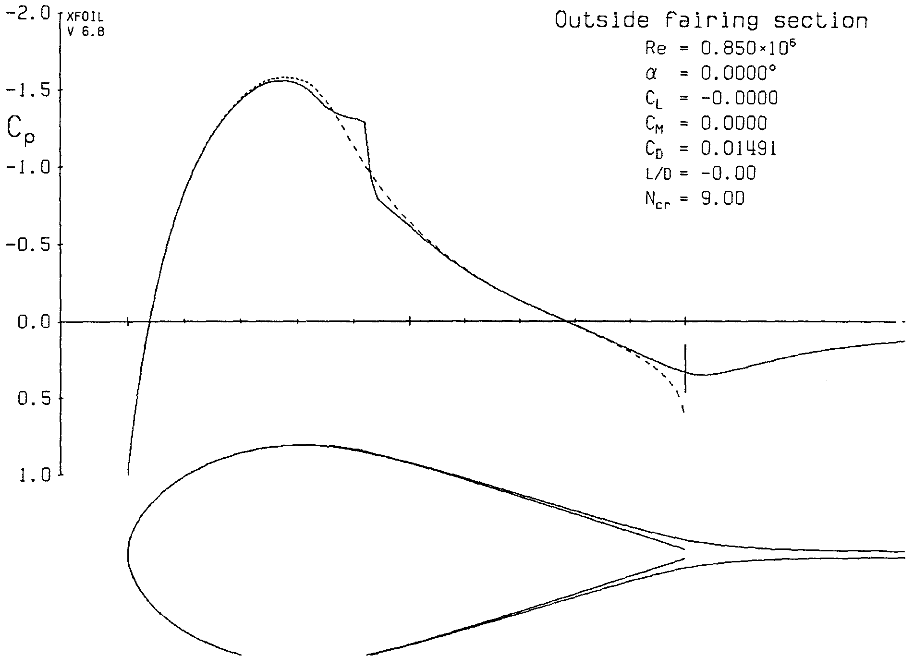

Figure C-11: Outside fairing section analysed at 0° AOA.

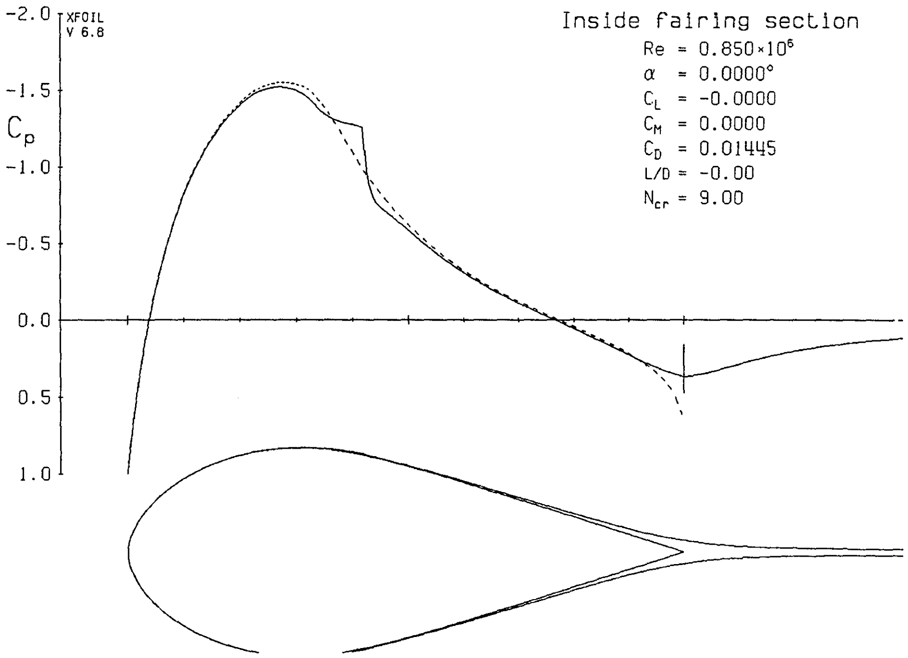

Figure C-12: Inside fairing section analysed at 0° AOA.

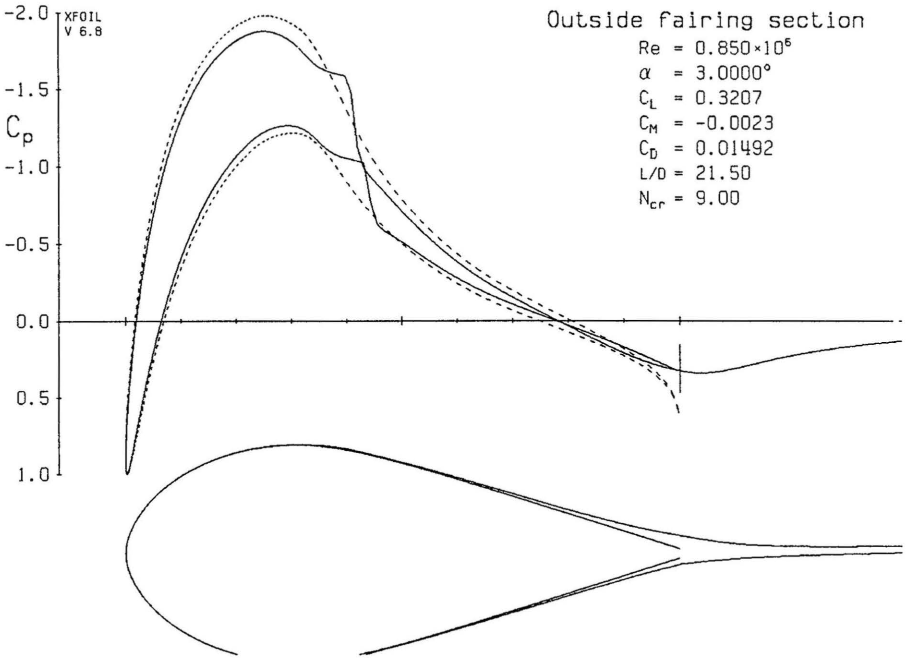

Figure C-13: Outside fairing section analysed at 3° AOA.

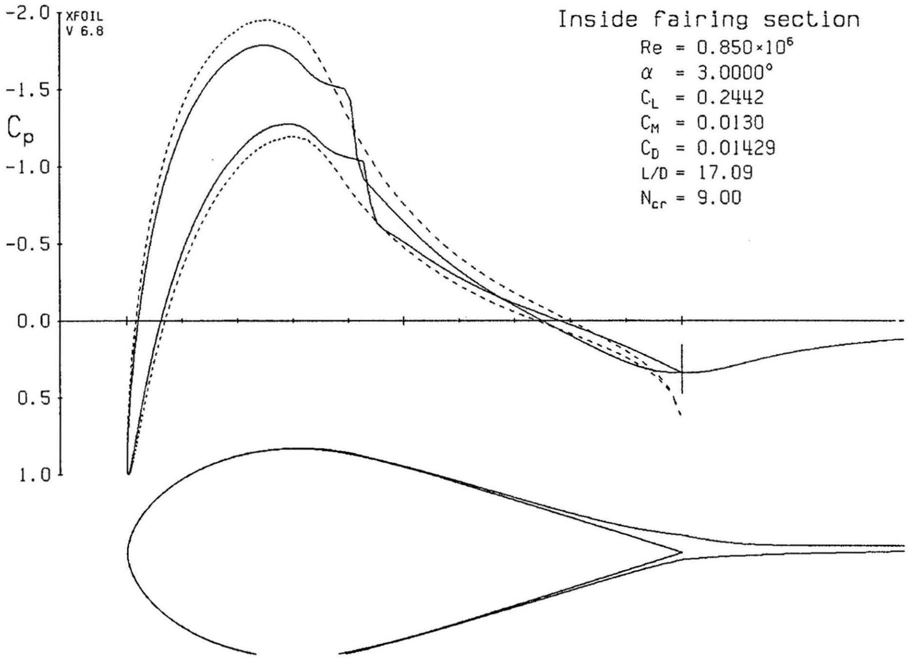

Figure C-14: Inside fairing section analysed at 3° AOA.

APPENDIX D: EVALUATION OF METHODS AND EQUIPMENT

APPENDIX D-1: SUMMARY OF EVALUATION TEST SERIES

Test matrix file	Hrp	α range	Model	Test section	Velocity	Output file	Comments
t0.tmf	-	-18 + 19 (+2°)	Generic model, tail on	Aero. - Ground effect strut	0	ls980034	Clino calibration
t0.tmf	-	-18 + 19 (+2°)	Generic model, tail on	Aero. - Ground effect strut	0	ls980035	Clino calibration
t0.tmf	180	0 – 16 (+2°), 9	Generic model, tail on	Aero - Ground effect strut	0	ls980036	Weight tares
t2.tmf	180	0 - 14 (+2°), 15, 16	Generic model, tail on	Aero - Ground effect strut	35	ls980037	Alpha scan
t2.tmf	220	0 - 18 (+2°)	Generic model, tail on	Aero - Ground effect strut	0	ls980038	Weight tares
t2.tmf	220	0 - 14 (+2°), 15 - 18 (+1°)	Generic model, tail on	Aero - Ground effect strut	35	ls980039	Alpha scan
t1.tmf	260	0 - 18 (+2°)	Generic model, tail on	Aero - Ground effect strut	0	ls980040	Weight tares
t2.tmf	260	0 - 14 (+2°), 15 - 18 (+1°)	Generic model, tail on	Aero - Ground effect strut	35	ls980041	Alpha scan
t2.tmf	300	0 - 14 (+2°), 15 - 18 (+1°)	Generic model, tail on	Aero - Ground effect strut	35	ls980042	Alpha scan
t2.tmf	340	0 - 14 (+2°), 15 - 18 (+1°)	Generic model, tail on	Aero - Ground effect strut	35	ls980043	Alpha scan
t1.tmf	340	0 - 18 (+2°)	Generic model, tail off	Aero - Ground effect strut	0	ls980044	Weight tares
t2.tmf	340	0 - 14 (+2°), 15 - 18 (+1°)	Generic model, tail off	Aero - Ground effect strut	35	ls980045	Alpha scan
t2.tmf	300	0 - 14 (+2°), 15 - 18 (+1°)	Generic model, tail off	Aero - Ground effect strut	35	ls980046	Alpha scan
t2.tmf	260	0 - 14 (+2°), 15 - 18 (+1°)	Generic model, tail off	Aero - Ground effect strut	35	ls980047	Alpha scan
t2.tmf	220	0 - 14 (+2°), 15 - 18 (+1°)	Generic model, tail off	Aero - Ground effect strut	35	ls980048	Alpha scan
t2.tmf	180	0 - 14 (+2°), 15, 16	Generic model, tail off	Aero - Ground effect strut	35	ls980049	Alpha scan
T1.tmf	180	0 - 16 (+2°)	Generic model, tail off	Aero - Ground effect strut	0	ls980050	Weight tares
t1.tmf	340	0 - 18 (+2°)	Generic model, i_t = +3°33'	Aero - Ground effect strut	0	ls980051	Weight tares
t2.tmf	340	0 - 14 (+2°), 15 - 18 (+1°)	Generic model, i_t = +3°33'	Aero - Ground effect strut	35	ls980052	Alpha scan
t2.tmf	260	0 - 14 (+2°), 15 - 18 (+1°)	Generic model, i_t = +3°33'	Aero - Ground effect strut	35	ls980053	Alpha scan
t2.tmf	180	0 - 14 (+2°), 15, 16	Generic model, i_t = +3°33'	Aero - Ground effect strut	35	ls980054	Alpha scan
t1.tmf	340	0 - 18 (+2°)	Generic model, i_t = -3°03'	Aero - Ground effect strut	0	ls980055	Weight tares
t2.tmf	340	0 - 14 (+2°), 15 - 18 (+1°)	Generic model, i_t = -3°03'	Aero - Ground eff strut	35	ls980056	Alpha scan
t2.tmf	260	0 - 14 (+2°), 15 - 18 (+1°)	Generic model, i_t = -3°03'	Aero - Ground eff strut	35	ls980057	Alpha scan
t2.tmf	180	0 - 14 (+2°), 15, 16	Generic model, i_t = -3°03'	Aero - Ground eff strut	35	ls980058	Alpha scan

Table D-1: Summary of evaluation tests

APPENDIX D-2: TAIL-ON DATA

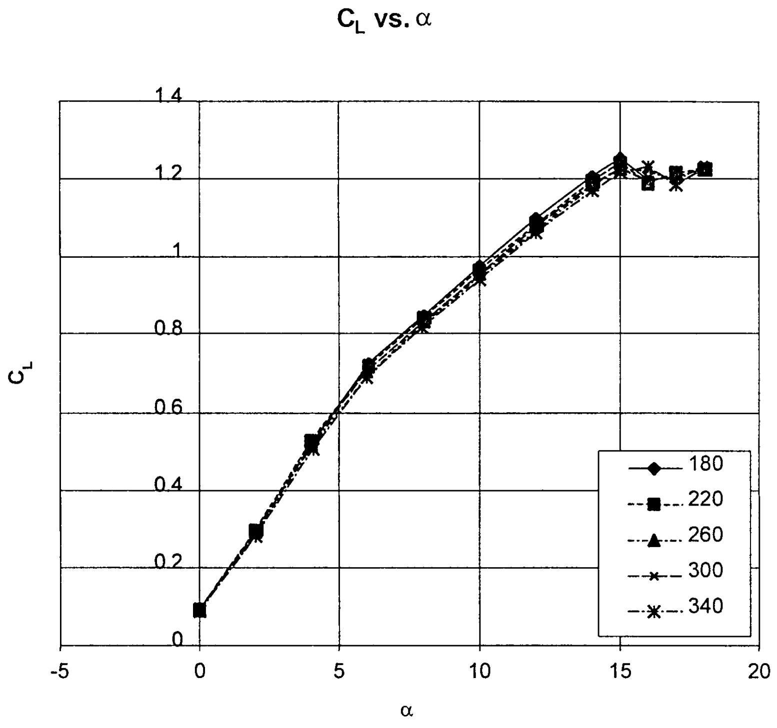

Figure D-1: Lift coefficient, tail-on

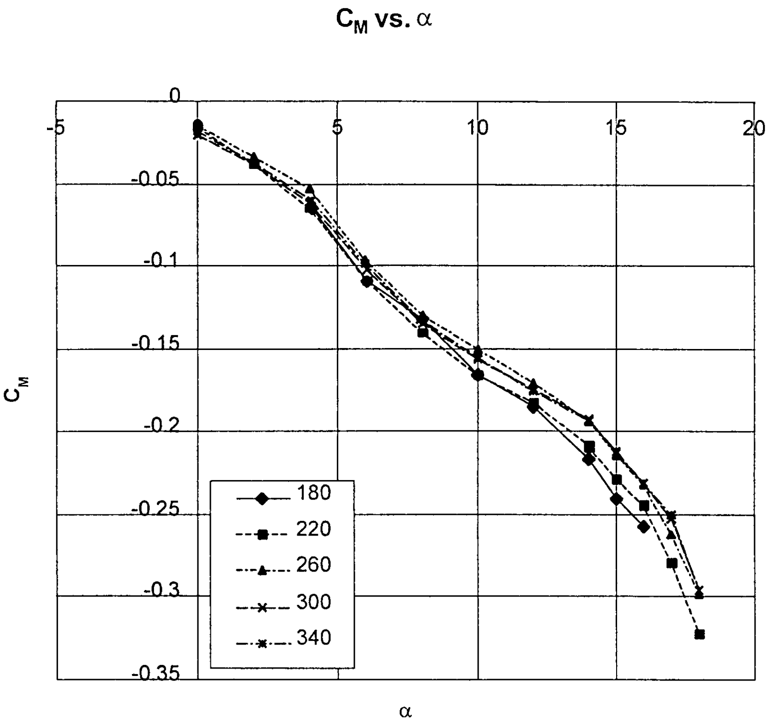

Figure D-2: Pitching moment coefficient, Tail-on

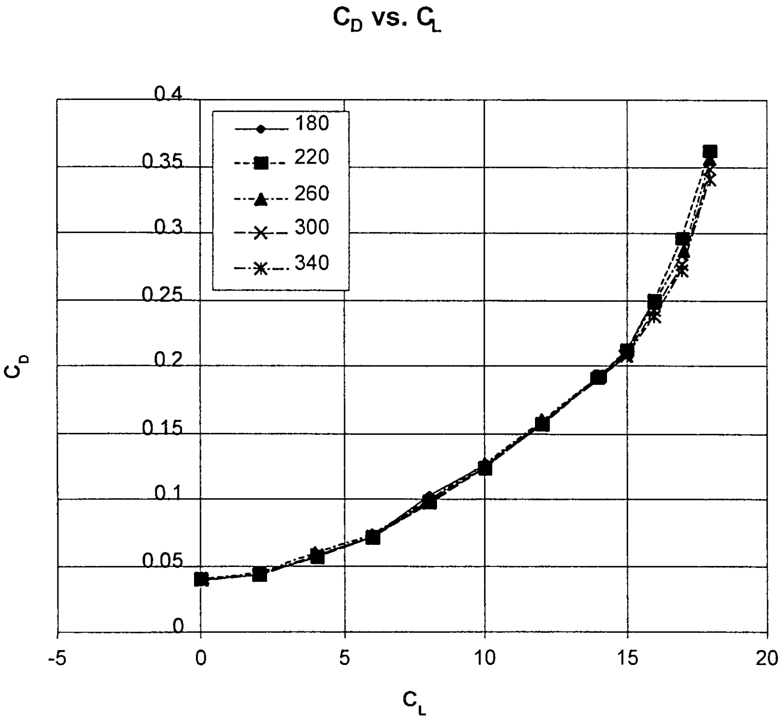

Figure D-3: Drag coefficient, Tail-on

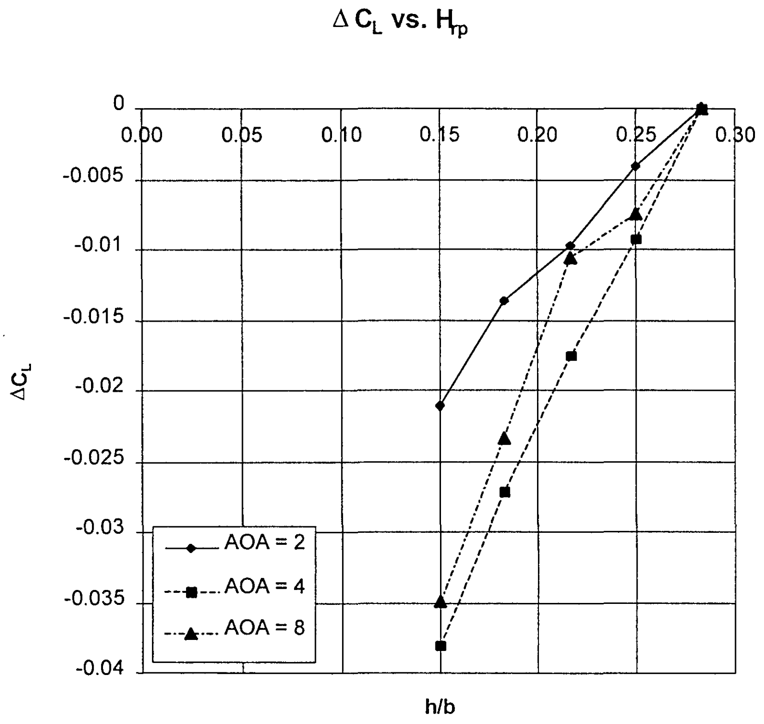

Figure D-4: Increment in lift-coefficient, tail-on

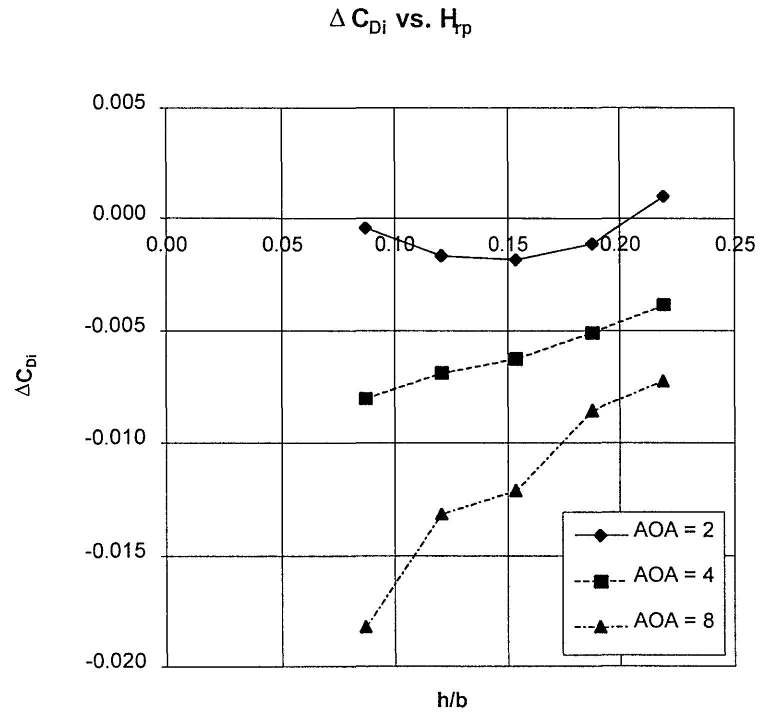

Figure D-5: Increment in induced drag coefficient, tail-on